Karlsruher Institut für Technologie

Fluorescence-Based Quantitative Characterization of Wnt Signaling Proteins Secreted by Living Cells

Zur Erlangung des akademischen Grades einer

DOKTORIN DER NATURWISSENSCHAFTEN (Dr. rer. nat.)

von der KIT-Fakultät für Physik des

Karlsruher Instituts für Technologie (KIT)

genehmigte

DISSERTATION

von

M.Sc. Ajaree Mongkolsittisilp

Tag der mündlichen Prüfung: 19.07.2024

Erstreferent: Prof. Dr. David Hunger

Korreferent: Prof. Dr. Kristin Grußmayer

Erklärung:

Ich versichere wahrheitsgemäß, die Arbeit selbstständig verfasst, alle benutzten Hilfsmittel vollständig und genau angegeben und alles kenntlich gemacht zu haben, was aus Arbeiten anderer unverändert oder mit Abänderungen entnommen wurde sowie die Satzung des KIT zur Sicherung guter wissenschaftlicher Praxis in der Fassung vom 05.10.2021 beachtet zu haben.

Karlsruhe, 12.06.2024 Ajaree Mongkolsittisilp

For my mom, Sivaporn Mongkolsittisilp, and my partner, Maximilian Schecher

Abstract

Wingless-related integration site (Wnt) proteins are evolutionarily conserved signaling molecules found across species. A unique characteristic of Wnt proteins is their lipid anchor, crucial for interactions with recipient cells but requiring structural adjustments for solubility in aqueous solutions. Wnt proteins are secreted via different transport modes, both on extracellular vesicles (EVs) and as non-EV-bound units.

This study characterized three human-derived Wnt proteins—WNT3a, WNT5a, and WNT11—labeled with mCherry2 or mScarlet. Using (ultra)centrifugation and size-exclusion chromatography, WNT-containing conditioned medium were separated into non-EV, small-EV, and large-EV fractions. Emission spectrum analysis revealed that over 95% of WNT proteins were secreted as non-EV-bound units. However, a dual-luciferase assay showed that EV-associated WNT3a proteins induced higher signaling activity than non-EV-bound WNT3a.

A combination of number and brightness (N&B) analysis and fluorescence intensity distribution analysis (FIDA) determined the number of WNT proteins per particle in the individual fractions. Each non-EV-bound WNT3a/5a/11 unit contained one WNT protein, while EVs exhibited a broad range, with most containing a single WNT3a/5a protein and a much smaller proportion containing tens of WNT3a/5a proteins. The average hydrodynamic radii of WNT-carrying particles, measured via fluorescence correlation spectroscopy (FCS), revealed similar sizes for WNT3a- and WNT5a-carrying particles. In contrast, non-EV-bound WNT11 appeared smaller than the non-EV-bound WNT3a/5a.

Further analysis suggested that non-EV-bound WNT3a and WNT5a proteins travel as lipid-containing nanoparticles. However, no positive results were obtained from co-diffusion and co-localization analyses with high-density lipoproteins. Additionally, results from dual-color fluorescence cross-correlation spectroscopy indicated that a small portion of WNT3a proteins co-diffuse with the Wnt-binding protein AFAMIN.

This dissertation integrates optical spectroscopy, dynamic light scattering, and fluorescence fluctuation spectroscopy to quantitatively characterize secreted WNT proteins, supported by robust data analysis. The experimental methodologies and associated challenges are discussed in detail throughout.

Table of Contents

Lists of Abbreviations

AB-CoraLite488	CoraLite Plus 488-conjugated Apolipoprotein AI antibody
AFAMIN	Afamin expressed in human
APD	Avalanche photodiode
BSA	Bovine serum albumin
DBSCAN	Density-based spatial clustering of applications with noise
DPBS	Dulbecco's Phosphate-Buffered Saline
EV	Extracellular vesicle
FCS	Fluorescence correlation spectroscopy
HEK293T	Human embryonic kidney 293T
MAD	Median absolute deviation
mWnt	Wnt protein expressed in mouse
N&B	Number and brightness
P100k	Pallet from centrifugation at 100,000 × g for 2 h
P14k	Pallet from centrifugation at 14,000 × g for 35 min
Rc	Recombinant
S/N	Signal-to-noise
SD	Standard deviation
SEM	Standard error of mean
sN&B	Scanning number and brightness
WNT	Wnt protein expressed in human

Additional abbreviations for specific chemicals and equipment that are rarely mentioned in the text can be found in Appendix A.1.

Lists of Variables

$\Delta\tau$	Shortest lag time in correlation function calculation, or temporal resolution (time bin) of intensity-time trace
ε	Molecular brightness
ε_1	Molecular brightness of monomeric fluorescent proteins
ε_λ	Extinction coefficient at the wavelength λ
ε_{A546}	Molecular brightness of Alexa Fluor 546
ε_{app}	Apparent molecular brightness
ε_n	Average molecular brightness of particles consisting of n fluorescent proteins
ε_r	Relative molecular brightness
η	Viscosity
θ_a	Angle between absorption transition dipole moment and polarization axis of incident light
θ_d	Angle between emission transition dipole moment and detected polarization axis
λ	Wavelength
λ_{em}	Maximum emission wavelength
λ_{ex}	Maximum excitation wavelength
μ	Mean
$\hat{\mu}$	Direction of absorption transition dipole moment and polarization axis of incident light
σ	*SD*
σ_n	*SD* of particle numbers
σ^2	Variance of photon counts
σ_d^2	Variance of photon numbers detected by the detector
σ_n^2	Variance of photon counts due to the change in the occupancy number
τ_D	Diffusional correlation time
τ_F	Characteristic time of the photophysical process

τ_R	Rotational correlation time
Φ_F	Quantum yield
A	Absorbance
c	Concentration
C_{12}	Concentration of particles with fluorophores of both species, i.e., concentration of bound species
C_{BG}	Proportion of emission spectrum of solution that comes from background
c_{chro}	Concentration of chromophores
C_{FP}	Proportion of emission spectrum of solution that comes from fluorescent protein
c_{pro}	Concentration of proteins
D	Translational diffusion coefficient
D_{app}	Apparent diffusion coefficient
D_R	Rotational diffusion coefficient
$\widehat{e_d}$	Detected polarization axis
$\widehat{e_e}$	Polarization axis of incident light
F	Photon number
$F(t)$	Times series of photon numbers
$F_i(t)$	Times series of photon numbers detected in channel i
f_m	Mobile fraction, i.e., proportion of mobile particles relative to the total number of particles
f_b	Fractions of fluorophores in the bright state
f_d	Fractions of fluorophores in the dark state
f_F	Photophysical fraction
f_R	Rotational amplitude
$G(\tau)$	Autocorrelation function with respect to lag time, τ, converging to 0 as $\tau \to \infty$
$\langle G(0) \rangle_{1-24}$	Average autocorrelation function calculated from all 24 segments
$G_D(\tau)$	Autocorrelation function of fluorescent particles of a single type undergoing 3-dimensional diffusion

$G_F(\tau)$	Autocorrelation function of fluorescent particles of a single type undergoing photophysical process
$G_i(0)$	Autocorrelation function amplitude of the fluorescence species i
$G_{large\ \tau}$	Autocorrelation function values at lag times equal to or greater than 10 ms
$G_R(\tau)$	Autocorrelation function of fluorescent particles of a single type undergoing rotational Brownian motion
$G_x(0)$	Cross-correlation function amplitude
$G_i(0)$	Amplitude of autocorrelation function from fluorophore species i
$g(\tau)$	Autocorrelation function with respect to lag time, τ, converging to 1 as $\tau \to \infty$
$g_{12}(\tau)$	Correlation function between intensity-time series $F_1(t)$ and $F_2(t+\tau)$, converging to 1 as as $\tau \to \infty$
$g_{av}(\tau)$	Symmetrized cross-correlation function, calculated from $\big(g_{12}(\tau) + g_{21}(\tau)\big)/2$
I	Fluorescence intensity (in counts per s or Hz)
I_{BG}	Intensity/emission spectrum of background
I_C	Background-corrected luminescence intensity of control luciferase in target cells
I_{FP}	Intensity/emission spectrum
I_{max}	maximum fluorescence intensity
I_r	Intensity normalized at the maximum excitation/emission
I_S	Background-corrected luminescence intensity of TCF/LEF luciferase in target cells
k_0	Decay rate
k_1	Absorption rate
k_B	Boltzmann constant
k_b	Rate at which the fluorophore transition from the dark to bright state
k_d	Rate at which the fluorophore transition from the bright to dark state
l	Optical path length
M_M	Molecular mass
N	Average number of fluorescently labeled particles in the observation volume
n	Number of fluorescent proteins/fluorophores per particle

NA	Numerical aperture
n_{app}	Apparent number of particles
N_{WNT}	Number of WNT proteins per particle
P	Laser power
P_a	Probability that a fluorophore absorbs light
P_d	Probability that an emitted photon is detected
PD	Power density
p_f	Apparent fluorescence probasbility
p_i	Probability that a fluorescent protein emits fluorescence
P_{sat}	Saturation excitation power
r_{Airy}	Radius of the Airy disk
r_h	Hydrodynamic radius
S	Structure parameter of the observation volume
S/N	Signal-to-noise ratio
S_0	Population in the ground electronic state
S_1	Population in the first electronic excited state
T	Temperature
t	Time
T_{tot}	Total recording time
V	Volume
V_{eff}	Effective volume
V_i^{ph}	Vector representing photon detected in channel i
$W(x,y,z)$	Spatial distribution of the detected light
w_0	Lateral extension of the detection volume, measured from the center to the point where the intensity drops to $1/e^2$ of the maximum
$w_{0,12}$	Root mean square of $w_{0,i}$ of both lasers
z_0	Axial extension of the detection volume, measured from the center to the point where the intensity drops to $1/e^2$ of the maximum

1. Introduction

Wnt (Wingless-related integration site) proteins are essential signaling molecules that activate Wnt signaling pathways in cells. They have been conserved throughout evolution in various species, including 19 different types that appear in humans[1]. The Wnt signaling pathway is one of the fundamental regulators for multiple cellular functions, such as growth, differentiation, and tissue homeostasis[2,3]. Malfunctions in the Wnt signaling pathway have been associated with a wide range of human diseases, such as cancer[4,5], neurodegenerative disease[6,7], and growth abnormalities[8,9]. Therefore, understanding the molecular properties of Wnt proteins and the mechanisms underlying Wnt signaling is beneficial for advancing therapeutic treatments and biological studies.

The Wnt signaling pathway entails the transfer of Wnt proteins from Wnt-producing cells to receiving cells, where the Wnt proteins interact with cell-surface receptors and/or co-receptors[10-12]. In order to understand the mechanisms of Wnt protein binding, researchers acquire Wnt proteins by collecting conditioned medium[†] from the Wnt-producing cells[13-16]. Despite the significance of this process, the physical properties of Wnt proteins present in the conditioned medium remain largely unknown.

Prior to their secretion, the majority of Wnt proteins undergo a post-translational lipidation[17], which adds an additional lipid anchor that is crucial for their binding interactions with receptor cells[18-21]. This lipid anchor is non-polar and needs to be protected in the aqueous intercellular environment in order to maintain the solubility of Wnt proteins. Prior studies have

[†] *Conditioned medium* is the liquid in which cells have been cultivated, and it contains biologically active components secreted from the cells.

proposed various possibilities for the structural arrangement of Wnt proteins to facilitate their diffusion through the hydrophilic intercellular environment (shown in Figure 1.1). These options include the formation of homo-oligomers[22], forming complexes with Wnt-binding proteins[23,24], the association of Wnts with lipoproteins or micelles[25,26], or the transportation of Wnts through extracellular vesicles‡ (EVs)[27].

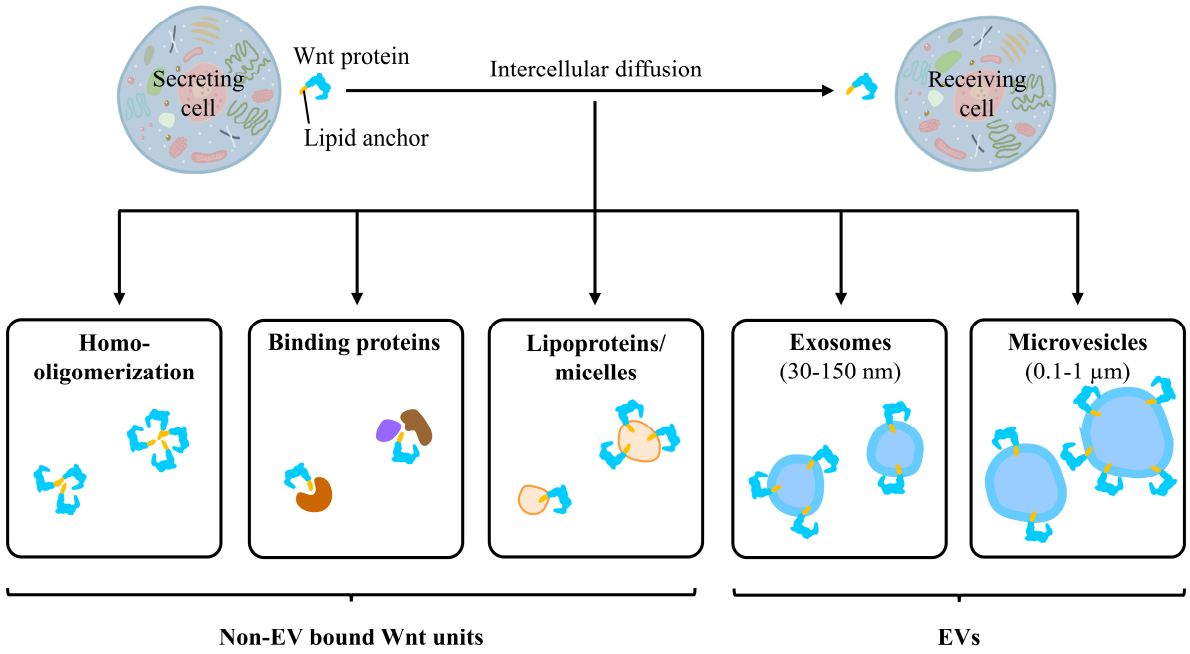

Figure 1.1. Arrangements of Wnt Proteins for Diffusion Through Intercellular Environments. The figure depicts how the lipid anchors (depicted in yellow) of the Wnt proteins (depicted in blue) can be protected, facilitating their stable diffusion in the hydrophilic extracellular space. From left to right, the following structural arrangements are illustrated: (1) homo-oligomerization of Wnt proteins[22], (2) formation of complexes with binding proteins (depicted in purple and brown)[23,24], (3) association with lipoproteins or micelles[25,26], (4) transport via exosomes[28], and (5) transport via microvesicles[29]. Exosomes and microvesicles are members of EVs, whereas Wnt oligomers, Wnt-binding protein complexes, lipoproteins, and micelles diffuse independently of EVs.

Recently, it has been suggested that Wnt proteins secreted via different transport mechanisms may possess varying degrees of biological functionality[22,27]. This raises the question of whether Wnt proteins exhibit identical biophysical properties across all transport modes. Understanding these properties is essential for elucidating the diverse mechanisms of

‡ *Extracellular vesicles* are lipid bilayer-enclosed particles formed secreted by cells that cannot replicate themselves[30].

Wnt signaling and enhancing the therapeutic potential of targeting Wnt-related pathways. This dissertation aims to address this question by characterizing the properties of Wnt proteins secreted by living cells, thereby providing new insights into the fundamental aspects of Wnt signaling.

The investigations of Wnt proteins were initially performed via in-vitro biochemical techniques such as chromatography and Western Blot[20,31], as well as structural modeling[32]. These approaches face constraints in terms of temporal resolution, specificity, sensitivity, and the ability to analyze Wnt proteins in their native form. In a pivotal advancement in 2018, DNA constructs were innovatively engineered for the expression of fluorescent protein-tagged mouse Wnt3a (mWnt3a) proteins[22]. By fusing each Wnt protein with a single fluorescent protein, this methodology enables precise quantification of secreted Wnt proteins and facilitates the specific observation of their dynamics. Consequently, this development opened up the possibility for the quantitative observation of Wnt proteins in real time and in a non-invasive manner, even in the presence of many unlabeled proteins.

The fluorescently labeled Wnt proteins can be characterized with a single-molecule sensitivity using advanced fluorescence fluctuation spectroscopy. Fluorescence correlation spectroscopy (FCS), developed by Magde, Elson, and Webb in the 1970s[33,34], has been extensively utilized in various research laboratories for the purpose of quantifying the number and diffusion characteristics of fluorescent particles within the small detection volume generated by a confocal microscopy setup. Additionally, Digman et al.[35] introduced number and brightness (N&B) analysis, which uses changes in fluorescence intensity to extract information about the brightness and stoichiometry of diffusing particles. Furthermore, fluorescence intensity distribution analysis (FIDA), proposed by Kask et al.[36,37] allows for the analysis of brightness distributions derived from photon counting histograms.

This dissertation presents a comprehensive analysis of three variants human Wnt (WNT) proteins — WNT3a, WNT5a, and WNT11 — secreted from human embryonic kidney 293T (HEK293T) cells. Each variant was fluorescently labeled with either mCherry2 or mScarlet , resulting in the following protein fusions: mCherry2-WNT3a, mScarlet-WNT3a, mCherry2-WNT5a, mScarlet-WNT5a, mCherry2-WNT11, and mScarlet-WNT11. The conditioned medium collected from the target protein fusions was separated into three distinct fractions based on particle size: (1) a large-EV fraction containing microvesicles[†]; (2) a small-EV fraction containing exosomes[‡]; and (3) a non-EV fraction, possibly encompassing Wnt

proteins secreted in the form of oligomers, lipoproteins, micelles, and binding proteins. To assess the distribution of WNT proteins across these three fractions, as well as the biophysical characteristics of WNT-transporting particles within each fraction, a combination of optical spectroscopy, dynamic light scattering, and fluorescence fluctuation spectroscopy was employed.

The remainder of this dissertation is structured as follows: Chapter 2 presents a summary of the fundamental concepts underlying this investigation. Chapter 3 supplies a detailed description of the materials and methods employed in this research. Chapters 4 through 7 present the results and discussions, with individual sample results included within the chapters or in the corresponding appendices. Chapter 8 presents the concluding remarks of the study as well as comments on potential areas for improvement and future research prospects. Each chapter is intended to be independent and self-contained.

For further details, Appendices A–E provide supplemental information corresponding to Chapters 3–7, respectively. Appendix F contains the custom programming scripts utilized in this research, while Appendix G lists the locations of all raw data files.

[†] *Microvesicles,* or *ectosomes,* are EVs derived from the cell plasma membrane, typically ranging from 100 nm to 1 μm in diameter[38,39].

[‡] *Exosomes* are a type of EVs formed within the endosomes of cells with diameter between 30 and 150 nm[29,38,40].

2. Background Knowledge

This chapter provides the necessary background information to comprehend this dissertation in its entirety. The first section of this chapter covers the theoretical background of fluorescence. The next section discusses the basic principles of fluorescence fluctuation spectroscopy, outlining detailed information on number and brightness (N&B) analysis, fluorescence correlation spectroscopy (FCS), and fluorescence intensity distribution analysis (FIDA). Lastly, a summary of the Wnt signaling pathway and Wnt protein transport is presented.

2.1 Fluorescence

Fluorescence is the spontaneous emission of radiation resulting from wavelength-specific excitation. When a molecule is excited, it transitions from the electronic ground state to an electronic excited state. Upon relaxation from this excited state, the molecule may undergo several processes, one of which is fluorescence, emitting light. These processes shall now be examined using the Perrin-Jablonski diagram.

2.1.1 Perrin-Jablonski Diagram

The Perrin-Jablonski diagram[41,42], or Jablonski diagram, illustrates the energy levels and possible transitions of fluorescent molecules, as shown in Figure 2.1. The diagram depicts various energy levels as horizontal lines ascending from bottom to top. The left side shows the

singlet electronic states (S_0, S_1, S_2, ...) which have a total spin angular momentum of zero, while the right side shows the triplet state (T) which has a total spin of one. Each electronic state consists of multiple vibrational energy levels (v), denoted by v = 0, 1, 2, etc. The thickest horizontal lines show the energy levels with v = 0. Transitions between energy states are illustrated as vertical arrows: solid arrow indicate radiative transitions, and dotted arrows indicate non-radiative transitions.

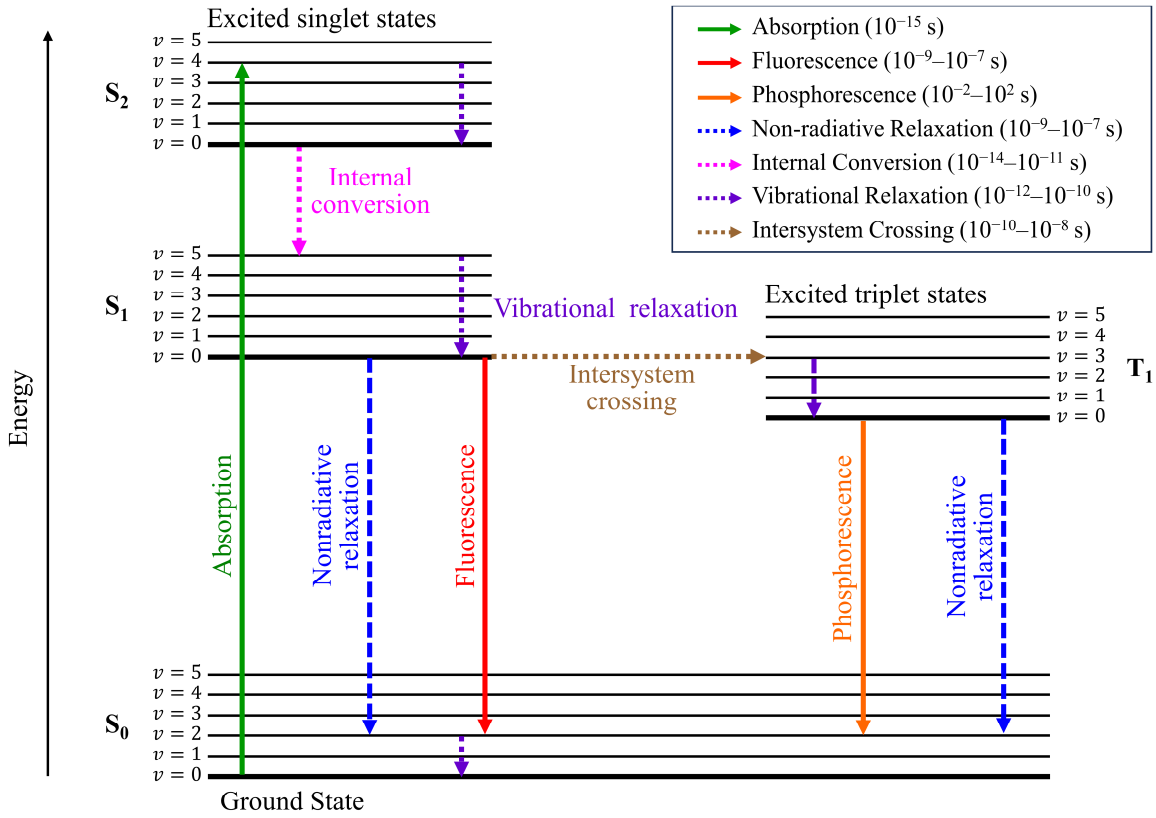

Figure 2.1. Perrin-Jablonski Diagram. The horizontal lines represent the energy levels of a molecule, with increasing energy from bottom to top. S and T respectively represent singlet (paired spin) and triplet (unpaired spin) states. The arrows represent nonradiative (dashed) and radiative (solid) energy transitions

According to Boltzmann's law, the proportion of molecules at the lowest vibrational level of the ground state, S_0 ($v = 0$), is approximately one at room temperature. In this electronic state, electrons fill the lowest energy molecular orbitals, up to the limit of their degeneracy. The highest energy occupied molecular orbital may not be fully occupied. In $\sim 10^{-15}$ s, light absorption advances the electron from the highest energy occupied molecular orbital to the lowest unoccupied molecular orbital or higher without changing its spin, transitioning the

molecule from the S_0 ($v = 0$) state to one of the singlet excited electronic states. Due to angular momentum conservation, direct excitation to a triplet excited state is not probable.

The excited state is a non-equilibrium state; therefore, the molecule will eventually lose energy and revert to the ground state. Upon entering an excited electronic state, the molecule undergoes rapid vibrational relaxation characterized by the energy dissipation through intermolecular collisions. Additionally, internal conversion can occur, typically facilitated by coupling between electronic and vibrational states. Vibrational relaxation and/or internal conversion relax the molecule to the lowest vibrational energy level of the first excited state (S_1 ($v = 0$)) state within 10^{-13}–10^{-10} s.

The molecule in the S_1 ($v = 0$) state may return to one of the vibrational energy levels of the ground (S_0) state within a timescale of 10^{-9}–10^{-7} s either through radiative relaxation, resulting in fluorescence, or non-radiative relaxation. Subsequently, the molecule further relaxes to the lowest vibrational energy level of the ground state via vibrational relaxation.

Another possible transition from the excited electronic state is intersystem crossing to an isoenergetic vibrational level in the triplet electronic state. This transition is generally rare and only occurs due to spin-orbit coupling. Intersystem crossing is sufficiently fast (10^{-10}–10^{-8} s) and could compete with fluorescence. During the transition from the triplet excited state (T_1) to the ground state (S_0), non-radiative de-excitation is predominant over radiative transition (phosphorescence). Phosphorescence, if observed, occurs at a significantly slower timescale than fluorescence, typically in the range of 10^{-2}–10^{2} s.

2.1.2 Characteristics of Fluorescence

Kasha's Rule

As fluorescence emission originates from the S_1 ($v = 0$) state regardless of the initial excited energy level, its properties are independent of the excitation wavelength[43].

Stokes Shift

According to Stokes' law[44], the wavelength of fluorescence emission always exceeds that of absorption. This increase in wavelength, termed the Stokes shift, predominantly arises from the energy dissipation due to solvent reorientation[45], with additional contributions from vibrational relaxation and internal conversion to a lesser extent.

Fluorescence Lifetime

Due to the random nature of fluorescence, fluorophores that are in the excited electronic state do not relax to the ground state simultaneously. In the simplest scenario, relaxation time distribution follows a single exponential decay, and the fluorescence lifetime denotes the time at which 63% of fluorophores in the excited electronic state have decayed.

Quantum Yield and Brightness

Quantum yield is defined as the ratio of the number of photons emitted as fluorescence to the number of absorbed photons is defined as quantum yield**.** While energy yield is always less than one due to non-radiative energy transfer, the quantum yield may approach unity if the non-radiative decay rate is much lower than the radiative decay rate. Conventionally, the brightness of a fluorophore is given by the product of its quantum yield (Φ_F) and the extinction coefficient (ε_λ) at the maximum excitation wavelength (λ_{ex}) This relationship is expressed as:

$$Brightness = \frac{\Phi_F \cdot \varepsilon_{\lambda_{ex}}}{1000}. \tag{2.1}$$

The dividing factor of 1000 is only a conventional scale factor for brightness comparison.

Asymptotic Relationship between Fluorescence Intensity and Excitation Power

When an ensemble of fluorophores is excited with increasing excitation power, the probability of excitation and photon emission initially rises proportionally with the excitation power. As a result, the average fluorescence intensity (I) is linearly dependent on the excitation power (P). At higher excitation powers, however, optical saturation occurs as a significant fraction of fluorophores reside in the electronic excited state, temporarily preventing further excitation.

Additionally, photobleaching, combined with flickering and blinking, reduces the effective number of fluorophores available for excitation and photon emission. Consequently, the fluorescence intensity transitions to an asymptotic relationship with increasing excitation power.

The relationship between I and P can be obtained by solving for the steady-state solution of the differential equations describing the temporal evolution of electronic state population occupancy. For instance, the dependence of I on P for molecules exhibiting two singlet states and one triplet state under continuous wave excitation is[46]

$$I = \frac{I_{max} \cdot P}{P + P_{sat}}, \tag{2.2}$$

where I_{max} denotes the maximum fluorescence intensity, and P_{sat} represents the saturation intensity, at which I attains half of its maximum value.

Generally, the values of I_{max} and $I_{ex,sat}$ are influenced by the photophysical characteristics and the rotational diffusion of the molecule[47], as well as the type of laser employed (continuous wave or pulsed excitations)[48]. Although the exact relationship between I and P of a specific system is intricate[46] and necessitates prior knowledge of electronic state populations and their transition rates[49], Equation (2.2) remains a reliable approximation in most scenarios[50].

2.1.3 Extrinsic Fluorophores

Organic Dyes

Organic dyes are planar molecules with sizes around 1–2 nm and molecular masses between 0.5–1.5 kDa. They usually exhibit large extinction coefficients (10^4–10^5 M^{-1} cm^{-1}) and high quantum yields[51]. The ATTO and Alexa Fluor dye families[52] are typical microscope calibration standards due to their stability. In particular, Alexa Fluor 488 and Alexa Fluor 546 are suitable for system calibration via FCS because they do not enter a triplet state (see the effect of triplet in FCS in Section 2.2.2).

Fluorescent Proteins

Common fluorescent proteins, belonging to the green fluorescent protein (GFP)-like family, consists of approximately 240 amino acids folded into a cylindrical structure measuring 2–3 nm in width and 4 nm in length (see Figure 2.2). Enclosed within this barrel structure is a chromophore, formed during a maturation process. Typically, fluorescent proteins mature within minutes to a few hours[53,54]. However, not all fluorescent proteins reach their mature form, and the proportion of functional fluorescent proteins to total fluorescent proteins is known as *maturation efficiency*. Upon excitation, the functional chromophores have a probability to emit fluorescence with average lifetime ranging from 1 to 4 ns[41,55].

To label target proteins with fluorescent proteins, genetic engineering enables the design of a DNA construct that leads to the synthesis of target proteins linked to fluorescent proteins by a short amino acid linker. A well-designed DNA construct ensures the specific binding of the fluorescent proteins to the target proteins without interfering with their activities. Following the transfection of the DNA construct into cells, the cells produce fluorescent protein-tagged proteins based on the DNA sequence.

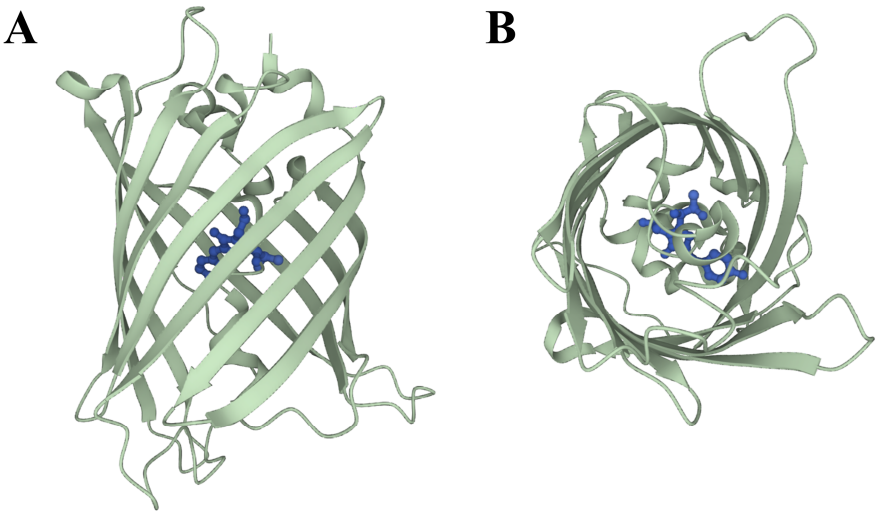

Figure 2.2. 3D Structure of GFP-like Fluorescent Proteins. Using eGFP as an example of fluorescent proteins, the graphic illustrates the overall barrel structure (A) and the top view of the barrel structure (B) with the chromophore (in blue) in the center. The figures were depicted based on the crystal structure obtained from[56].

2.2 Fluorescence Fluctuation Spectroscopy in Confocal Setup

Fluorescence fluctuation spectroscopy encompasses a group of analytical techniques that investigate the fluctuations in fluorescence intensity[57]. With a minuscule detection volume, such as that achieved through confocal microscopy, these techniques attain a single-molecule sensitivity.

In a confocal microscope, the objective focuses the laser beam to illuminate particles within the sample. Fluorescent particles absorb energy from the laser light and subsequently emit fluorescence. The confocal detection optics direct the emitted photons towards the detector, while a pinhole positioned before the detector excludes out-of-focus light, thereby creating a limited (~1 fL) detection volume.

When the sample volume significantly exceeds the laser focus, the effective *detection volume*, also known as the *observation volume*, is determined by the illuminated region of the sample from which the emitted photons are detected. The spatial distribution of the laser focus ($W(x,y,z)$) can be approximated as a 3D Gaussian function:

$$W(x,y,z) = \frac{2P}{\pi w_0} e^{\frac{-2x^2}{w_0^2}} e^{\frac{-2y^2}{w_0^2}} e^{\frac{-2z^2}{z_0^2}}, \tag{2.3}$$

where P is the laser power, w_0 is the $1/e^2$ lateral extension, and z_0 is the $1/e^2$ axial extension. When pulsed excitation is used, the average power can be used for P as long as the timescale of the observed phenomena is significantly longer than the pulse period[48]. The effective detection volume (V_{eff}) or sometimes called the observation volume, can be calculated by:

$$V_{eff} = \pi^{3/2} w_0^2 z_0 . \tag{2.4}$$

In the ideal scenario, detected photons arise solely from fluorescence generated by fluorophores within the laser focus (Figure 2.3). The average intensity is determined by the number of fluorescent particles present within the detection volume. Intensity fluctuations occur as particles diffuse into and out of the confocal volume, with the diffusion of brighter particles resulting in higher fluorescence intensity variations. Additionally, smaller particles exhibit shorter diffusion times through the observation volume, leading to correspondingly shorter intensity bursts.

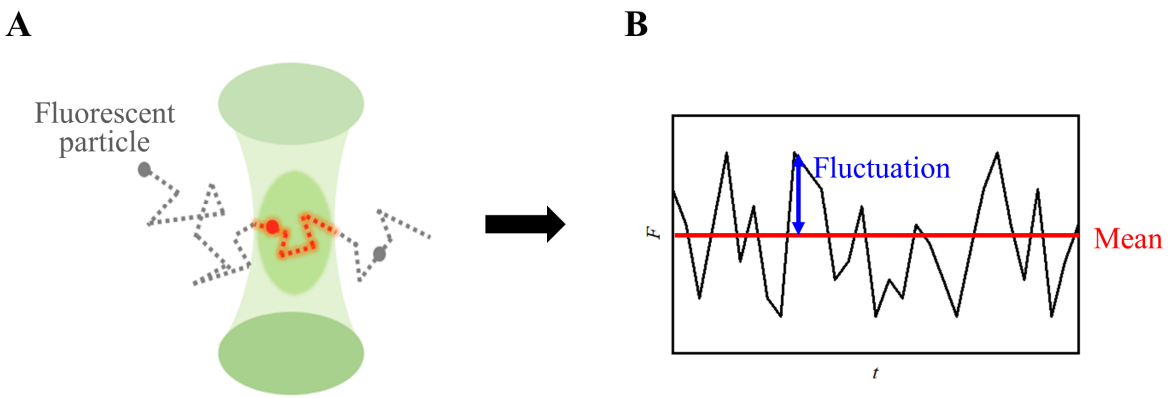

Figure 2.3. Intensity-Time Trace Resulting from Fluorescent Particle Diffusion

A: A fluorescent particle (depicted in grey) diffuses through the laser focus (depicted in green). The fluorescence signal is detected only when the particle is within the laser focus and emits fluorescence (depicted in red).

B: An intensity-time trace is constructed from the photon number (F) detected over time (t).

In fluorescence fluctuation spectroscopy, photon arrival times are recorded over time, and photons are sorted with a defined time bin to generate an intensity-time trace. Under experimental conditions, the signal-to-noise (S/N) ratio depends on the mean intensity (I) per second, total time of recording (T_{tot}), time bin ($\Delta\tau$), and the average number of particles in the observation volume (N) as follows[58-60]:

$$S/N = I \cdot \sqrt{\frac{T_{tot}\Delta\tau}{1+1/N}}. \tag{2.5}$$

This equation indicates that the minimum concentration of sample solution should ensure at least one particle per observation volume, i.e., $N \geq 1$. For $N > 1$, further increases in concentration do not significantly affect the S/N ratio. Various fluorescence fluctuation spectroscopy techniques address efficient methods for extracting mean intensity and quantifying intensity fluctuations in the presence of background noise. The following sections discuss two fluorescence fluctuation spectroscopy techniques: N&B analysis and FCS.

2.2.1 Number and Brightness (N&B) Analysis

N&B analysis[35,61] is a straightforward yet effective approach. It derives N and the molecular brightness (ε), which is the average number of emitted photons per particle, from only the mean and variance of photon numbers as follows:

Consider fluorescent particles diffusing through the confocal volume. The average photon count ($\langle F \rangle$) is

$$\langle F \rangle = \varepsilon N \, . \tag{2.6}$$

Even if the number of particles inside the observation volume remains constant, the number of photons detected would fluctuate. In photon counting detectors, the detected photon number approximately follows a Poisson distribution[62], thus the variance due to the shot noise of the detector (σ_d^2) is

$$\sigma_d^2 = \langle F \rangle = \varepsilon N \, . \tag{2.7}$$

As particles diffuse through the detection volume, the photon number fluctuates due to the change in the occupancy number. As diffusing particles obey Poissonian statistics, the standard deviation (SD) of the particle number is equal to $\sqrt{N}$. The SD of the emitted fluorescence is $\varepsilon\sqrt{N}$, and the variance due to the change in the occupancy number (σ_n^2) is

$$\sigma_n^2 = \varepsilon^2 N \, . \tag{2.8}$$

In total, the variance of the photon counts (σ^2) is

$$\sigma^2 = \sigma_d^2 + \sigma_n^2 = \varepsilon N + \varepsilon^2 N \, . \tag{2.9}$$

Solving Equations (2.6) and (2.9) simultaneously gives

$$N = \frac{\langle F \rangle^2}{\sigma^2 - \langle F \rangle} \tag{2.10}$$

and

$$\varepsilon = \frac{\sigma^2 - \langle F \rangle}{\langle F \rangle} \, . \tag{2.11}$$

Equations (2.10) and (2.11) are the key equations for determining the particle number and their average molecular brightness, thus the name N&B analysis. N&B analysis does not require a continuous intensity record, and the measurement duration is substantially smaller compared to other prominent methods such as FCS (Section 2.2.2). This decreases photobleaching and the risk of physiological processes occurring in cells during in-vivo measurement.

Background Correction

In the presence of an uncorrelated background of intensity F_0, the mean photon count is contaminated by the background intensity: $\langle F \rangle = \varepsilon N + F_0$. Performing derivation steps as described in the preceding section yields

$$N = \frac{(\langle F \rangle - F_0)^2}{\sigma^2 - \langle F \rangle}, \tag{2.12}$$

and

$$\varepsilon = \frac{\sigma^2 - \langle F \rangle}{\langle F \rangle - F_0}. \tag{2.13}$$

Effect of Non-Fluorescent Fluorescent Protein Fractions on Molecular Brightness

Due to fluorescent protein immaturities (Section 2.1) and photophysical processes such as long-lived dark states[63], a portion of fluorescent proteins are in a non-fluorescent state.

Consider an ensemble of identical particles, each consisting of n fluorescent proteins of brightness ε, under laser excitation. If n = 1, each particle is either 'bright' (containing a functional fluorescent protein) or undetected (containing non-functional fluorescent protein). Only the former contributes to the molecular brightness, so the ensemble-average molecular brightness is unaffected by the presence of the non-functional fluorescent proteins. When $n > 1$, some fluorescent proteins are functional, enabling particle detection, yet the total fluorescence intensity from the particle is reduced compared to the scenario where all fluorescent proteins in the particle are bright.

To account for the proportion of fluorescent proteins in the dark state, the apparent fluorescence probability (p_f), which is the probability that a fluorescent protein emits fluorescence, was defined. The probability of a particle having i bright fluorescent proteins and $n - i$ dark fluorescent proteins can be modelled by a binomial distribution: $p_i = \binom{n}{i} p_f^i (1 - p_f)^{n-i}$. Consequently, the ensemble-average molecular brightness (ε_n) can be expressed as[64,65]

$$\varepsilon_n = \varepsilon_1 + \varepsilon_1 (n - 1) p_f, \tag{2.14}$$

where p_f is the apparent fluorescence probability of the fluorescent proteins.

2.2.2 Fluorescence Correlation Spectroscopy (FCS)

FCS is the most well-established and widely used approach among the various fluorescence fluctuation spectroscopy techniques. The analysis of temporal variations in fluorescence intensity allows for the quantification of diffusion characteristics and concentration of fluorescent particles.

In comparison to N&B analysis, FCS incorporates an additional statistical procedure to examine the intensity fluctuations, namely the calculation of autocorrelation function and cross-correlation functions. The autocorrelation function, $g(\tau)$, reflects the degree of resemblance between a times series of photon numbers ($F(t)$) and itself at a time τ subsequent to it ($F(t+\tau)$) is computed by

$$g(\tau) = \frac{\langle F(t)F(t+\tau)\rangle}{\langle F(t)\rangle\langle F(t+\tau)\rangle}. \tag{2.15}$$

For stationary processes, i.e., processes in which the average value is unaffected by the time point at which the system is observed, $\langle F(t)\rangle = \langle F(t+\tau)\rangle$. In this case, the autocorrelation function becomes

$$g(\tau) = \frac{\langle F(t)F(t+\tau)\rangle}{\langle F(t)\rangle^2}. \tag{2.16}$$

The fluorescence intensity is a combination of the average intensity and the fluctuations, $\delta F(t)$: $F(t) = \langle F(t)\rangle + \delta F(t)$. Substituting this into the above equation yields

$$g(\tau) = \frac{\langle F(t)F(t+\tau)\rangle}{\langle F(t)\rangle^2} = \frac{\langle \delta F(t)\delta F(t+\tau)\rangle}{\langle F(t)\rangle^2} + 1\,. \tag{2.17}$$

Similarly, the cross-correlation function, which quantifies the degree of similarity between one intensity-time series ($F_1(t)$) and another intensity-time series at a later time τ ($F_2(t+\tau)$) is calculated by

$$g_{12}(\tau) = \frac{\langle F_1(t)F_2(t+\tau)\rangle}{\langle F_1(t)\rangle\langle F_2(t+\tau)\rangle} = \frac{\langle \delta F_1(t)\delta F_2(t+\tau)\rangle}{\langle F_1(t)\rangle\langle F_2(t)\rangle} + 1\,. \tag{2.18}$$

Differences between the cross-correlation functions obtained from calculating $g_{12}(\tau)$ and $g_{21}(\tau)$ could arise from asymmetrical relationships between the processes causing fluctuations in the two detection channels. Examples of such processes include flow or active transport between the observation volumes in which $F_1(t)$ and $F_2(t)$ are detected, or differences in photobleaching rates of the fluorophores. However, in systems that are in equilibrium and

without such asymmetry, a symmetrized cross-correlation function ($g_{av}(\tau)$) is calculated by averaging the cross-correlation values obtained from shifting each of the intensity-time series in turn, respectively:

$$g_{av}(\tau) = \frac{1}{2}\big(g_{12}(\tau) + g_{21}(\tau)\big)\,. \tag{2.19}$$

Even in single-color FCS, when only one species of fluorophores is concerned, cross-correlation function is often computed to minimize the effect of afterpulsing in sensitive detectors such as single-photon avalanche diodes (SPADs) or photomultiplier tubes (PMTs). Afterpulsing is an occurrence wherein a detector continues to record additional signals subsequent to the photon detection, despite the absence of actual photon incidences. This raises the autocorrelation value in a µs range. To avoid such afterpulsing effects, a 50:50 beam splitter is used to divide the signal into two detector channels. The species autocorrelation function is then calculated from the cross-correlation function of the fluorescence detected in the two detectors[66]. As afterpulsing happens on each detector individually, the cross-correlation function of the fluctuation due to afterpulsing is zero.

Conventionally, autocorrelation functions and cross-correlation functions are expressed in terms of $G(\tau) = g(\tau) - 1$ in order to have that the correlation values converge to zero as $\tau \to \infty$. Henceforth, this dissertation shall adhere to this convention.

2.2.2.1 Theoretical Autocorrelation Function Models

After determining the autocorrelation function, the core of FCS analysis involves fitting it to theoretical models that describe the investigated processes. This section provides an overview over the main theoretical components of FCS, which have been thoroughly explored in several publications and textbooks[67-72].

The derivation of the theoretical model of autocorrelation functions requires a mathematical expression of the fluorescence detected from the observation volume, given by

$$F(t) = \kappa \int W(\vec{r})C(\vec{r},t)d\vec{r}\,. \tag{2.20}$$

Here, κ represents the effects of fluorophore brightness and overall detection efficiency of the microscope. Substituting Equation (2.20) into Equation (2.17), the autocorrelation function can be written as:

$$G(\tau) = \frac{\iint W(\vec{r})W(\vec{r}')\langle \delta C(\vec{r},t)\delta C(\vec{r}',t+\tau)\rangle d\vec{r}d\vec{r}'}{\langle C\rangle^2 (\int W(\vec{r})d\vec{r})^2}. \tag{2.21}$$

With $W(\vec{r})$ as expressed in Equation (2.3), only the term $\langle \delta C(\vec{r},t)\delta C(\vec{r}',t+\tau)\rangle$, which depends on the process under study, is left for solving Equation (2.21).

Translational Diffusion

By solving the diffusion equation, the concentration fluctuation due to diffusion can be obtained as[67,73]:

$$\langle \delta C(\vec{r},t)\delta C(\vec{r}',t+\tau)\rangle = \langle C\rangle \frac{e^{-\frac{(\vec{r}-\vec{r}')^2}{4Dt}}}{8(\pi Dt)^{3/2}}. \tag{2.22}$$

where D is the diffusion coefficient of particles. Substituting this into Equation (2.21) yields the autocorrelation function of fluorescent particles of a single type undergoing free diffusion through an observation volume approximated as a 3D Gaussian (Figure 2.4)[67,73]:

$$G_D(\tau) = \frac{1}{N}\left(1+\frac{\tau}{\tau_D}\right)^{-1}\left(1+\frac{\tau}{S^2\tau_D}\right)^{-1/2}, \tag{2.23}$$

where S and τ_D stand for the structure parameter of the observation volume and the diffusional correlation time, respectively. The structural factor S is defined as the ratio of the axial extension to the radial extension, described as $S = z_0/w_0$, which is typically around 5 in an optimal microscopy setup[74]. In practice, this parameter is often set at a constant value throughout the experiments[67].

Equation (2.23) indicates that the average number of particles in the observation volume can be calculated from $N = \frac{1}{G(0)}$. This aligns with the analysis provided by N&B. From the right-hand side of Equation (2.17), the amplitude of the autocorrelation function is

$$G(0) = g(0) - 1 = \frac{\sigma^2}{\langle F(t)\rangle^2}. \tag{2.24}$$

The average number of particles is then

$$N = \frac{1}{G(0)} = \frac{\langle F(t)\rangle^2}{\sigma^2}, \tag{2.25}$$

which is identical to Equation (2.10), except for the absence of the term $-\langle F\rangle$ in the denominator.

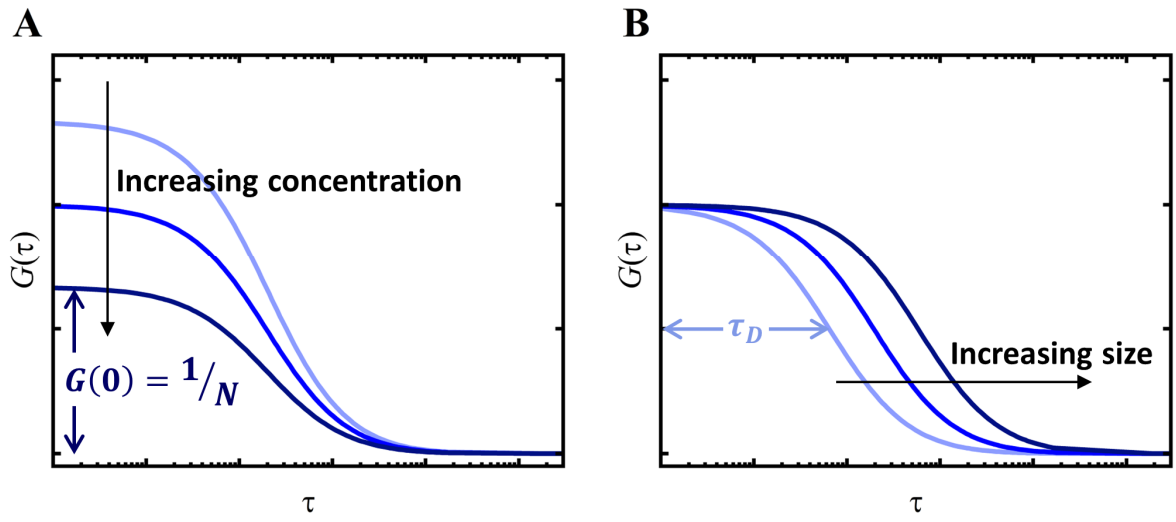

Figure 2.4. Autocorrelation Functions ($G(\tau)$) of Fluorescent Particles Diffusing Through a Three-Dimensional Gaussian Detection Volume, Generated from Equation (2.23)

A: Decreased autocorrelation function amplitude ($G(0)$) is observed with increased particle concentration, with $G(0)$ illustrated for lowest autocorrelation function curve.

B: Diffusion of particles with increasing size leads to a shift in the autocorrelation function towards larger timescales, with the diffusional correlation time (τ_D) depicted for the leftmost autocorrelation function curve.

The difference arises due to the calculation of $G(0)$ entailing the extrapolation of the autocorrelation function to a time lag of zero, rather than directly determining the autocorrelation function value at very small lag time. Shot noise is temporally uncorrelated and, therefore, do not impact this extrapolated value. The connection between particle numbers and autocorrelation function amplitudes in Equation (2.27) explains why FCS can only analyze samples within the concentration range of nM to sub µM. As the concentration increases, the autocorrelation function amplitude is too low in comparison to the uncertainty values.

The diffusional correlation time (τ_D) is the average time particles reside in the observation volume. This is related to the diffusion coefficient according to

$$\tau_D = \frac{w_0^2}{4D}. \tag{2.26}$$

Combining Equations (2.23) and (2.26) yields

$$G_D(\tau) = \frac{1}{N}\left(1 + \frac{4D\tau}{w_0^2}\right)^{-1}\left(1 + \frac{4D\tau}{S^2 w_0^2}\right)^{-1/2}. \tag{2.27}$$

Provided that the radius of the observation volume is calibrated in advance from a measurement on fluorescent dyes with known diffusion coefficient[75-77], Equation (2.27) enables a direct fitting for the diffusion coefficient.

According to the Stokes-Einstein equation[78,79], the diffusion coefficient of particles diffusing in a fluid with viscosity η at temperature T is related to their hydrodynamic radius, r_h, as

$$D = \frac{k_B T}{6\pi\eta r_h}, \tag{2.28}$$

where k_B is the Boltzmann constant. This equation, however, does not indicate a linear relationship between the diffusion coefficient and temperature since liquid viscosity also depends on temperature. The hydrodynamic radius or Stokes radius is the radius of a rigid sphere diffusing at the same diffusion coefficient as the particle under consideration. Proteins, for instance, are not spherical objects but rather intricate folds of varying compactness and shape, and the hydrodynamic radius of a peptide chain is also dependent upon its folding state[80]. The relative molecular mass of two substances may be determined by comparing their hydrodynamic radii and diffusion coefficients. Assuming identical densities of both substances, the molecular mass is proportional to their volume, V, and $M_M \propto V \propto r_h^3 \propto \frac{1}{D^3}$.

Photophysical Processes

Fluorophores can enter a reversible dark state through photophysical processes. For example, rare spin flips of excited electrons allow the transition from the excited singlet state to the triplet state[81]. Flickering, characterized by transitions between bright and dark states, in fluorescent proteins arises from minor conformational variations under physiological conditions since the surrounding cage structure significantly influences on the optical properties of the fluorescent protein chromophore[82,83]. In FCS measurements, light-driven conformational transitions, such as changes in isomerization[84-86], protonation state of chromophores[33,87], and/or transitions to long-lived excited states[63], are commonly observed[88].

The effects of photophysical processes can be generalized as the reversible transitions between a bright (B) and dark state (D) of fluorophores:

$$B \underset{k_B}{\overset{k_D}{\rightleftharpoons}} D$$

The rate constants k_D and k_B are the rates at which the fluorophore transition from the bright to dark state and vice versa. The fractions of fluorophores in the bright state (f_b) and in the dark state (f_d) can be described by the coupled differential equations:

$$\frac{d}{dt}\begin{bmatrix} f_b \\ f_d \end{bmatrix} = \begin{bmatrix} -k_D & k_B \\ k_D & -k_B \end{bmatrix}\begin{bmatrix} f_b \\ f_d \end{bmatrix}. \tag{2.29}$$

Solving Equation (2.29) and considering that the fluorescence intensity arises solely from the fluorophores in the bright state yield the contribution of photophysical processes to the autocorrelation function:

$$G_F(\tau) = 1 + \frac{f_F}{1-f_F} e^{-\tau/\tau_F}, \tag{2.30}$$

with $f_F = k_d \cdot (k_d + k_b)^{-1}$ and $\tau_F = (k_d + k_b)^{-1}$ representing the photophysical fraction of the molecules in the dark state and the characteristic time of the photophysical process, respectively.

Although fluorophores typically undergo several processes and fluorophores located in various regions of the laser beam are subject to varying levels of excitation intensity[89], previous studies have demonstrated that a single exponential function is often adequate for accurately representing autocorrelation function arising from photophysical process[67,90,91].

Rotational Diffusion

The probability that a molecule absorbs light (P_a) depends on the direction of its transition dipole moment ($\hat{\mu}$) relative to the polarization direction of the excitation light ($\widehat{e_e}$)[66,92]:

$$P_a \propto 3(\hat{\mu} \cdot \widehat{e_e})^2 \propto \cos^2\theta_a, \tag{2.31}$$

where θ_a is the angle between $\hat{\mu}$ and $\widehat{e_e}$. When the molecule emits fluorescence, the electric field of the emitted light is parallel to the fluorophore's transition dipole moment. Thus, the probability of detecting the emitted photon at a certain polarization direction (P_d) depends on the direction of the transition dipole moment and the detected polarization axis ($\widehat{e_d}$) as

$$P_d \propto 3(\hat{\mu} \cdot \widehat{e_d})^2 \propto \cos^2\theta_d \,, \tag{2.32}$$

with θ_d representing the angle between $\hat{\mu}$ and $\widehat{e_d}$.

Consider a fluorescent protein under a linearly polarized excitation. The fluorescence emission is minimized when the chromophore's transition dipole moment is perpendicular to the excitation polarization direction (Equation (2.31)). As the fluorescent protein rotates, along with its chromophore, the angle between the transition dipole moment and the polarization direction decreases, causing the fluorescence to increase and reach its maximum when the angle is zero. Conversely, fluorescence decreases as the transition dipole moment tilts away from the polarization direction.

For a fluorescent protein that rotates much slower than its fluorescence lifetime, the fluorescence fluctuations caused by molecular rotation exhibit the most pronounced contribution on the autocorrelation function when detected with a polarization direction parallel to the excitation polarization[93]. This point was demonstrated experimentally by adding a polarizer with the same polarization direction as the excitation in the detection path[94].

The derivation of the contribution of rotational diffusion to autocorrelation function is complicated, as outlined by[95,96]. In summary, the derivation involves solving the rotational diffusion equation[97] to obtain the probability of the chromophore rotating from one dipole moment direction to another over time τ, and then combining this with the absorption and detection probabilities (Equations (2.31)–(2.32)). Ultimately, the derivation yields the autocorrelation function contribution of the fluorescence fluctuations caused by rotational Brownian motion detected with linearly polarized excitation and parallel detection polarization[68,94]:

$$G_R(\tau) = 1 + f_R e^{-\tau/\tau_R} \,, \tag{2.33}$$

where f_R represents the rotational amplitude. The rotational correlation time (τ_R) is related to the rotational diffusion coefficient (D_R) as

$$\tau_R = \frac{1}{6D_R} \,. \tag{2.34}$$

The Stokes-Einstein-Debye relation[98] relates the rotational diffusion coefficient (D_R) of a molecule to its hydrodynamic radius:

$$D_R = \frac{k_B T}{8\pi\eta r_h^3}. \tag{2.35}$$

Equation (2.35) indicates that variations in molecular mass significantly impact the rotational diffusion coefficient: $M_M \propto V \propto r_h^3 \propto \frac{1}{D_R}$. Determining molecular mass from rotational diffusion is more sensitive than from translational diffusion. Moreover, calculating the rotational correlation time can be done without prior knowledge of the observation volume.

Despite these advantages, measuring rotational diffusion is less common than translational diffusion due to the challenges involved. Rotational diffusion occurs on a timescale of tens of ns, requiring a temporal resolution of a few ns. However, the S/N ratio decreases with shorter bin intervals (Equation (2.5)), necessitating longer measurements. This hinders molecular dynamics measurements and makes the analysis computationally intensive.

Antibunching

Antibunching is observed in experiments on solutions with very low (~1 nM) concentration. At this concentration, approximately one fluorophore is inside the observation volume at any given time. Consequently, at time $\tau = 0$ after detecting a photon, the probability of detecting another photon is zero, as the fluorophore is in the ground state and needs to absorb light to reach the excited state first. Once in the excited state, there is a time interval, determined by the finite fluorescence lifetime of fluorophores (Section 2.1.2), which typically ranges from 1 to 10 ns[55], before the fluorophore emits another photon. As τ increases, the probability of detecting another photon also increases.

To derive a theoretical model of the autocorrelation function arising from antibunching, the simplified model of Jablonski consisting of only two singlet electronic energy levels is considered. The vibrational energy levels are neglected since vibrational relaxation occurs much faster than the temporal resolution of the photon data processed in this research. The built-up triplet population, if present, occurs on a much slower rate than antibunching and can also be neglected. The model thus becomes:

$$S_0 \underset{k_0}{\overset{k_1}{\rightleftharpoons}} S_1$$

In the model, k_1 represents the absorption rate, k_0 represents the decay rate. S_0 and S_1 are the populations in the ground electronic state and in the first electronic excited state, respectively. Assuming $S_0 + S_1 = n$, the model can be mathematically expressed as

$$\frac{dS_1}{dt} = -k_0 S_1 + k_1\big(n - S_1(t)\big)\,. \tag{2.36}$$

Solving Equation (2.36) yields the time-dependent population of the excited state: $S_1(t) = \frac{k_1}{k_0+k_1}\big(1 - e^{-(k_0+k_1)t}\big)$. Subsequently, the contribution of antibunching to the autocorrelation function can be written as [99]:

$$G_A(\tau) = 1 - \frac{1}{n}e^{-\tau/\tau_A}\,, \tag{2.37}$$

where n is the number of fluorophores per particle and $\tau_A = (k_0 + k_1)^{-1}$ is the characteristic time of antibunching.

Autocorrelation Function of Multiple Processes

The autocorrelation function of molecules undergoing multiple processes is constructed by multiplying the correlation contributions from all processes involved. For example, consider the autocorrelation function of freely-diffusing fluorescent proteins excited by linearly polarized light and exhibiting flickering in fluorescence intensity:

$$G(\tau) = G_A(\tau)\cdot G_R(\tau)\cdot G_F(\tau)\cdot G_D(\tau)$$

$$G(\tau) = \frac{1}{N}\Big(1 - \frac{1}{n}e^{-\tau/\tau_A}\Big)\cdot\Big(1 + f_R e^{-\tau/\tau_R}\Big)\cdot\Big(1 + \frac{f_F}{1-f_F}e^{-\tau/\tau_F}\Big)\Big(1 + \frac{4D\tau}{w_0^2}\Big)^{-1} \times\Big(1 + \frac{4D\tau}{S^2 w_0^2}\Big)^{-1/2}\,. \tag{2.38}$$

The equation is plotted in Figure 2.5. Correlation functions are commonly graphed on a logarithmic timescale to improve the visualization of all processes over several orders of magnitudes of time.

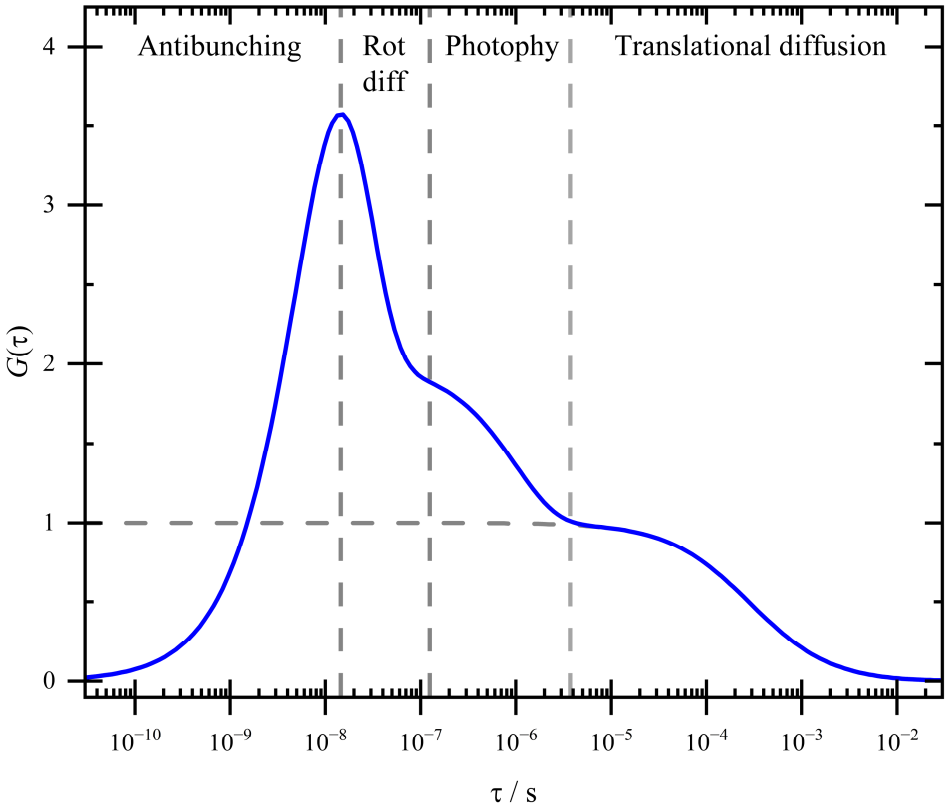

Figure 2.5. Autocorrelation Function ($G(\tau)$) of Fluorescent Proteins Undergoing Translational Diffusion, Flickering, Rotational Diffusion, and Antibunching. The graph is obtained by plotting Equation (2.38) with the parameters: $N = 1$, $n = 1$, $f_R = 5$, $f_F = 0.5$, $\tau_A = 2$ ns, $\tau_R = 16$ ns, $\tau_F = 1$ µs, $D = 100$ µm^2 s^{-1}, $S = 5$, and $w_0 = 340$ nm. The vertical dashed lines divide the regions where antibunching, rotational diffusion (rot diff), photophysical processes (photophy), and translational diffusion (left to right) dominate. The horizontal dashed line shows the amplitude $G(0) = 1/N$ from fitting the translational diffusion region with Equation (2.27).

2.2.2.2 Dual-Color Fluorescence Cross-Correlation Spectroscopy

Dual-color fluorescence cross-correlation spectroscopy studies the fluorescence emitted by two species of fluorophores of different colors to examine the co-diffusion of the two species. The sample is excited by two lasers with different excitation wavelengths. The emitted photons are spectrally separated by a dichroic mirror and directed towards different detectors. By employing pulsed interleaved excitation, which entails alternating between different laser wavelengths at tens-of-ns intervals, photons are temporally segregated, thereby eliminating spectral crosstalk[100,101]. Consequently, a positive amplitude in the resulting cross-correlation function indicates the co-diffusion of the two species, as shown in Figure 2.6.

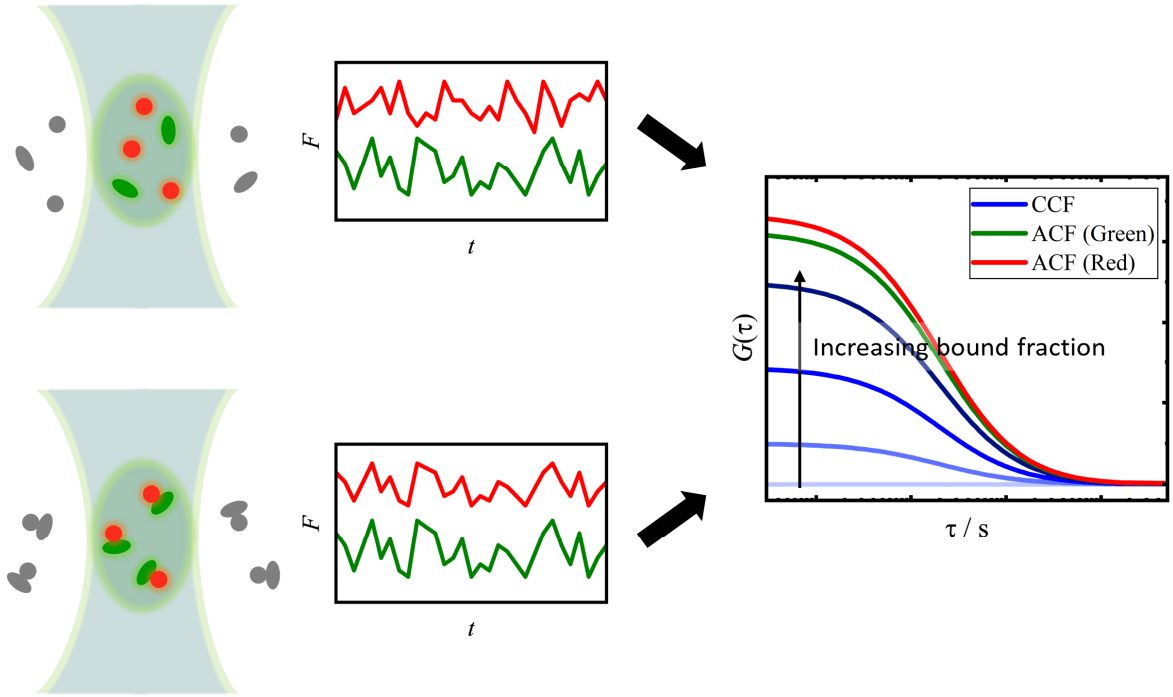

Figure 2.6. Co-Diffusion of Particles Observed via Dual-Color Fluorescence Cross-Correlation Spectroscopy. The figure illustrates the diffusion of fluorescent particles emitting green (depicted as ovals) or red (depicted as circles) fluorescence. On the left, independent diffusions of green and red species result in non-correlated intensity-time (F-t) traces (top), while co-diffusion of the two species leads to correlated fluorescence signals. On the right, the autocorrelation functions ($G(\tau)$) of the green and red particles are displayed. The cross-correlation function is represented in various shades of blue. The cross-correlation function amplitude increases as the bound fraction, defined as the ratio of the number of particles with both species to the total particle number, is higher.

Similar to Equation (2.20), fluorescence detected from fluorophore species i ($F_i(t)$), where $i = 1, 2$, can be expressed as:

$$F_i(t) = \kappa_i \int W_i(\vec{r})[C_i(\vec{r},t) + C_{12}(\vec{r},t)]d\vec{r}\,, \tag{2.39}$$

where κ_i denotes the effect of the brightness of fluorophore species i and the overall detection efficiency of detector channel i. C_{12} represents the concentration of particles with fluorophores of both species, i.e., concentration of the bound species. Substituting Equation (2.39) into Equation (2.17) yields the theoretical autocorrelation function of fluorophore species i:

$$\begin{aligned} G_i(\tau) = \frac{1}{(\langle N_i\rangle+\langle N_{12}\rangle)} \Bigg[& f_i \left(1+\frac{4D_i\tau}{w_{0,i}^2}\right)^{-1} \left(1+\frac{4D_i\tau}{S^2 w_{0,i}^2}\right)^{-1/2} \\ & +(1-f_i)\left(1+\frac{4D_{12}\tau}{w_{0,i}^2}\right)^{-1} \left(1+\frac{4D_{12}\tau}{S^2 w_{0,i}^2}\right)^{-1/2} \Bigg]. \end{aligned} \tag{2.40}$$

where subscriptions i and 12 denote the parameters of particles with fluorophore species i and those of particles with both species. The theoretical cross-correlation function from Equation (2.18) is

$$G_x(\tau) = \frac{\iint W_1(\vec{r})W_2(\vec{r}\prime)\langle\delta C_{12}(\vec{r},t)\delta C_{12}(\vec{r}\prime,t+\tau)\rangle d\vec{r}d\vec{r}\prime}{\int W_1(\vec{r})\langle C_1(\vec{r},t)+C_{12}(\vec{r},t)\rangle d\vec{r}\int W_2(\vec{r}\prime)\langle C_2(\vec{r}\prime,t)+C_{12}(\vec{r}\prime,t)\rangle d\vec{r}}$$

$$G_x(\tau) = \frac{N_{12}}{(N_1+N_{12})(N_2+N_{12})}\left(1+\frac{4D_{12}\tau}{w_{0,12}^2}\right)^{-1}\left(1+\frac{4D_{12}\tau}{S^2w_{0,12}^2}\right)^{-1/2}, \tag{2.41}$$

where $w_{0,12}$ is the root mean square of $w_{0,i}$ of both lasers, i.e., $w_{0,12}^2 = \frac{w_{0,1}^2+w_{0,2}^2}{2}$.

Assuming no reaction-induced quenching or destruction of fluorophores, the cross-correlation function amplitude ($G_x(0)$) is directly proportional to the concentration of bound species[102]:

$$C_{12} = \frac{G_x(0)}{G_1(0)\cdot G_2(0)\cdot V_{eff}}. \tag{2.42}$$

Here, $G_i(0)$ is the autocorrelation function amplitude of the fluorescence species i, and V_{eff} is calculated from the root mean square of $w_{0,i}$ and $z_{0,i}$.

2.2.3 Fluorescence Intensity Distribution Analysis (FIDA)

The N&B and FCS methods, while powerful, have limitations when applied to mixtures with broad distributions of oligomerization states. N&B analysis provides only an average molecular brightness, which reflects overall oligomerization but obscures the contributions from distinct species. FCS, although capable of fitting multiple species with different sizes, is often ineffective in resolving different oligomeric states due to the small mass (and hence diffusional correlation time) differences between them, which hinder accurate and precise separation. Furthermore, both N&B and FCS give greater weight to brighter particles, which may cause larger oligomers to dominate the results.

A well-established method to overcome these limitations is fluorescence intensity distribution analysis (FIDA)[36,37]. FIDA directly fits a frequency histogram of photon counts

recorded during a short bin time—short enough to ensure that particles remain within the observation volume and have a constant molecular brightness throughout the bin time.

The fundamental concept of FIDA involves constructing a fit function for the photon counting histogram. The confocal volume is discretized into small elements, each with a small size dV_i and a uniform spatial brightness B_i. The probability $P_i(n)$ of detecting n photons from fluorescent molecules in element i during the bin time T is given by

$$P_i(n) = \sum_{m=0}^{\infty} P(m)P(n|m)\,, \tag{2.43}$$

where $P(m)$ is the probability of finding m molecules in element i, given overall concentration c. $P(n|m)$ is the probability of detecting n photons when there are m molecules inside dV_i. Both $P(m)$ and $P(n|m)$ follow Poisson distribution, so Equation (2.43) becomes

$$P_i(n) = \sum_{m=0}^{\infty} \frac{(cdV_i)^m}{m!} e^{-cdV_i} \frac{(mqB_iT)^n}{n!} e^{-mqB_iT}\,, \tag{2.44}$$

where q is the molecular brightness of molecules at position $B_i = 1$. The total number of photons detected from the observation volume is $P(n) = \sum_{n=0}^{\infty} P_i(n)$.

Rather than calculating $P(n)$ directly, it is simpler to represent it by its generating function:

$$G(\xi) = \sum_{n=0}^{\infty} P_i(n)\,\xi^n\,. \tag{2.45}$$

Here ξ is conventionally set as $\xi = exp(i\varphi)$, which relates the probability to the generating function through a Fourier transformation. Substituting $P_i(n)$ from Equation (2.44) into Equation (2.45) and rearranging the equation yields

$$G(\xi) = e^{-cdV_i} \sum_{m=0}^{\infty} \frac{(cdV)^m}{m!} e^{-mqBT} \sum_{n=0}^{\infty} \frac{(m\xi qBT)^n}{n!}\,. \tag{2.46}$$

Note that the subscription i was left out for convenience. Using the identity $\sum_n x^n/n! = e^x$, this equation is simplified to

$$G(\xi) = exp\left[cdV\left(e^{(\xi-1)qBT} - 1\right)\right]. \tag{2.47}$$

The spatial integral over the observation volume is

$$G(\xi) = exp\left[C \int_V \left(e^{(\xi-1)qB(\vec{r})T} - 1\right)dV\right]. \tag{2.48}$$

For a mixture of multiple species j, the above equation becomes

$$G(\xi) = exp\left[\sum_j C_j \int_V \left(e^{(\xi-1)q_jB(\vec{r})T} - 1\right)dV\right]. \tag{2.49}$$

The calculation can be further simplified by introducing a variable $x = ln(B_0/B(\vec{r}))$, where $B_0 = B(0)$, resulting in the following equation:

$$G(\xi) = exp\left[\sum_j C_j \int_V \left(e^{(\xi-1)q_jB_0Te^{-x}} - 1\right)dV\right]. \tag{2.50}$$

The spatial brightness distribution $B(\vec{r})$ can be empirically characterized using the following expression for numerical calculation[37]:

$$\frac{dV}{dx} = \sum_{k=1}^{3} a_k x^k \,, \tag{2.51}$$

resulting in

$$G(\xi) = exp\left[\sum_j C_j \int_{x=0}^{2} \left(e^{(\xi-1)q_jB_0Te^{-x}} - 1\right)\left(\sum_{k=1}^{3} a_k x^k\right)dx\right]. \tag{2.52}$$

The upper limit of x is because we consider spatial integrating until the brightness drop to $B(0)/e^2$.

However, Equation (2.52) assumes that all fluorescence signals come solely from the fluorescent molecules. In a practical experimental setup, the background also contributes to the photon counts. For an uncorrelated background with a mean count rate λ, the photon number originating from the background also follows a Poisson distribution. In this case, the generating function becomes

$$G(\xi) = exp\left[(\xi - 1)\lambda T + \sum_j C_j \int_{x=0}^{2} \left(e^{(\xi-1)q_jB_0Te^{-x}} - 1\right)\left(\sum_{k=1}^{3} a_k x^k\right)dx\right]. \tag{2.53}$$

The inverse Fourier transform of this function is then used to fit the photon counting histogram.

2.3 Wnt Signaling Pathway

Cell signaling is a complex mechanism by which cells communicate and respond to external stimuli. The signaling pathway that employs Wnt proteins as carriers for signals is known as the Wnt signaling pathway. The Wnt signaling process begins when cells produce and release Wnt proteins, which are then transported to the receiving cells. The Wnt proteins bind to the receptors and/or co-receptors on the receiving cells' membrane. The binding initiates a cascade of signaling interactions within the receiving cells, eventually resulting in a biological response. This section provides a brief overview of each stage in reverse order, beginning with the signaling cascades.

Various Signaling Pathways are Activated by Wnt Proteins.

The Wnt ligands and their corresponding receptors/co-receptors can be categorized into two groups: those that engage in the canonical pathway and those engaging in the non-canonical pathway.

The canonical Wnt pathway involves a multifunctional protein known as β-catenin in the cytoplasm. In the absence of Wnt proteins, a destruction complex targets and degrades β-catenin. The binding of Wnt proteins to Frizzled receptors triggers a series of sequential processes that ultimately lead to the disintegration of the destruction complex, resulting in an accumulation of β-catenin in the cytoplasm. β-catenin is transported into the nucleus and co-activates TCF/LEF transcription factors, which are involved in cell proliferation, stem cell maintenance, and differentiation. Examples of canonical Wnt proteins in humans include WNT1, WNT2, WNT3a, WNT8a, WNT8b, WNT10a, and WNT10b [103]. The capitalized *WNT* is used to emphasize that these Wnt proteins are expressed in humans.

Non-canonical Wnt proteins are involved in activities that appear to be unrelated to β-catenin. The non-canonical Wnt pathways are classified into two groups: the planar cell polarity pathway and the Wnt/Ca^{2+} pathway. The planar cell polarity pathway regulates the actin cytoskeleton, enabling a targeted migration and polarized structural organization. The Wnt/Ca^{2+} pathway governs various cellular processes, such as cytoskeletal reorganization, cell migration, cell adhesion, and gene expression, by releasing intracellular Ca^{2+}. Examples of non-canonical Wnt proteins found in humans include WNT4, WNT5a, WNT6, and WNT11[103].

Wnt Proteins Exhibit Selectivity Towards (Co-)Receptors.

The Wnt signaling mechanisms in humans involve ten Frizzled receptors and other co-receptors such as LRP5/6 and Ror1/2[10,104,105]. Different Wnt ligands exhibit specific and competitive interactions with certain receptors and co-receptors[13,15,16]. The binding specificity of the Wnt proteins is believed to be regulated by their lipid moiety[106].

Intercellular Transport of Lipidated Wnt Proteins

All Wnt proteins typically have a mass of around 40 kDa[106] and have a secretion signal peptide in the N-terminus to induce the cellular release of the proteins. Before secretion, Wnt proteins are post-translationally modified by glycosylation and lipidation. Lipidation involves attaching a lipid moiety to a conserved cysteine residue near the C-terminus. The lipid anchors enable the Wnt proteins to associate with lipid rafts on the membrane of the Wnt-receiving cells. While the lipid anchors are crucial for bindings with the receptors[18-21], they may not be necessary for Wnt secretion, as is the case for Wnt11 proteins[18].

The hydrophobic nature of the lipid moiety restricts Wnt intercellular transportation. Figure 2.7 illustrates possible transport modes[107]. The transfer of Wnt proteins between neighboring cells could take place via lateral facilitated diffusion, mediated by the interaction with cell surface molecules, specifically heparin sulfate proteoglycans (HSPGs)[108]. Wnt transport via free diffusion is also possible but requires a structural arrangement to protect the lipid moiety (see Figure 1.1). Wnt proteins may form non-EV diffusing complexes to conceal their lipid anchors. The complexes can be formed by the arrangement of Wnt proteins into homo-oligomers[22], the formation of micelles[25,26], or the incorporation of lipid-binding proteins such as afamin, Swim, and secreted Frizzled-related proteins (sFRPs)[23,24,109,110]. In addition, there are EVs, specifically exosomes and microvesicles, that have been suggested to facilitate the transport of hydrophobic Wnt molecules[27]. Finally, Wnt proteins may also be transported through cytonemes, which are specialized signaling filopodia[111].

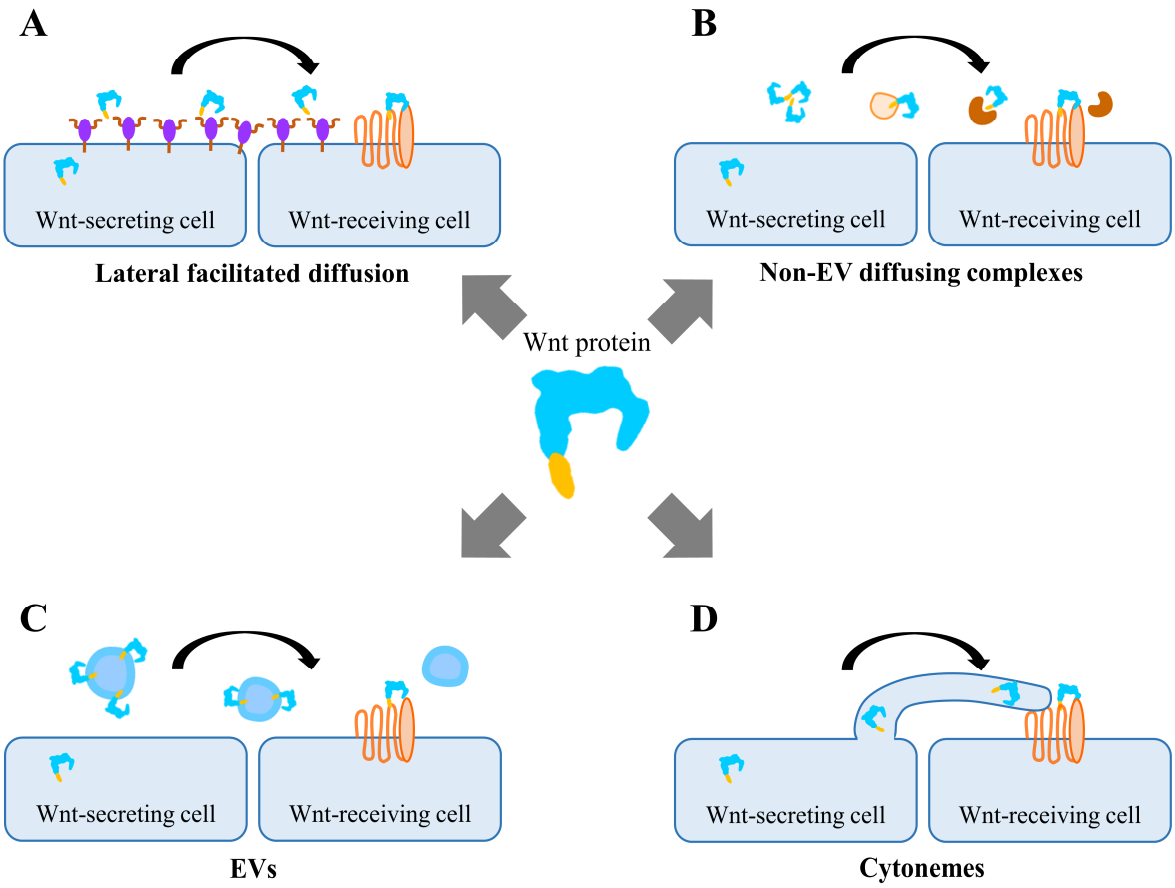

Figure 2.7. Intercellular Wnt Transport. The diagrams were adapted from Reference [111].

A: Lateral facilitated diffusion
B: Free diffusion of non-EV-bound Wnt protein units
C: EVs
D: Cytonemes

3. Materials and methods

This chapter provides an overview of the experimental methodologies used in this research. Detailed information on materials and equipment can be found in Appendix A.1, while cell handling and sample preparation protocols are outlined in Appendix A.2. Appendix A.4 contains documentation on sample quantities and the number of measurements. The main custom programming scripts are listed in Appendix F.

3.1 Separation of Non-EV, Small-EV, and Large-EV Fractions from Conditioned Medium

The isolation of non-EV, small EV, and large EV fractions from conditioned medium (prepared as described in Appendix A.2) involved a combination of (ultra)centrifugation and/or size exclusion chromatography, as illustrated in Figure 3.1. The procedure for mScarlet-WNT5a is distinct from the others and hence has its own section. All centrifugation and ultracentrifugation steps were performed at 4°C.

Fractions from Conditioned Medium Derived from Cells Expressing mCherry2-WNT3a/5a/11 or mScarlet-WNT3a/5a

Conditioned medium obtained from HEK293T cells underwent initial centrifugation at 4,000×g for 30 min to remove dead cells and cellular debris. Subsequently, large EVs were pelleted from 25 mL of conditioned medium by centrifugation at 14,000 × g for 35 min. The resulting pellet

was resuspended in 100 µL of cold (4°C) Dulbecco's Phosphate-Buffered Saline (DPBS). The supernatant (SN14k) was then concentrated to a volume of 100 µL using a Vivaspin 20 centrifugal device (50 kDa MWCO) and a Nanosep device (300 kDa MWCO) according to the manufacturer's protocol. Small EVs, resuspended in 180 µL DPBS, were isolated from the concentrated SN14k using the exo-spin mini size-exclusion column following the manufacturer's instructions. An alternative approach for small EV isolation involved the unconcentrated SN14k at 100,000 × g for 2 h. The supernatant post-ultracentrifugation (SN100k) was collected as the non-EV-bound fraction. To isolate exosomes, the pellet was resuspended in 100–200 µL of cold DPBS.

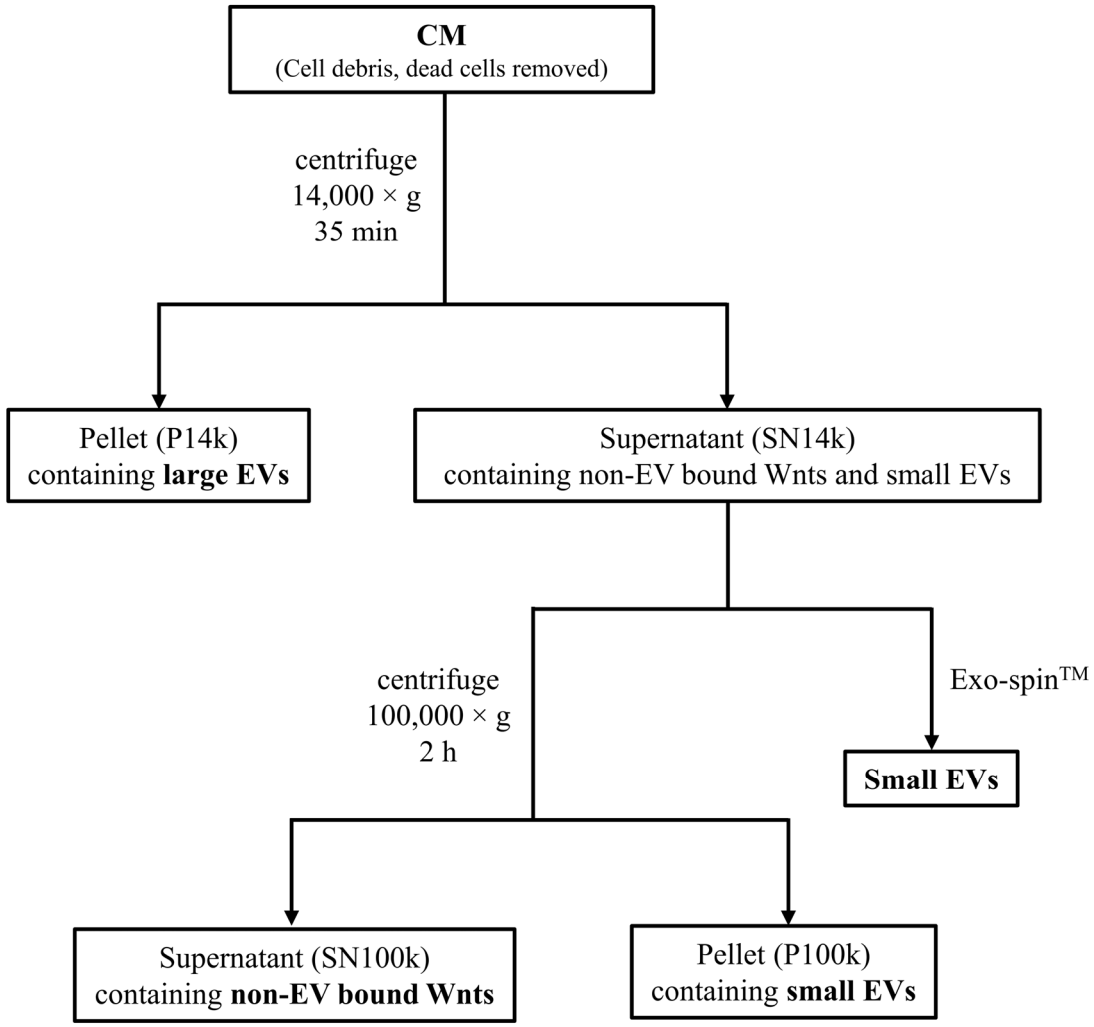

Figure 3.1. Separation of Non-EV, Small-EV, and Large-EV Fractions from Conditioned Medium

Fractions from Conditioned Medium Derived from Cells Expressing mScarlet-WNT5a [†]

120-150 ml of conditioned medium was centrifuged at 750 × g for 5 min and 1,500 × g for 15 min to remove dead cells and debris, respectively. Large EVs were then pelleted via centrifugation at 14,000 × g for 35 min. The resulting pellets were resuspended in 100–200 µL DPBS, and the supernatant (SN14k) was filtered through a 0.2 µm sterile filter. To isolate small EVs, the SN14k supernatant was centrifuged at 100,000 × g for 2 h. The small EVs in the pellet were resuspended in 100–200 µl of DPBS.

Sample Preparation for Optical Spectroscopy and Microscopy Measurements

Non-EV fractions of conditioned medium were centrifuged at 14,000 × g for 10 min. Small- and large-EV samples were pipetted up and down for 5 min to reduce the aggregation issue which is common in EV handling[29].

3.2 Non-Fluorescent Analytical Techniques

3.2.1 Dual-Luciferase Reporter Assay

In the luciferase reporter assay, the activity of the canonical Wnt signaling pathway was assessed via the expression level of the TCF/LEF reporter luciferase, reflecting the transcriptional activity of TCF/LEF transcription factors in response to canonical Wnt signaling events. Cells were seeded into a 96-well plate, transfected with the TCF/LEF reporter luciferase plasmid, and then treated with the proteins of interest. Activation of the TCF/LEF reporter luciferase plasmid by TCF/LEF transcription factors leads to the transcription of the luciferase gene, resulting in the accumulation of the luciferase enzyme in the cytoplasm. As a control, cells were also transfected with a constitutively active luciferase plasmid, which produces a different type of luciferase enzyme independent of external stimuli. This control serves to monitor transfection efficiency and cell viability.

[†] Samples prepared by Dr. Antonia Schubert, Heidelberg University and Matthias Schulz, University Medical Center Göttingen.

Before the bioluminescence readout, cells were lysed to extract the luciferases. The quantity of each luciferase was subsequently determined by adding the respective luciferin to the lysate and measuring the intensity of its bioluminescence. The activity of the canonical Wnt signaling pathway is determined by the following equation:

$$Activity = \frac{I_S}{I_C}, \tag{3.1}$$

where I_S and I_C denote the background-corrected luminescence intensities of the TCF/LEF luciferase and control luciferase in the target cells, respectively. The background intensities were determined by adding the luciferins in the wells without cells and measuring the intensities the same way. Finally, the relative signaling activity was calculated by normalizing the signaling activity in cells treated with the target proteins to that in mock-treated cells, which were under identical conditions but lacking the target proteins.

The detailed protocols for specific functionality tests are provided in Appendix A.3 for reference.

3.2.2 Dynamic Light Scattering

Dynamic light scattering was employed to obtain hydrodynamic radius distributions of all, both fluorescent and non-fluorescent, in the samples. Dynamic light scattering measurements were performed on different fractions of conditioned medium, including non-EV samples containing mCherry2-WNT3a/5a/11 and pcDNA[†], as well as on small-EV and large-EV samples containing mScarlet-WNT3a/5a/11 and pcDNA. To ensure consistency across measurements, five control measurements were conducted daily using 200-nm polystyrene beads dissolved in deionized water as a calibration standard.

To begin a dynamic light scattering measurement, 40 µl of sample solution was pipetted into a plastic cuvette. Then, the cuvette was inserted into the Zetasizer Nano-ZS instrument,

[†] pcDNA is a ‘backbone’ plasmid used to carry target genes introduced to mammalian cells.

where the sample was allowed to equilibrate for 30 min at a controlled temperature of 25.0 °C. Following temperature equilibration, a 633-nm He-Ne laser beam was directed towards the sample, and the intensity of the scattered light at an angle of 173° was recorded.

Each sample underwent 10 consecutive measurements, with a 5-min incubation period between measurements. After data acquisition, the autocorrelation function of the scattered intensity was automatically calculated. The Zetasizer analysis software then employed an exponential relaxation model[112] to fit the autocorrelation function, enabling extraction of the hydrodynamic diameter distributions of the particles.

3.3 Optical Spectroscopy

3.3.1 Absorption Spectrometer

The Cary-100 UV-VIS spectrophotometer was used to record the absorption spectra. The spectra were acquired by scanning the incident wavelength from 800 nm to 200 nm at a scanning rate of 600 nm/min. The switching between visible and UV lamps was set between 320 and 350 nm. Before conducting any absorption spectrum measurements, the absorbance of deionized water was measured as a baseline and subtracted from the absorption spectrum of the sample.

The concentration of a solution could be determined by applying the Beer-Lambert law [113], which establishes a relationship between absorbance, A, molar extinction coefficient at the peak absorption, $\varepsilon_{\lambda_{ex}}$, concentration, c, and optical path length, l, as follows:

$$A = \varepsilon_{\lambda_{ex}} cl \, . \tag{3.2}$$

This equation allows for the calculation of substance concentration given knowledge of the extinction coefficient. The 280 nm extinction coefficient of a protein can be derived from its amino acid sequence[114]. Refer to Table A.4 for the extinction coefficients at 280 nm of the fluorescent proteins used in this research.

3.3.2 Spectrofluorometer

The Fluorolog-3 spectrofluorometer was utilized for measuring excitation and emission spectra. Before initiating measurements, the spectrum of the lamp and water Raman emission were acquired to validate the instrument's functionality. To optimize spectral quality, adjustments could be made to the slit width of the monochromators and the integration time of the detector. Furthermore, the commercial program FluorEssence allowed for adjustments to the detected signal to compensate for factors such as dark count rate, excitation light fluctuations, and wavelength-dependent detector efficiency. These corrections were uniformly applied to all measurements conducted in this study.

3.3.3 Sample Preparation for Optical Spectroscopy Measurements

Except for the large-EV fraction, all samples were centrifuged at 14,000 × g for 10 min. 80 µL of sample solution was pipetted into a cuvette with a 3-mm light path. Between measurements, the cuvette underwent thorough rinsing with deionized water five times. Additionally, it was centrifuged with the opening turned outward for 2 min to remove residual water between uses.

3.3.4 Determination of mCherry2-WNT3a Concentration

Since the concentrations of mCherry2-WNT3a proteins in non-EV, small-EV, and large-EV samples are too low for absorbance determination, they were quantified through the analysis of emission spectra. Background intensity was determined by measuring the emission spectra of corresponding fractions of conditioned medium derived from cells transfected with pcDNA.

As a reference, the concentration of a mCherry2 purified from *E. Coli* stock solution (~10 µM) was determined based on absorbance at 280 nm. Subsequently, the mCherry2 stock solution underwent three sequential dilutions, each roughly by a factor of ten, to attain a reference fluorescent protein solution with a final concentration of approximately 10 nM, similar to the expected concentration of mCherry2-WNT3a in the samples. To ensure precise

dilution factor determination, emission spectra were acquired both before and after every dilution step, maintaining identical spectrometer settings throughout.

Finally, the emission spectra, I, of samples containing mCherry2-WNT3a underwent quantitative decomposition into the spectra of fluorescent protein, I_{FP}, and background, I_{BG}, using the equation:

$$I = C_{FP} I_{FP} + C_{BG} I_{BG} \,, \tag{3.3}$$

where C_{FP} and C_{BG} represent the contributions from the fluorescent protein and background, respectively. The concentration of mCherry2-WNT3a was calculated by multiplying C_{FP} with the concentration of the reference fluorescent protein solution. The concentration obtained from this approach is consistent with that obtained via FCS.

3.4 Time-Resolved Confocal Fluorescence Microscope Setups

The fluorescence fluctuation spectroscopy measurements were conducted using two fluorescence microscopes: a custom-built ‘M2’ confocal-STED microscopy system and a commercial MicroTime 200. Both setups feature similar confocal microscopy components, as illustrated in Figure 3.2.

Two lasers, ‘blue’ (473 nm in the M2 setup and 485 nm in the MicroTime 200 setup) and ‘green’ (561 nm in the M2 setup and 560 nm in the MicroTime 200 setup) were used in pulsed mode with a frequency 40 MHz, unless otherwise specified. All measurements, except for dual-color fluorescence cross-correlation spectroscopy, were conduct using only the green laser. The laser profiles are cleaned up and combined using a single optical fiber, which then guides the excitation light into the main optical unit.

Within the main optical unit, the laser beams are expanded to a size large enough to overfill the objective back aperture and directed to the major quad-band dichroic beam splitter. The major quad-band dichroic beam splitter reflects the light toward the galvo scanner, which adjusts the beams' lateral positions for raster scanning. Subsequently, the beams enter an

inverted microscope body and are focused onto the sample using a water immersion objective (60x 1.2 numerical aperture). The axial position of the laser focus within the sample is controlled by a piezo scanner attached to the objective in the M2 setup or a piezoelectric sample stage in the MicroTime 200 setup.

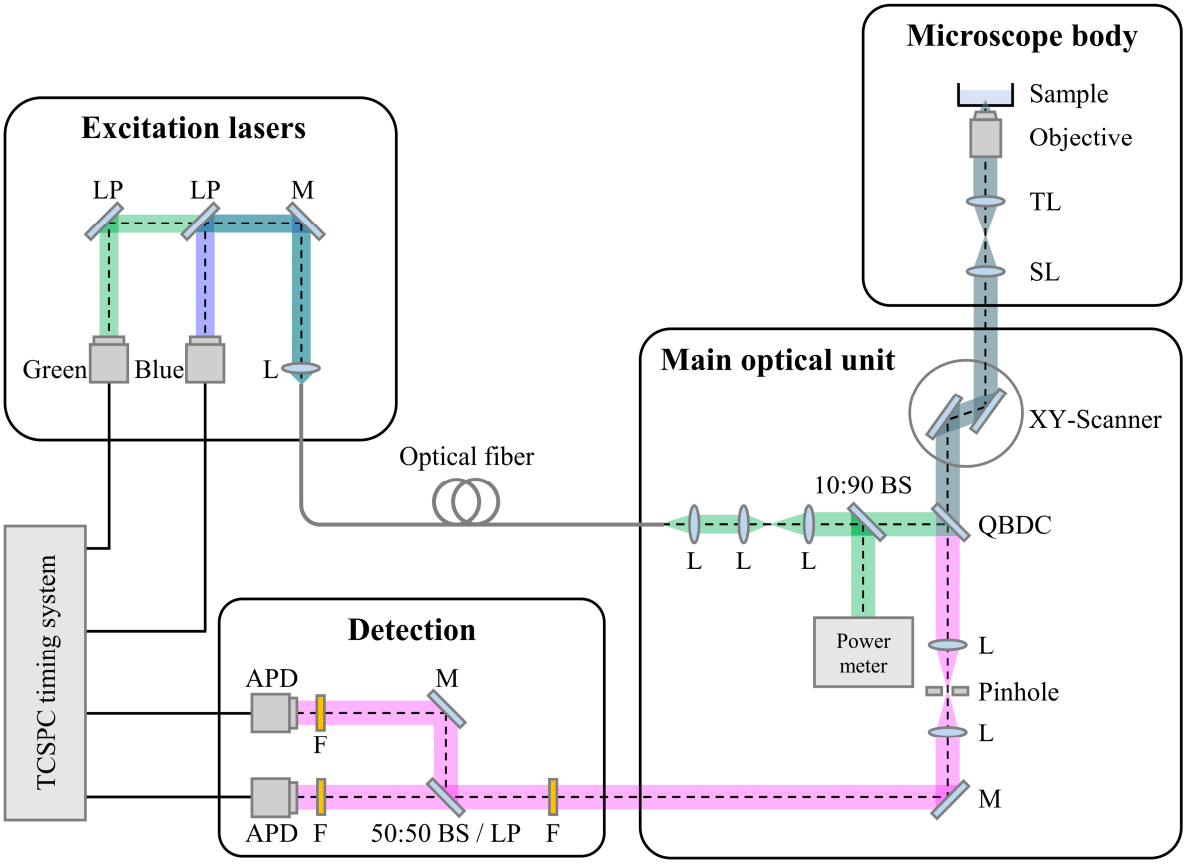

Figure 3.2. Time-Resolved Confocal Fluorescence Microscope Schematic. APD: avalanche photodiode; BS: beam splitter; F: filter; L: lens; LP: longpass dichroic mirror; M: mirror; QBDC: quad-band dichroic beam splitter; SL: scan lens; TL: tube lens.

The emitted light is collected by the same objective lens and passed through the quad-band dichroic beam splitter to separate it from the excitation light. To block out the out-of-focus light, the emission is detected through a 50-µm or a 75-µm (diameter) pinhole in the MicroTime setup and a 62.5-µm diameter optical fiber in the M2 setup.

Following this, the emitted light is directed into the detection section, which contains two avalanche photodiodes (APDs). Prior to entering the APDs, a common emission filter can

be installed to spectrally filter the emission light. The emission beam is then divided by either a 50:50 beam splitter (for single-color measurements) or a 560 nm longpass dichroic beam splitter (for dual-color fluorescence cross-correlation spectroscopy measurements). Additionally, an individual bandpass filter could be added in front of each APD. The emission filters used for each fluorescent dye or fluorescent protein are listed in Table 3.1. Photon arrival times were recorded using a Time-Correlated Single Photon Counting card.

Table 3.1. Bandpass Emission Filters and Excitation Wavelengths Used for Specific Dyes and Fluorescent Proteins

Dye / Fluorescent Protein	Filter (center/width)	Excitation Wavelength / nm
Alexa Fluor 488	525/50 nm	485
Alexa Fluor 546	600/37 nm or 609/62 nm	560 or 561
CoraLite Plus 488	525/50 nm	485
eGFP	525/50 nm	560 or 561
mCherry2	600/37 nm or 609/62 nm	560 or 561
mScarlet	600/37 nm or 609/62 nm	560 or 561
tdTomato	600/37 nm or 609/62 nm	485 and 560

In Vivo Measurements

Measurements on living cells were conducted within an incubation chamber equipped with a CO_2 mixing system to ensure physiological conditions were maintained at 37°C with 5% CO_2.

System Calibration

System calibration[75] was conducted to account for potential changes in setup alignment. This involves performing a 300-s FCS measurement on a 10 nM Alexa Fluor 546 dye solution in deionized water or DPBS. The 560 nm excitation was set at 0.7 kW cm^{-2}. The autocorrelation function was fitted with the pure diffusion model (Equation (2.27)), with fixed *S* parameter at 5.0. When data were collected using two APDs, the fit started at 1 µs, whereas when using a single APD, the fit began at 10 µs to minimize the effect from afterpulsing. Based on the published diffusion coefficient of Alexa Fluor 546, which is 341 $\mu m^2 s^{-1}$ at 22.5 ± 0.5°C [115], the lateral extension of the detection volume was calculated using Equation (2.26).

Power Density Calculation

The power density (PD) values reported in this dissertation were calculated using Equation (3.4):

$$PD = \frac{P}{\pi w_0^2}, \tag{3.4}$$

where P represents the laser power at the focal plane. The value of w_0 was obtained from the system calibration described in the previous subsection.

3.5 Apparent Fluorescence Probability of mCherry2 and mScarlet in Cytosol of Living HEK293T Cells Determined by N&B Analysis

Sample Preparation

HEK293T cells were seeded into an 8-well chamber and transfected with 0.5–1.0 µg plasmids per well to induce the expression of cytosolic mCherry2 and mScarlet oligomers. Subsequently, cells were incubated for a minimum of 24 h to allow the fluorescent proteins to mature before measurements were taken. To minimize background autofluorescence from cell debris and dead cells, the cell culture medium was exchanged with fresh medium before measurements.

Data Collection

Fluorescence emission was measured using excitation power densities of 0.4 kW cm^{-2} for mCherry2 and 0.2 kW cm^{-2} for mScarlet oligomers, respectively. The laser focus was positioned in the cytoplasm of a cell, and the emitted fluorescence was collected for 120 s. Background determination was performed by measuring at least three cells transfected with 0.75 µg MEM-eGFP[†] plasmid each day.

[†] The MEM-eGFP plasmids induce the expression of cells to have eGFP ... (Continued on next page)

... (Continued from previous page) on cell membrane. Since the setup lacks wide field illumination capability to observe the cell outline, MEM-eGFP was used to render the cell outline visible while minimizing effects on signals in red emission region.

Data Analysis

Photons were sorted with a time bin of 1 µs to construct intensity-time traces. Then, a segment-by-segment analysis was applied to the intensity-time traces[116,117]. Each 120-s intensity-time trace was divided into 24 segments of 5 s. An automatic selection algorithm, developed in MATLAB, was utilized to identify and exclude segments exhibiting 'extra' autocorrelation function values at large τ. The algorithm processed photon arrival times using a 1-µs time bin and computed the autocorrelation functions for individual segments.

For each segment, the algorithm estimated the autocorrelation function amplitude by averaging the autocorrelation values at lag times from 1 µs $\leq \tau \leq$ 20 µs: $G(0) = \langle G(1 \text{ µs} \leq \tau \leq 20 \text{ µs}) \rangle$. Similarly, the autocorrelation value at the large lag time ($G_{large\,\tau}$) was estimated by averaging the values at $\tau \geq 10$ ms, i.e., $G_{large\,\tau} = \langle G(\tau \geq 10 \text{ ms}) \rangle$.

The average autocorrelation function amplitude of all 24 segments, $\langle G(0) \rangle_{1-24}$, was calculated. If *SD* of $G_{large\,\tau}$ was less than $0.05 \cdot \langle G(0) \rangle_{1-24}$, no extra single-point fluctuations were assumed, and no segments were removed. Otherwise, if the SD of $G_{large\,\tau}$ equals or exceeds $0.05 \cdot \langle G_0 \rangle_{1-24}$, segments with $G_{large\,\tau}$ greater than the SD were removed. Measurements with more than 12 removed segments were discarded.

The photons of the remaining segments were re-binned using a time bin of 100-µs intervals. Equations (2.12)–(2.13) were used to compute the number of particles and molecular brightness of individual segments to mitigate the effects of photobleaching and laser fluctuations. Segments with particle numbers higher than 100, indicating high concentration of fluorescent proteins, were discarded.

For comparison of results acquired on different measurement days, the relative molecular brightness, ε_r, was determined by normalizing the molecular brightness to the median molecular brightness of monomers of the same fluorescent protein, $\langle \varepsilon_1 \rangle$, obtained on the same day:

$$\varepsilon_r = \frac{\varepsilon_n}{\langle \varepsilon_1 \rangle}. \tag{3.5}$$

The relative molecular brightness values across all measurement days were pooled together. Outlier measurements, defined as those with relative molecular brightness exceeding 3 *scaled MAD* from the median (Equation (3.12)), were excluded from the analysis.

The apparent fluorescence probability was then calculated by substituting the median relative molecular brightness values of dimeric fluorescent proteins into the following equation (derived from Equation (2.14)):

$$\varepsilon_r = 1 + (n-1)p_f. \tag{3.6}$$

3.6 Maturation Efficiency of Purified Fluorescent Proteins Determined Using a Base-Denaturation Approach

Data Collection

Fluorescent proteins purified from *E. Coli* were centrifuged at 14000×g for 10 min prior to measurement. Each fluorescent protein was diluted in a buffer solution at pH 7.4 (40 mM Na-PO_4, 300 mM NaCl). Parallelly, the fluorescent protein was diluted in a NaOH solution to adjust to a final pH 13. Four samples were prepared at each pH, and to maintain consistent dilution, all samples were prepared without readjusting the pipette. The samples were equilibrated for a minimum of 3 min before measurements. For each measurement, the sample was pipetted into a cuvette and the absorption spectrum was immediately recorded.

Data Analysis

The extinction coefficients of the fluorescent proteins at 280 nm at physiological pH (pH 7.4) were calculated using their amino acid sequences[114]. Previous studies have shown that fluorescent proteins undergo denaturation at pH 13, resulting in an extinction coefficient of 44,000 $M^{-1}cm^{-1}$ at a wavelength of 447 nm for the chromophores[118-120]. The Beer-Lambert law (Equation (3.2)) was applied to determine the concentration of proteins, c_{pro}, and chromophores, c_{chro}, in the samples at pH 7.4 and pH 13, respectively. The maturation

efficiency, p_f, can be defined as the quotient obtained by dividing the chromophore concentration by the protein concentration: $p_f = \frac{c_{chro}}{c_{pro}}$.

3.7 Determination of the Average Number of mScarlet-WNT Proteins per Secreted Particle Using N&B Analysis

The average number of mScarlet-WNT molecules on individual secretory particles was determined through the molecular brightness, which was calculated using the N&B analysis. The molecular brightness values of non-EV-bound units were measured using a stationary laser focus, while those of small and large EVs were measured using a scanning N&B approach.

3.7.1 Molecular Brightness of Non-EV-Bound mScarlet-WNT Units Determined Using N&B

Data Collection

Non-EV-bound mScarlet-WNT3a/5a/11 samples were excited using excitation power density of 0.7 kW cm^{-2}. Every measurement on non-EV-bound mScarlet-WNT3a and mScarlet-WNT11 units lasted 150 s. On the other hand, each measurement on non-EV-bound mScarlet-WNT5a units lasted 300 s. The background intensity was assessed by measuring the emission from the non-EV fraction of conditioned medium collected from cells transfected with pcDNA. To determine the molecular brightness of the monomeric reference, purified mScarlet was diluted in the background sample and performed the measurement using the same method as for mScarlet-WNT samples.

Data Analysis

Intensity-time traces were constructed by binning photons at 10-µs intervals based on their arrival time. Each intensity-time trace was divided into 5-s segments, and molecular brightness (Equation (2.13)) was calculated from every individual segment. Segments having molecular brightness that deviated from the median by a magnitude exceeding than 3 *scaled MAD* (Equation (3.12)) were discarded. The average molecular brightness obtained from the measurement was calculated from the remaining molecular brightness values.

3.7.2 Molecular Brightness of EVs Carrying mScarlet-WNT Proteins Determined Using FIDA

Data Collection

Photons emitted from EVs containing mScarlet-WNT3a/5a were recorded under the measurement conditions listed in Table 3.2. For background determination, emission from background samples, consisting of EVs derived from the conditioned medium of cells expressing pcDNA, was recorded. As a monomeric reference, purified mScarlet dissolved in the background sample was used.

Table 3.2. Measurement Conditions for Molecular Brightness of EVs

Sample	Focus Position	Date	Filter	*PD* / kw cm^{-2}	Measurement Length	# pixels / Frame	# measurements
Small EVs Carrying mScarlet-WNT3a							
1	Scanning	03.08.23	600/37	1.4	50 frames	400 × 400	8
2	Scanning	03.08.23	600/37	1.4	50 frames	400 × 400	8
3	Scanning	04.08.23	600/37	1.4	50 frames	400 × 400	8
4	Scanning	22.08.23	600/37	0.7	50 frames	400 × 400	6
5	Scanning	22.08.23	600/37	0.7	50 frames	400 × 400	8
6	Scanning	13.09.23	600/37	1.4	50 frames	400 × 400	8
Small EVs Carrying mScarlet-WNT5a							
1	Scanning	08.04.22	600/37	0.7	100 frames	200 × 200	15
2	Scanning	11.04.22	609/62	0.7	100 frames	200 × 200	12
3	Scanning	11.04.22	609/62	0.7	100 frames	200 × 200	12
4	Scanning	11.04.22	609/62	0.7	100 frames	200 × 200	12

Sample	Focus Position	Date	Filter	*PD* / kw cm^{-2}	Measurement Length	# pixels / Frame	# measurements
Large EVs Carrying mScarlet-WNT3a							
1	Scanning	17.04.23	609/62	2.0	100 frames	400 × 400	5
2	Scanning	17.04.23	609/62	2.0	100 frames	400 × 400	5
3	Scanning	18.04.23	609/62	2.0	100 frames	400 × 400	5
4	Scanning	18.04.23	609/62	2.0	100 frames	400 × 400	5
Large EVs Carrying mScarlet-WNT5a							
1	Scanning	03.11.21	600/37	1.4	400 frames	200 × 200	5
2	Scanning	03.11.21	600/37	1.4	400 frames	200 × 200	5
3	Scanning	05.05.23	600/37	0.7	100 frames	400 × 400	5
mScarlet							
1	Scanning	03.08.23	600/37	1.4	25 frames	400 × 400	3
2	Scanning	03.08.23	600/37	1.4	25 frames	400 × 400	3
3	Scanning	04.08.23	600/37	1.4	25 frames	400 × 400	3
4	Scanning	13.09.23	600/37	1.4	25 frames	400 × 400	3
Background, measured under 0.7 kW cm^{-2} excitation							
1	Scanning	22.08.23	600/37	0.7	25 frames	400 × 400	1
2	Scanning	22.08.23	600/37	0.7	25 frames	400 × 400	1
3	Scanning	08.04.22	600/37	0.7	50 frames	200 × 200	1
4	Scanning	05.05.23	600/37	0.7	25 frames	400 × 400	1
5	Scanning	19.09.23	600/37	0.7	25 frames	400 × 400	1
6	Scanning	19.09.23	600/37	0.7	24 frames	400 × 400	1
7	Scanning	20.09.23	600/37	0.7	25 frames	400 × 400	1
Background, measured under 1.4 kW cm^{-2} excitation							
1	Scanning	03.08.23	600/37	1.4	25 frames	400 × 400	1
2	Scanning	03.08.23	600/37	1.4	25 frames	400 × 400	1
3	Scanning	04.08.23	600/37	1.4	25 frames	400 × 400	1
4	Scanning	13.09.23	600/37	1.4	24 frames	400 × 400	1
5	Scanning	06.09.23	600/37	1.4	25 frames	400 × 400	1
6	Scanning	06.09.23	600/37	1.4	25 frames	400 × 400	1
7	Scanning	07.09.23	600/37	1.4	25 frames	400 × 400	1
8	Scanning	07.09.23	600/37	1.4	25 frames	400 × 400	1
9	Scanning	08.09.23	600/37	1.4	25 frames	400 × 400	1
10.1*	Stationary	03.11.21	600/37	1.4	300 s	–	1
10.2*	Scanning	03.11.21	600/37	1.4	500 frames	200 × 200	1
Alexa Fluor 546							
1	Stationary	03.11.21	609/62	0.7	300 s	–	1
2	Stationary	08.04.22	609/62	0.7	300 s	–	1
3	Stationary	11.04.22	609/62	0.7	300 s	–	1
4	Stationary	17.04.23	600/37	0.7	300 s	–	2
5	Stationary	18.04.23	609/62	0.7	300 s	–	1
6	Stationary	05.05.23	600/37	0.7	300 s	–	1
7	Stationary	03.08.23	600/37	0.7	60 s	–	10
8	Stationary	04.08.23	600/37	0.7	60 s	–	10

Sample	Focus Position	Date	Filter	*PD* / kw cm^{-2}	Measurement Length	# pixels / Frame	# measurements
9	Stationary	22.08.23	600/37	0.7	60 s	–	5
10	Stationary	13.09.23	600/37	0.7	60 s	–	10

* Data were collected on the same sample using different methods (stationary versus raster-scanning laser focus).

Data Analysis

Images of mScarlet-WNT3a/5a-loaded EVs underwent processing by a custom Python script to filter out aggregates based on the size of their images. The aggregate removal algorithm proceeded as follows. First, the images were binarized using an intensity threshold of 3 counts, a value determined from the pixel intensity histogram of background samples, where 99% of pixels exhibited a maximum intensity of 2. Next, large clusters within the binary images were identified using the density-based spatial clustering of applications with noise (DBSCAN) technique[121,122], implemented via the Python function *sklearn.cluster.DBSCAN*[123].

A pixel was classified as a core of a cluster if at least n additional signal pixels were present within a circle of radius r centered on that pixel. In this study, the following parameters were applied: n = 6, r = 1.5 for small EVs, and n = 22, r = 4 for large EVs. These parameters were chosen based on the maximum diameters of small EVs (150 nm[29,38,40]) and large EVs (1 µm[38,39]), as well as the radius of the Airy disk, r_{Airy}, determined by the Abbe criterion:

$$r_{Airy} = \frac{\lambda}{2 \cdot NA}, \tag{3.7}$$

where λ is the wavelength and NA is the numerical aperture of the objective. For the microscope used, the Airy disk radius is 233 nm, corresponding to a diameter of 466 nm.

Suppose a bright pixel is detected as the yellow pixel in Figure 3.3. The parameter r = 1.5 pixels means that the first direct and diagonal neighbours are considered, as depicted in the gray area in Panel A. The measurements employed raster scanning with a pixel (step) size of 250 nm, meaning the laser focus was shifted in 250-nm intervals. Hence, although a single small EV has a maximum size of 150 nm, it could be excited by two to three adjacent positions of the laser focus in both horizontal and vertical directions. Therefore, an image of a single small EV was estimated to resemble Figure 3.3B, with neighbouring bright pixels depicted in green. The parameter n = 6 means that the algorithm allows the pixel to be surrounded by up to five bright neighbouring pixels and still not be considered a core of a cluster. If there is one

more bright pixel (six bright neighbouring pixels in total), the yellow pixel is then considered a core of a cluster.

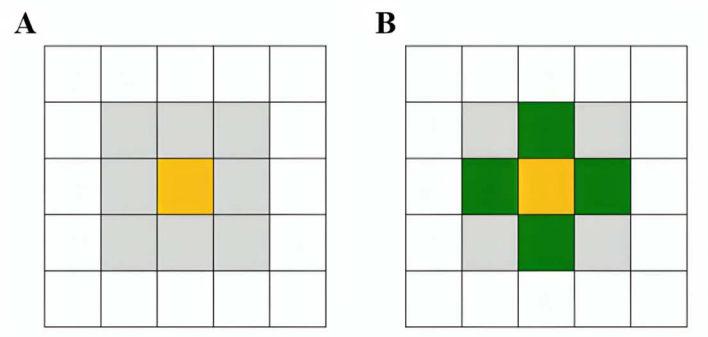

Figure 3.3. Illustrations of Parameter Selection for DBSCAN in Small-EV Imaging. The pixel being evaluated to determine if it is a core of a cluster is shown in yellow.
A: The grey area represents the region considered as a neighbour of the yellow pixel.
B: Estimated image of a single small EV. The four bright neighbouring pixels are shown in green.

For large EVs, when considering whether a pixel (depicted in yellow in Figure 3.4) is a core of a cluster, the parameter $r = 4$ means that DBSCAN considers the grey pixels in Figure 3.4 to be neighbours of the pixel in question. The expected maximum diameter of large EVs is 1 μm, covering four pixels, and this area is drawn as a circle around the yellow pixel. In Panel B, 20 green pixels represent the bright pixels corresponding to the detection of a large EV of this size. In the dissertation, $n = 22$ was used, meaning that if an additional two bright pixels are detected in the grey area, the yellow pixel would be considered a core of an aggregate.

Following the identification of a cluster core, the pixel values in the corresponding circular area of the raw images were discarded. The remaining pixel values were condensed into a unidimensional array for further analysis.

The data from reference monomeric mScarlet were analyzed using N&B analysis with the sliding-window technique[117]. This method involved calculating the molecular brightness based on photon numbers within a window size of 1×10^6 data points. The window was incrementally shifted by 1×10^3 data points. The molecular brightness for each window was calculated according to Equation (2.13). Values that deviated from the median by more than 3 3 *scaled MAD* (Equation (3.12)) were excluded, and the remaining data were then averaged to determine the average molecular brightness of the sample. To obtain the reference monomeric

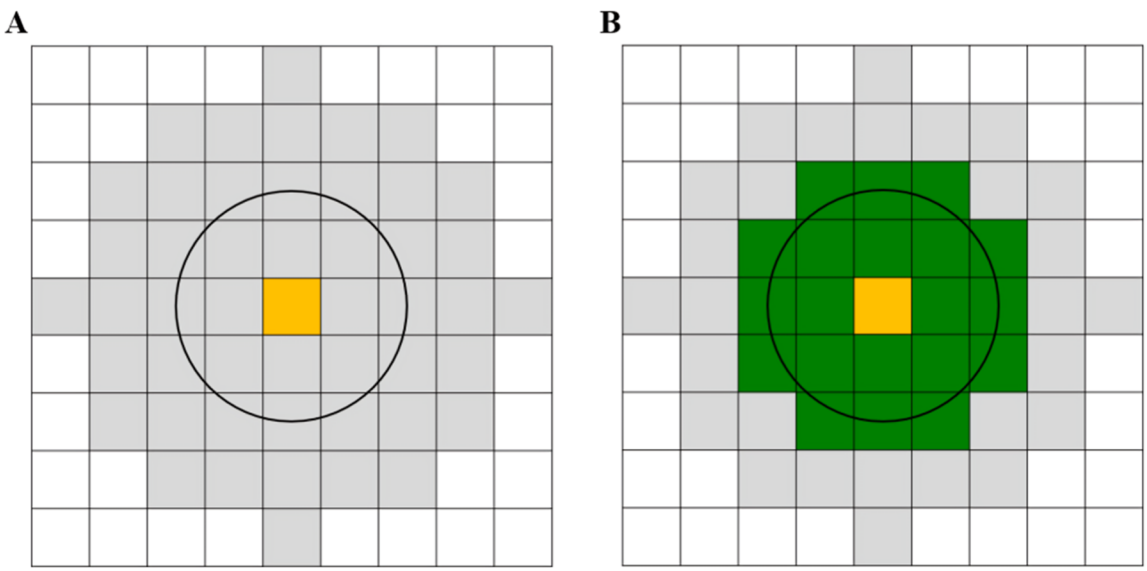

Figure 3.4. Illustrations of Parameters Selection for DBSCAN in Large-EV Images. The pixel being evaluated to determine if it is a core of a cluster is shown in yellow.

A: The grey area represents the region considered as the neighbour of the yellow pixel. The circle, drawn to scale, indicates the maximum size of a large EV, with a diameter of 1 μm.

B: Twenty neighbouring pixels are shown in green, representing the pixels that would appear bright if the largest single large EV were detected.

molecular brightness for each EV dataset, the molecular brightness of mScarlet was scaled based on the excitation power density, the filter used, and the microscope's detection efficiency, which is the molecular brightness of Alexa Fluor 546 from calibration measurements.

For small EVs carrying mScarlet-WNT3a, the data from two measurements were combined into a single photon counting histogram. Similarly, the data from three measurements on small EVs carrying mScarlet-WNT5a were combined into one photon counting histogram. For large EVs, each photon counting histogram was derived from a single measurement. These normalized photon counting histograms were then fitted using the normalized inverse Fourier transform of Equation (2.53). The model includes 5 components for small EVs and 6 components for large EVs, with each component corresponding to different multiplications of the molecular brightness of mScarlet. The parameters a_1, a_2, a_3, and B_0 were obtained by fitting the photon counting histogram of Alexa Fluor 546, measured during microscope calibration, with the constraints $\int B(\vec{r})d\vec{r} = 1$ and $\int B^2(\vec{r})d\vec{r} = 1$.[37] The mean background λ was determined from the signal measured in control samples containing EVs from cells transfected with pcDNA, suspended in DPBS.

The fit was performed using MATLAB's nonlinear solver, *fmincon*, with χ^2 as the objective function to be minimized[36,124]. For fitting photon counting histograms with multiple brightness components, the divider in χ^2 for bins with zero photon counts was set to 10^{-7} to prevent ignoring zero-photon bins, which could otherwise lead to an overestimation of bright particles.

3.7.3 Determining the Number of mScarlet-WNT Proteins per Particle

The relative molecular brightness of each sample was calculated by dividing its molecular brightness by the molecular brightness of the monomeric reference mScarlet (Equation (3.5)). The relative molecular brightness values were used to compute the number of mScarlet-WNT proteins per particle, n, using Equation (3.6) and the maturation efficiency, p_f, of mScarlet expressed in the cytoplasm of HEK293T cells.

3.8 Software Correlators for FCS

Custom MATLAB scripts were developed to compute correlation values based on the photon arrival times recorded on the time-correlated single photon counting card, enhancing flexibility in data management.

Utilizing a multiple-tau technique[60,125,126], correlation functions were computed on a logarithmic time lag scale. The lag timescale was divided into q groups, each comprising $p/2$ data points. In this research, the positive integers p and q were set at 16 and 18, respectively. The interval between consecutive lag time points was determined as $2^{k-1}\Delta\tau$, where $\Delta\tau$ represents the shortest lag time, and k is the group index ($k = 1, 2, \ldots, q$). The m^{th} lag time was calculated according to the equation:

$$\tau_m = \begin{cases} m\Delta\tau & 0 < m \leq \frac{p}{2} \\ \tau_{m-1} + \Delta\tau 2^{\left\lfloor \frac{m-1-p/2}{p/2} \right\rfloor} & \frac{p}{2} < m \leq (q+1)\frac{p}{2} \end{cases}, \tag{3.8}$$

where $\lfloor x \rfloor$ represents the integer part of x.

For correlation functions with $\Delta\tau \geq 0.5$ μs, photons were initially binned with a time bin of Δτ to generate intensity-time traces denoted as $F_1(i)$ and $F_2(i)$ for the two channels, where i denotes the index of the time bin ($i = 1, 2, \ldots M$). For autocorrelation function calculation, $F_1(i)$ and $F_2(i)$ were identical. Next, correlation values with lag time in the first group ($k = 1$) were then calculated by[127]

$$G(m\Delta\tau) = (M-m)\frac{\sum_{i=1}^{M-m} F_1(i)F_2(i+m)}{\left(\sum_{i=1}^{M-m} F_1(i)\right)\left(\sum_{i=1}^{M-m} F_2(i+m)\right)}. \tag{3.9}$$

To compute correlation values at lag times in the subsequent groups, $k = 2, \ldots, q$, intensity-time traces were binned with a coarser time resolution of $\Delta\tau \cdot 2^{m-1}$ before applying Equation (3.9) to acquire the correlation values.

Correlation functions with lag times beginning at less than 0.5 μs were calculated via the time-tag-to correlation algorithm[67,128]. Photon data were represented as two-column vectors, equivalent to intensity-time traces binned with a time bin of $\Delta\tau$, while excluding bins with zero photon counts. In these vectors, the first column contained photon arrival times, t_i, in the unit of $\Delta\tau$, while the second column stored the corresponding photons counts, F_i, detected between t_i and t_{i+1}.

For each lag time τ, photon arrival times were stored with a temporal resolution (time bin) of $\Delta\tau = \tau/7$. This specific choice of resolution ensures a systematic error below 10^{-3} for exponentially decaying correlation functions[129]. To calculate the correlation value of photon data vectors $V_1^{ph} = \left\{t_i^{(1)}, F_i^{(1)}\right\}$ and $V_2^{ph} = \left\{t_i^{(2)}, F_i^{(2)}\right\}$, the first column of F_2^t was shifted by 7 units, resulting in $\tilde{V}_2^{ph} = \left\{\tilde{t}_i^{(2)}, F_i^{(2)}\right\} = \left\{t_i^{(2)} + 7, F_i^{(2)}\right\}$. Following that, the correlation function in Equation (3.9) was calculated as

$$G(\tau) = G(7 \cdot \Delta\tau) = (M-7)\frac{\sum_{t_i^{(1)} = \tilde{t}_j^{(2)}} F_i^{(1)} \cdot F_j^{(2)}}{\left(\sum_{t_i^{(1)} > 7} F_i^{(1)}\right)\left(\sum_{t_i^{(2)} \leq T} F_i^{(2)}\right)}, \tag{3.10}$$

where M is the total measurement time in units of $\Delta\tau$. The time columns $t_i^{(1)}$ and $\tilde{t}_j^{(2)}$ were compared using the MATLAB built-in function *ismember( )*.

3.9 Application of FCS to Determine Translational Diffusion Coefficients

3.9.1 Non-EV-Bound mCherry2-WNT Units

Data Collection

A total of 18 100-s, 18 50-s, and 12 50-s intensity-time traces were obtained from each non-EV-bound mCherry2-WNT3a, mCherry2-WNT5a, and mCherry2-WNT11 sample using a stationary laser focus. The excitation power densities were set to 0.65 kW cm^{-2}, 1.30 kW cm^{-2}, and 1.95 kW cm^{-2}, respectively. Throughout the measurement, the samples remained inside the incubator set at 25.0 ± 0.1°C.

Data Analysis

Photons detected after 14 ns of each excitation pulse were removed to minimize the background effects, and the intensity-time trace was constructed from the remaining photon arrival times. Then, the intensity time trace was divided into 5-s segments, and the autocorrelation function was computed for each segment. The autocorrelation functions obtained from each sample with the same excitation power were averaged. Subsequently, the average autocorrelation functions from each sample acquired at different power densities were globally fitted with Equation (6.2) with shared N and D.

The w_0 values were calibrated daily from FCS measurements on Alexa Fluor 546 (Section 3.4). Finally, Equation (2.28) was applied to determine the average hydrodynamic radii from the to the diffusion coefficients of the non-EV-bound mCherry2-WNT3a/5a/11 units.

3.9.2 Small and Large EVs

Data Collection

Fluorescence emission from the mScartlet-WNT3a/5a-loaded EVs samples described in Section 3.7.2 was measured using a stationary laser focus under the measurement conditions listed in Table 3.3.

Table 3.3. FCS Measurement Conditions for EVs

Sample	Date	Filter	PD / kW cm^{-2}	Total Measurement Time / s
Small EVs carrying mScarlet-WNT3a				
1	03.08.23	600/37	0.7	1,860
2	03.08.23	600/37	0.7	1,800
3	04.08.23	600/37	0.7	1,800
4	22.08.23	600/37	0.7	1,800
5	22.08.23	600/37	0.7	1,800
6	13.09.23	600/37	0.7	1,800
Small EVs carrying mScarlet-WNT5a				
1	08.04.22	600/37	0.7	1,500
2	11.04.22	609/62	0.7	1,500
3	11.04.22	609/62	0.7	1,500
4	11.04.22	609/62	0.7	1,500
Large EVs carrying mScarlet-WNT3a				
1	17.04.23	609/62	1.0	600
2	17.04.23	609/62	1.0	600
3	18.04.23	609/62	1.0	600
4	18.04.23	609/62	1.0	600
Large EVs carrying mScarlet-WNT5a				
1	03.11.21	600/37	1.4	1,200
2	03.11.21	600/37	1.4	300
3	05.05.23	600/37	1.4	1,500

Data Analysis

Individual intensity-time traces were divided into 30-second segments, and autocorrelation functions were computed for each segment. These autocorrelation functions were then fitted to a pure diffusion model comprising a single species (Equations (2.23) and (6.6)) to determine

the diffusional correlation time. To exclude photophysical contributions, the autocorrelation function curves were fitted starting from 0.76 ms for both small and large EVs. Segments with a fit yielding $R^2 > 0.9$ were accepted.

For segments with $R^2 < 0.9$, further fitting was performed using a pure-diffusion model comprising two diffusing species (Equation (6.7)). For segments with $R^2 > 0$, the particle number-weighted average diffusional correlation time was calculated from the two diffusional correlation times obtained from the fit. Segments returning $R^2 < 0.9$ were discarded.

From the diffusional correlation times of each segment, the hydrodynamic radius of small EVs was calculated using the combination of Equations (2.26) and (2.28), while that of large EVs was calculated using the combination of Equations (2.28) and (6.9). The median hydrodynamic radius of individual segments in each sample was then used to represent the value for each sample.

3.10 Polarization-Dependent Fluorescence Correlation Spectroscopy for the Determination of Rotational Diffusion Coefficient

Data Collection

The non-EV fractions of conditioned medium obtained from cells expressing mCherry2-WNT3a, mCherry2-WNT5a, and mCherry2-WNT11 were diluted with DPBS to achieve a concentration of ~2 nM. As a reference, purified mCherry2 was diluted in the non-EV fraction of conditioned medium gathered from cells transfected with pcDNA, with a diluting ratio matching that of the non-EV mCherry2-WNT3a/5a/11 samples.

Measurements were conducted using the green laser operating in continuous wave mode. The excitation laser, directed into the main optical unit as depicted in Figure 3.2, passed through a λ/4 wave plate to convert elliptical to linear polarization, followed by a λ/2 wave plate to adjust the polarization direction. An additional polarizer ensured stable optical alignment. The linearly polarized light, set at 25 kW cm^{-2}, was focused onto the sample. The emitted light

transversed through a polarizing beam splitter in the same polarization direction as the excitation light. Photon emissions from each sample were recorded at 10-min intervals, accumulating to the total measurement time of at least 50 min.

Data Analysis

Each 10-min measurement underwent segmentation into 5-s intervals, from which the corresponding autocorrelation functions were computed. Segments exhibiting a total photon count deviating more than 3 *scaled MAD* from the median were excluded from further analysis. The remaining autocorrelation functions were then averaged to derive the final autocorrelation function for each sample. Next, the average autocorrelation functions obtained from the same sample types were averaged to provide the final autocorrelation function.

3.11 Dual-Color Fluorescence Cross-Correlation Spectroscopy

Sample Preparation

For the dual-color fluorescence cross-correlation spectroscopy measurement between non-EV-bound mCherry2-WNT units and CoraLite Plus 488-conjugated apolipoprotein AI antibody, the following steps were undertaken: The antibody stock solution was diluted in DPBS in a series of 1:10 steps to attain a dye concentration of 540 nM. This 540-nM antibody solution was further diluted in all non-EV fractions of conditioned medium containing mCherry2-WNT3a/5a/11 to achieve concentrations of 50 nM and 10 nM. As a negative control, purified mCherry2 was diluted in the non-EV fraction of conditioned medium obtained from cells transfected with pcDNA, reaching a final concentration of 10 nM. Following that, the samples were incubated at room temperature for a minimum of 3 h before commencing measurements.

For the dual-color fluorescence cross-correlation spectroscopy measurement between non-EV-bound mCherry2-WNT units and human afamin (AFAMIN)-eGFP-His, the following steps were followed: HEK293T cells stably expressing mCherry2-WNT3a/5a/11 were transfected with 0.75 and 1.5 µg plasmids of AFAMIN-eGFP-His using Xfect according to the

mamufacturer's protocol. 5 h post-transfection, the medium was replaced with FluoroBrite Dulbecco's Modified Eagle Medium supplemented with 1% sodium pyruvate. 3 d after the medium exchange, the conditioned medium was collected and centrifuged at 14,000 × g for 35 minutes to remove dead cells, cell debris, and large EVs. As a negative control, conditioned medium was prepared with same procedure on HEK293T cells transfected with pcDNA. Purified mCherry2 was diluted in the control sample to the final concentration of 5 nM.

Data Collection

The measurements employed a pulsed interleave excitation mode, emitting alternating 485-nm and 560-nm laser pulses every 25 ns, both operating at a frequency of 20 MHz. Emitted fluorescence underwent spectral separation using a 560 nm longpass dichroic beam splitter. The overlap of the blue and green excitation foci underwent daily calibration by conducting a 300-second measurement on a 10 nM purified tdTomato, with excitation power densities set at 1.1 kW cm^{-2} (485 nm) and 0.6 kW cm^{-2} (560 nm).

For dual-color fluorescence cross-correlation spectroscopy measurements with CoraLite Plus 488-conjugated apolipoprotein AI antibody, the samples were excited with a 485-nm laser at 1.1 kW cm^{-2} and a 560-nm laser at 2.4 kW cm^{-2}. For dual-color fluorescence cross-correlation spectroscopy measurements with AFAMIN-eGFP-His, samples were excited with 485-nm laser at 4.5 kW cm^{-2} and 560-nm laser at 1.8 kW cm^{-2}. Each sample was measured for 10 min.

Data Analysis

An intensity-time trace was constructed from the photons detected by the APD behind the 525/50 nm (center/width) filter within a 25-ns window after the 485-nm laser pulses. Likewise, another intensity-time trace was created from the photons arriving at the APD behind the 600/37 nm (center/width) filter within a 25-ns window after the 560-nm laser pulses. Thereafter, autocorrelation functions and cross-correlation function were computed from these intensity-time traces.

3.12 Investigation of Translational Diffusion Under the Effect of methyl-β-cyclodextrin (MβCD)

Data Collection

100 µL of each sample was added to individual wells of BSA-coated 8-well chambers. Right before starting the measurements, 100 µL of either DPBS, 20 mM MβCD, or 80 mM MβCD was added to the respective samples. A series of 24 5-min measurements were conducted on all samples containing MβCD, while at least 12 5-min measurements were taken on samples with added DPBS. Any alterations in viscosity resulting from the MβCD treatment were assessed through the diffusion coefficients of 10 nM purified mCherry2 in the non-EV fraction of conditioned medium obtained from cells transfected with pcDNA. DPBS or MβCD was added to these samples in a similar manner as with the mCherry2-WNT samples. Each sample underwent 12 5-min measurements.

All measurements were conducted using an excitation power density of 1.8 kW cm^{-2}. Throughout the measurements, the 8-well chamber was kept inside the microscope incubator at 25.0°C and sealed to prevent evaporation.

Data Analysis

Photons detected within 14 ns after the laser pulses were used to construct the intensity-time traces. Each intensity-time trace was segmented into 1-s intervals, and the autocorrelation function was computed individually for each segment. Segments with mean intensities further from the median than 3 *scaled MAD* (Equation (3.12)) were excluded from each measurement, and the autocorrelation functions of the remaining segments were averaged before fitting as described in Section 7.1.

3.13 Statistical Analysis

In addition to mean, standard deviation (*SD*), and standard error of the mean (*SEM*), median and median absolute deviation (*MAD*) were used to represent data with skewed distributions. The median is a more robust estimator of central tendency than the mean, as it is less sensitive

to outliers (breakdown point of 0.5 versus 0)[130]. The *MAD* represents the distribution of dataset $\{x_1, x_2, x_3, \dots, x_n\}$ with respect to the median and is calculated as[131]

$$MAD = median\{|x_i - median\{x_i\}|\}. \tag{3.11}$$

For outlier removal, unless specified otherwise, the criterion used was *scaled MAD*, defined as

$$scaled\ MAD = b \cdot median\{|x_i - median\{x_i\}|\}, \tag{3.12}$$

where the scaling factor b is set to 1.4826 to rescale *MAD* to the *SD* for data assumed to follow a normal distribution.

For fitting of correlation curves, the most widely used Levenberg–Marquardt algorithm [67] was applied using OriginPro. The fit returns the standard error of the fit, which is equivalent and reported as *SD*.

4. General Characterization of WNT Proteins Secreted Externally by Living Cells

Fluorescently tagged Wnt proteins have been extensively studied using various DNA constructs, including Wnt genes derived from zebrafish[132,133], frog[134-136], mouse[22,137], and chicken[138]. In this study, novel DNA constructs for three human-derived WNT proteins—WNT3a, WNT5a, and WNT11—were introduced[†]. Each WNT protein is fused to a red fluorescent protein, either mCherry2 or mScarlet, via a flexible linker.

The chapter begins with the verification that these new DNA constructs lead to secretion of the intended proteins. The presence of mCherry2/mScarlet in the conditioned medium collected from cells transfected with these DNA constructs were confirmed through the analysis of the emission spectra of the conditioned medium. Functionality of the WNT fusion proteins was validated using dual-luciferase reporter assays, a widely used biological technique for signaling activity measurements[139].

Wnt proteins are known to be transported both independently of EVs and on EVs [12,107]. It has been proposed that these different transport modes play roles in regulating short-range and lone-range signaling[22,140]. Recent studies have demonstrated that active Wnt proteins are transported via exosomes[27,141]. However, research on Wnt-receptor interactions often used

[†] The constructs for mCherry2/mScarlet-WNT3a, mCherry2-WNT5a, and mCherry2/mScarlet-WNT11 were designed by Julia Kuhlman, a technician in AG Nienhaus, APH, KIT, while the construct for mScarlet-WNT5a was designed by Dr. Antonia Schubert, Heidelberg University.

conditioned medium from cells transfected with Wnt DNA constructs[15,16], which provided average results from Wnt proteins in various transport modes. This raises the question of what percentage of Wnt proteins present in conditioned medium are in individual transport modes.

To address this, conditioned medium gathered from cells expressing mCherry2/mScarlet-WNT3a/5a/11 proteins were separated into non-EV, small-EV, and large-EV fractions using (ultra)centrifugation and/or size-exclusion chromatography. The efficiency of the separation methodologies was assessed by evaluating the size distributions of particles in individual fractions using dynamic light scattering. Subsequently, the concentrations of WNT proteins in individual fractions were compared through the analysis of their emission spectra. To explore potential differences in signaling activities induced by Wnt proteins in different transport modes, the activities of different fractions of secreted mCherry2-WNT3a were measured using the dual-luciferase TCF/LEF reporter assays.

4.1 Emission Spectra of Conditioned Medium

Conditioned medium is a complex medium containing a variety of proteins and lipids. The fluorescence emitted by conditioned medium containing mCherry2/mScarlet-WNT3a/5a/11 proteins is a result of both the fluorescence of the fluorescent proteins and the autofluorescence of the cell culture media (background). Since the cell culture medium has generally considerably lower autofluorescence in the red emission region compared to the green region (Figure 4.1A), WNT proteins were labeled with red fluorescent proteins, specifically mCherry2 and mScarlet. Their emission spectra are shown in Figure 4.1B.

Figure 4.1C-H show the emission spectra of conditioned medium gathered from HEK293T cells expressing mCherry2-WNT3a, mScarlet-WNT3a, mCherry2-WNT5a, mScarlet-WNT5a, mCherry2-WNT11, and mCherry2-WNT11. For precise background determination, the emission spectrum of the control conditioned medium harvested from HEK293T cells transfected with pcDNA was measured. The emission spectrum of each conditioned medium was fitted with the superposition of the emission of the fluorescent protein and that of the background (Equation (3.3)). All of the spectra are well fitted with R^2 between 0.99–1.00, indicating that the conditioned medium contains either mCherry2 or mScarlet, as intended.

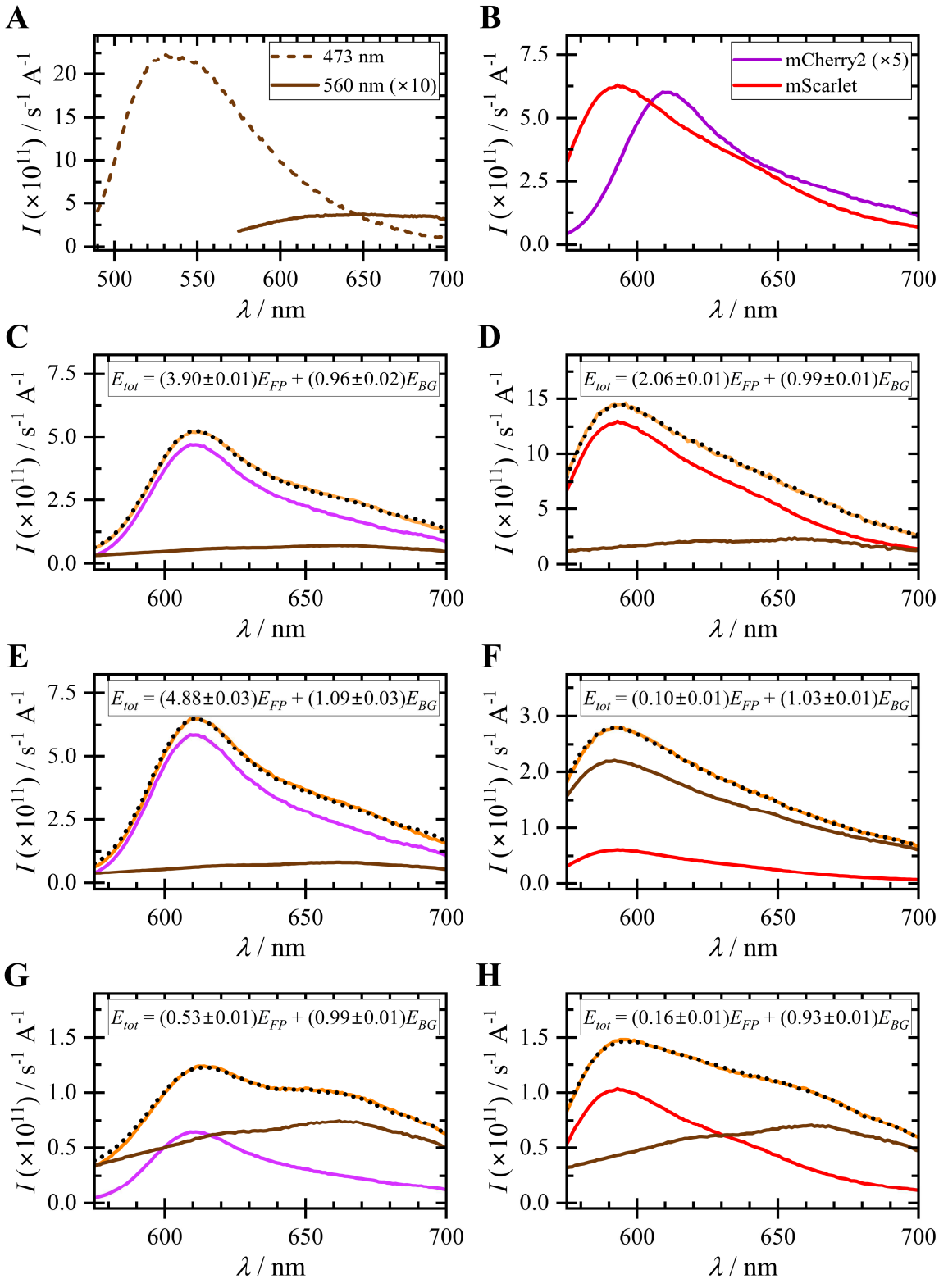

Figure 4.1. Emission Spectra of Conditioned Medium Compared to Spectra of Purified Fluorescent Proteins and Background. Emission intensity (*I*) was recorded using 560-nm (solid lines) or 485-nm (dashed lines) excitation, with a 5 nm side entrance/exit slit width.

A: Autofluorescence of the cell culture medium (Dulbecco's modified Eagle medium supplemented with 10% Exo-depleted Fetal bovine serum and 1% sodium pyruvate)

B: Emission spectra of 10 nM mCherry2 (purple) and mScarlet (red) purified from *E. Coli*

(Continued on next page)

(Continued from previous page)

C–H: Emission spectra of conditioned medium containing mCherry2-WNT3a (C), mScarlet-WNT3a (D), mCherry2-WNT5a (E), mScarlet-WNT5a (F), mCherry2-WNT11 (G), and mScarlet-WNT11 (H) are displayed in orange with lines of best fit (black, dotted). Below each conditioned medium's spectra, contributions from the corresponding fluorescent protein and background are plotted in brown.

In addition, the fit returned a C_{BG} value close to 1 in all conditioned medium samples, indicating that the background emission in mCherry2/mScarlet-WNT conditioned medium is similar to that in control conditioned medium from cells transfected with pcDNA. The background emission spectra in the mScarlet-WNT5a conditioned medium (Figure 4.1F) differs from the other conditioned medium samples (Figure 4.1C–E,G–H) due to the inclusion of the pH indicator Phenol Red during cell culture.

It is important to note that cell expression levels at the time of conditioned medium collection may vary among the mCherry2/mScarlet-WNT samples; therefore, these spectra cannot be used to compare the secretion levels of different mCherry2/mScarlet-WNT proteins.

4.2 Qualitative Activity Test of Secreted WNT Proteins

The secretion of WNT proteins into the conditioned medium is a crucial step, but it is equally important to verify the functionality of the secreted proteins. TCF/LEF luciferase reporter assays were employed to assess canonical Wnt signaling activity in cells treated with mCherry2/mScarlet-WNT3a/5a/11 proteins. The results are expressed as the relative activity, which is the signaling activity normalized with the signaling activity in mock-treated cells.

4.2.1 Activation of Canonical Wnt Signaling Pathway by Secreted WNT3a Proteins

Figure 4.2 shows the relative canonical Wnt signaling activities in cells after incubation in the conditioned medium from cells transfected with mCherry2-WNT3a, mScarlet-WNT3a, and pcDNA (mock treatment) for 14 h. The average relative activities of the canonical Wnt pathway

induced by mCherry2-WNT3a conditioned medium and mScarlet-WNT3a conditioned medium are 19 ± 7 and 5 ± 2 (mean ± *SEM*), respectively.

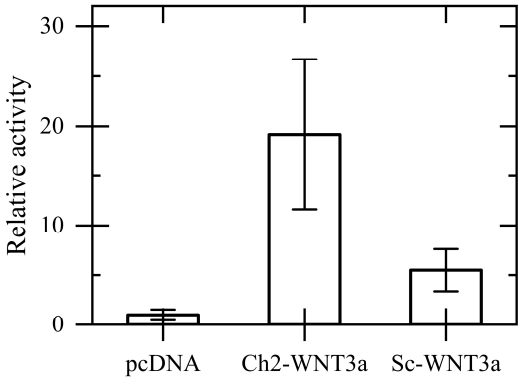

Figure 4.2. Relative Activities of the Canonical Wnt Signalling Pathway Induced by mCherry2-WNT3a and mScarlet-WNT3a Conditioned Medium. Bars represent the mean, and error bars represent the *SEM*. Both mCherry2-WNT3a and mScarlet-WNT3a conditioned media result in significantly higher canonical WNT signalling activity compared to the pcDNA-conditioned medium (mock treatment).

4.2.2 Suppression of Canonical Wnt Signaling Pathway by Secreted WNT5a/11 Proteins

Although there are several standard reporter assays for measuring the canonical Wnt signaling activity (e.g., those employed in here and in previous works[142,143]), there is no standardized approach for directly quantifying the activity of the non-canonical Wnt signaling, e.g., those triggered by WNT5a and WNT11. However, the canonical and non-canonical pathways compete for several effector proteins, such as receptors, rendering them antagonistic[144-147]. To probe this antagonism, recombinant (rc) human WNT3a or mouse Wnt3a (mWnt3a) was applied to the cells to activate the canonical Wnt pathway. Simultaneously, the cells were treated with the target non-canonical Wnt proteins to observe the reduction in canonical Wnt signaling activity.

The effects of mCherry2-WNT5a and mCherry2/mScarlet-WNT11 were probed by incubating cells in the corresponding conditioned medium with rc WNT3a for 14 h. The relative canonical Wnt signaling activities are shown in Figure 4.3A. The canonical Wnt signaling activity of the control (treated with conditioned medium collected from cells transfected with

pcDNA) cells exposed to rc WNT3a is 34 ± 9 (mean ± *SEM*) fold of those without rc WNT3a. Cells treated with rc WNT3a and mCherry2-WNT5a, mCherry2-WNT11, or mScarlet-WNT11 conditioned medium, on the other hand, have lower levels of canonical Wnt signaling activities (mean ± *SEM*) of 11 ± 3, 10 ± 3, and 11 ± 4.

The functionality of mScarlet-WNT5a[†] was tested by transfecting cells with either mScarlet-WNT5a or the control pcDNA. After a 16-h incubation with rc mWnt3a, the relative canonical Wnt signaling activity in cells transfected with pcDNA is 5 ± 2 (mean ± *SEM*), while cells treated with mScarlet-WNT5a demonstrate reduced relative activity of 1.1 ± 0.8 (mean ± *SEM*).

Assuming that the mock-treated cells were exposed to comparable concentrations of endogenous WNT and other proteins, the activation (suppression) of canonical Wnt signaling should come from mCherry2/mScarlet-WNT3a (mCherry2/mScarlet-WNT5a/11). Since the concentrations of fluorescent protein-WNT proteins applied to the cells varied, only a qualitative conclusion can be drawn here that the mCherry2/mScarlet-WNT3a/5a/11 proteins produced according to the new DNA constructs are biologically functional.

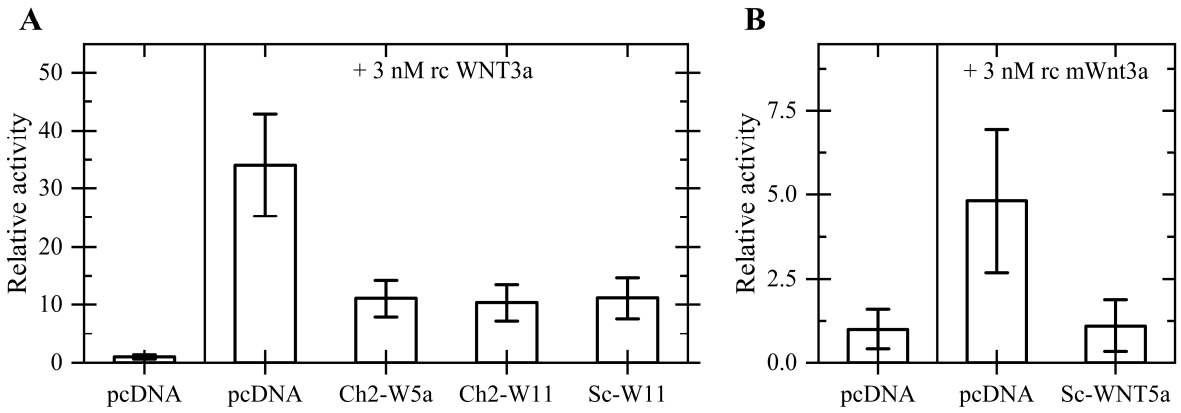

Figure 4.3. Relative Canonical WNT Signalling Pathway Activities Induced by mCherry2/mScarlet-WNT5a/11. Bars represent the mean, and error bars represent the *SEM*. The left and right sides of the boxes indicate the relative activities in cells without treatment and those treated with rc WNT3a/mWnt3a, respectively.

A: Addition of mCherry2-WNT5a (Ch2-WNT5a), mCherry2-WNT11 (Ch2-WNT11), or mScarlet-WNT11 (Sc-WNT11) reduced the canonical Wnt signaling activities that are induced by rc WNT3a.

B: mScarlet-WNT5a (Sc-WNT5a) suppressed canonical Wnt signaling activity that is induced by rc mWnt3a.

[†] The experiment was performed by Dr. Antonia Schubert, Heidelberg University.

4.3 Radius Distribution of Particles in Non-EV, Small-EV, and Large-EV Fractions Determined Using Dynamic Light Scattering

The intensity-weighted hydrodynamic radius distributions of particles in the non-EV, small-EV, and large-EV fractions were determined using dynamic light scattering. It is important to note that while converting intensity-weighted radius distributions to number-weighted distributions is theoretically feasible, its practical application is limited to homogenous samples with precisely known optical properties. Unfortunately, meeting this criterion is challenging in the context of this study. The non-EV samples comprise diverse proteins and lipids of varying sizes, rendering the determination of a precise refractive index value unfeasible. Similarly, the refractive index of EVs is dependent on their size[148], making it difficult to accurately determine outside the 100–200 nm diameter range.

The intensity-weighted hydrodynamic radius distributions (Figure 4.4) generally display a bimodal pattern, with the highest average percentages of particles found within the smallest size categories. Since the scattered intensity is directly proportional to the sixth power of the particle radius ($I \propto r^6$)[149], a few larger particles can significantly influence the size distributions. Therefore, the pronounced peaks at smaller radii suggest that the majority of the population is comprised of smaller particles.

The size distributions of particles within the non-EV samples remain consistent across all sample types. Two distinct populations are observed, peaking at average hydrodynamic radii of approximately 5 nm and 80 nm. The former group exceeds the typical size of individual proteins, and they may belong to lipoproteins particles or non-membranous extracellular nanoparticles such as exomeres or supermeres[150,151]. The larger particle group is likely exosomes, predominantly observed within the small-EV fractions.

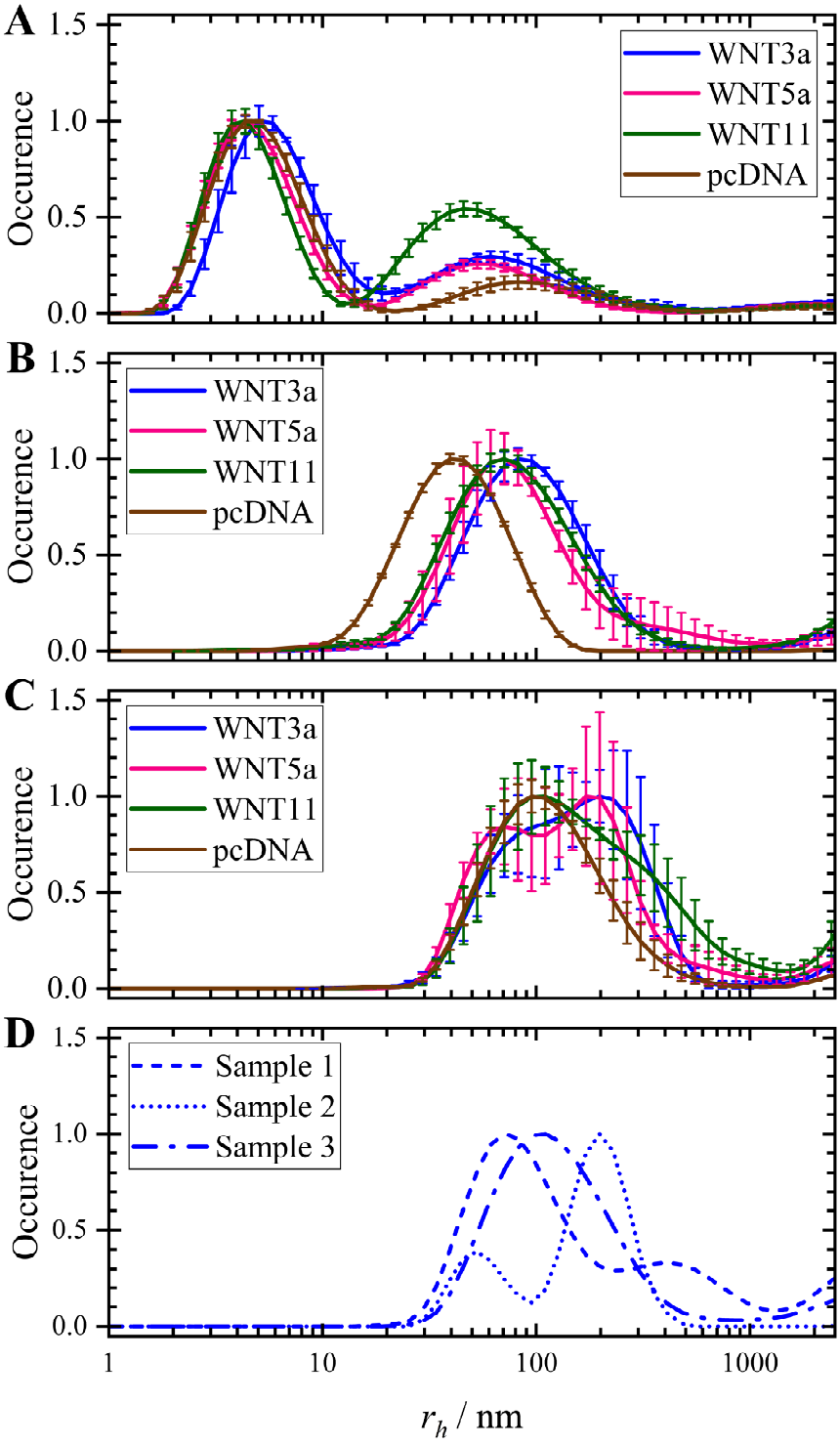

Figure 4.4. Intensity-Weighted Hydrodynamic Radius (r_h) Distributions of Particles in Non-EV, Small-EV, and Large-EV Samples Obtained Using Dynamic Light Scattering. The graphs show the average number of occurrences, normalized to the maximum occurrence values, with *SEM* as error bars.

A–C: Hydrodynamic radius distributions averaged from all samples

A: Particles in non-EV fractions isolated from conditioned medium of cells transfected with mCherry2-WNT3a (blue), mCherry2-WNT5a (pink), mCherry2-WNT11 (green), and pcDNA (brown)

(Continued on next page)

(Continued from previous page)

B–C: Particles in small- (B) and large- (C) EV fractions isolated from conditioned medium of cells transfected with mScarlet-WNT3a (blue), mScarlet-WNT5a (pink), mScarlet-WNT11 (green), and pcDNA (brown)

D: r_h, distributions of individual large-EV samples containing mScarlet-WNT5a (distinguished by different line styles)

The particle size distributions in the small-EV samples exhibit peaks corresponding to radii of approximately 40–90 nm, consistent with the expected diameter range for exosomes (30-150 nm)[29,38,40]. The particle size distributions in the large-EV samples, on the other hand, are shifted towards larger diameters and are broader, aligning with the expected size range for microvesicles (100 nm – 1 µm)[38,39] The results indicate that the separation of particle sizes into distinct fractions is not perfectly precise, and some particles associated with other fractions may be present in any given fraction. Additionally, larger particles with radii exceeding 1 µm, indicative of EV aggregates, were identified. The size distributions of particles within the large-EV samples are broader and more heterogeneous, as evidenced by diverse results across various samples (see Figure 4.4D and Figure B.1 in Appendix B). Interestingly, a slight shift in size distribution towards larger sizes was observed in the small and large EV samples derived from mScarlet-WNT conditioned medium, compared to those derived from pcDNA conditioned medium. While the exact cause of this shift remains elusive, technical issues such as fluorescence interference from mScarlet can be ruled out, given its low (< 1%) excitation efficiency at 633 nm (Appendix A.1).

To summarize, the dynamic light scattering data indicate the capacity to separate particles in the conditioned medium based on their sizes by the utilization of centrifugation and/or size exclusion chromatography. Nevertheless, these methods are insufficient for completely separating different particle types. Lastly, it is imperative to note that dynamic light scattering detects both fluorescent and non-fluorescent particles, implying that the observed hydrodynamic radii are not exclusive to WNT-carrying particles. The radii of only fluorescently labeled particles determined using FCS are presented in Chapter 6.

4.4 Relative Wnt Concentrations in Non-EV, Small-EV, and Large-EV Fractions

Having established the success of the conditioned medium separation procedures, the next step is to quantify the relative concentrations of WNT proteins secreted in individual fractions. To that end, the emission spectra of all fractions were obtained using excitation wavelength of 560 nm. For background determination, control conditioned medium gathered from cells transfected with pcDNA was processed in the same way. Equation (3.3) was applied to fit the mCherry2/mScarlet-WNT3a/5a/11 conditioned medium spectra, after which the background components were subtracted. Due to the low signal-to-background ratio in the EVs containing mCherry2-WNT11, the emission spectra from mCherry2-WNT11 samples were excluded.

The background-corrected spectra of small and large EVs were rescaled with the concentration factors introduced during sample preparation (as described in Section 3.1) to determine their relative concentrations in the original conditioned medium. Figure 4.5A-E displays the rescaled spectra, normalized to the maximum emissions of the non-EV fraction. By comparing the spectral areas of individual fractions within the original conditioned medium sample, the relative concentrations of fluorescent protein-WNT proteins were determined.

The results indicate that the majority of fluorescent protein-WNT proteins, over 95%, are found in the non-EV fraction (Figure 4.5F). A small percentage, up to 4%, is transported on small EVs, while an even smaller percentage, ~1%, is found on large EVs. No significant differences were observed between WNT3a/5a proteins labeled with mCherry2 and mScarlet. One may conclude that the WNT secretion via distinct transport mechanisms are not influenced by the fluorescent proteins and that the fusion DNA constructs are comparable. The precision of the mScarlet-WNT5a data is lower due to less precise concentration factors recorded during sample preparation.

It is important to note that unlabeled endogenous WNT proteins do not appear in the emission spectra. Yet, these results remain valid assuming that all fractions comprise equivalent quantities of unlabeled WNT proteins, which are significantly lower in quantity relative to fluorescently tagged WNT proteins due to the overexpression of mCherry2/mScarlet-WNT proteins in cells. The extent to which overexpression influences the proportions of WNT

proteins that are secreted in individual fractions remains to be determined through future research.

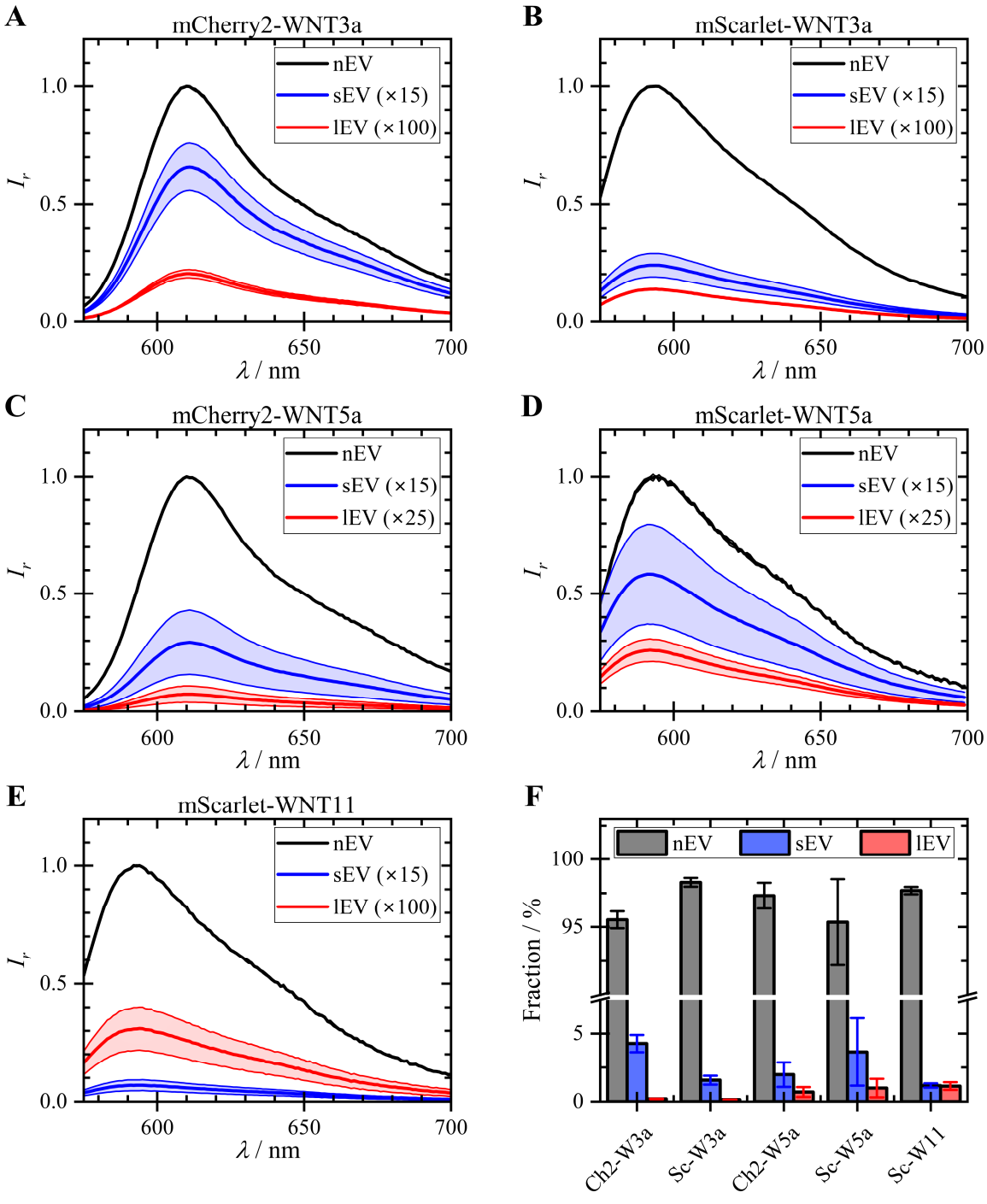

Figure 4.5. Emission Spectra and Relative Concentrations of WNT3a/5a/11 Proteins Secreted Non-EV, Small-EV and Large-EV fractions. Non-EV (nEV), small-EV (sEV), and large-EV (lEV) fractions are presented in black, blue, and red, respectively. (Continued on next page)

(Continued from previous page)

A-E: Normalized background-corrected emission intensity (I_r) of mCherry2-WNT3a, mScarlet-WNT3a, mCherry2-WNT5a, mScarlet-WNT5a and mScarlet-WNT11 in individual fractions. The spectra were measured using 560-nm excitation with the entrance/exit slit width of 5 nm. The multiplying factors indicated in the figure legends are applied to I_r to enhance the visibility of the spectral shapes. Lines indicate the mean; shaded areas represent the *SEM*.

F: Percentages of mCherry2-WNT3a (Ch2-W3a), mScarlet-WNT3a (Sc-W3a), mCherry2-WNT5a (Ch2-W5a), mScarlet-WNT5a (Sc-W5a), and mScarlet-WNT11 (Sc-W11) proteins in individual fractions, calculated from the relative spectral areas. The bars show the average values, and the error bars present the *SEM*.

4.5 Signaling Activities Induced by Different Fractions of Secreted mCherry2-WNT3a

By fitting the emission spectra of non-EV, small-EV, and large-EV fractions of conditioned medium containing mCherry2-WNT3a, as described in Section 4.1, the concentrations of mCherry2-WNT3a in individual samples were determined. Subsequently, all individual samples were diluted to a concentration of mCherry2-WNT3a of 2.5 nM (based on only functional mCherry2) before being applied to cells. After 14 h, the canonical Wnt signaling activities were assessed using the TCF/LEF Luciferase assay (Figure 4.6). For the mock treatment, the control conditioned medium (from cells transfected with pcDNA) was processed in the same manner as the mCherry2-WNT3a conditioned medium. Since the control conditioned medium does not contain fluorescent protein for concentration determination, the non-EV, small-EV, and large-EV fractions were diluted 1:2.4, 1:9.6, 1:3.0, respectively, which are the average dilution factors of the equivalent fractions containing mCherry2-WNT3a.

The result showed that the mCherry2-WNT3a in all fractions are biological active. The mCherry2-WNT3a-induced relative signaling activities in non-EV, small-EV, and large-EV samples were found to be 39 ± 8, 91 ± 9, and 68 ± 10 (mean ± *SEM*), in that order. Notably, mCherry2-WNT3a proteins associated with EVs exhibited higher signaling activities. The impact of mCherry2-WNT3a on small and large EVs do not differ when considering the uncertainty.

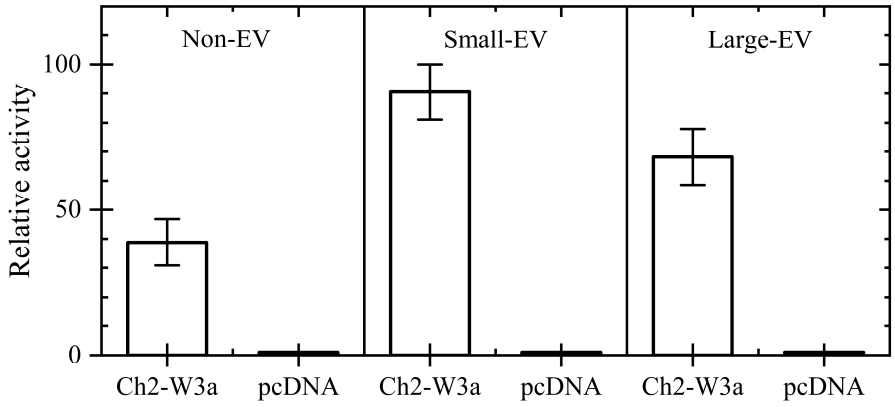

Figure 4.6. Relative Signaling Activities Induced by Non-EV, Small-EV, and Large-EV Fractions of mCherry2-WNT3a Conditioned Medium. The bars show the average values and error bars show *SEM*. Significantly lower canonical Wnt signaling activity is observed for non-EV-bound mCherry2-WNT3a (Ch2-W3a) units compared to mCherry-WNT3a proteins associated with small and large EVs.

4.6 Discussion

This chapter provides the bulk characterizations (without single-molecule resolution) of samples from conditioned medium containing secreted mCherry2/mScarlet-WNT3a/5a/11. Red fluorescent proteins were used because the autofluorescence of cell culture medium is lower in the red emission region compared to the green emission region. As a control, samples collected from cells transfected with only the DNA backbone, pcDNA, without fluorescent labeling or exogenous WNT proteins, were characterized in a similar manner.

At first inspection, the emission spectra of the conditioned media indicate that the plasmids induced cells to release the respective fluorescent proteins, which were designed and biologically validated to be linked with WNT proteins, into the conditioned medium. The conditioned media collected from cells transfected with the same set of plasmids were then confirmed to be biologically active using a dual-color luciferase assay. Therefore, it can be concluded that the plasmids used in this research lead to the correct secretion of fluorescent proteins and active WNT proteins. Note that previous studies have shown that fluorescent protein labels may reduce the activity of Wnt proteins[22,137], an issue that is beyond the scope of the present work.

Following this, the conditioned media were separated into non-EV, small-EV, and large-EV fractions using (ultra)centrifugation and/or size-exclusion chromatography. Particle size distributions obtained from dynamic light scattering analysis indicate successful sorting

based on particle size; however, cross-contamination between fractions was observed. This should be taken into account when interpreting the results of this study.

Subsequently, given that each WNT protein is labeled with one fluorescent protein, this enables precise quantitative measurement of the fluorescent protein-WNT concentration in individual samples. This approach was utilized to measure the fluorescent emission spectra from individual fractions of each fluorescent protein-WNT variant in this study, which revealed that less than 5% of WNT3a/5a/11 proteins are associated with EVs, while the majority diffuse as non-EV-bound units.

Due to the inherent limitations of the separation techniques used to isolate non-EV, small EV, and large EV fractions, as indicated by dynamic light scattering, the percentage estimates should be interpreted with caution. Nonetheless, the results strongly support the conclusion that the majority of fluorescent protein-WNT proteins are transported in the non-EV fraction, as the magnitude of the observed differences is unlikely to be attributed mainly to contamination between fractions.

Lastly, a dual-luciferase reporter assay was employed to determine the canonical signaling activity in live cells induced by different fractions of conditioned medium containing mCherry2-WNT3a. The results show that mCherry2-WNT3a proteins associated with EVs exhibited higher signaling activities. These findings point in the direction that non-EV-bound WNT units are less stable than EVs and lose their functionality after a few days, similar to the conclusion drawn by Takada et al. that non-EV-bound Wnt units are more active in short-range signaling[22]. Nonetheless, as shown by dynamic light scattering, each fraction likely contained particles from other fractions, and the observed signaling activity could partially result from cross-contamination between fractions. Therefore, it is recommended that this experiment be repeated in the future if improved sample preparation techniques become available.

4.7 Summary

This chapter provided the validation of the proteins secreted based on newly introduced DNA constructs for synthesis of WNT3a, WNT5a, and WNT11 proteins tagged with mCherry2/mScarlet. The active mCherry2/mScarlet-WNT3a/5a/11 proteins synthesized based

on these constructs were confirmed using emission spectra combined with dual-luciferase reporter assays.

Via (ultra)centrifugation and/or size-exclusion chromatography, the non-EV, small-EV, and large-EV fractions were successfully isolated, though not perfectly, from conditioned medium. Subsequent examination of emission spectra from individual conditioned medium fractions of every WNT protein revealed that less than 5% of WNT3a/5a/11 proteins are present on EVs, whereas the majority diffuse as non-EV-bound units. Nonetheless, a dual-color luciferase reporter assay showed that mCherry2-WNT3a proteins carried on EVs induce higher canonical Wnt signaling activity compared to the non-EV-bound form. This highlights the need to separately analyze the WNT proteins in individual fractions, which will be covered in the upcoming chapters.

5. Determination of Wnt Protein Numbers per Particle

This chapter presents an analysis of the numbers of Wnt proteins per particle in the non-EV, small-EV, and large-EV fractions of the conditioned medium. Previous studies have suggested that each secreted Wnt particle may carry multiple Wnt proteins, implying at the potential for Wnt protein homo-oligomerization[22,152]. These conclusions were primarily based on the observations that the total mass of the secreted Wnt particles exceeds the predicted mass of monomeric Wnt proteins. Nonetheless, rather than additional Wnt proteins, the extra mass could also indicate the presence of other structures, such as Wnt-binding proteins[23,24,109,110] or lipoproteins or micelles[25,26].

This study aimed to determine the numbers of Wnt proteins per particle based on fluorescent signals originating from fluorescent proteins fused with Wnt proteins, ensuring that the conclusions were specifically influenced by Wnt proteins and not by other components. First, the advantages of using the mScarlet fusion for brightness determination, as compared to mCherry2, are discussed. Next, the molecular brightness values of mScarlet-WNT3a/5a/11-carrying particles were determined and compared to those of purified mScarlet, known to be monomeric, in order to derive the number of WNT3a/5a/11 proteins per particle. For non-EV-bound WNT proteins, molecular brightness was determined using a simple yet effective N&B analysis. On the other hand, high-heterogeneity samples, namely small-EV and large-EV fractions, were analyzed using FIDA. As a result, the number of WNT proteins per particle provides deeper insight into different modes of Wnt secretion.

5.1 Comparison between mCherry2 and mScarlet for Molecular Brightness Determination

For the accurate determination of molecular brightness, it is imperative to employ fluorescent proteins with both high brightness and apparent fluorescence probability. Utilizing fluorescent proteins with superior brightness enhances the signal-to-background ratio, consequently augmenting the differentiation between particles harboring varying numbers of fluorescent proteins. Moreover, the utilization of fluorescent proteins exhibiting high apparent fluorescence probability further accentuates the disparities in molecular brightness among particles containing different fluorescent protein quantities.

5.1.1 Evaluation of mCherry2 and mScarlet Brightness

The quantum yield and extinction coefficient of mCherry2[153] are 0.22 and 79,400 M^{-1} cm^{-1}, while those of mScarlet[154] are 0.7 and 100,000 M^{-1} cm^{-1}. Consequently, the brightness values resulting from excitation at λ_{ex} for mCherry2 and mScarlet are 17.5 and 70, respectively. Upon excitation at 560 nm, the excitation efficiencies for mCherry2 and mScarlet are at 58% and 79% of the maximum excitations[55]. Hence, the fluorescence intensity emitted by mScarlet surpasses that of mCherry2 by a factor of 5.5. Detection through a 600/37 nm (center/width) bandpass filter further amplifies this difference, where the signal emitted by mScarlet exceeds that of mCherry2 by a factor of 6.7, as determined based on the emission spectra in Figure 4.1B. Hence, mScarlet presents a superior choice, offering heightened signal-to-background ratio.

5.1.2 Determination of Apparent Fluorescence Probabilities of mCherry2 and mScarlet

5.1.2.1 Apparent Fluorescence Probability of mCherry2 and mScarlet Expressed in the Cytosol of Living Cells, Determined by N&B Analysis

The apparent fluorescence probability of fluorescent proteins can be determined by acquiring the molecular brightness of particles known to be consisting of one and n fluorescent proteins then applying Equation (3.6). In this study, cells were transfected with DNA constructs designed for the expression of fluorescent protein oligomers[†], which consist of n fluorescent proteins connected in a chain. The available DNA constructs were monomeric (1×) mCherry2, dimeric (2×) mCherry2, monomeric (1×) mScarlet, dimeric (2×) mScarlet, and trimeric (3×) mScarlet.

Control Measurement: The N&B Approach and Excitation Power Requirements

The N&B approach requires that the excitation power remain well below the threshold at which the fluorescence intensity versus excitation power curve exhibits asymptotic behavior (discussed in Section 2.1.2). Excessive excitation power can lead to deviations in photon count statistics from the Poisson distribution, thereby violating a fundamental assumption of the N&B analysis. To ensure reliable results, control measurements were conducted to determine the excitation power range in which fluorescence intensity remains linearly dependent on excitation power density.

Control measurements were performed to identify the optimal excitation power for measuring dimeric mCherry2 and trimeric mScarlet by assessing the average fluorescence intensity at varying excitation power densities. The focus on the largest oligomeric form of each fluorophore was due to their slower diffusion, which results in prolonged exposure to the laser

[†] The DNA constructs were designed by Julia Kuhlmann, a technician in AG Nienhaus, APH, KIT.

focus. Importantly, the excitation power levels determined for the larger oligomers were found to be suitable for use with smaller ones as well.

As a result, excitation power densities of 0.4 kW cm^{-2} and 0.2 kW cm^{-2} were selected for mCherry2 oligomers and mScarlet oligomers, respectively. These power densities are the highest that still maintain a linear relationship between fluorescence intensity and power density, as demonstrated in Figure 5.1.

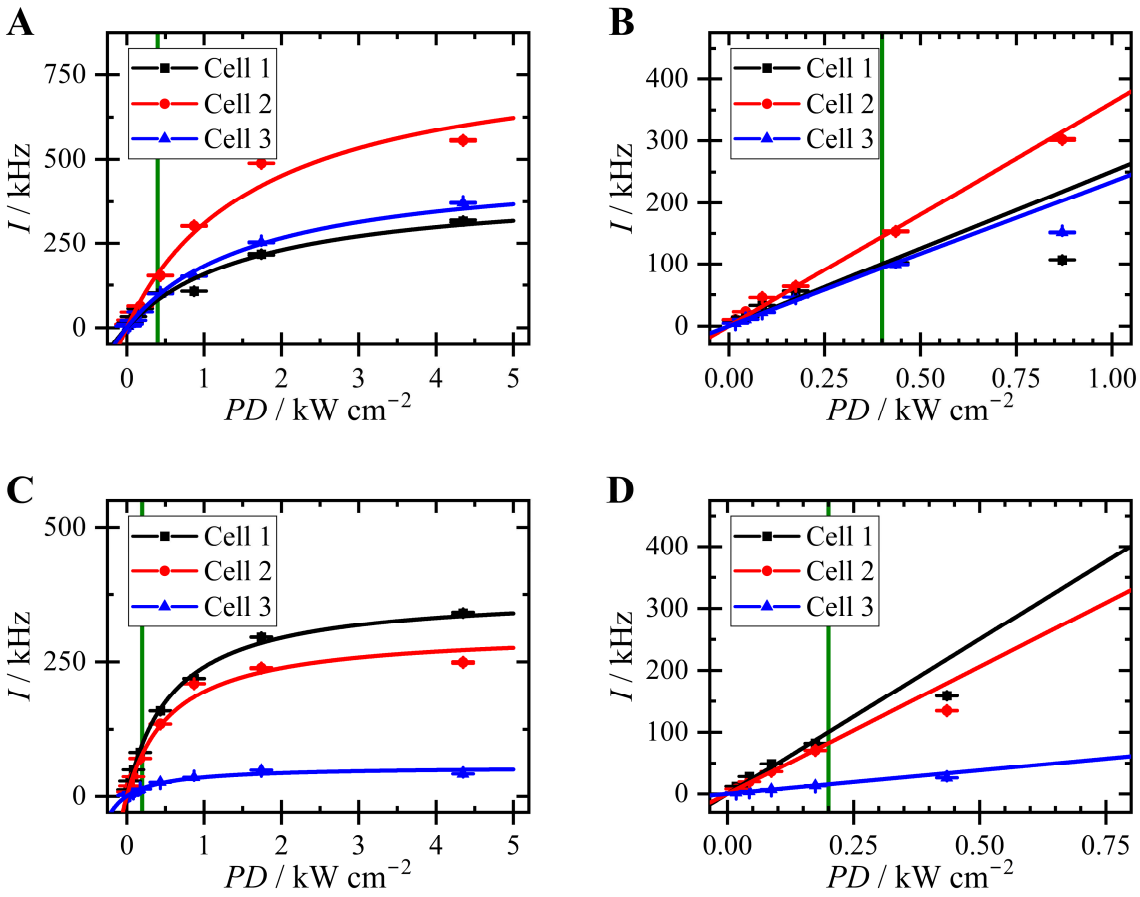

Figure 5.1. Dark Count-Subtracted Intensity (*I*) versus Excitation Power Density (*PD*) for Dimeric mCherry2 (A–B) and Trimeric mScarlet (C–D) Expressed in the Cytosol of Living Cells. The data points represent the mean, with error bars indicating the *SEM*. Different symbols and colors (black squares, red circles, blue triangles) correspond to measurements from different cells. For each fluorescent protein, the left graph displays the entire range of measurements, while the right graph shows a zoomed-in view of the initial region. In panels A and C, trendlines of matching colors were obtained through global fitting with Equation (2.2) using shared PD_{sat}. In panels B and D, trendlines of matching colors were fitted using the linear equation: $I = m \cdot PD$, where m is the slope. The average dark count was determined from three measurements taken with the laser shutter closed. Vertical green lines indicate the specific power densities used in further measurements.

In the zoomed-in views (Figure 5.1B,D), the intensity versus power density graphs up to 0.45 kW cm^{-2} were fitted with a linear equation, resulting in R^2 values of 0.97 for dimeric mCherry2 and 0.99 for trimeric mScarlet). Additionally, fitting the intensity against excitation power density graphs with Equation (2.2) resulted in saturation power densities of 1.7 ± 0.2 kW cm^{-2} (R^2 = 0.98) or dimeric mCherry2 and 0.58 ± 0.04 kW cm^{-2} (R^2 = 0.99) for trimeric mScarlet, values significantly above the power densities used in further measurements.

Following this, live-cell measurements were performed on cytosolic mCherry2 oligomers and mScarlet oligomers. To ensure the reproducibility of the results, measurements on mCherry2 oligomers were conducted across six cell generations, while those for mScarlet oligomers were conducted across four cell generations. The photons recorded in each measurement were sorted into intensity-time traces using a specific time bin, which requires careful consideration as will be explain now.

Effect of Time Bin on Apparent Molecular Brightness

While a larger time bin increases the mean photon count per bin, resulting in a higher *S/N* ratio, it is important to apply a small enough time bin to avoid the presence of apparent immobile particles. In this context, the term *apparent immobile* does not imply particles that are not moving but refers to the number of particles that appear unchanged between subsequent bins (see Figure 5.2A).

The presence of an immobile fraction primarily impacts the variance attributed to the occupation number, denoted as σ_n^2. Therefore, while Equations (2.6) and (2.7) remain valid, Equation (2.8) transforms to:

$$\sigma_n^2 = f_m \varepsilon^2 N \, . \tag{5.1}$$

Here, f_m, ε, and n represent the mobile fraction, molecular brightness, and particle number, respectively. The mobile fraction is defined as the proportion of mobile particle number to the total particle number. Solving Equations (2.6), (2.7), and (5.1) for the actual particle number and actual molecular brightness yields:

$$N = f_m \frac{\langle F \rangle^2}{\sigma^2 - \langle F \rangle} \quad \text{and} \quad \varepsilon = \frac{1}{f_m} \frac{\sigma^2 - \langle F \rangle}{\langle F \rangle} \, . \tag{5.2}$$

Consequently, the apparent number of particles, n_{app}, and the apparent molecular brightness, ε_{app}, calculated from the obtained intensity-time trace are

$$N_{app} = \frac{1}{f_m} N \quad \text{and} \quad \varepsilon_{app} = f_m \varepsilon \,. \tag{5.3}$$

In the presence of an immobile particles ($f_m < 1$), the analysis yields an artificially higher apparent number of particles and a lower apparent molecular brightness.

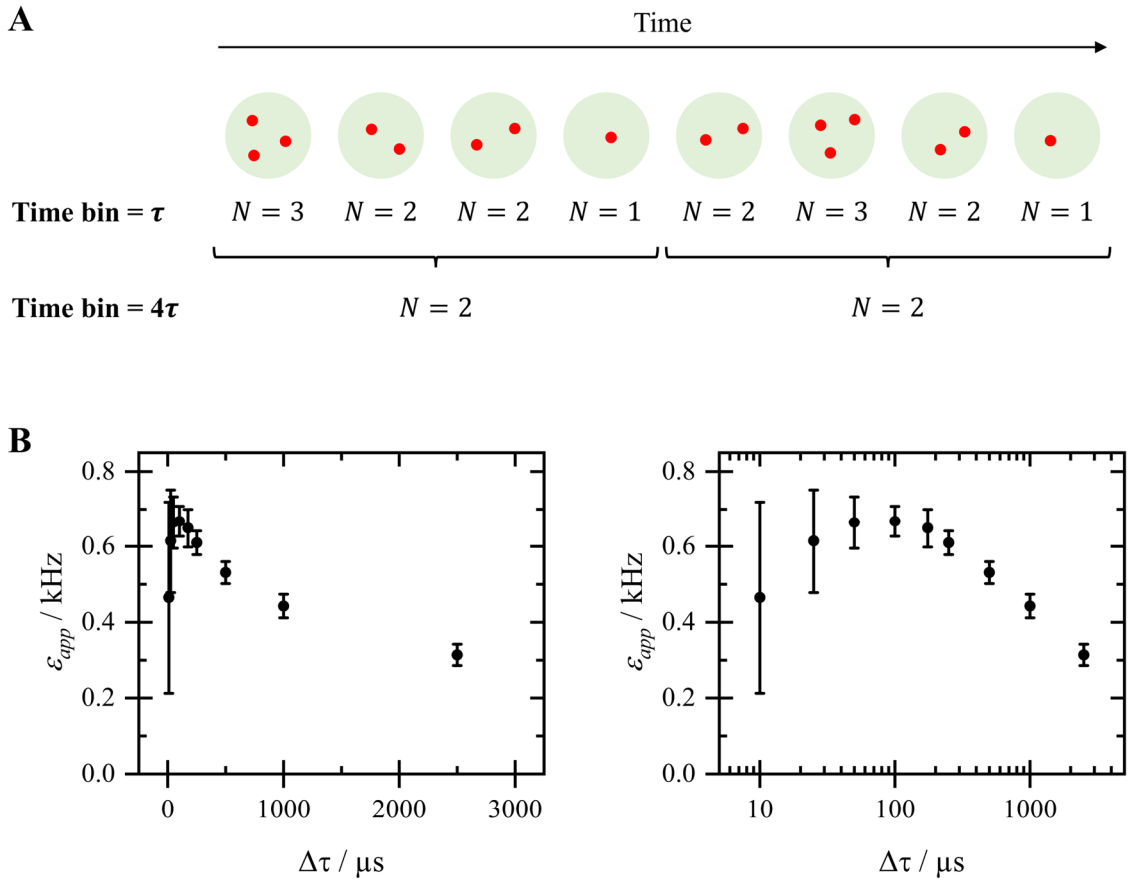

Figure 5.2. Effect of Time Bin on Apparent Number of Particles and Apparent Molecular Brightness

A: Fluorescent particles (red circles) detected in the observation volume (green circles). When the time bin τ is smaller than the average time that the particles spend in the observation volume, the particle number (N) detected in each time interval fluctuates as particles move into or out of the observation volume. …
(Continued on next page)

(Continued from previous page) … Conversely, with a larger time bin of 4τ, these fluctuations are averaged out, resulting in the appearance of two immobile particles.

B: Apparent molecular brightness (ε_{app}) of cytosolic monomeric mScarlet obtained from intensity-time traces constructed with different time bins ($\Delta\tau$), plotted on linear (left) and logarithmic (right) time axes. Data points represent mean, and error bars represent *SEM* (from 7 cells).

This behavior is demonstrated in the apparent molecular brightness of monomeric mScarlet in Figure 5.2B. Initially, increasing the time bin reduces the uncertainty of the measurement, but exceeding ~100 µs results in a reduction of the apparent molecular brightness. Therefore, all N&B analyses on cytosolic fluorescent proteins were subsequently performed using a time bin of 100 µs. As the measurement was performed on monomeric mScarlet, this time bin is automatically small enough for dimeric and trimeric mScarlet as larger oligomers diffuse slower. The time bin of 100 µs is also applicable to mCherry2 oligomers, as mScarlet and mCherry2 have similar structures and molecular masses[55], resulting in the same diffusion coefficient.

Automated Selection Algorithm

After processing photon data to create intensity-time traces with a time bin of 100 µs, many intensity-time traces display extra fluctuations that should not be caused solely by fluorescent protein diffusion. An example of the intensity-time traces with fluctuations mainly caused by fluorescent protein diffusion is shown Figure 5.3A. In contrast, the intensity-time trace in Figure 5.3B shows additional fluctuations. The overall intensity decrease may be attributed to photobleaching, which could be addressed through the segment-by-segment analysis outlined in Section 3.5. Furthermore, the intensity-time trace contains high intensity bursts (such as at 42 s), which possibly indicate a vesicle passing through the observation volume. These single large-fluctuation points were removed using an automated selection algorithm. This algorithm calculated the autocorrelation functions of intensity within individual segments and excluded those with high autocorrelation values at lag time τ > 10 ms (see Figure 5.3C–D).

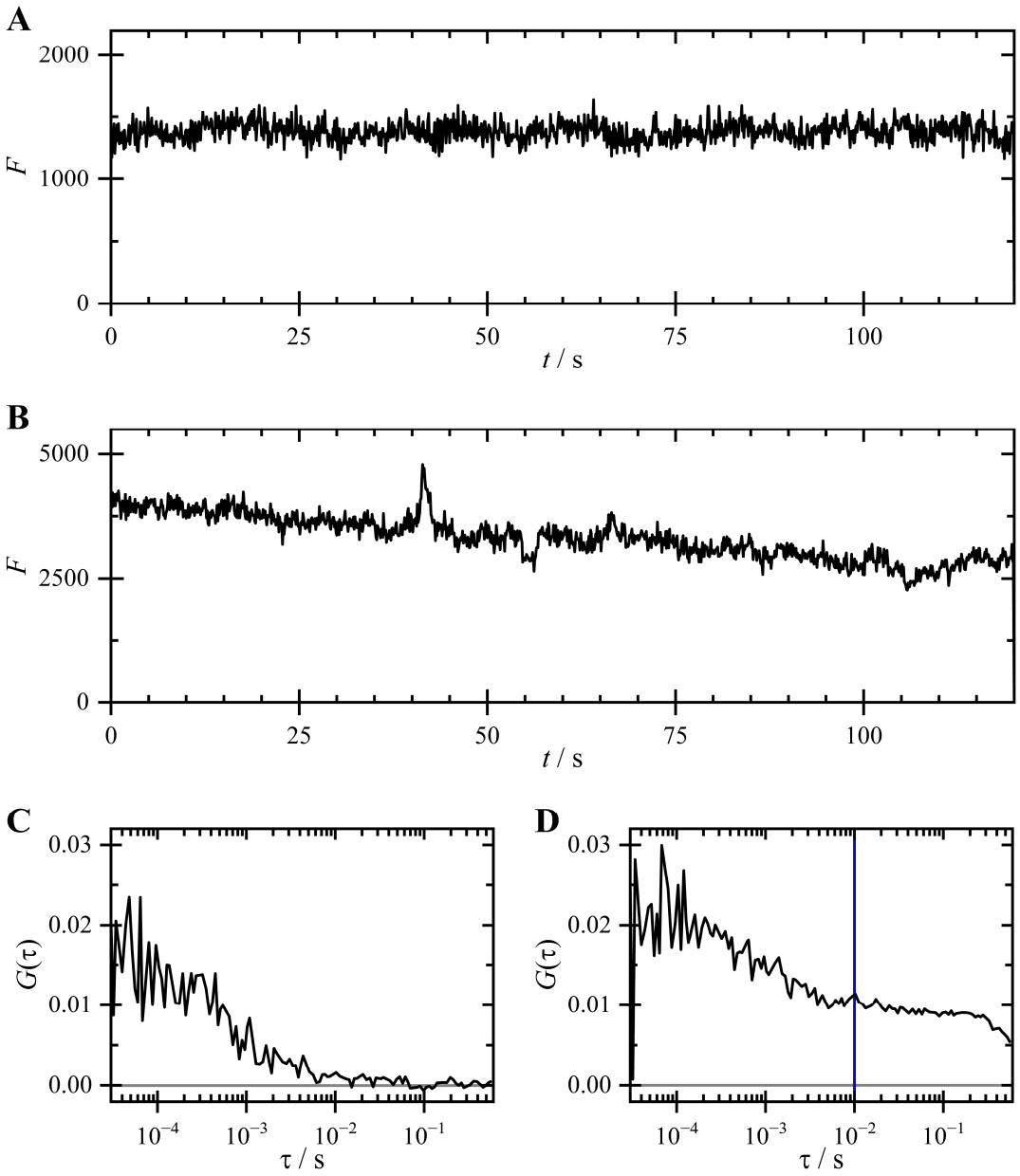

Figure 5.3. Examples of Intensity-Time Traces and Segment-Wise Autocorrelation Function Curves from Cytosolic Dimeric mCherry2

A–B: Photon count (F) versus time (t) graphs

C–D: Autocorrelation functions ($G(\tau)$) of the intensity-time trace in B from t = 0–5 s (C) and 40–45 s (D). The autocorrelation function in (D) shows high autocorrelation function values (more than 5% of the amplitude) at a large timescale (from the blue line rightwards), resulting in the exclusion of the segment t = 40–45 s by the selection algorithm.

Molecular Brightness of mCherry2 and mScarlet Oligomers

The segment-by-segment analysis yielded the molecular brightness of mCherry2 and mScarlet oligomers. The relative molecular brightness, calculated by normalizing the molecular

brightness of fluorescent proteins by the average molecular brightness of monomers of the same fluorescent protein (Equation (3.5)), of mCherry2 and mScarlet oligomers are presented in Figure 5.4. The relative molecular brightness values (mean ± SEM) of monomeric mCherry2 and dimeric mCherry2 are 1.00 ± 0.05 and 1.43 ± 0.11. In addition, the relative molecular brightness values for monomeric, dimeric, and trimeric mScarlet are as follows (mean ± SEM): 1.00 ± 0.07, 1.48 ± 0.14, and 1.58 ± 0.25, respectively.

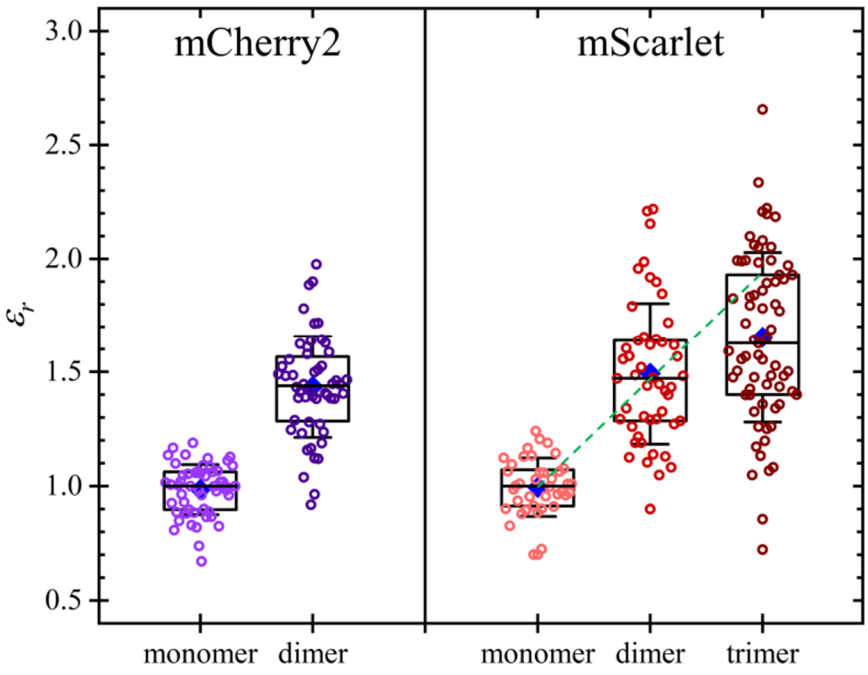

Figure 5.4. Relative Molecular Brightness (ε_r) of Cytosolic mCherry2 and mScarlet Oligomers. Each data point corresponds to a 120-s measurement taken on an individual cell. Boxes represent data points within the 25th to 75th percentile range, blue diamonds: mean, middle line: median, and whisker: *SD*. The dashed green line displays the linear projection from the median values of the relative molecular brightness of monomeric and dimeric mScarlet.

If all chromophores were functional, the trimeric and dimeric fluorescent proteins would be threefold and twofold brighter than the monomer. However, because not all fluorescent proteins in the oligomers are functional, the dimeric and trimeric fluorescent proteins exhibit lower average molecular brightnesses (Table 5.1). Furthermore, despite Equation (3.6) forecasting a linear relationship between the relative molecular brightness and fluorescent protein number, trimeric mScarlet has a lower average relative molecular brightness than predicted by the linear relationship. This deviation may be attributed to a reduced probability

of correct protein folding and chromophore maturation in mScarlet when incorporated into extended oligomeric chains. Additionally, the trimeric structure is more likely to experience photobleaching of one chromophore, causing the trimer to emit fluorescence as though it were a dimer. This issue could be mitigated by employing scanning N&B approach, as reported by Dunsing et al.[64]

Table 5.1. Relative Molecular Brightness of mCherry2 and mScarlet Oligomers and the Resulting Apparent Fluorescence Probabilities. The values are reported as median ± *MAD*.

Fluorescent Protein	Monomeric	Dimeric	Trimeric	Apparent Fluorescence Probability
mCherry2	1.00 ± 0.05	1.43 ± 0.11	-	43 ± 11%
mScarlet	1.00 ± 0.07	1.48 ± 0.14	1.58 ± 0.25	48 ± 15%

These factors collectively contribute to an overall reduction in the observed molecular brightness. To account for these effects, the apparent fluorescence probabilities were empirically determined using the molecular brightness values of monomeric and dimeric fluorescent proteins. The resulting calculations yielded apparent fluorescence probabilities of 43 ± 11% (median ± *MAD*) for mCherry2 and 48 ± 15% (median ± *MAD*) for mScarlet.

5.1.2.2 Maturation Efficiency of mCherry2 and mScarlet Determined by the Base-Denaturation Approach

To ascertain the apparent fluorescence probabilities obtained by N&B, maturation efficiencies of mCherry2 and mScarlet were determined. Although other factors can cause fluorescent proteins to appear dark such as long-lived excited states[63], the primary reason for common fluorescent proteins is the incomplete maturation process.

The determination of fluorescent protein maturation efficiency involves assessing the ratio of chromophore concentration to protein concentration in samples of fluorescent proteins purified from *E. Coli*. Chromophore and protein concentrations were determined by analyzing absorption spectra (Figure 5.5) obtained from mCherry2 and mScarlet stock solutions, which

were diluted to a final pH of 13 and pH 7.4, respectively. Both solutions underwent the same dilution process.

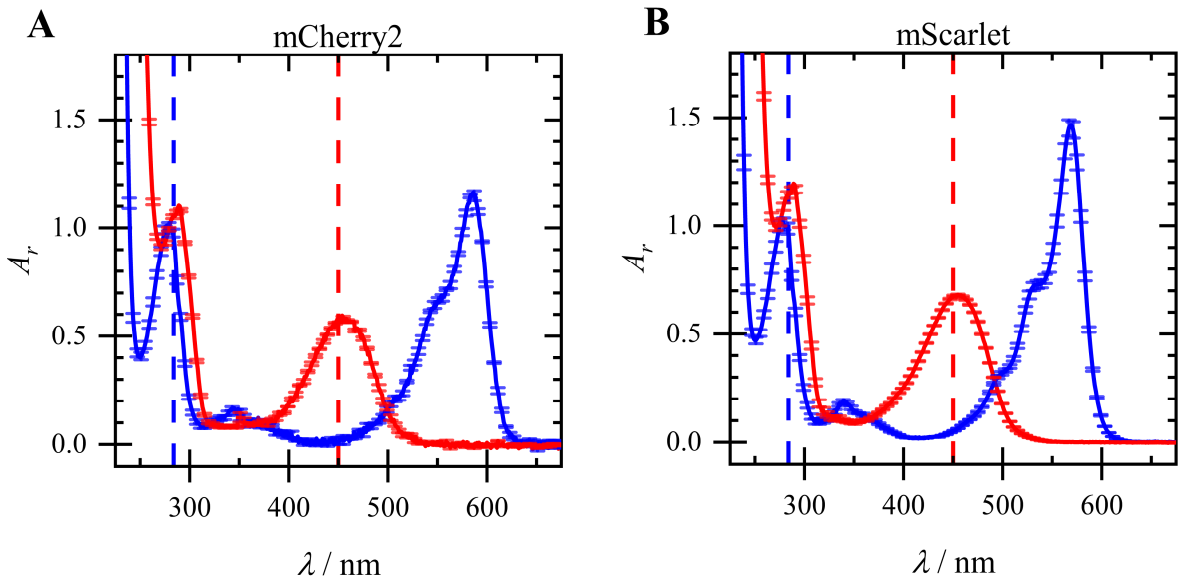

Figure 5.5. Absorption Spectra of mCherry2 (A) and mScarlet (B) at pH 7.4 (blue) and pH 13 (red). The y-axis shows relative absorbance (A_r), with absorbance values normalized such that the absorbance at 280 nm at pH 7.4 is set to 1. The vertical dashed blue and red lines indicate wavelengths of 280 nm and 447 nm, respectively. The plots represent mean values with *SEM* error bars from four replicates, all using the same stock solution.

The chromophore concentration was derived using the established knowledge that the ε_{447} for denatured chromophores at pH 13 is 44,000 M^{-1} cm^{-1} [118-120]. Conversely, the protein concentration was calculated based on the absorbance of fluorescent proteins at physiological pH (pH 7.4). Assuming that the samples contained only mCherry2 or mScarlet, the ε_{280} of proteins based on their DNA sequences were calculated to be 34,380 M^{-1} cm^{-1} [114].

The study revealed that the purified fluorescent proteins mCherry2 and mScarlet exhibited maturation efficiencies of 44 ± 1% and 52 ± 1% (mean ± *SD*), respectively. However, the interpretation of these maturation efficiencies requires careful consideration. Firstly, the accuracy of this approach is highly dependent on the purity of the purified fluorescent proteins. Any contamination by additional proteins in the samples would result in an increased absorption peak at 280 nm under pH 7.4 conditions, thereby introducing potential inaccuracies. Secondly, since the fluorescent proteins analyzed were obtained from only a single purification batch, the stated uncertainties are likely underestimations of the true uncertainties.

For researchers interested in other fluorescent proteins, the maturation efficiencies of additional proteins, including moxNeonGreen, eGFP, and mCherry, are provided in Appendix C.2.

In summary, the fluorescence signal of mScarlet is 6.7 times higher than that of mCherry2, and mScarlet exhibits a slightly higher apparent fluorescence probability. Consequently, the mScarlet-tagged variants of WNT3a, WNT5a, and WNT11 were used to determine the number of WNT proteins per particle.

5.2 Molecular Brightness of Non-EV-Bound mScarlet-WNT3a/5a/11 Units

This research employed N&B analysis to determine the average molecular brightness (number of photons emitted per particle) of mScartlet-WNT3a/5a/11 carriers in non-EV, small-EV, and large-EV fractions. The background intensity was measured in the control samples that have been prepared by processing the conditioned medium from cells transfected with pcDNA in the same manner. Purified mScarlet diluted in the control samples was used as a reference to obtain the molecular brightness of monomers.

The molecular brightness values of non-EV-bound mScarlet-WNT3a, mScarlet-WNT5a, and mScarlet-WNT11 units were acquired using the N&B method with stationary laser focus, with an excitation power density of 0.7 kW cm^{-2}. As a control measurement, the apparent molecular brightness versus time bin graph of purified mScarlet in the control non-EV fraction of conditioned medium collected from cells transfected with pcDNA was constructed (Figure 5.6A). To reduce the apparent immobile fraction, time bin should not exceed 30 µs (detailed derivation in Section 5.1.2.1). As the time bin is determined by the smallest particles to be measured, this conclusion also applies to measurements on small and large EVs.

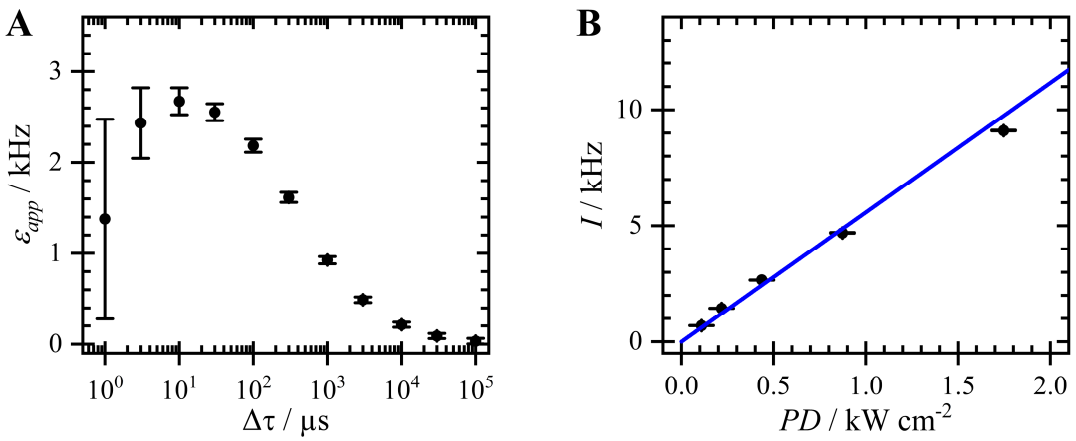

Figure 5.6. Control Measurements for N&B Measurements on Non-EV-Bound mScarlet-WNT Units. Points: mean; error bars: *SEM*.

A: Apparent molecular brightness (ε_{app}) of purified mScarlet versus bin time ($\Delta\tau$). All points (mean ± *SEM*) were analyzed from photons recorded for 300 s.

B: Background-corrected intensity (I) versus excitation power density (PD) measured from non-EV-bound mScarlet-WNT5a using 560-nm excitation. The fit with linear equation (blue line) returned R^2 of 0.98. The I against PD curve for the entire measured PD range is presented in Figure C.4 in Appendix C.

Additionally, a control measurement on the excitation power was performed on non-EV-bound mScarlet-WNT5a solution (Figure 5.6B), showing that the power density of 0.6 kW cm^{-2} is within the region where emitted intensity is linearly dependent on excitation power density. The full range of the fluorescence intensity versus excitation power data from the control measurement is presented in Figure C.4 in Appendix C. A significantly higher saturation power density (~30 kW cm^{-2}) was observed compared to the mScarlet expressed in the cytosol of living cells (~2 kW cm^{-2}; Section 5.1.2.1). This discrepancy arises because mScarlet molecules diffuse more slowly in the cytosol than in a liquid solution such as water or conditioned medium, resulting in prolonged exposure to the excitation laser and an increased probability of photobleaching. Although the power control measurement was performed only on non-EV-bound mScarlet-WNT5a, this power is applicable to mScarlet-WNT3a and mScarlet-WNT11, as their sizes were assumed to be not significantly larger than that of mScarlet-WNT5a. This assumption is confirmed in Section 6.2.

The relative molecular brightness values are presented in Figure 5.7. The values of mScarlet-WNT3a and mScarlet-WNT11 are plotted separately from those of mScarlet-WNT5a due to differences in sample preparation, specifically the presence of phenol red in mScarlet-WNT5a samples. As shown in Figure 4.1F, the increased background considerably lowers the

signal-to-background ratio; however, the background is uncorrelated (Figure C.5 in Appendix C) and can be treated as constant, allowing background correction via Equations (2.12)–(2.13).

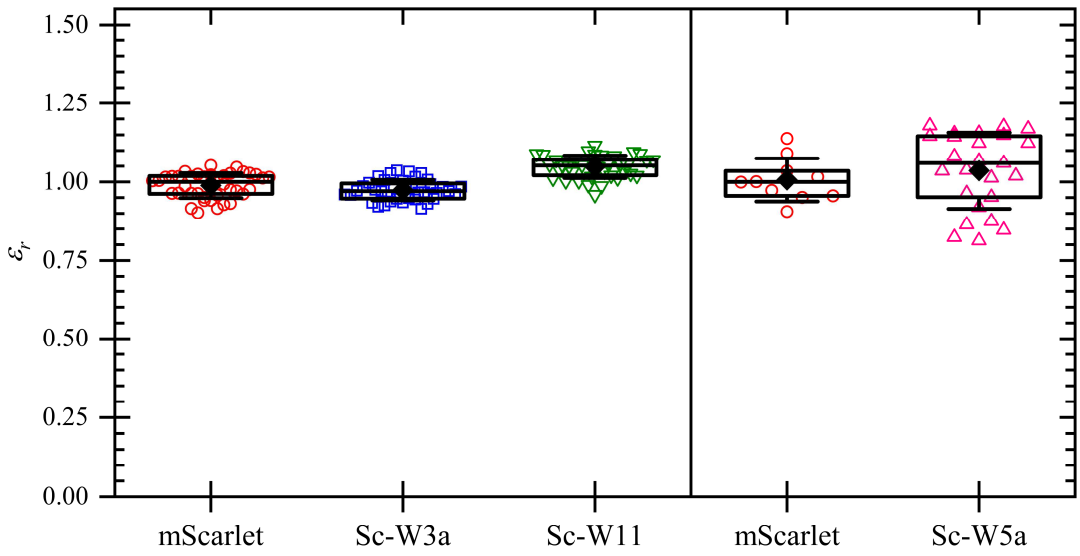

Figure 5.7. Relative Molecular Brightness of Non-EV-Bound mScarlet-WNT3a (Sc-W3a), mScarlet-WNT5a (Sc-W5a), and mScarlet-WNT11 (Sc-W11) Units. The left and right sides of the figure show the relative molecular brightness (ε_r) of the samples without and containing phenol red, respectively. Each data point represents a single measurement. The boxes show the 25th–75th percentile range, while the whiskers represent the range of mean ± *SD*. The central lines denote the median; the blue diamond dots represent the mean.

The results show that non-EV-bound mScarlet-WNT3a, mScarlet-WNT5a, and mScarlet-WNT11 units have relative molecular brightness values of 0.97 ± 0.02, 1.05 ± 0.03, and 1.06 ± 0.09 (median ± *MAD*). Consequently, each non-EV-bound mScarlet-WNT3a/5a/11 unit contains a single functional mScarlet.

5.3 Molecular Brightness of Small and Large EVs carrying mScarlet-WNT3a/5a proteins

The fluorescence signals emitted from EVs were collected using a galvo scanner, which shifted the laser focus position in a raster scan pattern to account for their slow diffusion. This approach improved statistical data collection while minimizing photobleaching. The pixel dwell time in

raster-scanning measurements is equivalent to the bin time in stationary-focus measurements. Based on prior control measurements of purified mScarlet (Figure 5.6A), a pixel dwell time of 30 µs was selected.

Small and large EVs containing mScarlet-WNT3a, mScarlet-WNT5a, or mScarlet-WNT11 proteins were measured with a power density between 0.6–2.0 kW cm^{-2}, where the relationship between emitted intensity and power density remains linear (Figure 5.8). Notably, the same power density could be used for both small and large EVs due to the limited exposure time of EVs to laser determined by the pixel dwell time, not the EV size.

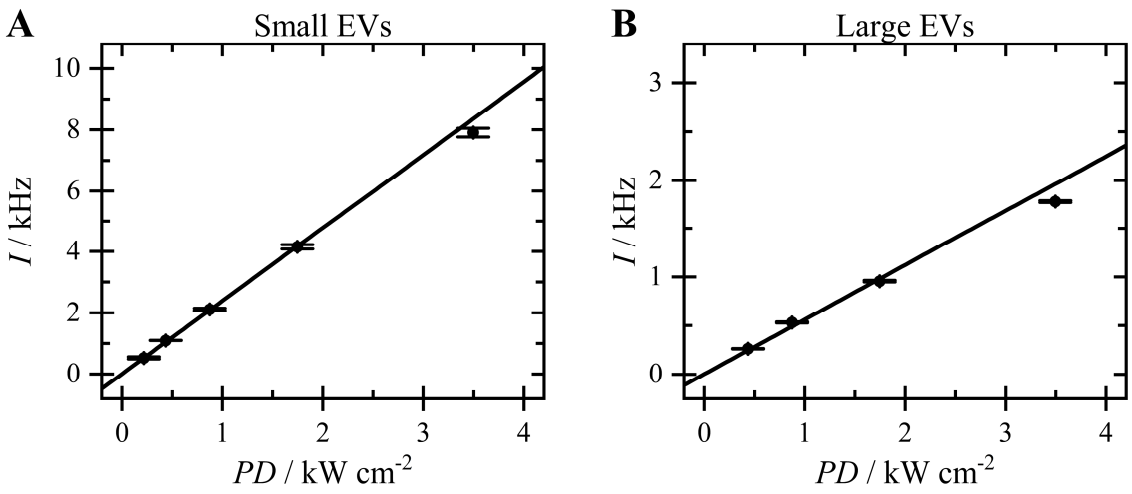

Figure 5.8. Background-Corrected Intensity (*I*) Detected from EVs Carrying mScarlet-WNT5a with Respect to Power Density (*PD*). Data points show mean values from three 100-frame measurements, with *SEM* as error bars. Best-fit lines were obtained by linear regression with the y-intercept fixed at zero: $I = m \cdot PD$. The I against PD curve for the entire measured PD range is presented in Figure C.6 in Appendix C.
A: Small EVs: m = 2.39 ± 0.02 (mean ± *SD*); R^2 = 1.0
B: Large EVs: m = 0.56 ± 0.02 (mean ± *SD*); R^2 = 0.99

5.3.1 Cluster removal algorithm via DBSCAN

The measurements yielded images of EVs in solution, which were processed to eliminate signals originating from extra-large particles present in the samples. These particles could stem from EV aggregation, as observed in the dynamic light scattering results in Section 4.3. Moreover, inherent imperfections in EV isolations led to the presence of supplementary

particles, such as cell debris in large EV samples or large EVs in small EV samples. Hence, a Python script was developed for automated cluster removal to eliminate large particles from EV images.

Firstly, the program converts an image into its binary equivalent by applying a threshold that excludes 99% of the background (Figure 5.9). Subsequently, the density-based clustering non-parametric algorithm DBSCAN was implemented to identify significant clusters, relying on a priori information regarding the diameters of small EVs (30–150 nm)[29,38] and large EVs (100 nm – 1 μm)[39]. Following this, large clusters are deleted from the original image. Examples of the processed images are displayed in Figure 5.10.

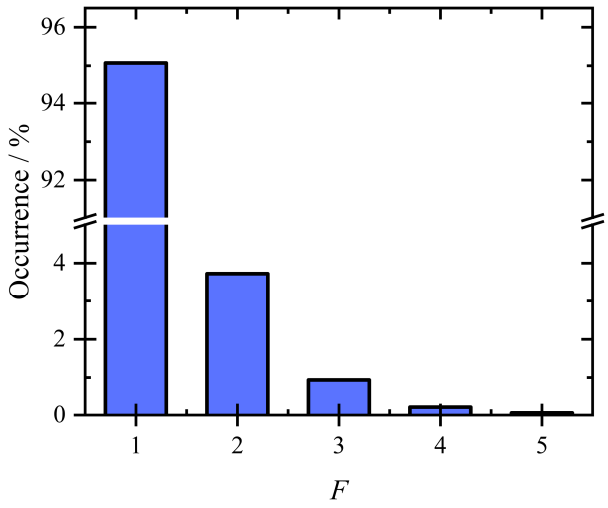

Figure 5.9. Histogram of Photon Counts (*F*) on Individual Pixels of Images Obtained from the Control Small-EV Sample Isolated from Conditioned Medium Collected from Cells Transfected with pcDNA. The number of occurrences is converted into percentages. Pixels with zero photon count are not included. 99% of the pixels have photon counts less than 3.

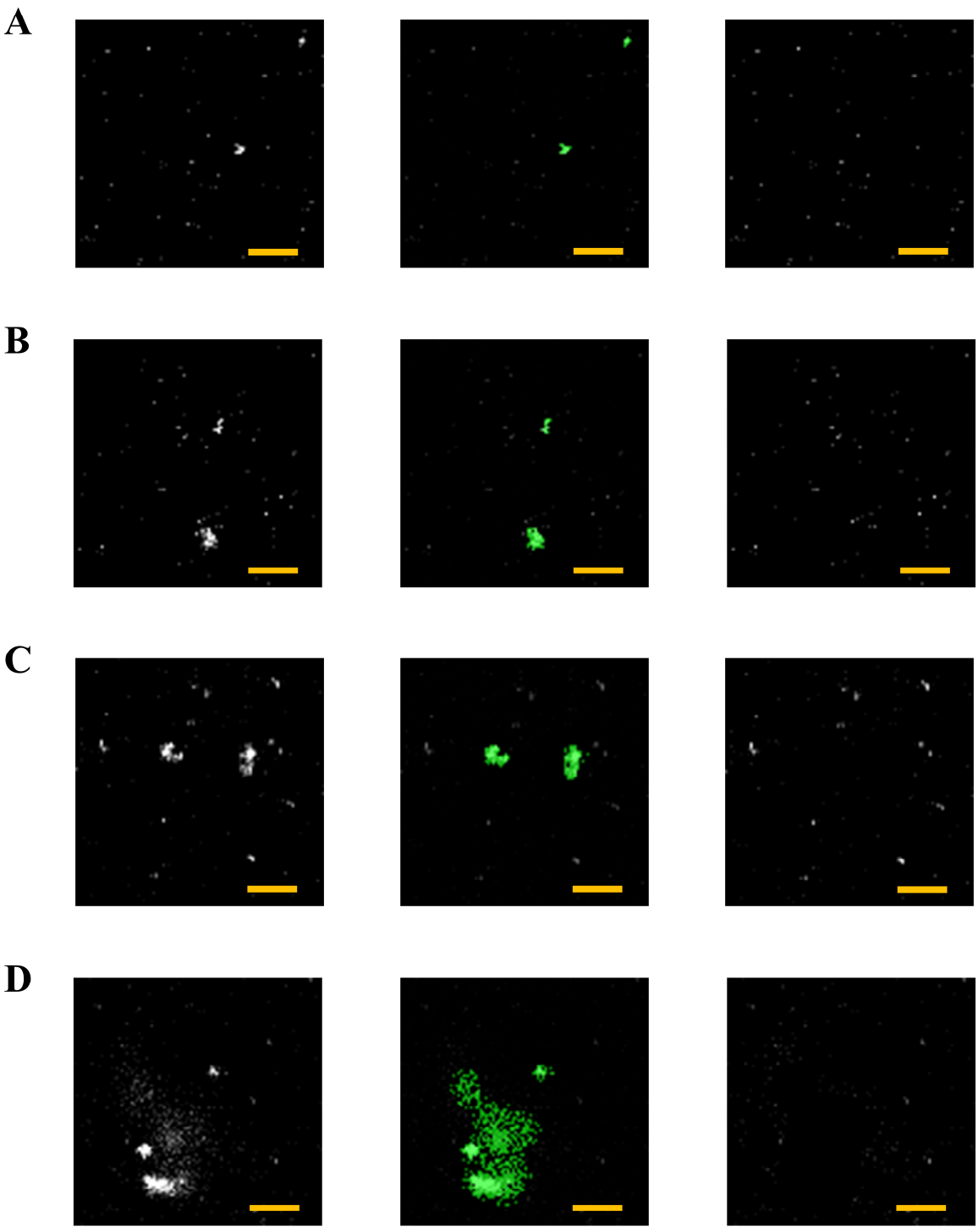

Figure 5.10. Images of Small EVs (A–B) and Large EVs (C–D) Containing mScarlet-WNT3a Proteins Before and After Automated Cluster Removal. The yellow scale bars represent a distance of 5 µm.
Left column: Raw images
Middle column: Raw images, overlaid with detected cluster positions marked in green
Right column: Processed images after the removal of large clusters

5.3.2 Photon Counting Histogram

Figure 5.11B–E shows the photon counting histograms of EVs constructed from images that were processed using the cluster removal procedure described in Section 5.3.1. In contrast to the photon counting histogram of purified mScarlet (Figure 5.11A), the EV histograms exhibit significant brightness heterogeneity. Consequently, the average molecular brightness from N&B analysis, which is biased by the brighter particles, is unsuitable for determining the number of WNT proteins. To overcome this limitation, FIDA was employed to extract species-specific concentration and brightness values.

The EV photon counting histograms were fitted to a heuristic multi-component model representing several EV populations, each characterized by a distinct relative molecular brightness, i.e., different numbers of mScarlet molecules (Equation (2.53)). For small EVs, the model incorporated presumed components corresponding to the relative molecular brightness of 1, 20, 60, 150, and 300, while for large EVs an additional component representing relative molecular brightness of 600 was included to account for the broader tail observed in the histogram. The parameters describing the observation volume (a_1, a_2, a_3, and B_0 in Equation (2.53)) were calibrated daily using measurements on Alexa Fluor 546 (listed in Table C.5 in Appendix C). The model also included a background contribution based on the signal measured from DPBS samples containing EVs from cells transfected with pcDNA (listed in Table C.6 in Appendix C). A control analysis on the images from purified mScarlet—whose FIDA model contained only a single component (1 mScarlet protein per particle)—confirmed that the molecular brightness determined by FIDA is consistent to that obtained from N&B analysis (results listed in Table C.7 in Appendix C).

The fit photon counting histograms of fluorescence emitted from EVs yielded concentrations for individual components as reported in Appendix C.4.3. The weighted average relative molecular brightness, calculated using the concentration as a weight, is very similar across all small and large EV samples and only slightly above 1 (see Table 5.2). A closer inspection reveals that the first component, which represents the monomer with a relative molecular brightness of 1, has a significantly higher concentration (in the nM range) compared to the brighter components (with concentrations in the fM–pM range). To facilitate comparison among these brighter components, a weighted relative molecular brightness was calculated excluding the monomeric component, as shown in Table 5.3.

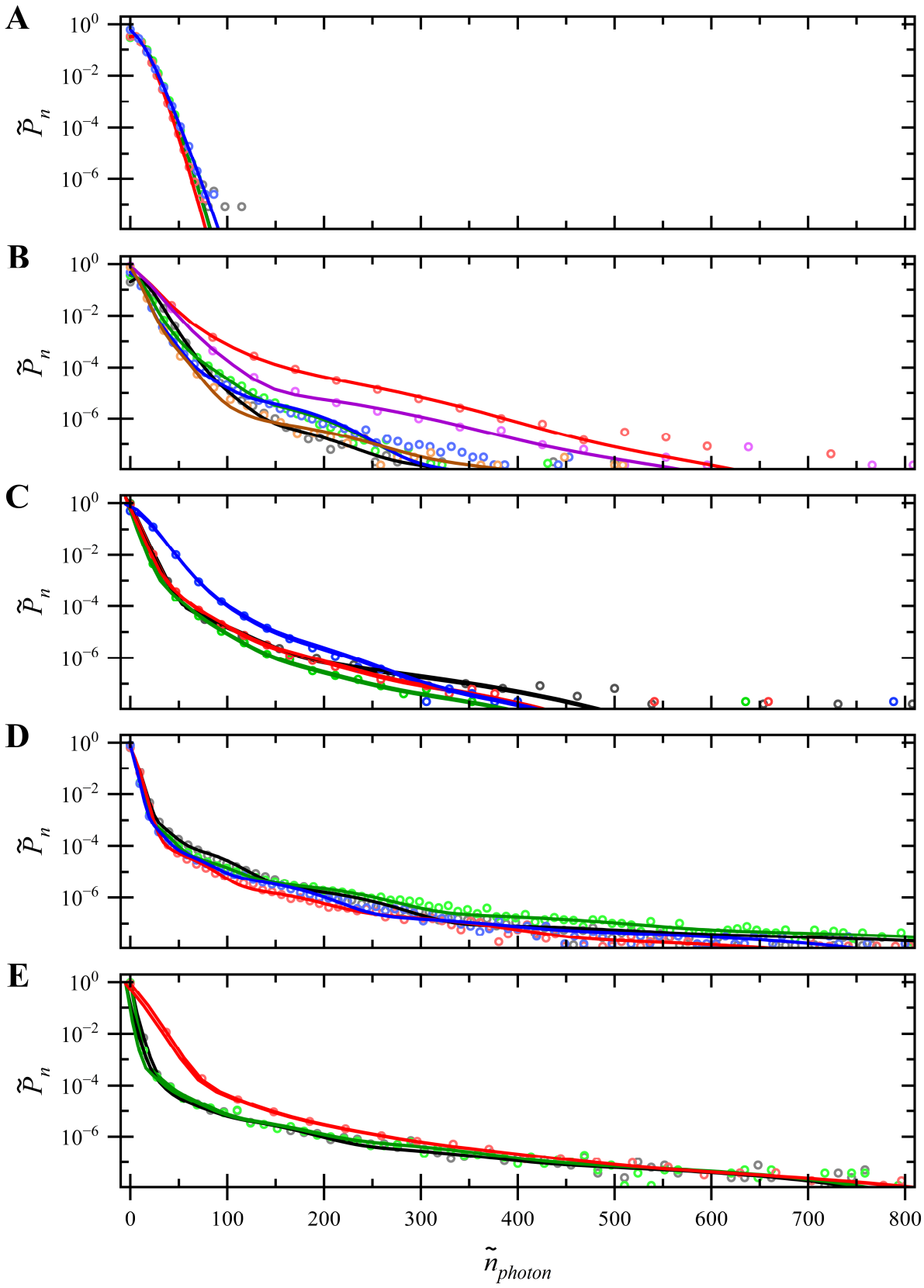

Figure 5.11. Photon Counting Histograms of Purified mScarlet and EVs. The horizontal axis represents the number of photons normalized by the brightness of purified mScarlet ($\tilde{n}_{photon}$), as determined by N&B analysis and adjusted for excitation power, emission filter, and detection efficiency of the ... (Continued on next page)

(Continued from previous page) ... microscope. The vertical axis shows the number of events normalized so that the total number of events equals one ($\tilde{P}_n$). Different colors correspond to different samples. Note that because the vertical axis is logarithmic, points corresponding to 0 events are not displayed.

A: purified mScarlet
B: small EVs containing mScarlet-WNT3a
C: small EVs containing mScarlet-WNT5a
D: large EVs containing mScarlet-WNT3a
E: large EVs containing mScarlet-WNT5a

Table 5.2. Relative Molecular Brightness Values of Small and Large EVs Carrying mScarlet-WNT3a/5a, Weighted Averages from All Brightness Components. All values for individual samples are reported as the mean ± *SEM*. The overall mean ± *SEM* in the last row was calculated with 1/*SEM* as weight. The fitted values for individual components are provided in Appendix C.4.

Sample	Small EVs		Large EVs	
	mScarlet-WNT3a	mScarlet-WNT5a	mScarlet-WNT3a	mScarlet-WNT5a
1	1.04 ± 0.21	1.03 ± 0.11	1.07 ± 0.12	1.09 ± 0.87
2	1.09 ± 0.20	1.09 ± 0.02	1.10 ± 0.07	1.32 ± 0.69
3	1.10 ± 0.02	1.06 ± 0.19	1.02 ± 0.18	1.02 ± 0.17
4	1.21 ± 0.09	1.06 ± 0.21	1.09 ± 0.10	–
5	1.07 ± 0.04	–	–	–
6	1.06 ± 0.08	–	–	–
Mean ± *SEM*	**1.10 ± 0.02**	**1.08 ± 0.01**	**1.08 ± 0.02**	**1.08 ± 0.08**

Table 5.3. Relative Molecular Brightness Values of Small and Large EVs Carrying mScarlet-WNT3a/5a, Weighted Averages Excluding the First ($\varepsilon_r = 1$) Brightness Component. All values for individual samples are reported as the mean ± *SEM*. The overall mean ± *SEM* in the last row was calculated with 1/*SEM* as weight. The fitted values for individual components are provided in Appendix C.4.

Sample	Small EVs		Large EVs	
	mScarlet-WNT3a	mScarlet-WNT5a	mScarlet-WNT3a	mScarlet-WNT5a
1	21 ± 7	39 ± 21	27 ± 3	30 ± 12
2	22 ± 5	23 ± 2	28 ± 5	32 ± 3
3	21 ± 1	24 ± 2	33 ± 6	35 ± 31
4	23 ± 3	22 ± 5	28 ± 2	–
5	21 ± 2	–	–	–
6	20 ± 4	–	–	–
Mean ± *SEM*	**21 ± 1**	**23 ± 2**	**28 ± 1**	**32 ± 1**

5.4 Discussion

This chapter aims to provide a better understanding of the number of Wnt proteins carried by individual secreted units, achieved through molecular brightness, i.e., the fluorescence intensity emitted per particle.

The WNT3a/5a/11 proteins in this study were labeled with two fluorescent protein options: mCherry2 and mScarlet. In terms of brightness, which directly affects the signal-to-noise ratio, the advantage of mScarlet over mCherry2 is evident, as the estimated fluorescent signal from mScarlet is approximately seven times that of mCherry2.

Nevertheless, the use of mScarlet was uncertain, as mCherry2 was reported by Dunsing et al.[64] to have an apparent fluorescence probability nearly double that of mScarlet. This is important because a higher apparent fluorescence probability leads to a larger gap in molecular brightness among different oligomerizations, making the conclusions about the oligomerization state more precise. However, this conclusion could not be accepted without further validation, as the same publication reports a maturation efficiency of mScarlet (40 ± 5%), which contradicts the 86 ± 3% presented by another study[155]. To clarify this, the apparent fluorescence probabilities of mCherry2 and mScarlet were examined using N&B analysis performed on cytosol of living cells. The measurements yielded apparent fluorescence probabilities of 43 ± 11% (median ± *MAD*) for mCherry2 and 48 ± 15% (median ± *MAD*) for mScarlet. The apparent fluorescence probability of mScarlet from these results agrees with that of Dunsing et al., while the value for mCherry2 differs.

Following this, to confirm the apparent fluorescence probabilities, the maturation efficiency of mCherry2 and mScarlet was measured on purified fluorescent proteins from *Escherichia coli*, using the well-established spectroscopic base-denaturation approach. As a result, the maturation efficiencies of mCherry2 and mScarlet were found to be 44 ± 1% and 52 ± 1% (mean ± *SD*), respectively, both supporting the apparent fluorescence probabilities determined previously in this research.

Interestingly, the maturation efficiencies obtained from the base-denaturation approach closely align with the apparent fluorescence probabilities of mCherry2 and mScarlet, despite the two approaches being fundamentally different. Specifically, the apparent fluorescence probability is influenced not only by maturation efficiency but also by factors such as

fluorophore flickering. Additionally, the fluorescent proteins used in these analyses were expressed in different host systems: human cells (eukaryotes) and *Escherichia coli* (prokaryotes).

Based on the improved brightness and apparent fluorescence probability of mScarlet, the mScarlet-WNT3a/5a/11 variants were measured to determine the number of WNT proteins per particle. For the non-EV-bound mScarlet-WNT units, N&B analysis resulted in relative molecular brightness (median ± *MAD*) values of 0.97 ± 0.02 (mScarlet-WNT3a), 1.05 ± 0.03 (mScarlet-WNT5a), and 1.06 ± 0.09 (mScarlet-WNT11). Hence, each non-EV-bound mScarlet-WNT3a, mScarlet-WNT5a, or mScarlet-WNT11 unit essentially contains one WNT protein per particle. This suggests that the solubilization of the non-EV-bound WNT3a, WNT5a, and WNT11 proteins primarily occurs via co-diffusing proteins and/or lipids, rather than the formation of homo-oligomers. The possibility of hetero-oligomerization with other unlabelled WNT proteins as the main transport mode is also ruled out, as the cells were treated with antibiotics to overexpress labelled WNT proteins. Therefore, the likelihood of the sample containing enough unlabelled WNT to form oligomers with the majority of the labelled WNT proteins is minimal.

Subsequently, the number of mScarlet-WNT3a/5a proteins loaded onto each EV was determined using FIDA. The analysis yielded the following average relative molecular brightness values (mean ± *SEM*): small EVs containing mScarlet-WNT3a had a brightness of 1.10 ± 0.02, while small EVs containing mScarlet-WNT5a had a brightness of 1.08 ± 0.01. For large EVs, the relative molecular brightness values were 1.08 ± 0.02 for those containing mScarlet-WNT3a and 1.08 ± 0.08 for those containing mScarlet-WNT5a.

However, the average relative molecular brightness alone does not fully represent the data, as photon counting histograms reveal significant heterogeneity in the molecular brightness of the EV population (see Figure 5.11B–E). These histograms show a main peak corresponding to particles with a relative brightness of 1, along with a long tail representing particles with much higher relative molecular brightness but at significantly lower concentrations (two to three orders of magnitude less).

To account for this heterogeneity, the concentration-weighted average relative molecular brightness of all components, excluding the main peak, were calculated. The results are as follows (mean ± *SEM*): 21 ± 1 for small EVs containing mScarlet-WNT3a, 23 ± 2 for

small EVs containing mScarlet-WNT5a, 28 ± 1 for large EVs containing mScarlet-WNT3a, and 32 ± 1 for large EVs containing mScarlet-WNT5a. These values indicate the number of bright mScarlet proteins on each particle.

To calculate the total number of WNT proteins, it is necessary to account for the WNT proteins tagged with non-fluorescent mScarlet, as stated in Equation (3.6). The apparent fluorescence probability of mScarlet, 48 ± 15% (median ± *MAD*), was used, a value assumed to be consistent with that of mScarlet in the WNT fusions, given that the proteins fold under similar physiological conditions (both within the cytosol of HEK293T cells). After applying this correction, the total number of mScarlet-WNT3a proteins on small EVs is 43 ± 5 (mean ± *SEM*), and the total for mScarlet-WNT5a on small EVs is 48 ± 7 (mean ± *SEM*). For large EVs, the corresponding values are 58 ± 7 (mean ± *SEM*) for mScarlet-WNT3a and 65 ± 7 (mean ± *SEM*) for mScarlet-WNT5a. It should be noted that this correction was not necessary for the non-EV fraction or for the main peak, as particles with non-fluorescent mScarlet are not detected at all when there is only one mScarlet-WNT protein per particle.

It should be noted that although some of the WNT5a data collected in this research were analyzed and presented in another publication[156], differences in the final numbers of mScarlet-WNT5a proteins per EV in this dissertation may arise due to different data selection and treatment methods used.

The results show that particles in EV fractions consist of two distinct sub-populations. One sub-population contains tens of WNT proteins per particle, with no observed difference in the number of mScarlet-WNT3a and mScarlet-WNT5a proteins. In this group, large EVs carry more WNT proteins than small EVs. The other sub-population, present at concentrations hundreds to thousands of times higher, consists of particles with a single WNT3a/5a protein per particle.

The origin of these two sub-populations remains unclear. Some of the smaller particles may result from cross-contamination of non-EV-bound mScarlet-WNT units into the EV fractions, while the very bright particles might arise from EV aggregation. However, it cannot be ruled out that the diverse brightness populations result from underlying physiological factors. The current analysis does not enable the determination of which particles do not belong to the small or large EV fractions without simultaneously considering both the size and brightness of individual particles. This issue could be addressed by analyzing individual intensity bursts

separately, characterizing the specific particle size and brightness from each burst[157]. Such an approach would facilitate the identification of particles outside the expected size range, enabling the exclusion of those with anomalous molecular brightness.

Regarding the analysis of WNT protein numbers per particle in all fractions presented in this chapter, it is important to note that the numbers obtained do not include unlabeled endogenous WNT proteins. Nevertheless, the proportion of unlabeled proteins is likely much lower than those labeled with mScarlet due to the overexpression of mScarlet-WNT in the cells. Therefore, the underestimation of WNT protein numbers should be minimal. On the other hand, the transfection process and overexpression of the proteins may influence the number of WNT proteins released, which requires further investigation.

To enhance the precision of WNT protein quantification, it is recommended to find a red fluorescent protein with a higher apparent fluorescence probability while maintaining high brightness. Currently, eGFP is widely recognized for its high maturation efficiency (~70%[64]), but its applicability for characterizing proteins in the non-EV fraction is limited by the high background in the green-emission region of cell culture media (as shown in Section 4.1).

5.5 Summary

To determine the number of WNT proteins per particle, mScarlet proves to be a superior labeling option compared to mCherry2 due to its enhanced brightness and higher apparent fluorescence probability. Using the N&B analysis, it was demonstrated that non-EV-bound WNT3a, WNT5a, or WNT11 units each contain, on average, one WNT protein per particle. This indicates that, unless packaged in EVs, the majority of WNT3a/5a/11 proteins do not diffuse as a homo-oligomer in the extracellular space.

Furthermore, FIDA provided insights into the number of WNT3a/5a proteins secreted in EVs. In both small and large EV populations, WNT3a and WNT5a are primarily present as single proteins per particle, similar to the non-EV fraction. However, a small sub-population within both small and large EVs contains particles with tens of WNT3a/5a proteins, with large EVs carrying more WNT3a/5a proteins per particle than small EVs.

6. Hydrodynamic Radii of Secreted Wnt Particles

A review of the current literature reveals a significant gap in the available information regarding the hydrodynamic radii of secreted WNT entities in conditioned medium. When considering non-EV-bound Wnt units, existing data on the sizes of Wnt proteins have been obtained through structural analysis or biochemical techniques, which often entail purification of the proteins[22,158,159]. Notably, Takada et al.[22] attempted to determine the average hydrodynamic radius of GFP-mWnt3a proteins using FCS but encountered challenges in achieving sufficient precision. Furthermore, investigations concerning Wnt-loaded EVs (for example, in References [143,160]) commonly assume that the they possess the average size of all EVs.

This chapter aims to address this knowledge gap by examining the hydrodynamic radii of secreted WNT3a, WNT5a, and WNT11 entities to gain insight into their structural arrangement in the extracellular milieu. FCS was employed to exclusively measure the hydrodynamic radii of particles containing mCherry2/mScarlet-WNT proteins. To that end, a comprehensive analysis was conducted to evaluate the suitability of mCherry2 and mScarlet as choices for FCS measurements. Subsequently, the translational diffusion coefficients of non-EV-bound mCherry2-WNT units were determined, which were then used to calculate the hydrodynamic radii. Additionally, polarization-dependent FCS was implemented to obtain the rotational diffusion characteristic times of the non-EV-bound mCherry2-WNT units. Finally, the translation diffusion observed using FCS provides information about the hydrodynamic radii of both small and large mScarlet-WNT-loaded EVs.

6.1 Flickering of mCherry2 and mScarlet

Flickering between bright and dark states in fluorescent proteins can manifest across a wide range of timescales, from sub-milliseconds[87,161-164] to seconds[165,166]. In the context of FCS, the influence of flickering on the observed dynamics of fluorescent particles within the detection volume is critical to consider. When the particle transitions into a dark state, its intensity decreases, mimicking the effect of the particle leaving the observation volume. Consequently, the autocorrelation function of the particles displays an apparent reduction in diffusional correlation time.

Flickering effects on the autocorrelation functions of mCherry2 and mScarlet were investigated through FCS measurements conducted at various excitation power densities ranging from 0.6 to 2.0 kW cm^{-2}. Figure 6.1A-B presents the autocorrelation functions obtained from single samples of purified mCherry2 (Panel A) and mScarlet (Panel B) diluted in buffer. The autocorrelation functions for both mCherry2 and mScarlet shift leftward as the excitation power density increases.

As mCherry2 exhibits lower emission intensity, the measurements were repeated for three independent samples to improve the statistics of the autocorrelation function. Subsequently, the autocorrelation functions of both mCherry2 and mScarlet were fitted using a *pure diffusion* model (Equation (2.27)):

$$G(\tau) = G_D(\tau) = \frac{1}{N}\left(1 + \frac{4D\tau}{w_0^2}\right)^{-1}\left(1 + \frac{4D\tau}{S^2 w_0^2}\right)^{-1/2} \tag{6.1}$$

returned diffusion coefficients which varied with power density. The resulting diffusion coefficients (mean ± *SD*) were 108 ± 2 μm^2 s^{-1} (at 0.7 kW cm^{-2}) and 114 ± 1 μm^2 s^{-1} (at 2.0 kW cm^{-2}) for mCherry2, and 140 ± 4 μm^2 s^{-1} (at 0.6 kW cm^{-2}) and 202 ± 4 μm^2 s^{-1} (at 1.8 kW cm^{-2}) for mScarlet. These diffusion coefficients are evidently inaccurate as diffusion coefficients are independent of the excitation power, and hence they will be called apparent diffusion coefficients, D_{app}. Notably, they exceed the expected value of 102 μm^2 s^{-1} for the diffusion coefficient of GFP-like fluorescent proteins at 25.0°C.[†]

[†] The value was calculated based on the reported value of 95 μm^2 s^{-1} at 22.5 ± 0.5°C [115,163,167]. Since the uncertainty of the reported diffusion coefficient is not provided, ... (Continued on next page)

(Continued from previous page) ... the uncertainty of the calculated value cannot be determined. However, considering the temperature uncertainty, the minimum uncertainty is estimated to be ±2°C.

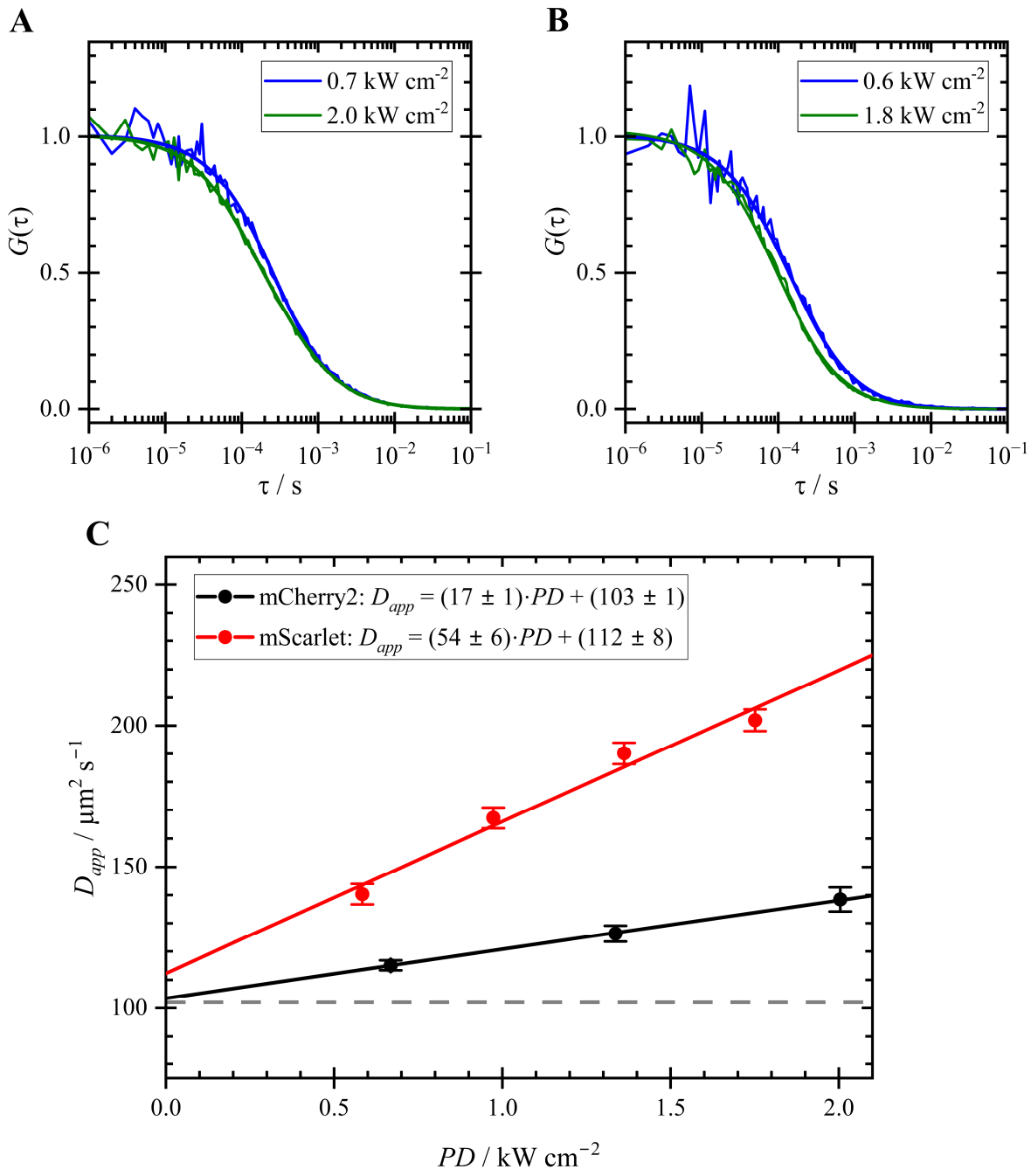

Figure 6.1. Autocorrelation Functions and Apparent Diffusion Coefficients of mCherry2 and mScarlet. The complete list of fit parameters is provided in Appendix D.1.

A: Autocorrelation functions ($G(\tau)$) of purified mCherry2 excited at power densities of 0.7 kW cm^{-2} (blue) and 2.0 kW cm^{-2} (green). The autocorrelation functions were normalized using fit values at τ = 1 µs. The fit curves were obtained by fitting with Equation (6.1), yielding R^2 of 0.997 for both autocorrelation functions.

(Continued on next page)

(Continued from previous page)

B: Autocorrelation functions of purified mScarlet excited at power densities of 0.6 kW cm^{-2} (blue) and 1.8 kW cm^{-2} (green). The autocorrelation functions were normalized and fitted using the same method as described for Panel A, resulting in R^2 values of 0.993 for 0.6 kW cm^{-2} and 0.997 for 1.8 kW cm^{-2}.

C: Apparent diffusion coefficient (D_{app}) as a function of power density (PD) of mCherry2 (black) and mScarlet (red). Data for mScarlet were collected from multiple short measurements, totalling 12 min for each power density. For mCherry2, data were obtained from three independent measurements, with total durations of 84 min, 51 min, and 42 min at power densities of 0.7 kW cm^{-2}, 1.3 kW cm^{-2}, and 2.0 kW cm^{-2}, respectively. Each data point represents the mean, and error bars indicate the *SD*. The fit equations are shown in the graph legends, with the slope and intercept expressed as mean ± *SD*. … The R^2 values for the fits were 0.999 (mCherry2) and 0.974 (mScarlet). The dashed gray line represents the diffusion coefficient of a GFP-like fluorescent protein, 102 µm^2 s^{-1}.

Achieving an accurate analysis of diffusion coefficients necessitates discerning the diffusion process from the flickering process. The first approach involves fitting the autocorrelation curves using the pure diffusion model, followed by extrapolating the result to zero power (the y-intercept of the D_{app} against PD graph) under the assumption of a linear relationship between D_{app} and PD. Application of this method yielded apparent diffusion coefficients at zero power of 103 ± 1 µm^2 s^{-1} (mean ± *SD*) for mCherry2 and 112 ± 8 µm^2 s^{-1} (mean ± *SD*) for mScarlet, respectively (Figure 6.1C).

The second approach involves fitting the autocorrelation functions using a *diffusion-flickering* model (derived from Equations (2.27) and (2.30)):

$$G(\tau) = G_F(\tau) \cdot G_D(\tau) = \frac{1}{N}\left(1 + \frac{f_F}{1-f_F} e^{-\tau/\tau_F}\right)\left(1 + \frac{4D\tau}{w_0^2}\right)^{-1}\left(1 + \frac{4D\tau}{S^2 w_0^2}\right)^{-1/2}, \qquad (6.2)$$

which includes two additional fit parameters to account for the flickering process. Through global fitting of the autocorrelation functions obtained at various laser powers with shared diffusion coefficients, the diffusion coefficients for mCherry2 and mScarlet were determined to be 105 ± 2 µm^2 s^{-1} and 128 ± 9 µm^2 s^{-1} (mean ± *SD*), respectively. The fitted autocorrelation functions and corresponding fit parameters are presented in Appendix D.2.1.

For mCherry2, both approaches were effective in determining diffusion coefficients, yielding values close to the actual diffusion coefficient of 102 µm^2 s^{-1}. In contrast, both methods were insufficient in accounting for flickering in mScarlet, resulting in an overestimation of the diffusion coefficient. To investigate the underlying cause, a comparative analysis of the flickering behavior of mCherry2 and mScarlet is required.

To that end, autocorrelation functions obtained at different excitation power densities were fitted with the diffusion-flickering model, with the fixed diffusion coefficient set to 102 $\mu m^2\ s^{-1}$. Figure 6.2A–B presents the fit curves and contributions of diffusion and flickering of the autocorrelation functions of both mCherry2 and mScarlet obtained at the same excitation power density of 1.95 kW cm^{-2}. Flickering contributes approximately 20% to the correlation amplitude at lag time 1 µs for mCherry2 at and more than 50% for mScarlet, indicating a larger impact on the apparent diffusion coefficient.

The photophysical fraction of mCherry2 and mScarlet increases (Figure 6.2C) and the characteristic time of the photophysical process decreases (Figure 6.2D) with laser power density, indicating that the flickering is light-driven. Based on these findings, the failure to acquire the accurate diffusion coefficient of mScarlet via the first approach (fitting with the pure diffusion model) could be explained by the strong nonlinear behavior of flickering parameters in relation to power density. Furthermore, the failure of the second approach for mScarlet could be attributed to the photophysical characteristic time being too close to the diffusional correlation time. This overlap makes the two components highly dependent, rendering it impossible to decouple them. To effectively separate two diffusing species, the diffusional characteristic time of one species must be at least 1.6 times greater than the other[168]. This ratio should be similar for distinguishing between diffusion and flickering as the functions describing diffusion and flickering exhibit high similarities (see blue and green lines in Figure 6.2A-B). Equation (2.26) estimates the diffusional correlation time of fluorescent proteins at ~280 µs (with known w_0 = 340 nm). This is ~1.0–1.6 times the photophysical characteristic time of mScarlet, compared to ~1.7–4.3 for mCherry2.

Therefore, mCherry2 is more suitable for sizing via FCS, prompting measurements to be conducted on the mCherry2-tagged variant to determine the hydrodynamic radii of non-EV WNT3a, WNT5a, and WNT11. Nonetheless, Figure 6.2B indicates that the flickering contribution of mScarlet decreases to less than 0.01 of the correlation amplitude at $\tau \sim 0.5$ ms. As the diffusional correlation time of EVs is expected to be greater than 1 ms, the hydrodynamic radii of small and large EVs were determined using the mScarlet variant, given its higher brightness compared to mCherry2.

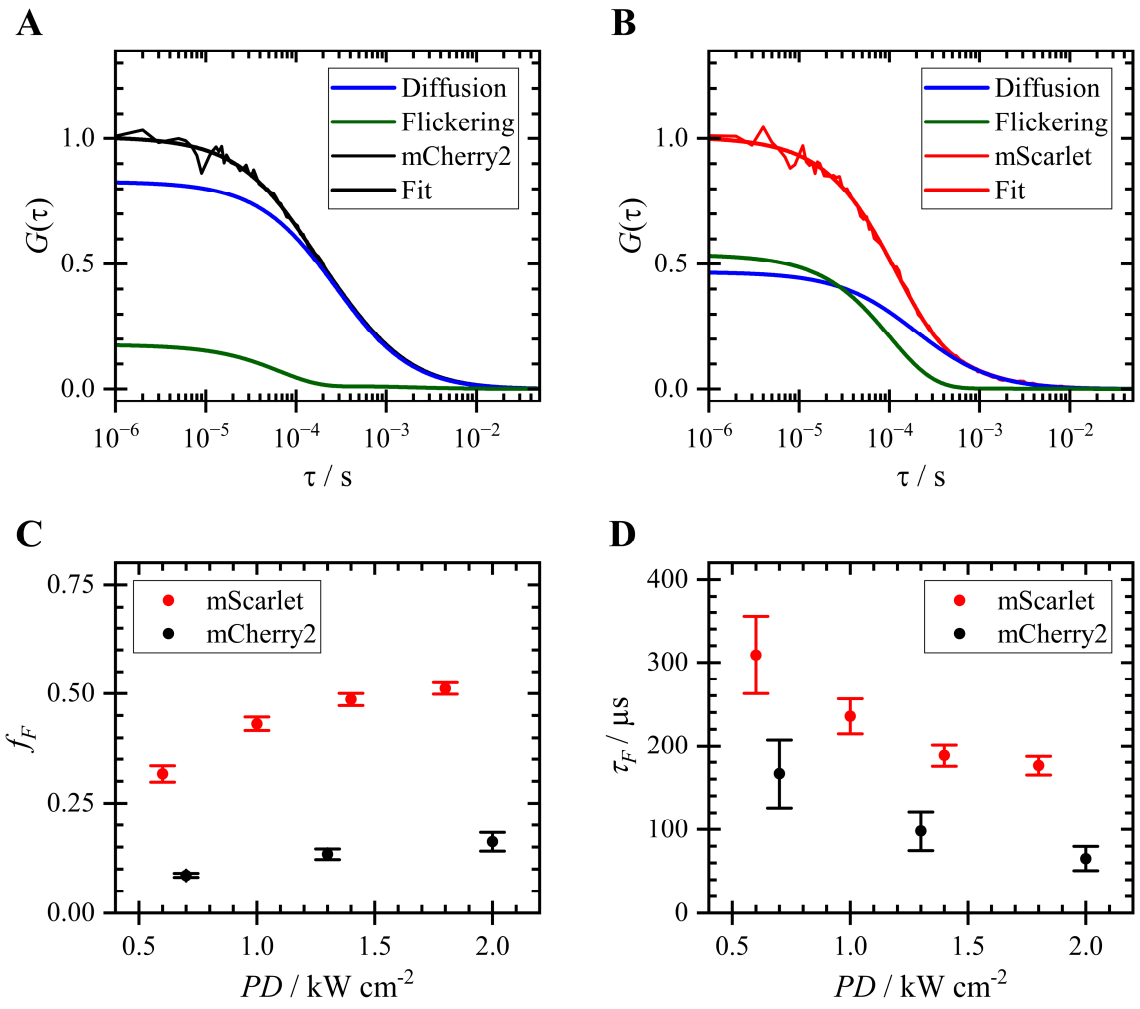

Figure 6.2. Comparison of Flickering Effects in mCherry2 (Black) and mScarlet (Red). The full list of fit parameters is provided in Appendix D.2.2.

A: Normalized autocorrelation function ($G(\tau)$) of mCherry2 measured with 2.0 kW cm^{-2} excitation (identical to the data shown in Figure 6.1A). The autocorrelation function was fitted using the *diffusion-flickering* model (Equation (6.2)). The blue and green lines show the diffusion and flickering contributions to the total autocorrelation functions, respectively.

B: Normalized autocorrelation function of mScarlet measured with 1.8 kW cm^{-2} excitation (identical to the data shown in Figure 6.1B). The autocorrelation function was analyzed in the same manner as in Panel A.

C: Photophysical fraction (f_F) as a function of power density (PD) observed in mCherry2 (black) and mScarlet (red). Data points: mean; error bars: *SD*.

D: Photophysical characteristic time (τ_F) as a function of power density observed in mCherry2 (black) and mScarlet (red). Data points: mean; error bars: *SD*.

6.2 Hydrodynamic Radii of Non-EV-Bound mCherry2-WNT Units Determined via Translational Diffusion Coefficients

The hydrodynamic radii of non-EV-bound mCherry2-WNT3a, mCherry2-WNT5a, and mCherry2-WNT11 units were determined via FCS measurements with a 560-nm excitation at laser power densities of 0.65 kW cm^{-2}, 1.30 kW cm^{-2}, and 1.95 kW cm^{-2}. To account for potential viscosity variations of conditioned medium from water, purified mCherry2 diluted in the control non-EV fraction of conditioned medium from cells transfected with pcDNA served as a conversion standard.

Initial analysis of the autocorrelation functions for a representative sample of each type (Figure 6.3) shows that all non-EV-bound mCherry2-WNT units exhibit slower diffusion compared to purified mCherry2. Among the WNT complexes, the autocorrelation function curves progressively shift from left to right, reflecting an increase in size from mCherry2-WNT11 to mCherry2-WNT5a, and finally to mCherry2-WNT3a.

To quantify the diffusion coefficients, the autocorrelation functions for all samples were analyzed using both approaches outlined in Section 6.1 to account for flickering of mCherry2. Nevertheless, it was found that the pure diffusion model (Equation (6.1)) failed to adequately fit the autocorrelation functions of mCherry2-WNT complexes. Consequently, only the diffusion-flickering model (Equation (6.2)) were applied. Variations in autocorrelation functions observed at different laser power densities were attributed exclusively to light-induced flickering. Therefore, a global fitting approach was implemented, simultaneously fitting for a shared diffusion coefficient value for each sample type.

The reference mCherry2 yielded a diffusion coefficient of 111 ± 3 $\mu m^2\ s^{-1}$ (mean ±; *SEM* = 2), slightly deviating from the diffusion coefficient of GFP-like fluorescent proteins in buffer (102 $\mu m^2\ s^{-1}$; see Section 6.1). Non-EV-bound mCherry2-WNT3a and mCherry2-WNT5a units exhibited nearly identical average diffusion coefficients of 38 ± 8 $\mu m^2\ s^{-1}$ (mean ± *SD*; *SEM* = 3) and 39 ± 11 $\mu m^2\ s^{-1}$ (mean ± *SD*; *SEM* = 6), respectively. Non-EV-bound mCherry2-WNT11 units exhibited faster diffusion, with a diffusion coefficient of 60 ± 1 $\mu m^2\ s^{-1}$ (mean ± *SD*; *SEM* = 0.5). The complete list of fit parameters is provided in Appendix D.3.

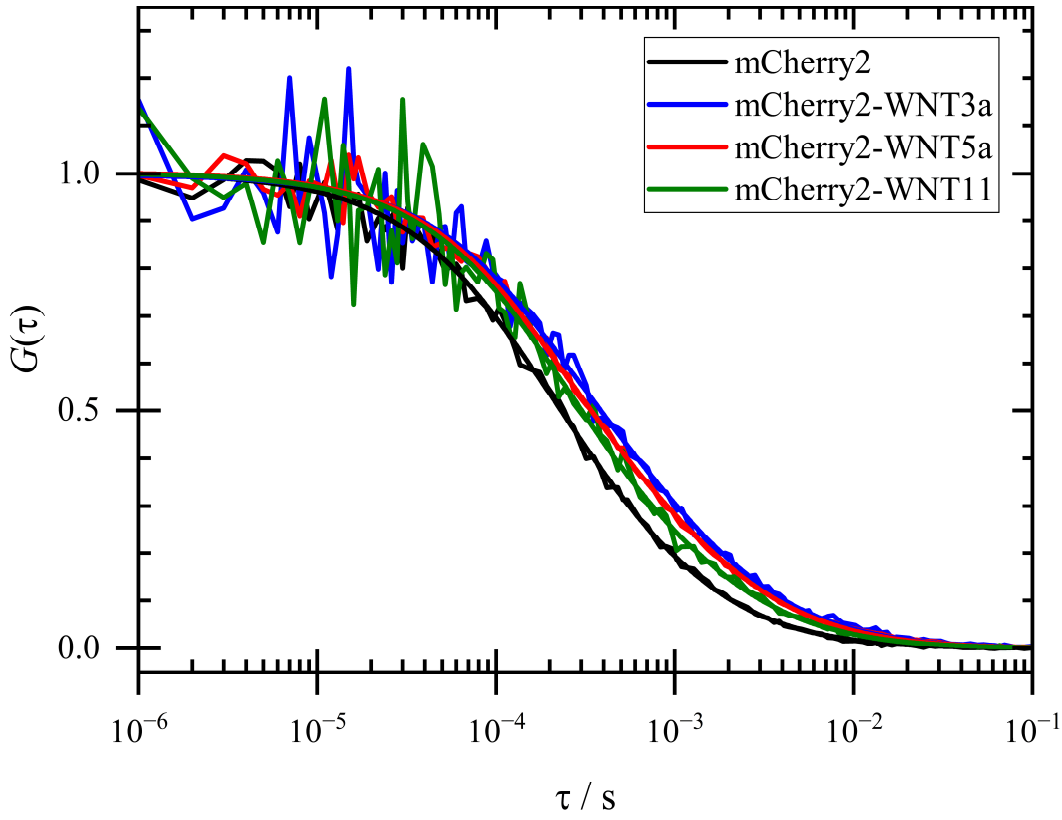

Figure 6.3. Autocorrelation Functions ($G(\tau)$) of Purified mCherry2 (Black) and Non-EV mCherry2-WNT3a (Blue), mCherry2-WNT5a (Red), and mCherry2-WNT11 (Green). The autocorrelation function displayed for each sample type corresponds to one sample, measured with an excitation of 0.65 kW cm^{-2}. The curve is normalized to the fit value at 1 µs, which was obtained using Equation (6.2). The list of fit parameters is provided in Appendix D.3.

Utilizing the known diffusion coefficient of GFP-like fluorescent proteins[115,163,167], the hydrodynamic radius of mCherry2 was calculated through Equation (2.28) to be 2.6 ± 0.1 nm. Following that, based on the ratio between the diffusion coefficients of mCherry2 and mCherry2-WNT entities, the hydrodynamic radii of non-EV-bound mCherry2-WNT3a, mCherry2-WNT5a, and mCherry2-WNT11 units were determined to be 7.7 ± 1.7 nm, 7.3 ± 2.1 nm, and 4.9 ± 0.2 nm (mean ± *SD*), respectively.

6.3 Rotational Brownian Motion of Non-EV-Bound mCherry2-WNT Units

This study aimed to achieve a higher precision in determining the hydrodynamic radii of non-EV-bound mCherry2-WNT3a/5a/11 units. This could be accomplished by measuring the rotational diffusion coefficients, which are proportional to r_h^{-3} (Equation (2.35)), in contrast to translational diffusion coefficients, which are proportional to r_h^{-1} (Equation (2.28)).

In the investigation of rotational diffusion of non-EV mCherry2-WNT3a/5a/11 particles, linearly polarized excitation and detection were employed. As discussed in Section 2.2.2, this technique faces challenges in acquiring adequate data at the tens of ns timescale to overcome shot noise effects. Hence, achieving a delicate balance between maximizing signal-to-noise ratio through high power and preserving the ability to discern rotational diffusion from flickering demands careful optimization of the excitation power (Figure 6.4).

To optimize the excitation power, FCS measurements were conducted on a non-EV-bound mCherry2-WNT3a sample at various excitation power densities: 0.76 kW cm^{-2} for 40 min, 2.5 kW cm^{-2} for 20 min, 7.6 kW cm^{-2} for 20 min, 25 kW cm^{-2} for 10 min, 76 kW cm^{-2} for 10 min, and 250 kW cm^{-2} for 5 min. The average autocorrelation functions are depicted in Figure 6.4, alongside the lines of best fit generated from the diffusion-flickering model (Equation (6.2)).

At low excitation power (Figure 6.4A–B), the observation of rotational diffusion is not possible due to significant uncertainty. In contrast, at moderately high excitation power levels (Figure 6.4C–D), the autocorrelation functions exhibit a plateau around 1 µs before transitioning into the rotational diffusion region as lag time decreases. Conversely, excessive excitation power obscures the separation between rotational diffusion and flickering processes (Figure 6.4E–F). Consequently, further FCS measurements were performed with an excitation power density of 25 kW cm^{-2}.

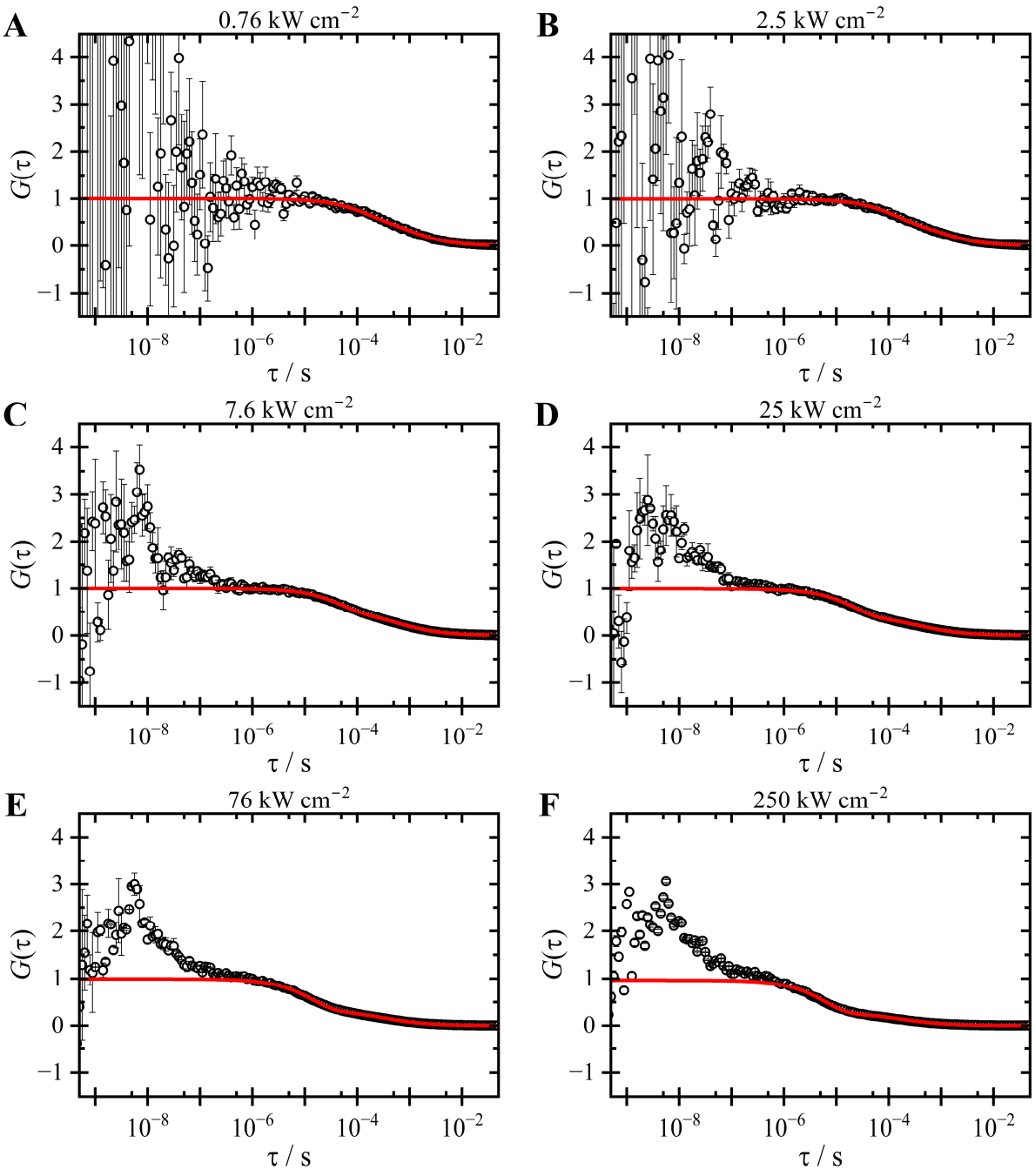

Figure 6.4. Determination of Optimal Laser Power for Observing Rotational Diffusion. Autocorrelation functions ($G(\tau)$) of non-EV-bound mCherry2-WNT3a units, fitted with the diffusion-flickering model (Equation (6.2)) displayed in red lines. The autocorrelation functions were normalized to the fit value at τ = 1 µs. Each data point represents a correlation value, with error bar indicating the *SEM*. The excitation power density used in each measurement is denoted above each graph. Refer to Appendix D.4 for emission intensity versus power density graph.

The average autocorrelation functions were obtained for purified mCherry2, mCherry2-WNT3a, mCherry2-WNT5a, and mCherry2-WNT11, as displayed in Figure 6.5. These autocorrelation functions were analyzed using a comprehensive fitting model that accounts for fluctuations arising from particles undergoing translational diffusion, photophysical processes, and two rotational diffusion components. The model equation, based on Equation (2.38), is given as

$$G(\tau) = G_A(\tau) \cdot G_{R1}(\tau) \cdot G_{R2}(\tau) \cdot G_F(\tau) \cdot G_D(\tau)$$

$$G(\tau) = \frac{1}{N}\left(1 - \frac{1}{n}e^{-\tau/\tau_A}\right)\left(1 + f_{R1}e^{-\tau/\tau_{R1}}\right)\left(1 + f_{R2}e^{-\tau/\tau_{R2}}\right)\left(1 + \frac{f_F}{1-f_F}e^{-\tau/\tau_F}\right) \times \left(1 + \frac{4D\tau}{w_0^2}\right)^{-1}\left(1 + \frac{4D\tau}{S^2 w_0^2}\right)^{-1/2}. \quad (6.3)$$

For subsequent fitting, the factor $1/n$ in the antibunching contribution is defined as f_A. Introducing C as the ratio of the amplitudes f_{R1} to f_{R2}, i.e., $C = f_{R1}/f_{R2}$, Equation (6.6) can be rearranged as

$$G(\tau) = \frac{1}{N}\left(1 - f_A e^{-\tau/\tau_A}\right)\left(1 + f_R\left(\frac{C}{C+1}\right)e^{-\tau/\tau_{R1}}\right)\left(1 + f_R\left(\frac{1}{C+1}\right)e^{-\tau/\tau_{R2}}\right) \times \left(1 + \frac{f_F}{1-f_F}e^{-\tau/\tau_F}\right)\left(1 + \frac{4D\tau}{w_0^2}\right)^{-1}\left(1 + \frac{4D\tau}{S^2 w_0^2}\right)^{-1/2}. \quad (6.4)$$

The rotational amplitudes of the rotational diffusion components, f_{R1} and f_{R2}, can be calculated using the following relationships:

$$f_{R1} = f_R\left(\frac{C}{C+1}\right), \quad f_{R2} = f_R\left(\frac{1}{C+1}\right). \quad (6.5)$$

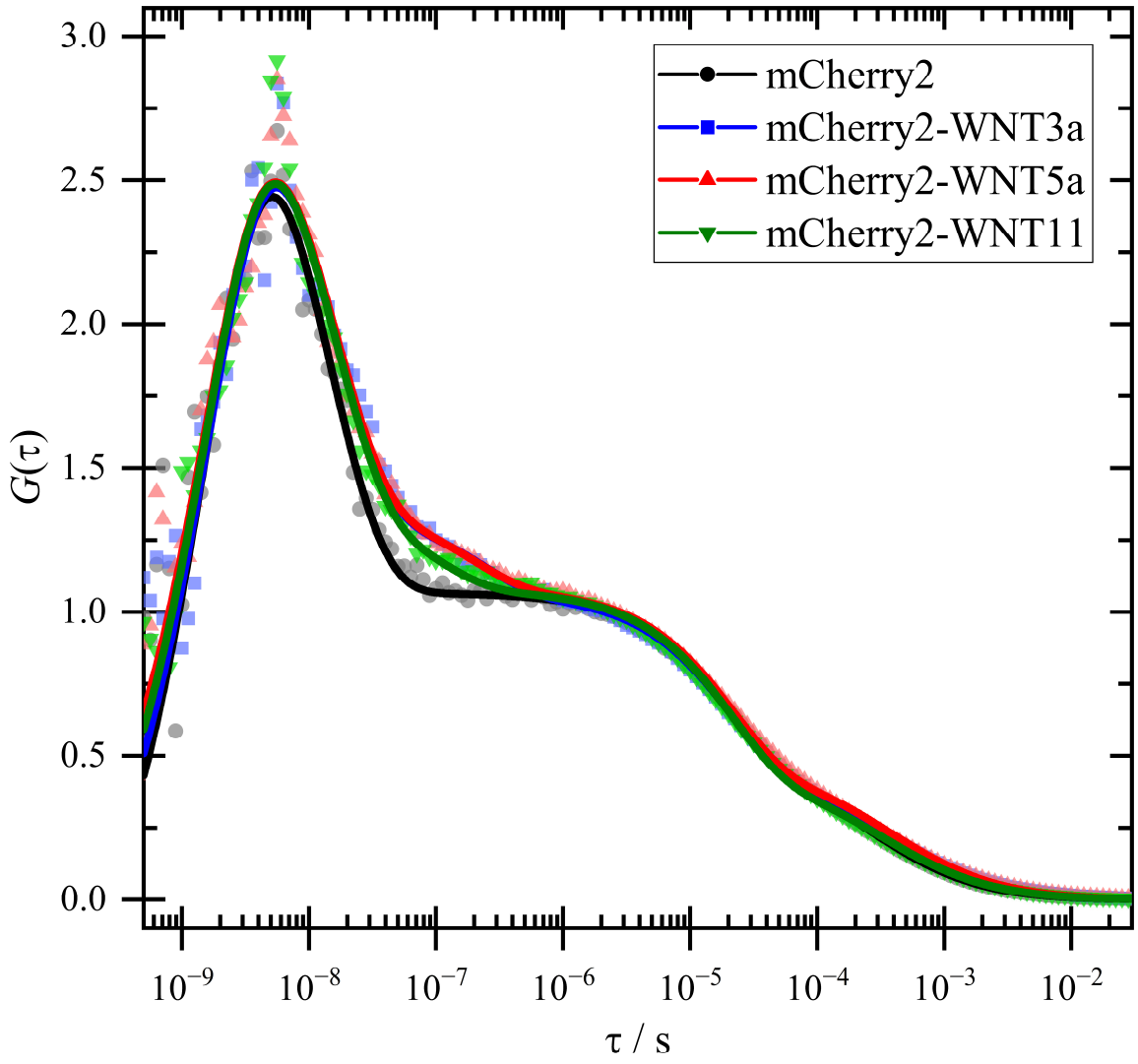

Figure 6.5. Autocorrelation Functions ($G(\tau)$) of Non-EV-Bound mCherry2-WNT3a/5a/11 Units, Compared to Purified mCherry2, Obtained via Polarization-Dependent FCS. The autocorrelation function values are represented by the following symbols: black circle for purified mCherry2, blue square for mCherry2-WNT3a, red triangle for mCherry2-WNT5a, and green inverted triangle for mCherry2-WNT11. The fit lines, depicted in the corresponding colors, were generated by fitting with Equation (6.4) , starting from 1 ns. A list of the fit parameters can be found in Appendix D.4.

The inclusion of two rotational diffusion processes in the model accounts for the presence of a flexible linker, a polypeptide of 12 amino acids (~4 nm), connecting mCherry2 to WNT proteins within all mCherry2-WNT fusions. While the entire particle is rotating, the mCherry2 molecule may also undergo independent rotation, to some degree, around the flexible linker. As shown in Figure 6.6, using a single decay term for rotational diffusion in mCherry2-WNT particles produced significantly inferior results compared to two decay terms.

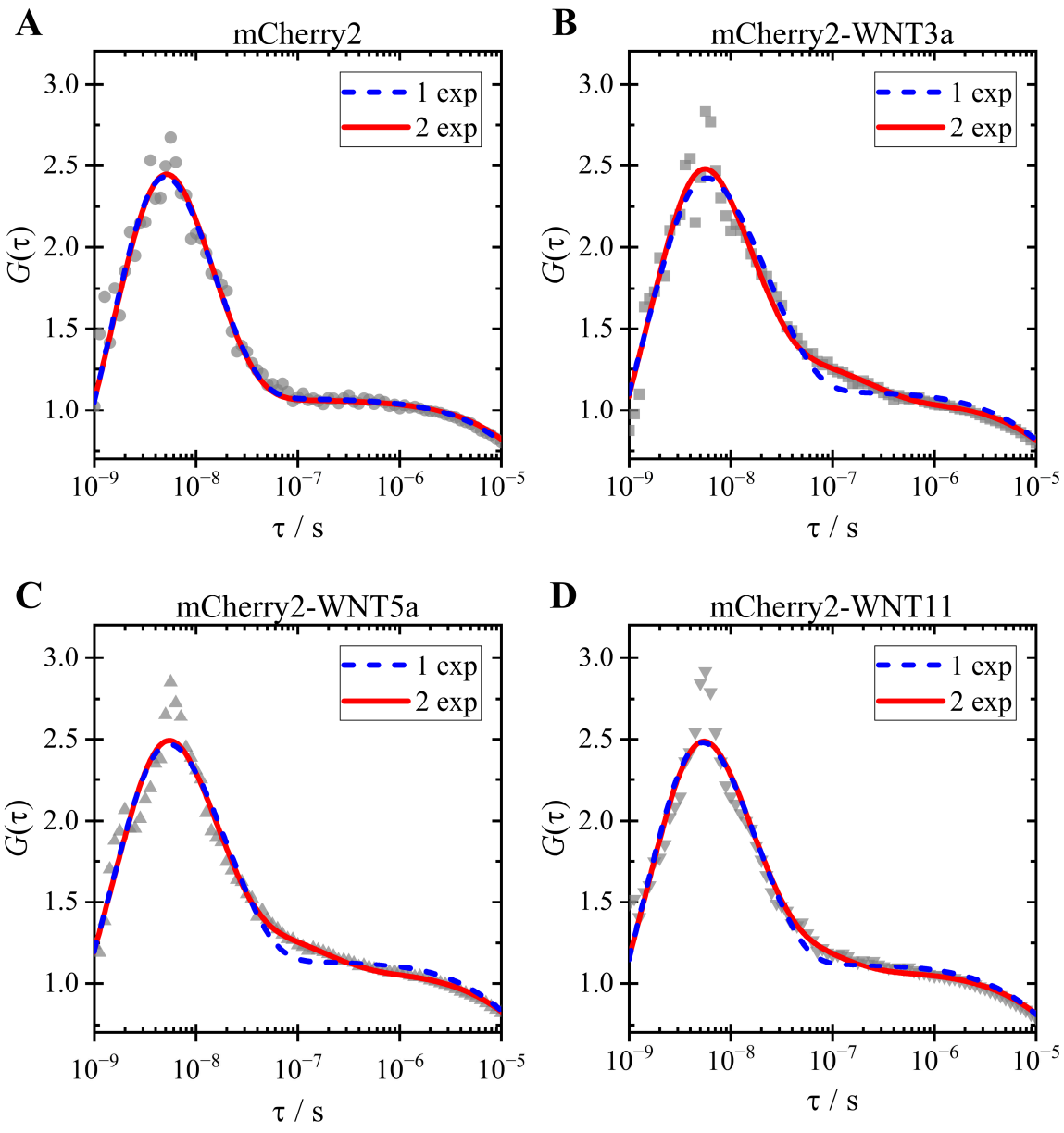

Figure 6.6. Zoomed-in Autocorrelation Function Curves ($G(\tau)$) from Figure 6.5 Ranging from 1 ns to 10 µs to Emphasize the Contributions of Rotational Diffusion of mCherry2 (A), mCherry2-WNT3a (B), mCherry2-WNT5a (C), and mCherry2-WNT11 (D). The blue, dashed lines and solid, red lines represent fits including one and two exponential decay terms for rotational diffusion, respectively. The full list of fit parameters is provided in Appendix D.4.

On the other hand, the autocorrelation function of purified mCherry2 was accurately fitted with a single exponential term representing rotational diffusion, resulting in a rotational correlation time of τ_{R1} = 15 ± 1 ns, consistent with previously reported values for monomeric GFP-like fluorescent proteins [86,163,169]. Furthermore, fitting the autocorrelation function of

purified mCherry2 with Equation (6.4) yielded a result where the second rotational correlation time was found to be equivalent to the first term (Table 6.1).

Table 6.1. Parameters Describing Rotational Diffusion and Antibunching of mCherry2 and Non-EV-Bound mCherry2-WNT3a/5a/11 Units. The table presents values as mean ± *SD*. Additional fit parameters are provided in Appendix D.4.

Sample	τ_{R2} / ns	$C = f_{R1}/f_{R2}$	τ_A / ns	$n = 1/f_A$
mCherry2	18 ± 6	4.9 ± 1.0†	1.9 ± 0.1†	0.89 ± 0.03
mCherry2-WNT3a	225 ± 86			0.92 ± 0.03
mCherry2-WNT5a	190 ± 72			0.97 ± 0.03
mCherry2-WNT11	99 ± 35			0.95 ± 0.03

† Global parameters (shared across the simultaneous fit for all sample types)

The lines of best fit in Figure 6.5 were generated by simultaneously fitting all correlation curves with Equation (6.4). Assuming uniform photophysical properties for mCherry2 across all samples, global fits were conducted using a shared photophysical characteristic time and an antibunching characteristic time. The first rotational correlation time, τ_{R1}, which characterizes the rotational Brownian motion of mCherry2, was set to the previously determined value of 15 ns. Additionally, as all WNT proteins are linked to the mCherry2 molecule by the same linker, the ratio of the amplitudes f_{R1} and f_{R2} was also set as a global parameter. However, the antibunching amplitude was not fixed to reach zero correlation because some samples contained high (~5 nM) concentrations of mCherry2-WNT, which could result in simultaneous excitation of multiple fluorescent proteins.

The analysis returned an antibunching characteristic time of 1.9 ± 0.1 ns (mean ± *SD*), which agrees with the measured fluorescence lifetime of mCherry2 (1.6 ± 0.1 ns (mean ± *SEM*); see Appendix D.5). The estimated number of chromophores per particle is close to one, aligning with results obtained from N&B analysis (Table 6.1). However, the high concentration of fluorescent particles and significant noise in the autocorrelation functions for $\tau < 1$ ns hindered precise quantitative conclusions from being drawn from the antibunching analysis.

The translational diffusion coefficients differed from those determined in Section 6.2 due to heightened flickering and photobleaching induced by the high excitation intensity. The larger rotational correlation times were determined as τ_{R2} = 18 ± 6 ns, 225 ± 86 ns, 190 ± 72 ns, and 99 ± 35 ns (mean ± *SD*) for mCherry2, mCherry2-WNT3a, mCherry2-WNT5a, and

mCherry2-WNT11, respectively. The smaller and larger rotational correlation times of mCherry2 are indistinguishable within experimental uncertainty, indicating that the fluorescent particles in the samples are homogeneous in size. Additionally, the analysis yielded an f_{R1}/f_{R2} ratio of 4.9 ± 1.0 (mean ± *SD*), indicating that the independent rotation of the mCherry2 molecule dominates the rotational motion of mCherry2-WNT particles. As a result, precise rotational diffusion coefficients of non-EV-bound mCherry2-WNT units could not be determined. Nevertheless, the trend in rotational correlation times indicates a size ranking from largest to smallest as mCherry2-WNT3a, mCherry2-WNT5a, and mCherry2-WNT11, supporting the findings from translational diffusion in Section 6.2.

6.4 Hydrodynamic Radii of Small and Large EVs

The hydrodynamic radii of small and large EVs carrying mScarlet-WNT3a/5a proteins were determined using FCS. Fluorescence intensity-time traces were acquired for each measurement; however, these traces posted a challenge due to the presence of numerous high-intensity bursts, as examplified in Panel A of Figure 6.7–Figure 6.10. Since autocorrelation function values are proportional to the square of the intensity, larger intensity bursts can dominate and distort the shape of the average autocorrelation function curve.

To address this issue, the hydrodynamic radii of EVs were analyzed using a segment-by-segment approach. Instead of fitting the average autocorrelation function from the entire measurement at once, small portions of the intensity-time trace were analyzed individually, as demonstrated in previous literature [170-173]. In this study, intensity-time traces were divided into 30-s segments, and the autocorrelation function for each segment was calculated and fitted separately. Examples of individual autocorrelation functions are shown in Panels B–F of Figure 6.7–Figure 6.10.

As shown in Section 6.1, the flickering contribution of mScarlet decreases to less than 1% of the total autocorrelation function amplitude at $\tau \sim 0.5$ ms. Therefore, every autocorrelation function was initially fitted with a pure diffusion model comprising one component (Equation (2.23)):

$$G(\tau) = \frac{1}{N}\left(1 + \frac{\tau}{\tau_D}\right)^{-1}\left(1 + \frac{\tau}{S^2\tau_D}\right)^{-1/2} \tag{6.6}$$

starting from 0.76 ms. To ensure reliable results, criteria were established for determining the acceptance of a fit. Given the large volume of data analyzed in this study, the focus was on reproducibility and automation, avoiding manual data selection. Although the reduced χ^2 function ($\chi^2_\mu \sim 1$) is commonly used to assess the goodness of nonlinear fits, Wohland et al[67] (Section 8.5.1, Page 8-17) reported that, in practice, well-fitted parameters often yield $\chi^2_\mu < 1$. As a result, experimenters either aim to minimize χ^2_μ, regardless of its value being less than 1, or adopt alternative criteria. In this work, we found that rejecting fits with $R^2 < 0.9$ was effective in excluding the majority of fits with extremely poor residuals, providing a robust criterion for fit selection. While this threshold may not eliminate all suboptimal fits, it ensures a reproducibility in the analysis.

The autocorrelation functions with $R^2 < 0.9$ were subsequently fitted using a pure diffusion model comprising two components[172]:

$$G(\tau) = \frac{1}{N}\left[f\left(1 + \frac{\tau}{\tau_{D1}}\right)^{-1}\left(1 + \frac{\tau}{S^2\tau_{D1}}\right)^{-1/2} + (1-f)\left(1 + \frac{\tau}{\tau_{D2}}\right)^{-1}\left(1 + \frac{\tau}{S^2\tau_{D2}}\right)^{-1/2}\right], \tag{6.7}$$

where N is the average number of particles in the observation volume. f is the weight factor of species 1, and τ_{D1} and τ_{D2} are the diffusional correlation times of species 1 and 2, respectively. Then weighed-average diffusional correlation time was then calculated using:

$$\tau_D = f\tau_{D1} + (1-f)\tau_{D2}\,. \tag{6.8}$$

If the R^2 is still less than 0.9 after this fitting process, the autocorrelation function was discarded.

To present typical autocorrelation functions and corresponding fits without bias, the first 150 s of measurements from the sample with an average diffusional correlation time in the middle of each sample type are shown in Figure 6.7–Figure 6.10. The number of autocorrelation functions fitted with one- and two-component models, as well as those that were discarded, is reported in Appendix D.6.

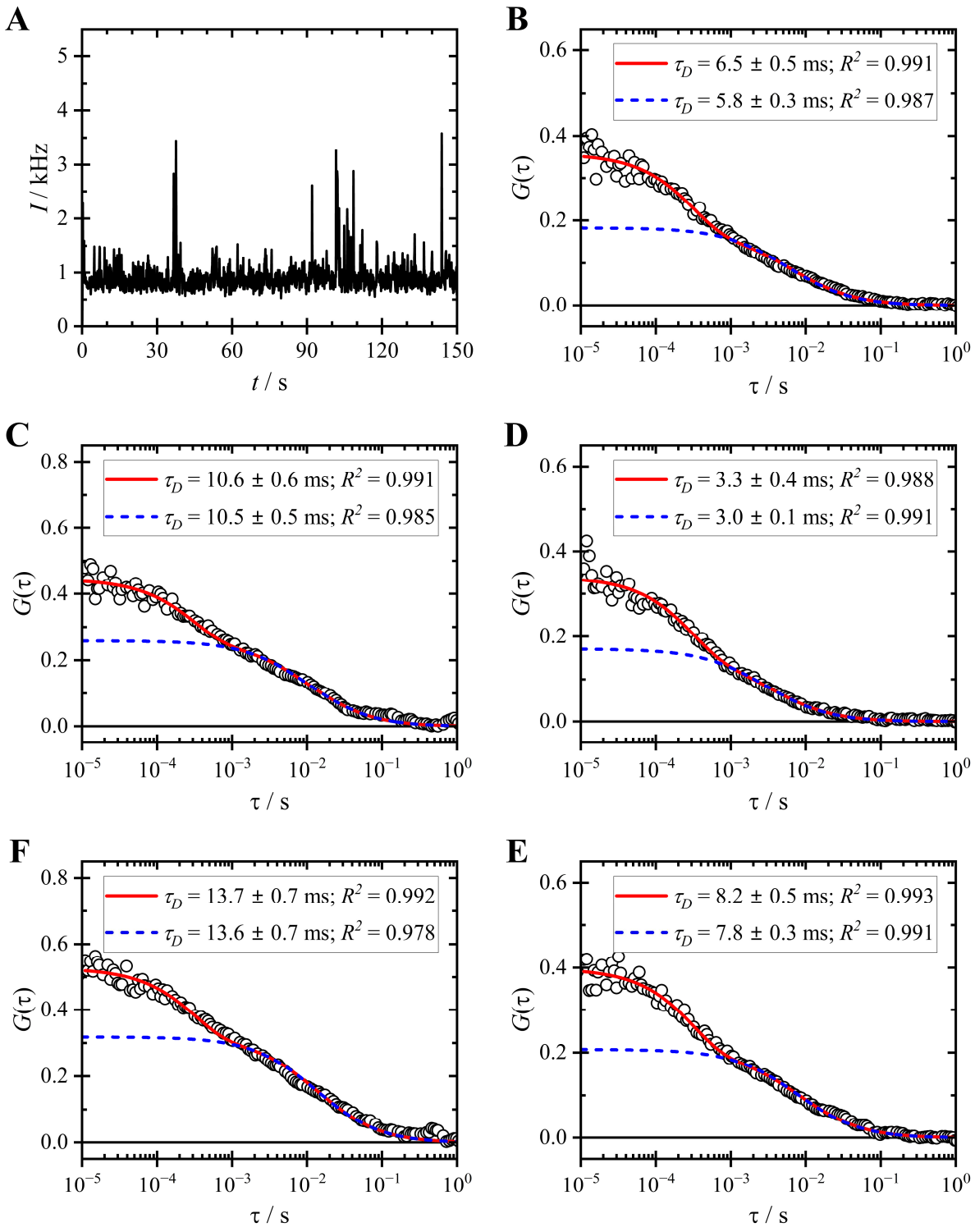

Figure 6.7. Examples of Intensity-Time Trace and Autocorrelation Functions from Small EVs Carrying mScarlet-WNT3a

A: Intensity-time (I-t) trace for the first 150 s of the measurement, generated with a bin time of 100 ms.

B–F: Autocorrelation functions ($G(\tau)$) calculated from 30-s segments of the intensity-time trace: 0–30 s (B), 30–60 s (C), 60–90 s (D), 90–120 s (E), and 120–150 (F). The blue dashed line represent the fit with the pure diffusion model (Equation (6.6)), and the red solid lines represent the fit with the diffusion-flickering model (Equation (6.10)) The legends display the diffusional correlation times (mean ± *SD*) and R^2 values obtained from the fits.

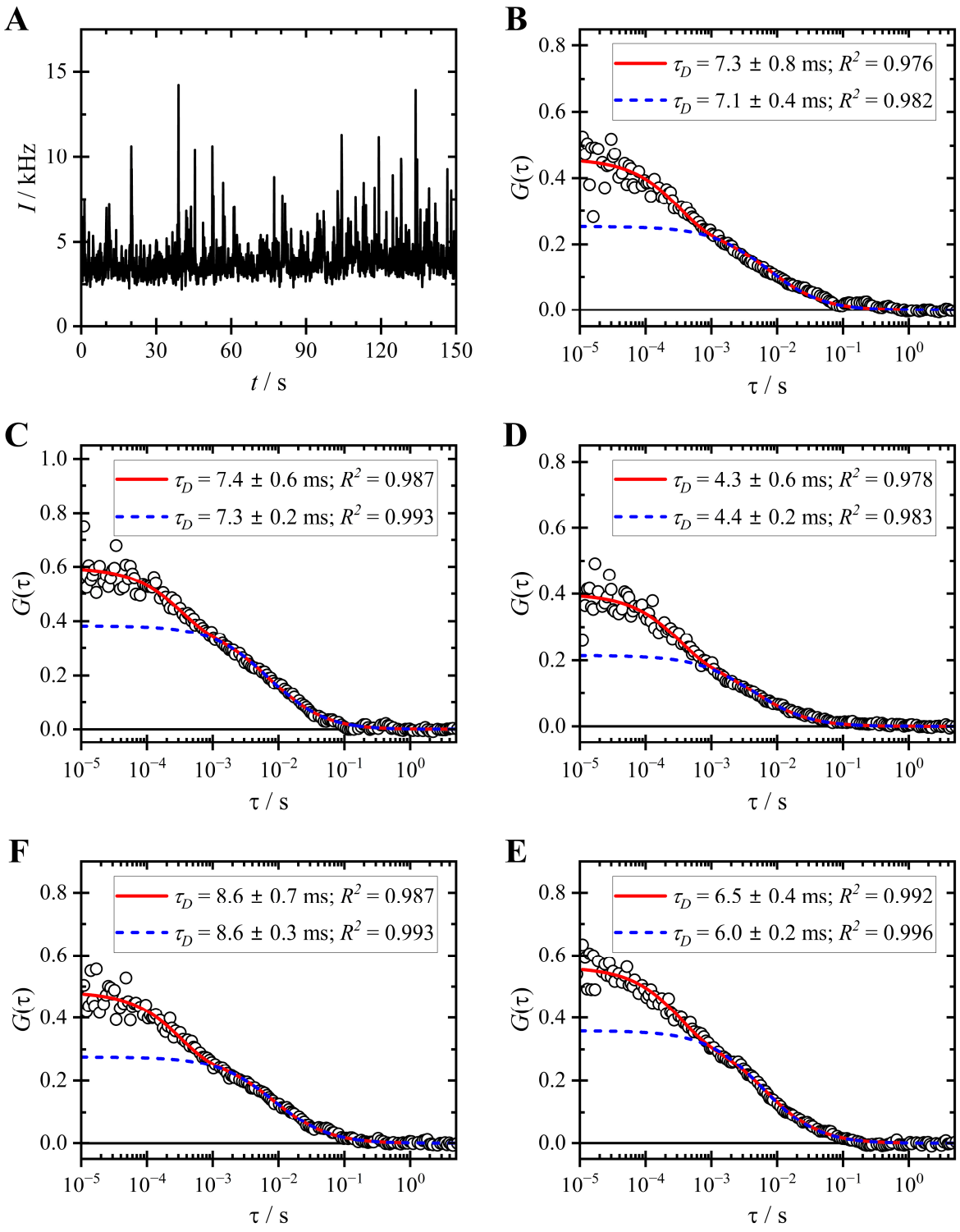

Figure 6.8. Examples of Intensity-Time Trace and Autocorrelation Functions from Small EVs Carrying mScarlet-WNT5a

A: Intensity-time (I-t) trace for the first 150 s of the measurement, generated with a bin time of 100 ms.

B–F: Autocorrelation functions ($G(\tau)$) derived from 30-s segments of the intensity-time trace, displayed and fitted in the same manner described in Figure 6.7.

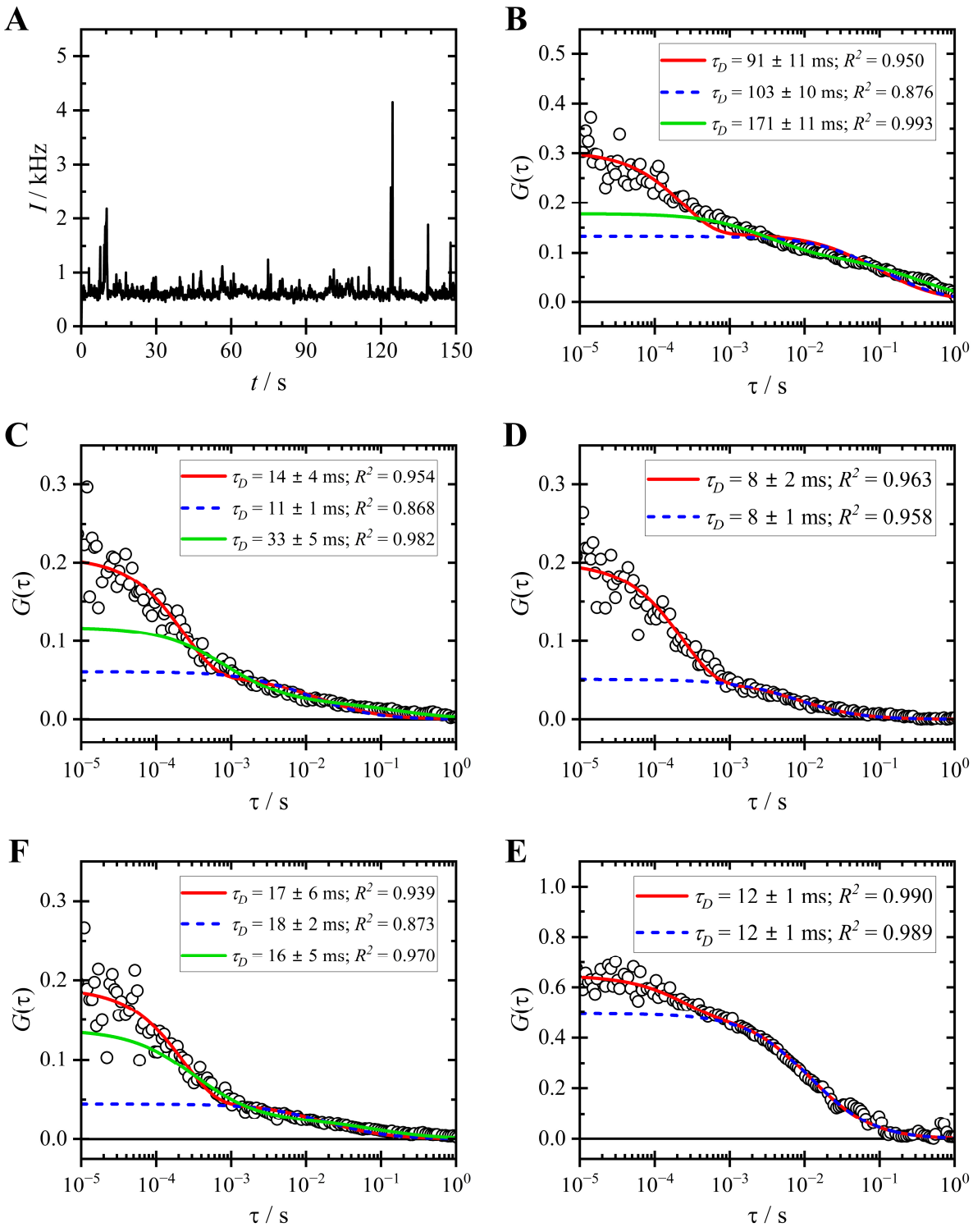

Figure 6.9. Examples of Intensity-Time Trace and Autocorrelation Functions from Large EVs Carrying mScarlet-WNT3a

A: Intensity-time (I-t) trace for the first 150 s of the measurement, generated with a bin time of 100 ms.

B–F: Autocorrelation functions ($G(\tau)$) derived from 30-s segments of the intensity-time trace, displayed and fitted in the same manner described in Figure 6.7. The green lines in (B), (C), and (F) represent the two-component pure diffusion model (Equation (6.7)), used when the one-component pure diffusion model returned $R^2 < 0.9$. The fit parameters for the green lines are: (B) $f = 0.51 \pm 0.01$, $\tau_{D1} = 3.2 \pm 0.4$ ms, $\tau_{D2} = 346 \pm 21$ ms; (C) $f = 0.82 \pm 0.01$, $\tau_{D1} = 0.9 \pm 0.2$ ms, $\tau_{D2} = 176 \pm 28$ ms; … (Continued on next page)

(Continued from previous page) ... (F) f = 0.82 ± 0.05, τ_{D1} = 0.3 ± 0.2 ms, τ_{D2} = 87 ± 13 ms.

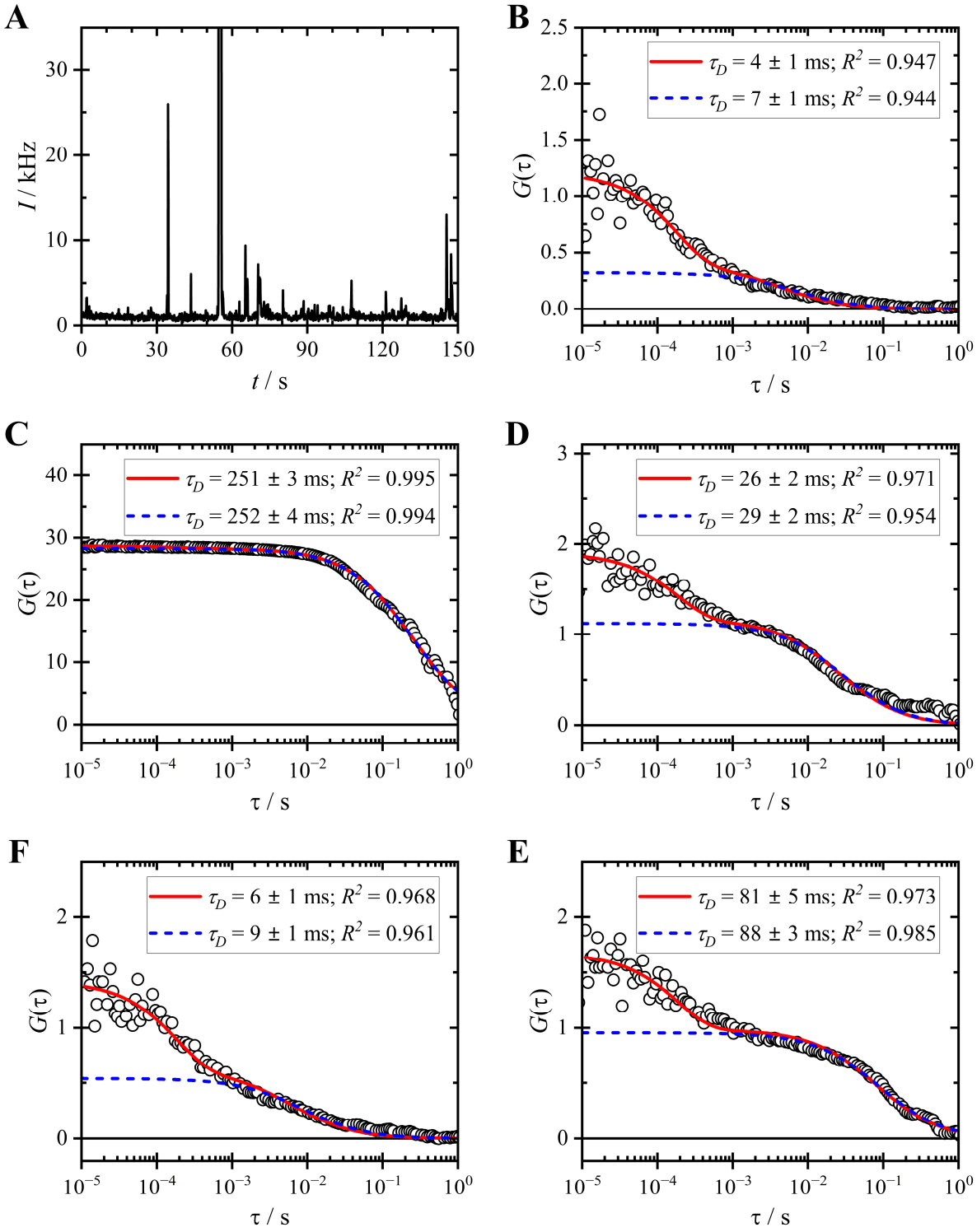

Figure 6.10. Examples of Intensity-Time Trace and Autocorrelation Functions from Large EVs Carrying mScarlet-WNT5a

A: Intensity-time (I-t) trace for the first 150 s of the measurement, generated with a bin time of 100 ms. The burst at 55 s reached an intensity of 452 kHz, exceeding the vertical axis range displayed in the figure.

B–F: Autocorrelation functions ($G(\tau)$) derived from 30-s segments of the intensity-time trace, displayed and fitted in the same manner described in Figure 6.7.

To calculate the hydrodynamic radii of EVs, it is important to note that the relationship between the diffusion coefficient and the diffusional correlation time in Equation (2.26) applies only when particles are significantly smaller than the observation volume (on the order of a few tens of nanometers in radius)[172,174,175]. For large EVs whose sizes are comparable to the observation volume, one must also consider the time it takes for a particle to travel a distance equal to its diameter. Consequently, Equation (2.26) must be modified to:[172]

$$\tau_D = \frac{w_0^2 + r_h^2}{4D}, \tag{6.9}$$

which was then used in combination with the Stokes–Einstein relation (Equation (2.28)).

The resulting hydrodynamic radii are listed in Table 6.2. The large uncertainty in each sample arises from both the board size range of particles and the presence of particle aggregates. The latter is a common issue in the EV preparation, particularly when EVs are isolated by pelleting through centrifugation[29]. This problem leads to the presence of larger particles, as shown by the extended tail of the histogram of hydrodynamic radii in Figure 6.11. To mitigate the influence of aggregates on the reported hydrodynamic radii, the median was used to represent the central value instead of the mean.

Table 6.2. Hydrodynamic Radii of Small and Large EVs Carrying mScarlet-WNT3a/5a, Obtained by Fitting with the Pure Diffusion Model (Equations (6.6)–(6.7)). All values for individual samples are given as the median ± *MAD*. The number of segments and fit parameters are reported in Appendix D.6.1.

Sample	r_h / nm			
	Small EVs mScarlet-WNT3a	**Small EVs mScarlet-WNT5a**	**Large EVs mScarlet-WNT3a**	**Large EVs mScarlet-WNT5a**
1	75 ± 27	63 ± 21	208 ± 91	42 ± 26
2	213 ± 73	96 ± 26	181 ± 124	142 ± 80
3	55 ± 17	63 ± 16	131 ± 74	565 ± 171
4	149 ± 53	86 ± 33	235 ± 154	–
5	34 ± 10	–	–	–
6	37 ± 7	–	–	–
Mean ± *SEM*	**94 ± 29**	**77 ± 8**	**189 ± 22**	**249 ± 160**

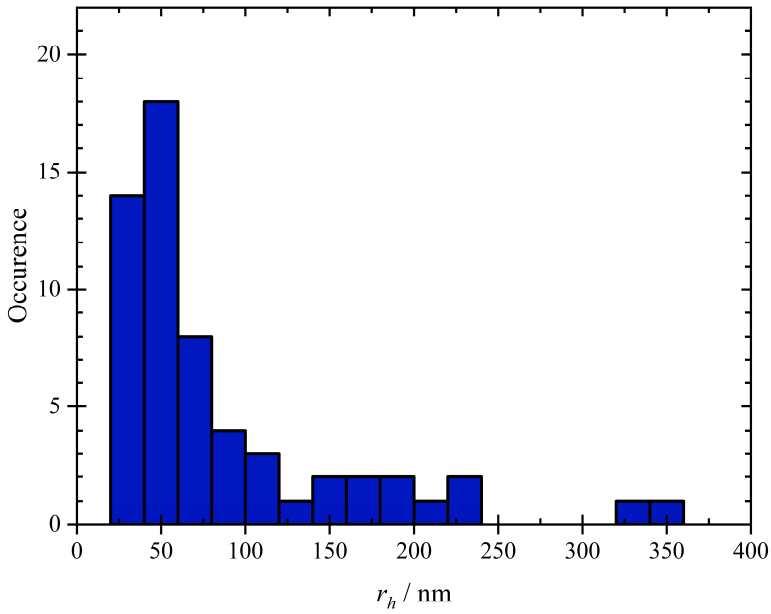

Figure 6.11. Histogram of the Hydrodynamic Radii (r_h) Obtained from Small EVs Carrying mScarlet-WNT3a (Same Sample as Shown in Figure 6.7)

To verify the adequacy of the pure-diffusion model, the same autocorrelation functions were also fitted (starting at 0.01 s) using diffusion-flickering models with one component (Equation (6.10)) and two components (Equation (6.11)):[157]

$$G(\tau) = \frac{1}{N}\left(1 + \frac{f_F}{1-f_F} e^{-\tau/\tau_F}\right)\left(1 + \frac{\tau}{\tau_{D1}}\right)^{-1}\left(1 + \frac{\tau}{S^2\tau_{D1}}\right)^{-1/2}. \tag{6.10}$$

and

$$G(\tau) = \frac{1}{N}\left(1 + \frac{f_F}{1-f_F} e^{-\tau/\tau_F}\right)\left[f\left(1 + \frac{\tau}{\tau_{D1}}\right)^{-1}\left(1 + \frac{\tau}{S^2\tau_{D1}}\right)^{-1/2} + (1-f)\left(1 + \frac{\tau}{\tau_{D2}}\right)^{-1}\left(1 + \frac{\tau}{S^2\tau_{D2}}\right)^{-1/2}\right]. \tag{6.11}$$

For each sample, the photophysical characteristic time was fixed to the value determined for mScarlet at the same power density (Section 6.1). In contrast to the pure-diffusion model, fitting with the two-component diffusion-flickering model proved difficult to converge and highly sensitive to initial fit parameters, owing to the model's increased complexity and additional parameters. Moreover, the two-component diffusion-flickering model did not significantly improve the R^2 value compared to the one-component diffusion-flickering model—potentially

because the fitting procedure and R^2 calculation include the flickering portion (τ = 0.01–0.76 ms) of the autocorrelation function.

When comparing the pure-diffusion model to the diffusion-flickering model (Figures Figure 6.7–Figure 6.10), the one-component pure-diffusion model (blue dashed lines) and the one-component diffusion-flickering model (red solid lines) yield similar diffusional correlation times, confirming the adequacy of the pure-diffusion model. Likewise, a comparison of the average hydrodynamic radii of small EVs from the pure-diffusion model (Table 6.2) and the diffusion-flickering model (Table 6.3) shows that both approaches produce essentially the same values. For large EVs, the mean hydrodynamic radii obtained with the pure-diffusion model are slightly higher, although this difference is negligible when considering the *SEM*. The main source of discrepancy appears when using the two-component model. In the diffusion-flickering model, the flickering component influences the R^2 calculation, making it easier to exceed the $R^2 > 0.9$ threshold and reducing the need for a two-component fit. Nevertheless, in Figure 6.9B, C, and F, employing the two-component model (green lines) does improve the accuracy of certain autocorrelation function fits. Overall, these findings suggest that the pure-diffusion model provides the most reliable final values.

Table 6.3. Hydrodynamic Radii of Small and Large EVs Carrying mScarlet-WNT3a/5a, Obtained by Fitting with the Diffusion-Flickering Model (Equations (6.10)–(6.11)). All values for individual samples are given as the median ± *MAD*. The number of segments and fit parameters are reported in Appendix D.6.

Sample	r_h / nm			
	Small EVs mScarlet-WNT3a	**Small EVs mScarlet-WNT5a**	**Large EVs mScarlet-WNT3a**	**Large EVs mScarlet-WNT5a**
1	76 ± 26	63 ± 17	172 ± 73	30 ± 18
2	222 ± 69	90 ± 24	162 ± 89	127 ± 83
3	57 ± 17	63 ± 15	100 ± 46	470 ± 212
4	153 ± 50	85 ± 31	243 ± 188	–
5	40 ± 10	–	–	–
6	38 ± 8	–	–	–
Mean ± *SEM*	**98 ± 30**	**75 ± 7**	**169 ± 29**	**209 ± 134**

6.5 Discussion

In this chapter, FCS was applied to determine the hydrodynamic radii of WNT-carrying particles in the non-EV, small-EV, and large-EV fractions. The measurement and analysis procedures demand meticulous attention to several factors.

A primary consideration is the choice of fluorescent probe. Here, red fluorescent proteins mCherry2 and mScarlet were used, achieved by genetically fusing the fluorescent protein to the WNT proteins. This approach circumvents typical challenges associated with fluorescent dye labeling—such as low binding affinity and nonspecific binding—which can introduce correlated background signals in FCS. However, a drawback of fluorescent protein labeling can be a relatively low signal-to-noise ratio, emphasizing the need for sufficiently bright proteins. From Section 5.1.1, mScarlet is approximately seven times brighter than mCherry2, indicating that mScarlet may be the more suitable option at first glance.

However, control measurements of purified mCherry2 and mScarlet yielded different insights regarding diffusion coefficients. Two approaches were used to account for flickering in fluorescent proteins when determining diffusion coefficients: (1) fitting the autocorrelation functions obtained at various excitation powers with a pure-diffusion model and then plotting the apparent diffusion coefficient versus power density to extrapolate to zero power, and (2) fitting the autocorrelation functions directly with the diffusion-flickering model.

Both approaches produced nearly identical diffusion coefficients for mCherry2 (103 ± 1 $\mu m^2\ s^{-1}$ from the first approach and 105 ± 2 $\mu m^2\ s^{-1}$ from the second approach), consistent with the expected diffusion coefficient (102 $\mu m^2\ s^{-1}$) for GFP-like fluorescent proteins, calculated based on previous publications[115,163,167]. However, for mScarlet, the first and second approaches returned diffusion coefficients of 112 ± 8 $\mu m^2\ s^{-1}$ and 128 ± 9 $\mu m^2\ s^{-1}$, respectively. This discrepancy from the expected value arises because the photophysical fraction of mScarlet is roughly three times larger than that of mCherry2, resulting in greater interference from photophysical effects in the autocorrelation functions. Additionally, the photophysical characteristic time of mScarlet is longer and closer to its diffusional correlation time, which impedes clear separation of flickering from diffusion.

These findings highlight the importance of conducting thorough control measurements to characterize the photophysical properties of new fluorescent proteins before using them for

diffusion coefficient determinations. Accurate diffusion coefficients can only be obtained when the photophysical and diffusion processes can be clearly distinguished. Because the DNA structure suggests that the hydrodynamic radii of non-EV WNT3a/5a/11 units (including the fluorescent protein) are not substantially larger than those of purified fluorescent proteins, their diffusional correlation times could be influenced by the photophysical characteristic time of mScarlet. Consequently, the hydrodynamic radii of these non-EV WNT units were determined using the mCherry2-labeled constructs.

FCS measurements of non-EV-bound mCherry2-WNT3a, mCherry2-WNT5a, and mCherry2-WNT11 units yielded diffusion coefficients (mean ± *SD*) of 38 ± 8 $\mu m^2\ s^{-1}$ and 39 ± 11 $\mu m^2\ s^{-1}$, and 60 ± 1 $\mu m^2\ s^{-1}$, respectively. Comparing these values to that of mCherry2 in conditioned medium (111 ± 3 $\mu m^2 \cdot s^{-1}$, mean ± *SD*) gave hydrodynamic radii (mean ± *SD*) of 7.7 ± 1.7 nm (mCherry2-WNT3a), 7.3 ± 2.1 nm (mCherry2-WNT5a), and 4.9 ± 0.2 nm (mCherry2-WNT11). All hydrodynamic radius values exceed the stokes radius of 3.6 nm predicted from their DNA sequences, which include only the WNT protein, the fluorescent protein, and a linker. Hence, this discrepancy likely arises from additional structures around the lipidated WNT proteins. Notably, the average radius of mCherry2-WNT11 lies between the predicted value and those of mCherry2-WNT3a/5a, supporting the proposal that WNT11 secretion does not require lipidation[18]. As a result, the non-EV mCherry2-WNT11 fraction may contain both lipidated and unlipidated forms, producing an intermediate hydrodynamic radius.

Several possibilities for additional co-diffusing structures have been proposed as shown in Figure 1.1: (1) other WNT proteins, forming WNT homo-oligomers[22], (2) WNT-binding proteins[23,24], (3) lipoproteins or micelles[25,26]. However, the N&B results in Chapter 5 suggest that homo-oligomerization of WNT proteins is unlikely to be the dominant mechanism. Thus, the primary possibilities are WNT-binding proteins and lipoproteins/micelles. Considering the known size ranges of the proposed WNT-binding proteins (Table 6.4), the hydrodynamic radii obtained here exceed those ranges. Consequently, lipoproteins/micelles, which range from 7 to 80 nm in diameter [176], are likely the main additional components.

These findings compliment the dynamic light scattering results (Section 4.3), which showed dominant peaks at a hydrodynamic radius of ~5 nm. This size is larger than typical proteins, indicating that lipid-containing nanoparticles constitute much of the non-EV fraction. However, those particles could be unlabeled and may not contain WNT proteins. By employing

FCS, it is now evident that, on average, the additional co-diffusing structures in WNT-containing particles are more likely lipid-based—or at least not exclusively protein-based.

Table 6.4. Molecular Mass of Proposed Wnt-Binding Proteins

Protein	M_M / kDa	Remark
AFAMIN[177]	87	
Secreted Wingless-interaction molecule (Swim)[23]	50–100	Mammalian Swim has not been found.
Human secreted frizzled-related protein (FrzB)[178]	~40	FrzB was reported to travel with Cres.
Crescent (Cres)[179]	30	

One limitation of determining the hydrodynamic radius from the translational diffusion coefficient is its relatively low sensitivity to particle size, given that $D \propto r_h^{-1}$ (Equation (2.28)). By contrast, the rotational diffusion coefficient, which follows $D \propto r_h^{-3}$ (Equation (2.35)), provides substantially greater sensitivity. Consequently, polarization-dependent FCS was used to measure the rotational Brownian motion of non-EV-bound mCherry2-WNT3a/5a/11 units, aiming to improve the precision of hydrodynamic radius determinations. This approach is in principle feasible because, as demonstrated in Chapter 5, each particle typically contains only one WNT protein (and thus one chromophore). If multiple chromophores were present in the observation volume simultaneously, the dipole-moment changes from particle rotation would cancel one another, reducing the detected fluorescence fluctuations.

The autocorrelation functions obtained from polarization-dependent FCS measurements of non-EV-bound mCherry2-WNT3a, mCherry2-WNT5a, and mCherry2-WNT11 could not be well-fitted with a single rotational term but required two rotational diffusion components. One term, with a rotational correlation time of 15 ± 1 ns, corresponds to the independent rotation of mCherry2. This behavior arises because mCherry2 is linked to the WNT protein by a flexible linker, allowing it to ‘tumble’ independently of the rotation of the entire WNT unit. The second term, with a larger rotational correlation time, represents the rotation of the whole WNT unit.

Nonetheless, the first rotational term dominates the autocorrelation functions, contributing approximately five times more than the second term. This dominance, caused by the relatively free rotation of mCherry2, prevents precise determination of the rotational diffusion coefficient for the entire WNT unit. Nonetheless, the ranking of the larger rotational

correlation times—mCherry2-WNT3a (225 ± 86 ns), mCherry2-WNT5a (190 ± 72 ns), and mCherry2-WNT11 (99 ± 35 ns, mean ± *SD*)—reflects the hydrodynamic radius ranking from largest to smallest. This consistency supports the hydrodynamic radii obtained from translational diffusion measurements.

For future studies, designing a shorter flexible linker between the WNT protein and the fluorescent protein could reduce the independent rotation of mCherry2, enabling more accurate determination of the rotational diffusion coefficient for the entire WNT unit. Additionally, performing these measurements at lower concentrations of mCherry2-WNT proteins could allow the use of antibunching amplitudes to confirm the number of WNT proteins per particle, complementing N&B analysis.

Furthermore, the hydrodynamic radii of WNT3a/5a-loaded EVs were determined. The EVs' large sizes result in diffusional correlation times on the order of ms, enabling FCS measurements on EVs with mScarlet-labeled WNT while minimizing interference from flickering. The autocorrelation functions from individual 30-s segments were fitted using the pure diffusion model, starting at 0.76 ms. This analysis yielded average hydrodynamic radii (mean ± *SEM*) of 94 ± 29 nm and 189 ± 22 nm for small and large EVs carrying mScarlet-WNT3a, respectively, and 77 ± 8 nm and 249 ± 160 nm (large EVs) for small and large EVs carrying mScarlet-WNT5a, respectively. Fitting the same autocorrelation function s using the diffusion-flickering model produced similar results: 98 ± 30 nm and 169 ± 29 nm for small and large EVs carrying mScarlet-WNT3a, and 75 ± 7 nm and 209 ± 134 nm for small and large EVs carrying mScarlet-WNT5a, respectively. Since both fit models provided consistent results, the pure diffusion model was preferred due to its simplicity and its limited fitting range, which ensures that R^2 more directly reflects the quality of the fit around EV diffusion.

Note that part of the data from mScarlet-WNT5a-loaded EVs was used in another publication[156]. The differences in the reported hydrodynamic radii between that publication and this dissertation are due to variations in data selection and treatment.

The hydrodynamic radii obtained generally overlap with the expected size ranges of exosomes (15–75 nm[29,38,40]) and microvesicles (50–500 nm[38,39]), as well as the size ranges detected by dynamic light scattering (Section 4.3). In addition, a closer examination of the results (Table 6.2) reveals significant uncertainty in the hydrodynamic radius of each sample, reflecting the broad size distribution, heterogeneity, and presence of aggregates. The *SEM* of the

hydrodynamic radius across different samples of the same type highlights variations among samples, which could arise from differences in cell physiological conditions, emphasizing the importance of consistent EV collection across different cell generations. Additional factors contributing to these variations include imperfections in EV separation methods, leading to cross-contamination between fractions, and potential aggregation or fragmentation caused by freezing and thawing during storage. These issues underscore the critical need for strict adherence to high-standard EV handling protocols, such as the guidelines released by the International Society for Extracellular Vesicles[30].

Here, limitations of the current study should be acknowledged. First, the data for large EVs carrying mScarlet-WNT5a are insufficient, as indicated by the significant scatter in the median hydrodynamic radii of individual samples. Second, relying solely on R^2 as the criterion for accepting fits is not ideal. Residual analysis should also be incorporated to assess fit reliability, with residuals expected to exhibit no discernible patterns and scatter randomly around zero. Hence, automated methods for evaluating residual patterns without manual intervention should be developed for effective reproducible data analysis in the future. Third, the presence of varying intensity bursts in the fluorescence intensity traces does not fully comply with the fundamental requirement of signal stationarity in FCS. Excluding these bursts could generally mitigate artefacts caused by non-stationary signal components. Notably, this must be done with caution in the context of EV measurements, as discarded intensity bursts may arise from individual EVs, which are intrinsically heterogeneous in brightness.

Additionally, there is room for improvement in the measurement methods. Wyss et al. [157] propose an analysis pipeline that combines detection of intensity bursts in intensity-time traces, representing individual EVs passing through the detection volume, with both brightness and autocorrelation function analysis to determine EV size. For large EVs, the sampling rate could be enhanced using scanning FCS[180,181], which can also be combined with three-dimensional particle tracking [182].

6.6 Summary

Flickering of mScarlet is more pronounced than that of mCherry2 and persists over a longer timescale. Thus, the diffusion coefficients of non-EV-bound WNT units were measured using the mCherry2-tagged version. The translational diffusion coefficients indicate hydrodynamic radii of non-EV-bound WNT3a, WNT5a, and WNT11 units that are larger than predicted from their DNA constructs. This additional size suggests the presence of additional structure co-diffusing with the secreted WNT proteins, aligning with the biological aspect that the WNT proteins are lipidated and require a shield for their lipid anchors.

Furthermore, the hydrodynamic radii of non-EV mCherry2-WNT3a and mCherry2-WNT5a particles are larger compared to non-EV mCherry2-WNT11 particles. This contrast is also supported from their rotational correlation times, although determining the precise rotational diffusion coefficients is not feasible due to the flexible nature of the linkers between the WNT proteins and mCherry2. This finding also supports the conclusion of a previous study[18] that lipidation is not necessary for secretion of Wnt11 proteins.

In addition, the hydrodynamic radii of WNT3a/5a-loaded EVs were determined based on the mScarlet-tagged WNT variant, as interference from flickering was expected to subside before the diffusional correlation time of the EVs. The hydrodynamic radii of small EVs and large EVs carrying mScarlet-WNT3a/5a overlap with the expected size ranges of exosomes and microvesicles, respectively. High uncertainties were observed in the hydrodynamic radius of particles within each EV sample, as well as across different samples, reflecting the heterogeneity of particles present in the EV fractions.

7. Investigation of Co-Migrating Structures of Non-EV-Bound Wnt Units

The emission spectra of conditioned medium reveal that the majority of WNT proteins are secreted independently from EVs (refer to Chapter 4), suggesting that research findings based on Wnt proteins in conditioned medium are primarily influenced by the non-EV fraction. In those studies, various strategies have been employed to maintain the activity of the Wnt proteins, including the supplementation of the detergent CHAPS[80], the fetal bovine serum [183], the glycoprotein afamin[24,137], or a combination of phospholipid and cholesterol[184]. These additives are believed to enhance the solubility of lipidated Wnt proteins in the extracellular milieu and preventing Wnt protein aggregation.

Furthermore, N&B analysis showed that each non-EV-bound WNT3a/5a/11 unit in conditioned medium supplemented with fetal bovine serum contains only one WNT protein (see Chapter 5), while FCS demonstrated that these particles exhibit larger hydrodynamic radii compared to the predicted size of the WNT protein (and fluorescent protein) alone (see Chapter 6). This increase in size suggests the possible solubilization of Wnt proteins by co-migrating proteins and/or lipids.

As the observed hydrodynamic radii of non-EV mCherry2-WNT3a, mCherry2-WNT5a, and mCherry2-WNT11 (Section 6.2) are larger than typical proteins, this chapter first focuses on examining the potential for Wnt proteins traveling as part of lipid-containing nanoparticles. Furthermore, given that Wnt3a[25] and Wnt5a[26] proteins were shown to be transported on high-density lipoproteins, which are globular vesicles which cells typically use for transporting lipid with a diameter range of 7–14 nm[185], dual-color fluorescence cross-correlation spectroscopy was employed to detect co-diffusion between mCherry2-WNT3a/5a/11 and high-density

lipoproteins. Lastly, co-diffusion between afamin and Wnt3a proteins, as suggested by previous structural analysis[32] and evidence of co-purification[24], was quantitatively and specifically investigated. Dual-color fluorescence cross-correlation spectroscopy was utilized to observe positive cross-correlation between mCherry2-WNT3a and human afamin (AFAMIN)-eGFP. The cross-correlation amplitude was then used to calculate the proportion of Wnt3a co-diffusing with AFAMIN.

7.1 Possibility of WNT3a/5a Proteins Diffusing as Part of Lipid-Containing Nanoparticles

To explore the potential that non-EV-bound WNT3a/5a proteins are transported with lipid-containing nanoparticles, methyl-β-cyclodextrin (MβCD) was added to the non-EV fractions of conditioned medium containing mCherry2-WNT3a/5a. MβCD is an oligosaccharide composed of seven glucopyranose monomers, forming a cylindrical structure with a hydrophobic cavity and a hydrophilic exterior[186]. It has been shown that MβCD could be used to desorb cholesterol from membranes[187-190].

FCS measurements were started 1 min after the application of 10 mM and 40 mM MβCD and continued for 120 min (121 min in total after MβCD addition). Figure 7.1 shows the average autocorrelation function curves recorded between 1–6 min and 101–121 min. The autocorrelation functions of non-EV-bound mCherry2-WNT3a and mCherry2-WNT5a units after 101–121 min shift to the left compared to the average autocorrelation functions from the 1–6 min. The shifts are more pronounced at a higher MβCD concentration of 40 mM. These findings indicate that MBCD reduces the size of non-EV-bound WNT3a and WNT5a units. It is important to note that cholesterol depletion already occurred within the first 6 min, so the size shifts shown in this figure do not fully reflect the entire size changes.

To account for changes in medium viscosity due to MβCD, three control samples of purified mCherry2 were diluted in EV-depleted conditioned medium (non-EV fraction) obtained from cells transfected with pcDNA. Different amounts of MβCD solution were added to the control samples, resulting in final MβCD concentrations of 0 mM (only DPBS was added), 10 mM, and 40 mM. FCS measurements were taken on individual samples, and the

autocorrelation functions were fitted with a composite model incorporating both diffusion (Equation (2.23)) and flickering (Equation (2.30)) contributions:

$$G(\tau) = G_F(\tau) \cdot G_D(\tau) = \frac{1}{N}\left(1 + \frac{f_F}{1-f_F} e^{-\tau/\tau_F}\right)\left(1 + \frac{\tau}{\tau_D}\right)^{-1}\left(1 + \frac{\tau}{S^2\tau_D}\right)^{-1/2} \tag{7.1}$$

for the diffusional correlation time.

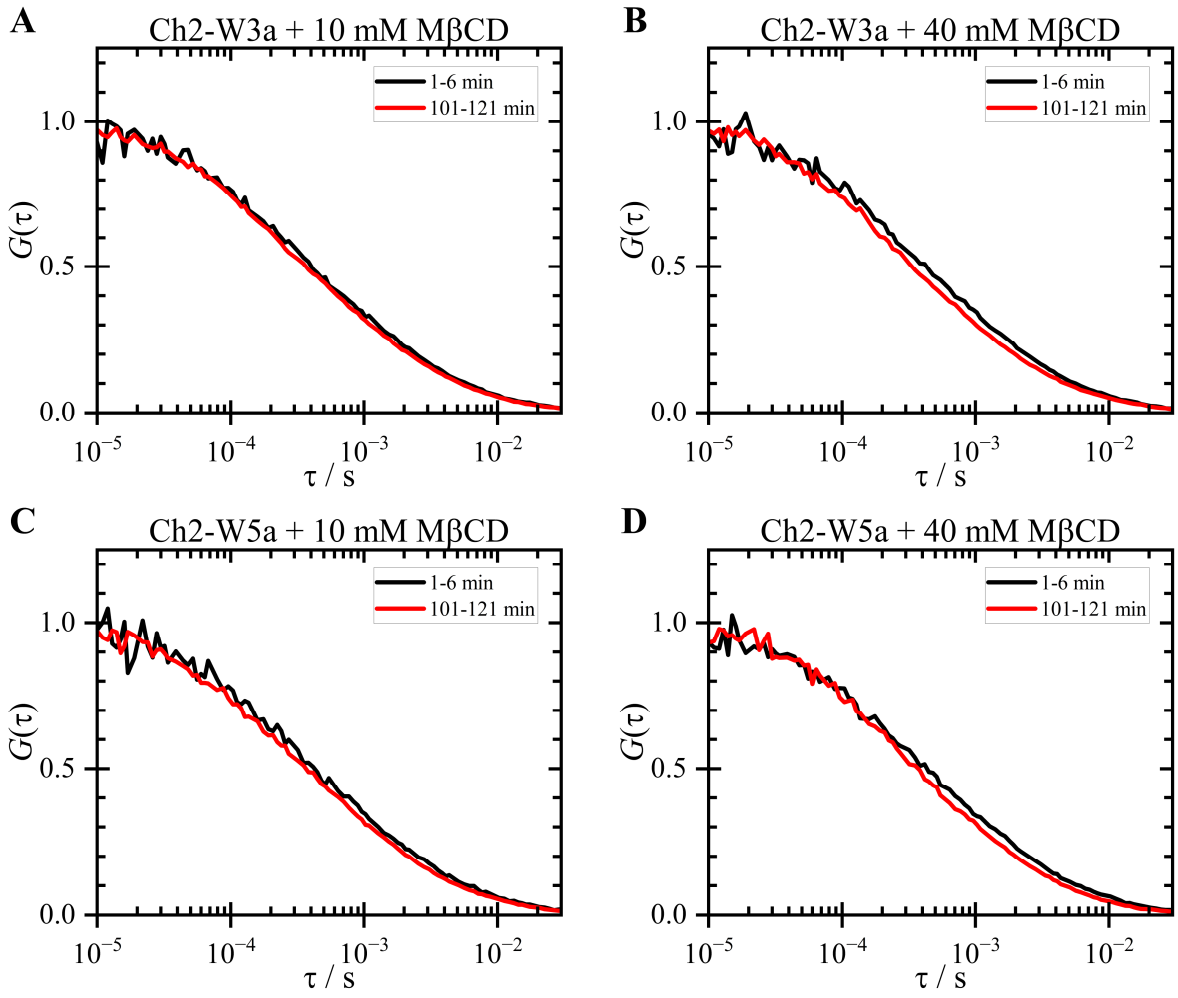

Figure 7.1. Autocorrelation Functions ($G(\tau)$) of Non-EV-Bound mCherry2-WNT3a (A–B) and mCherry2-WNT5a (C–D) Units. The left and right columns show autocorrelation functions obtained with10 mM and 40 mM MβCD added, respectively. The black and red lines show the averaged autocorrelation functions from 1–6 min and 101–121 min after adding MβCD, respectively. All autocorrelation functions are normalized to make $G(\tau = 1\ \mu s) = 1$.

Figure 7.2 shows the average diffusional correlation time of purified mCherry2 in the control samples, normalized to the value from conditioned medium with 0 mM MβCD. A higher concentration of MβCD leads to an increase in mCherry2's diffusional correlation time, indicating slower diffusion due to increased viscosity. This ratio was then multiplied by the diffusional correlation time of mCherry2-WNT3a/5a samples with 0 mM MβCD to predict the diffusional correlation time immediately after the addition of MβCD ($t = 0$) to the samples.

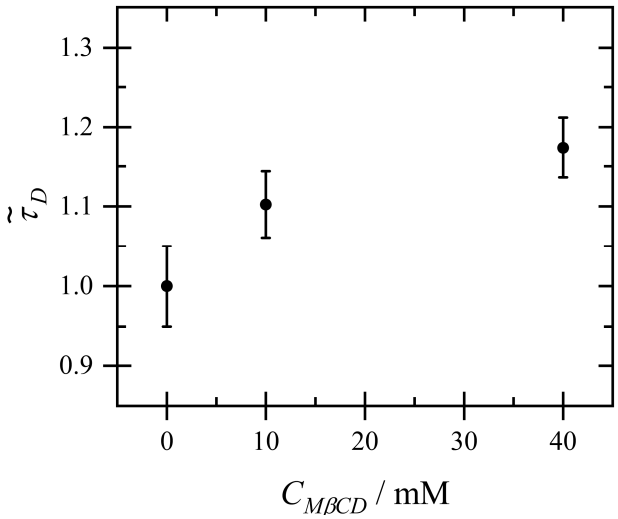

Figure 7.2. Normalized Diffusional Correlation Time ($\tilde{\tau}_D$) of Purified mCherry2 versus the MβCD Concentration ($C_{M\beta CD}$). The $\tilde{\tau}_D$ values are diffusional correlation time normalized to the diffusional correlation time at $C_{M\beta CD}$ = 0. The increase in $\tilde{\tau}_D$ with respect to $C_{M\beta CD}$ reflects the increase in viscosity of conditioned medium upon mixing with MβCD. Data points represent the mean values, and error bars indicate the *SD*. A list of fit parameters and individual results are provided in Appendix E.1.1.

To characterize the temporal development of diffusion of non-EV-bound mCherry2-WNT3a/5a after the addition of MβCD, each 120-min measurement was divided into six 20-min intervals. The autocorrelation function for each interval was computed and fitted with Equation (7.1), yielding the average diffusional correlation time for each 20-min interval. The temporal development of the diffusional correlation time, normalized to the predicted diffusional correlation time at $t = 0$, as a result of MβCD addition, is plotted in Figure 7.3.

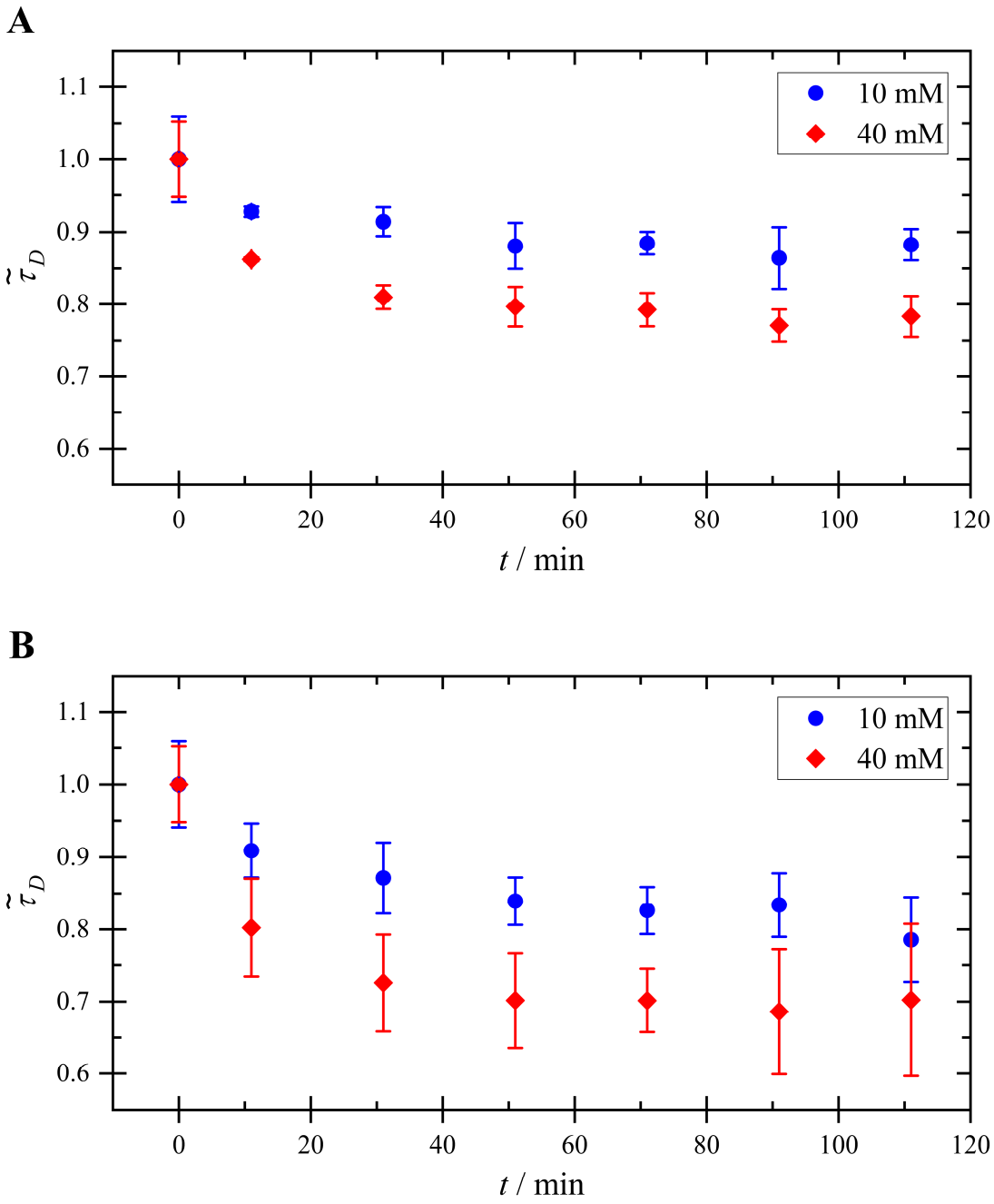

Figure 7.3. Normalized Diffusional Correlation Time ($\tilde{\tau}_D$) of Non-EV-Bound mCherry2-WNT3a (A) and mCherry2-WNT5a (B) as a Function of Time (t). Data points represent the average diffusional correlation times, normalized to the values at t = 0. The error bars show *SD*. The blue circles and red diamonds represent the data from 10 mM and 40 mM MβCD, respectively. Results for individual samples and fit parameters are provided in Appendix E.1.2–E.1.3.

After 111 min, 10 mM MβCD reduced the normalized diffusional correlation time of mCherry2-WNT3a to 0.88 ± 0.02 (mean ± *SD*). This corresponds to a 12 ± 6% (mean ± *SD*) reduction in hydrodynamic radius, and consequently a 31 ± 13% (mean ± *SD*) reduction in

mass. The effect is more pronounced with the addition of 40 mM MβCD, as the normalized diffusional correlation time decreased to 0.78 ± 0.03 (mean ± *SD*). This corresponds to a 22 ± 5% (mean ± *SD*) in hydrodynamic radius, and consequently 52 ± 9% (mean ± *SD*) reduction in mass.

Similarly, the normalized diffusional correlation time of mCherry2-WNT5a was reduced to 0.79 ± 0.06 (mean ± *SD*) by 10 mM MβCD and to 0.70 ± 0.11 (mean ± *SD*) by 40 mM MβCD. These reductions in the diffusional correlation time correspond to 21 ± 7% and 30 ± 11% (mean ± *SD*) reductions in hydrodynamic radius from 10 mM and 40 mM MβCD, respectively. These radius reductions are equivalent to 51 ± 14% (10 mM MβCD) and 65 ± 17% (40 mM MβCD) mass reductions (mean ± *SD*).

7.2 Possibility of Wnt Proteins Being Transported by High-Density Lipoproteins

Among lipoproteins, the size range of high-density lipoproteins matches with the sizes of non-EV-bound WNT3a/5a/11 units. Thus, this study focused on the potential transport of WNT proteins by high-density lipoproteins, which contain Apolipoprotein AI as a major protein component[191,192].

Non-EV-bound mCherry2-WNT3a, mCherry2-WNT5a, and mCherry2-WNT11 units were incubated with 50 nM CoraLite Plus 488-conjugated apolipoprotein AI antibody (AB-CoraLite 488) for 3 h before being subjected to dual-color fluorescence cross-correlation spectroscopy measurements. A negative control was prepared by mixing the same quantity of AB-CoraLite 488 into the control EV-depleted conditioned medium along with 10 nM purified mCherry2. (Refer to Appendix E.2 for a positive control demonstrating the overlap of the laser foci.)

Figure 7.4 displays the resulting autocorrelation functions and cross-correlation functions. The cross-correlation function amplitudes between mCherry2-WNT3a/5a/11 and the AB-CoraLite 488 are very close to zero, with none surpassing the cross-correlation function amplitude of the negative control. Any slight cross-correlation function values observed may stem from spectral cross-talk. Thus, based on dual-color fluorescence cross-correlation

spectroscopy, no evidence suggests that mCherry2-WNT3a, mCherry2-WNT5a, mCherry2-WNT11 are transported by high-density lipoproteins.

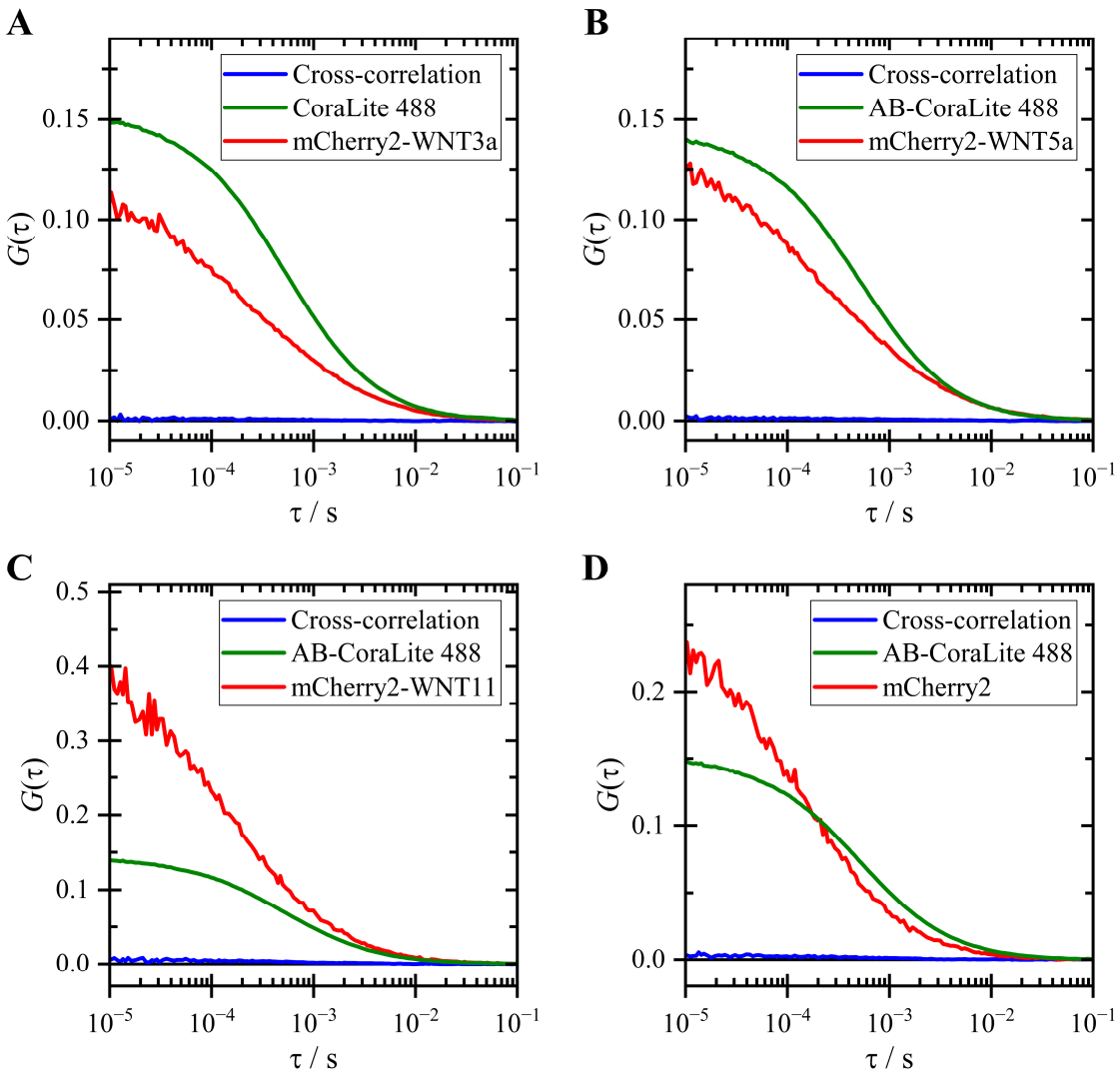

Figure 7.4. Cross-Correlation Functions ($G(\tau)$) Between mCherry2-WNT and AB-CoraLite 488. The cross-correlation functions are displayed in blue, and the autocorrelation functions of AB-CoraLite 488 are displayed in green. The autocorrelation functions of mCherry2-WNT3a (A), mCherry2-WNT5a (B), mCherry2-WNT11 (C), and purified mCherry2 (D) are depicted in red.

Additionally, mScarlet-WNT3a proteins were extracted from the non-EV mScarlet-WNT3a sample using *RFP-catcher* (detailed in Appendix A.2.3), consisting of 50–150 µm agarose beads with red fluorescent protein antibody immobilized on the surface. Figure 7.5A

shows the pellet forming as the mScarlet of the mScarlet-WNT3a fusion binds to the RFP-catcher. Following this, the sample was incubated overnight with the AB-CoraLite 488, and the pellet was pipetted on the surface of a coverslip and imaged (Figure 7.5B). Comparing the image in the green emission channel with that of the negative control (Figure 7.5C), which is the sample prepared the same way but without the antibody, reveals no AB-CoraLite 488 on the beads.

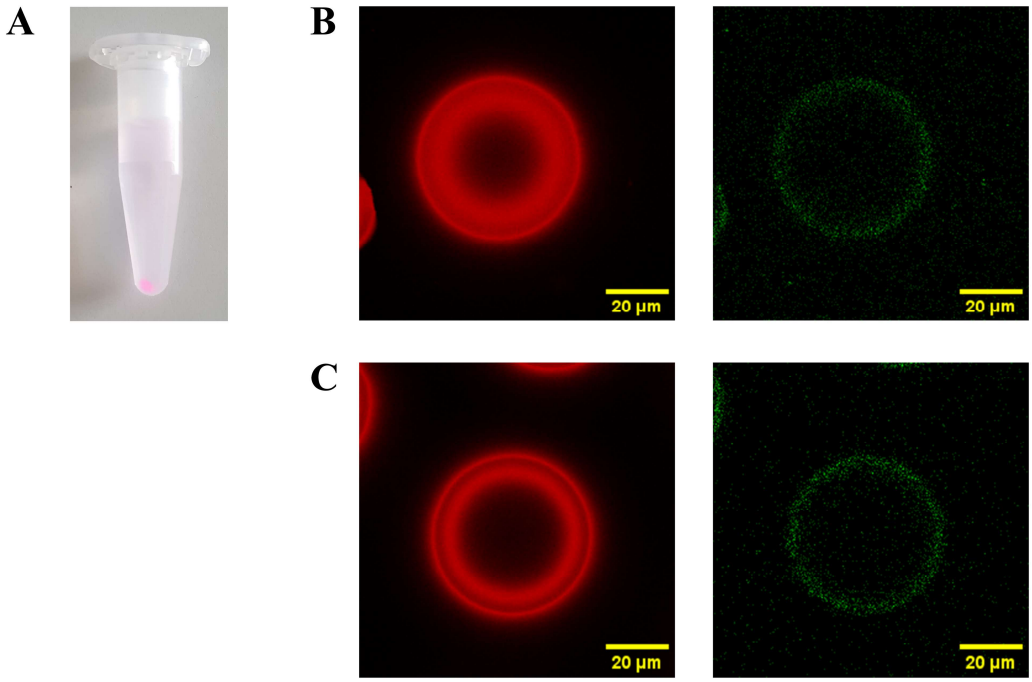

Figure 7.5. RFP-Catcher Incubated with Non-EV-Bound mScarlet-WNT3a Solution

A: Pellet of mScarlet-WNT3a forming at the bottom of the microcentrifuge tube as mScarlet-WNT3a binds with RFP-catcher

B–C: Images of RFP catchers incubated with non-EV mScarlet-WNT3a particles the red-emission (left) and green-emission (right) channels

B: The RFP-catcher was also incubated with AB-CoraLite 488.

C: The RFP-catcher was not incubated with AB-CoraLite 488 (negative control).

7.3 Possibility of WNT3a Proteins Co-Diffusing with AFAMIN

To investigate the potential co-diffusion between mCherry2-WNT3a and AFAMIN, cells stably expressing mCherry2-WNT3a were transfected with 0.75 µg and 1.5 µg of AFAMIN-eGFP plasmid. The conditioned media were collected after 3 d, and large EVs were removed via centrifugation. The results of the dual-color fluorescence cross-correlation spectroscopy measurement are shown in Figure 7.6.

As a negative control, cells not expressing mCherry2-WNT3a were transfected with AFAMIN-eGFP, and the conditioned medium was mixed with purified mCherry2. Fitting the autocorrelation function of AFAMIN-eGFP in the negative control conditioned medium (Figure 7.6C) with the diffusion-flickering model (Equation (6.2)) yielded a diffusion coefficient of 60.7 ± 0.4 $\mu m^2\ s^{-1}$ (mean ± *SD*) for AFAMIN-eGFP. This value agrees with the expected diffusion coefficient (~60 $\mu m^2\ s^{-1}$) calculated from the ratio between mass of AFAMIN-eGFP (100 kDa)[†] and a GFP-like fluorescent protein (~27 kDa). Hence, the observed autocorrelation functions in the green emission channel are attributable to AFAMIN-eGFP.

While the cross-correlation function between AFAMIN-eGFP and mCherry2-WNT3a has a non-zero amplitude (Figure 7.6A), the amplitude is significantly lower than their corresponding autocorrelation function amplitudes. The autocorrelation functions were fitted using the diffusion-flickering model (Equation (6.2)), and the cross-correlation functions were fitted using the pure diffusion model (Equation (6.1)) as the flickering of eGFP and mCherry2 are uncorrelated.

It is important to acknowledge the potential presence of EVs in the conditioned medium, raising the possibility that the obtained cross-correlation functions result from EVs containing both mCherry2-WNT3a and AFAMIN-eGFP. However, fitting with a model for molecules containing a single species yielded successful results with $R^2 > 0.95$ (see Figure 7.6B and Table E.14), suggesting that the cross-correlation originates from homogeneous particles rather than heterogeneous EVs. Furthermore, the diffusion coefficients of the co-species were higher than expected for EVs (see Table E.14).

[†] The molecular mass of AFAMIN is 87 kDa [177].

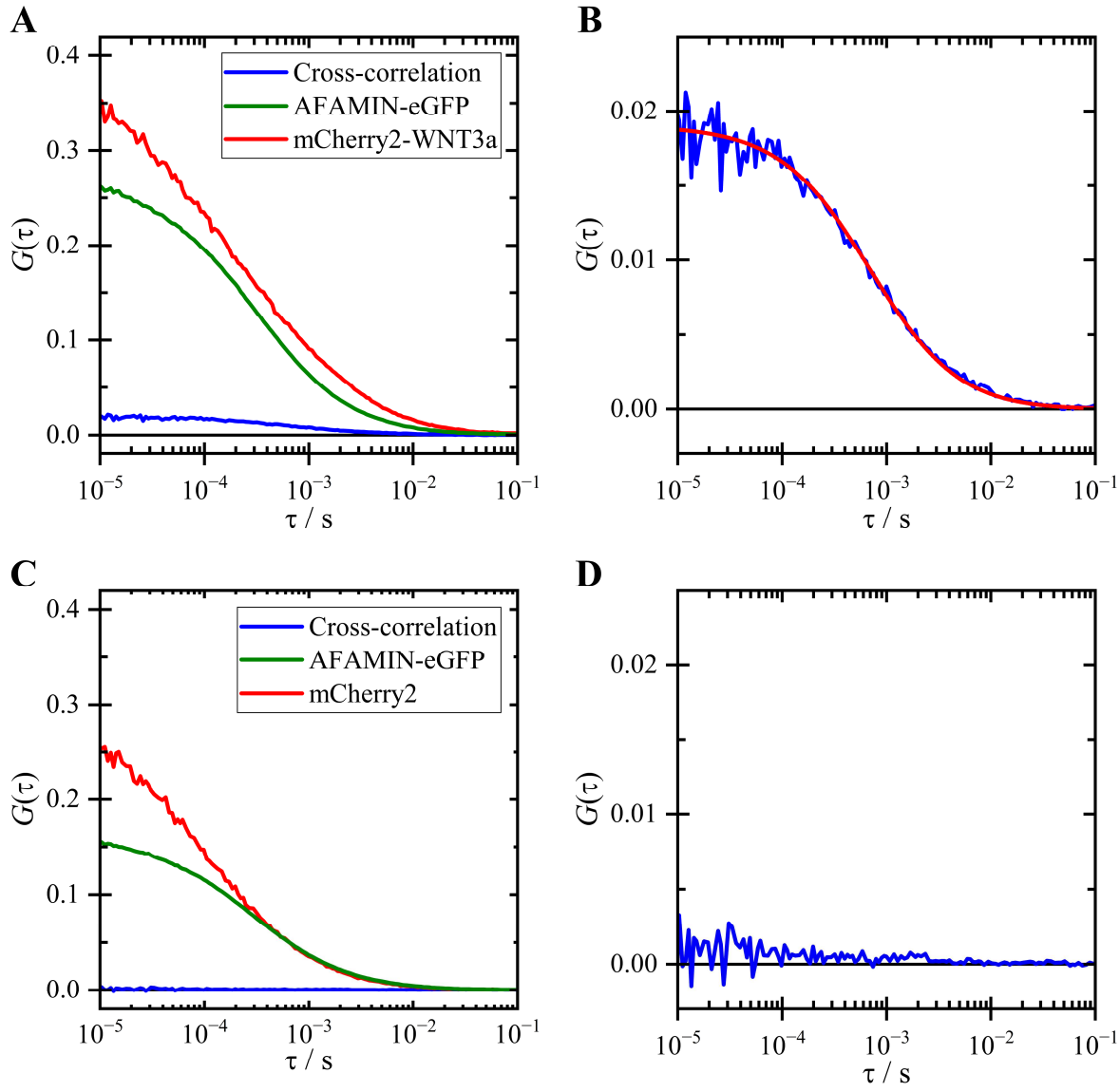

Figure 7.6. Dual-Color Fluorescence Cross-Correlation Spectroscopy Results Between mCherry2-WNT3a and AFAMIN-eGFP

A–B: Cross-correlation functions ($G(\tau)$) obtained from conditioned medium collected from cells expressing mCherry2-WNT3a transfected with 0.75 µg AFAMIN-eGFP, compared to autocorrelation functions of each channel (A) and fitted with the pure diffusion model (B).

C–D: Cross-correlation functions obtained from purified mCherry2 diluted in the negative control conditioned medium, compared to autocorrelation functions of each channel (C) and zoomed-in with the same scaling as in Panel B (D).

The bound fractions, calculated as the ratio between the concentration of mCherry2-WNT3a proteins co-diffusing with AFAMIN-eGFP to the concentration of all mCherry2-WNT3a proteins, are 9.6 ± 0.4% and 12.0 ± 0.7% (mean ± *SD*) for conditioned media from cells transfected with 0.75 µg and 1.5 µg AFAMIN-eGFP, respectively. In contrast, the same analysis returned the bound fractions for the negative control as 1.0 ± 1.3% (mean ± *SD*, 0.75

µg AFAMIN-eGFP) and 0.8 ± 0.9% (mean ± *SD*, 1.5 µg AFAMIN-eGFP). (See Appendix E.4 for fit parameters and individual results.)

7.4 Discussion

This chapter investigates the structures that co-diffuse with secreted non-EV-bound WNT units to shield their hydrophobic lipid moiety. Based on the size of the secreted particles, the initial focus was on lipid-containing nanoparticles. To that end, MβCD, an oligosaccharide with the ability to desorb cholesterol[187-190], was added to the non-EV fraction of conditioned medium containing mCherry2-WNT3a. FCS measurements on mCherry2-WNT3a, starting immediately after MβCD application, show a significantly decreased diffusional correlation time. The reductions in diffusional correlation time are equivalent to 31 ± 13% and 52 ± 9% (mean ± *SD*) mass reductions due to 10 mM and 40 mM MβCD, respectively. An identical experiment was performed on non-EV-bound mCherry2-WNT5a units, resulting in mass reductions of 51 ± 14% (mean ± *SD*) with 10 mM MβCD and 65 ± 17% (mean ± *SD*) with 40 mM MβCD. However, the same experiment could not be performed on mCherry2-WNT11, as the concentration was too low to obtain a precise and conclusive temporal trend of diffusional correlation time.

For both WNT3a and WNT5a, the mass reduction percentages are significant even at 10 mM MβCD, and the values increase with 40 mM MβCD. These results suggest that the mass reductions are indeed the result of MβCD, indicating that cholesterol contributes significantly to the size of non-EV-bound mCherry2-WNT3a and mCherry2-WNT5a units. Although the ratios of mass reductions are not 1:4 (from 10 mM to 40 mM), this can be explained by nonspecific binding between MβCD and unlabelled lipid particles, or to the surface of the 8-well chamber.

Therefore, it can be concluded that non-EV-bound WNT3a and WNT5a travel as part of lipid-containing nanoparticles, such as lipoproteins, as has been suggested[25,26]. Additionally, non-membranous extracellular nanoparticles, such as exomeres or supermeres, fit into the size range of hydrodynamic radii of non-EV-bound WNT units found in Chapter 6, and exomeres have been reported to be enriched with cholesterol[193]. This could introduce another category of possible WNT co-diffusing particles to be explored in future studies.

The possibility of mCherry2-WNT3a, mCherry2-WNT5a, and mCherry2-WNT11 being transported on high-density lipoproteins was investigated using dual-color fluorescence cross-correlation spectroscopy. The results show that none of the cross-correlation function amplitudes between mCherry2-WNT3a/5a/11 and AB-CoraLite 488, which was used to label high-density lipoproteins, exhibited a positive correlation. This finding was further confirmed by images of mScarlet-WNT3a accumulated on the RFP-catcher, where, after an overnight incubation with AB-CoraLite 488, no AB-CoraLite 488 was detected attached to the mScarlet-WNT3a on the RFP-catcher.

It is important to acknowledge that this conclusion is limited by several factors. First, the binding affinity of the antibody to apolipoprotein AI is unknown, which hinders the determination of the necessary antibody concentration for observing visibly bound particles. In addition, the labeling efficiency of CoraLite Plus 488 dyes with the antibodies is unknown. As a result, the exact proportion of the detected CoraLite Plus 488 signals that are actually from the dyes linked to apolipoprotein antibodies remains uncertain. Therefore, the negative results presented here are not conclusive without further characterization of the corresponding binding affinities.

Furthermore, according to the maturation efficiency of mCherry2 (see Chapter 5), more than 50% of the WNT proteins were labeled with non-fluorescent mCherry2. These non-fluorescent mCherry2-labeled WNT proteins that bind to the antibody would not contribute to the cross-correlation. Therefore, future studies should consider using fluorescent proteins with higher maturation efficiency.

Moreover, the mechanisms governing WNT transport may vary depending on cell types. The WNT proteins investigated in this study were secreted from kidney cells, a cell type not typically associated with lipoprotein secretion, in contrast to, for instance, fibroblast cells used in a prior study[25]. Therefore, a positive result may be observed when testing non-EV-bound WNT units secreted by different cell types.

Continuing with the same approach, the co-diffusion of mCherry2-WNT3a and AFAMIN-eGFP was quantified using dual-color fluorescence cross-correlation spectroscopy. The cross-correlation amplitudes, relative to the autocorrelation amplitudes, show that 9.6 ± 0.4% and 12.0 ± 0.7% (mean ± SD) of mCherry2-WNT3a co-diffuse with AFAMIN-eGFP for conditioned media from cells transfected with 0.75 µg and 1.5 µg AFAMIN-eGFP,

respectively. Although the signal-to-background ratio is affected by mCherry2's low maturation efficiency, these percentages are valid because they represent a ratio of the total number of mCherry2-WNT3a in the samples, and both components are similarly affected by mCherry2's maturation efficiency.

Therefore, the results indicate that while WNT3a could co-diffuse with AFAMIN, this is not the primary transport mode for non-EV-bound WNT3a proteins. This suggests that multiple co-diffusing structures could be involved in WNT protein transport, and the hydrodynamic radii of non-EV-bound WNT units presented in Chapter 6 represent the average of a mixture of all types of co-diffusing species.

To conclusively demonstrate that WNT3a co-diffuses with AFAMIN, further experiments are recommended, including an additional ultracentrifugation step to remove EVs from the conditioned medium. These experiments should also involve varying the amount of AFAMIN transfected in the cells and constructing a binding curve of the bound fraction versus AFAMIN concentration (see, e.g., the methodology in Reference [194]). For further studies, the methodology presented here can also be applied to investigate the AFAMIN co-migrating with WNT5a and WNT11.

7.5 Summary

FCS revealed the effect of MβCD in reducing the size of non-EV-bound mCherry2-WNT3a and mCherry2-WNT5a units, suggesting that WNT3a and WNT5a proteins may be secreted as lipid-containing nanoparticles such as lipoproteins, exomeres, and supermeres. High-density lipoproteins, a subtype of lipoproteins, were examined due to their size range covering that of non-EV-bound WNT3a/5a/11 units. However, no evidence was found to support the transport of WNT proteins on high-density lipoproteins through dual-color fluorescence cross-correlation spectroscopy and imaging. Consequently, the possibilities of WNT proteins being secreted on exomeres and supermeres remain.

Additionally, the potential co-diffusion of WNT proteins with binding proteins such as AFAMIN was also explored. Positive cross-correlation function in dual-color fluorescence cross-correlation spectroscopy measurements suggest that WNT3a proteins could co-diffuse

with AFAMIN, although the majority of WNT3a proteins are transported via different mechanisms.

8. Conclusion

Wnt proteins are notable for their unique post-translational modification through lipidation, which adds a lipid anchor to aid in docking on the receiving cell membranes. This lipid anchor necessitates structural arrangements of Wnt proteins to diffuse in aqueous extracellular space. Using a combination of fluorescence-based characterization techniques, this study provided quantitative information on how the Wnt proteins are 'packaged'.

Via (ultra)centrifugation and size-exclusion chromatography, secreted WNT3a/5a/11-containing particles were fractionated into non-EV-bound WNT units, small EVs, and large EVs. Emission spectrum analysis revealed that more than 95% of WNT3a, WNT5a, and WNT11 proteins are secreted as non-EV-bound units, with the remaining proteins associated with EVs. A dual-luciferase reporter assay showed that WNT3a proteins from all fractions are biologically active. However, EV-associated WNT3a induced higher canonical Wnt signaling activities, suggesting that EV-associated WNT3a proteins may remain active longer, as previously hypothesized by Takada et al[22].

The structural arrangements of secreted non-EV-bound WNT proteins were investigated at single-molecule resolution using number and brightness (N&B) analysis and fluorescence correlation spectroscopy (FCS). N&B analysis showed that non-EV-bound WNT3a, WNT5a, and WNT11 proteins do not form homo-oligomers in conditioned medium supplemented with fetal bovine serum, consistent with prior studies for WNT3a[22]. Each non-EV-bound unit contained one WNT protein but appeared larger than a simple combination of a fluorescent protein and a WNT protein, with WNT3a and WNT5a particles being larger than WNT11. The extra size likely stems from additional structures shielding the lipid anchors of these proteins. The smaller size of WNT11 particles supports the hypothesis that WNT11 may be released without lipidation[18], with only a portion of secreted WNT11 proteins being lipidated and traveling with these additional structures.

Further investigation into the additional structures protecting the lipid anchors revealed a hydrodynamic radius reduction of mCherry2-WNT3a and mCherry2-WNT5a particles due to MβCD. This reduction in size indicates that WNT3a and WNT5a proteins are secreted on lipid-containing nanoparticles. A fraction of WNT3a proteins could possibly also travel with Wnt-binding protein AFAMIN, suggesting that WNT proteins may be secreted via several mechanisms, with observed properties representing an ensemble average of all transport modes.

Moreover, fluorescence intensity distribution analysis (FIDA) revealed that EVs containing mScarlet-WNT3a/5a proteins consist of two distinct sub-populations. One sub-population, which is more abundant, contains, on average, one WNT3a/5a protein per particle. The other, much less abundant (by 2–3 orders of magnitude), contains tens of WNT3a/5a proteins per particle. Within this latter group, large EVs were found to carry more WNT3a/5a proteins than smaller EVs. The heterogeneity in EV populations is reflected not only in brightness but also in hydrodynamic radii, as observed by FCS. It is important to note that these results would benefit from a larger statistical sample size, as measuring more samples is more valuable than repeating measurements on the same sample.

In addition, the secretion mechanisms and properties of WNT-carrying particles might vary depending on cell type and overexpression levels. Further research is needed to investigate these mechanisms in different cell types or using endogenously secreted Wnt proteins, which are present at lower concentrations and pose challenges for measurement. Recent techniques[195] for analyzing correlation functions from finite statistics could be applied to characterize Wnt proteins in low-concentration samples.

In a broader context, this study underscores the advantages of fluorescent protein labeling for WNT proteins or any proteins of interest. Unlike antibody-based labeling, where binding efficiency and dye-to-protein ratio are often uncertain, fluorescent protein labeling at the genetic level ensures precise 1:1 labeling. With this controlled ratio between WNT proteins and labels, molecular brightness can be accurately interpreted to determine the number of WNT proteins per particle. Additionally, overexpression of fluorescently tagged WNT proteins ensures their dominance in the measurements, minimizing the influence of endogenous, unlabeled WNT proteins.

Overall, this study demonstrates the effectiveness of fluorescence-based characterization techniques, particularly N&B, FIDA, and FCS, in analyzing fluorescently labeled particles in complex media. The experimental and analytical processes outlined in this

dissertation have proven robust and reproducible, with potential applications extending beyond the study of Wnt proteins to the analysis of other EVs and biomolecular complexes released from living cells.

As a final remark, future research using similar concepts may benefit from the following recommendations to enhance the characterization process. First, the flexible linker between the fluorescent protein and the protein of interest should be designed to be just long enough to avoid interference with the protein's biological function, but not excessively long. Subsequently, measuring the hydrodynamic radius of particles with higher precision can be achieved by determining their rotational diffusion coefficient using polarization-dependent FCS. Finally, using alternative red fluorescent proteins with higher maturation efficiency would improve the accuracy of quantifying the number of target proteins per particle.

References

1 Katoh, M. WNT and FGF gene clusters. *International journal of oncology* **21**, 1269-1273 (2002).

2 Steinhart, Z. & Angers, S. Wnt signaling in development and tissue homeostasis. *Development* **145**, dev146589 (2018).

3 Teo, J.-L. & Kahn, M. The Wnt signaling pathway in cellular proliferation and differentiation: a tale of two coactivators. *Advanced drug delivery reviews* **62**, 1149-1155 (2010).

4 Polakis, P. Wnt signaling in cancer. *Cold Spring Harbor perspectives in biology* **4**, a008052 (2012).

5 Duchartre, Y., Kim, Y.-M. & Kahn, M. The Wnt signaling pathway in cancer. *Critical reviews in oncology/hematology* **99**, 141-149 (2016).

6 Purro, S. A., Galli, S. & Salinas, P. C. Dysfunction of Wnt signaling and synaptic disassembly in neurodegenerative diseases. *Journal of molecular cell biology* **6**, 75-80 (2014).

7 Libro, R., Bramanti, P. & Mazzon, E. The role of the Wnt canonical signaling in neurodegenerative diseases. *Life sciences* **158**, 78-88 (2016).

8 Clevers, H. Wnt/β-catenin signaling in development and disease. *Cell* **127**, 469-480 (2006).

9 Clevers, H. & Nusse, R. Wnt/β-catenin signaling and disease. *Cell* **149**, 1192-1205 (2012).

10 Niehrs, C. The complex world of WNT receptor signalling. *Nature reviews Molecular cell biology* **13**, 767-779 (2012).

11 Langton, P. F., Kakugawa, S. & Vincent, J.-P. Making, exporting, and modulating Wnts. *Trends in cell biology* **26**, 756-765 (2016).

12 Routledge, D. & Scholpp, S. Mechanisms of intercellular Wnt transport. *Development* **146**, dev176073 (2019).

13 Dijksterhuis, J. P. *et al.* Systematic mapping of WNT-FZD protein interactions reveals functional selectivity by distinct WNT-FZD pairs. *Journal of Biological Chemistry* **290**, 6789-6798 (2015).

14 DeBruine, Z. J., Xu, H. & Melcher, K. Assembly and architecture of the Wnt/β-catenin signalosome at the membrane. *British journal of pharmacology* **174**, 4564-4574 (2017).

15 Voloshanenko, O., Gmach, P., Winter, J., Kranz, D. & Boutros, M. Mapping of Wnt-Frizzled interactions by multiplex CRISPR targeting of receptor gene families. *The FASEB Journal* **31**, 4832 (2017).
16 Kozielewicz, P. *et al.* Quantitative profiling of WNT-3A binding to all human frizzled paralogues in HEK293 cells by NanoBiT/BRET assessments. *ACS Pharmacology & Translational Science* **4**, 1235-1245 (2021).
17 Hosseini, V. *et al.* Wnt lipidation: Roles in trafficking, modulation, and function. *Journal of cellular physiology* **234**, 8040-8054 (2019).
18 Aponte Santamaria, D. F. *The role of lipids in Wnt secretion and function*, (2023).
19 Franch-Marro, X., Wendler, F., Griffith, J., Maurice, M. M. & Vincent, J.-P. In vivo role of lipid adducts on Wingless. *Journal of cell science* **121**, 1587-1592 (2008).
20 Willert, K. *et al.* Wnt proteins are lipid-modified and can act as stem cell growth factors. *Nature* **423**, 448-452 (2003).
21 Kurayoshi, M., Yamamoto, H., Izumi, S. & Kikuchi, A. Post-translational palmitoylation and glycosylation of Wnt-5a are necessary for its signalling. *Biochemical Journal* **402**, 515-523 (2007).
22 Takada, R. *et al.* Assembly of protein complexes restricts diffusion of Wnt3a proteins. *Communications biology* **1**, 165 (2018).
23 Mulligan, K. A. *et al.* INAUGURAL ARTICLE by a Recently Elected Academy Member: Secreted Wingless-interacting molecule (Swim) promotes long-range signaling by maintaining Wingless solubility. *Proceedings of the National Academy of Sciences of the United States of America* **109**, 370 (2012).
24 Mihara, E. *et al.* Active and water-soluble form of lipidated Wnt protein is maintained by a serum glycoprotein afamin/α-albumin. *Elife* **5**, e11621 (2016).
25 Neumann, S. *et al.* Mammalian Wnt3a is released on lipoprotein particles. *Traffic* **10**, 334-343 (2009).
26 Kaiser, K. *et al.* WNT5A is transported via lipoprotein particles in the cerebrospinal fluid to regulate hindbrain morphogenesis. *Nature communications* **10**, 1498 (2019).
27 Gross, J. C., Chaudhary, V., Bartscherer, K. & Boutros, M. Active Wnt proteins are secreted on exosomes. *Nature cell biology* **14**, 1036-1045 (2012).
28 Rautou, P.-E. & Mackman, N. Vol. 125 1601-1604 (Am Heart Assoc, 2012).
29 Yamashita, T., Takahashi, Y., Nishikawa, M. & Takakura, Y. Effect of exosome isolation methods on physicochemical properties of exosomes and clearance of exosomes from the blood circulation. *European Journal of Pharmaceutics and Biopharmaceutics* **98**, 1-8 (2016).
30 Théry, C. *et al.* Minimal information for studies of extracellular vesicles 2018 (MISEV2018): a position statement of the International Society for Extracellular Vesicles and update of the MISEV2014 guidelines. *Journal of extracellular vesicles* **7**, 1535750 (2018).
31 Fu, L. *et al.* Wnt2 secreted by tumour fibroblasts promotes tumour progression in oesophageal cancer by activation of the Wnt/β-catenin signalling pathway. *Gut* **60**, 1635-1643 (2011).
32 Naschberger, A. *et al.* Structural evidence for a role of the multi-functional human glycoprotein afamin in Wnt transport. *Structure* **25**, 1907-1915. e1905 (2017).
33 Magde, D., Elson, E. & Webb, W. W. Thermodynamic fluctuations in a reacting system—measurement by fluorescence correlation spectroscopy. *Physical review letters* **29**, 705 (1972).
34 Magde, D., Elson, E. L. & Webb, W. W. Fluorescence correlation spectroscopy. II. An experimental realization. *Biopolymers: Original Research on Biomolecules* **13**, 29-61 (1974).

35 Digman, M. A., Dalal, R., Horwitz, A. F. & Gratton, E. Mapping the number of molecules and brightness in the laser scanning microscope. *Biophysical journal* **94**, 2320-2332 (2008).
36 Kask, P. *et al.* in *Fluorescence Spectroscopy, Imaging and Probes: New Tools in Chemical, Physical and Life Sciences* 153-181 (Springer, 2002).
37 Kask, P., Palo, K., Ullmann, D. & Gall, K. Fluorescence-intensity distribution analysis and its application in biomolecular detection technology. *Proceedings of the National Academy of Sciences* **96**, 13756-13761 (1999).
38 Théry, C., Ostrowski, M. & Segura, E. Membrane vesicles as conveyors of immune responses. *Nature reviews immunology* **9**, 581-593 (2009).
39 Menck, K., Sivaloganathan, S., Bleckmann, A. & Binder, C. Microvesicles in cancer: Small size, large potential. *International journal of molecular sciences* **21**, 5373 (2020).
40 Yang, D. *et al.* Progress, opportunity, and perspective on exosome isolation-efforts for efficient exosome-based theranostics. *Theranostics* **10**, 3684 (2020).
41 Valeur, B. & Berberan-Santos, M. N. *Molecular fluorescence: principles and applications*. (John Wiley & Sons, 2012).
42 Gomes, A. J., Lunardi, C. N., Rocha, F. S. & Patience, G. S. Experimental methods in chemical engineering: Fluorescence emission spectroscopy. *The Canadian Journal of Chemical Engineering* **97**, 2168-2175 (2019).
43 Kasha, M. Characterization of electronic transitions in complex molecules. *Discussions of the Faraday society* **9**, 14-19 (1950).
44 Stokes, G. G. XXX. On the change of refrangibility of light. *Philosophical transactions of the Royal Society of London*, 463-562 (1852).
45 Lakowicz, J. R. *Principles of fluorescence spectroscopy*. (Springer, 2006).
46 Davis, L. M. & Shen, G. Accounting for triplet and saturation effects in FCS measurements. *Current pharmaceutical biotechnology* **7**, 287-301 (2006).
47 Enderlein, J. Dependence of the optical saturation of fluorescence on rotational diffusion. *Chemical physics letters* **410**, 452-456 (2005).
48 Gregor, I., Patra, D. & Enderlein, J. Optical saturation in fluorescence correlation spectroscopy under continuous-wave and pulsed excitation. *ChemPhysChem* **6**, 164-170 (2005).
49 Giuliano, C. & Hess, L. Nonlinear absorption of light: optical saturation of electronic transitions in organic molecules with high intensity laser radiation. *IEEE Journal of Quantum Electronics* **3**, 358-367 (1967).
50 Enderlein, J., Gregor, I., Patra, D., Dertinger, T. & Kaupp, U. B. Performance of fluorescence correlation spectroscopy for measuring diffusion and concentration. *ChemPhysChem* **6**, 2324-2336 (2005).
51 Nienhaus, G. U. & Nienhaus, K. Fluorescence labeling. *Fluorescence microscopy: from principles to biological applications*, 133-164 (2017).
52 Panchuk-Voloshina, N. *et al.* Alexa dyes, a series of new fluorescent dyes that yield exceptionally bright, photostable conjugates. *Journal of Histochemistry & Cytochemistry* **47**, 1179-1188 (1999).
53 Balleza, E., Kim, J. M. & Cluzel, P. Systematic characterization of maturation time of fluorescent proteins in living cells. *Nature methods* **15**, 47-51 (2018).
54 Milo, R. & Phillips, R. *Cell biology by the numbers*. (Garland Science, 2015).
55 Lambert, T. J. FPbase: a community-editable fluorescent protein database. *Nature methods* **16**, 277-278 (2019).
56 Arpino, J. A., Rizkallah, P. J. & Jones, D. D. Crystal structure of enhanced green fluorescent protein to 1.35 Å resolution reveals alternative conformations for Glu222. *PloS one* **7**, e47132 (2012).

57 Van Orden, A., Fogarty, K. & Jung, J. Fluorescence fluctuation spectroscopy: a coming of age story. *Applied spectroscopy* **58**, 122A-137A (2004).
58 Qian, H. On the statistics of fluorescence correlation spectroscopy. *Biophysical chemistry* **38**, 49-57 (1990).
59 Wenger, J. *et al.* Nanoaperture-enhanced signal-to-noise ratio in fluorescence correlation spectroscopy. *Analytical chemistry* **81**, 834-839 (2009).
60 Wohland, T., Rigler, R. & Vogel, H. The standard deviation in fluorescence correlation spectroscopy. *Biophysical journal* **80**, 2987-2999 (2001).
61 Nagy, P., Claus, J., Jovin, T. M. & Arndt-Jovin, D. J. Distribution of resting and ligand-bound ErbB1 and ErbB2 receptor tyrosine kinases in living cells using number and brightness analysis. *Proceedings of the National Academy of Sciences* **107**, 16524-16529 (2010).
62 Chen, Y., Müller, J. D., So, P. T. & Gratton, E. The photon counting histogram in fluorescence fluctuation spectroscopy. *Biophysical journal* **77**, 553-567 (1999).
63 Acharya, A. *et al.* Photoinduced chemistry in fluorescent proteins: curse or blessing? *Chemical Reviews* **117**, 758-795 (2017).
64 Dunsing, V. *et al.* Optimal fluorescent protein tags for quantifying protein oligomerization in living cells. *Sci. Rep.* **8**, 10634 (2018).
65 Vámosi, G. *et al.* EGFP oligomers as natural fluorescence and hydrodynamic standards. *Sci. Rep.* **6**, 33022 (2016).
66 Felekyan, S., Kalinin, S., Sanabria, H., Valeri, A. & Seidel, C. A. Filtered FCS: Species Auto-and Cross-Correlation Functions Highlight Binding and Dynamics in Biomolecules. *ChemPhysChem* **13**, 1036-1053 (2012).
67 Wohland, T., Maiti, S. & Macháň, R. *An introduction to fluorescence correlation spectroscopy*. (IOP Publishing, 2020).
68 Schwille, P. & Haustein, E. Fluorescence correlation spectroscopy. *A tutorial for the Biophysics Textbook Online (BTOL). Biophysical Society, Rockville, MD* (2002).
69 Ries, J. & Schwille, P. Fluorescence correlation spectroscopy. *BioEssays* **34**, 361-368 (2012).
70 Krichevsky, O. & Bonnet, G. Fluorescence correlation spectroscopy: the technique and its applications. *Reports on Progress in Physics* **65**, 251 (2002).
71 Elson, E. L. Fluorescence correlation spectroscopy: past, present, future. *Biophysical journal* **101**, 2855-2870 (2011).
72 Rigler, R. & Elson, E. S. *Fluorescence correlation spectroscopy: theory and applications*. Vol. 65 (Springer Science & Business Media, 2012).
73 Elson, E. L. & Magde, D. Fluorescence correlation spectroscopy. I. Conceptual basis and theory. *Biopolymers* **13**, 1-27 (1974).
74 Banachowicz, E., Patkowski, A., Meier, G., Klamecka, K. & Gapinski, J. Successful FCS experiment in nonstandard conditions. *Langmuir* **30**, 8945-8955 (2014).
75 Rüttinger, S. *et al.* Comparison and accuracy of methods to determine the confocal volume for quantitative fluorescence correlation spectroscopy. *Journal of microscopy* **232**, 343-352 (2008).
76 Rüttinger, S. *et al.* in *European Conference on Biomedical Optics.* 6630_6612 (Optica Publishing Group).
77 Buschmann, V., Krämer, B., Koberling, F., Macdonald, R. & Rüttinger, S. Quantitative FCS: determination of the confocal volume by FCS and bead scanning with the microtime 200. *Application Note PicoQuant GmbH, Berlin* (2009).
78 Einstein, A. On the motion of small particles suspended in liquids at rest required by the molecular-kinetic theory of heat. *Ann. Phys.* **17**, 549-560 (1905).

79 Peskir, G. On the diffusion coefficient: The Einstein relation and beyond. *Stoch. Models* **19**, 383-405 (2003).
80 Wilkins, D. K. *et al.* Hydrodynamic radii of native and denatured proteins measured by pulse field gradient NMR techniques. *Biochem.* **38**, 16424-16431 (1999).
81 Widengren, J., Rigler, R. & Mets, Ü. Triplet-state monitoring by fluorescence correlation spectroscopy. *Journal of fluorescence* **4**, 255-258 (1994).
82 Nienhaus, G. U., Müller, J. D., McMahon, B. H. & Frauenfelder, H. Exploring the conformational energy landscape of proteins. *Physica D: Nonlinear Phenomena* **107**, 297-311 (1997).
83 Pakhomov, A. A. & Martynov, V. I. GFP family: structural insights into spectral tuning. *Chemistry & biology* **15**, 755-764 (2008).
84 Chmyrov, V., Spielmann, T., Hevekerl, H. & Widengren, J. Trans–cis isomerization of lipophilic dyes probing membrane microviscosity in biological membranes and in live cells. *Analytical chemistry* **87**, 5690-5697 (2015).
85 Widengren, J. & Schwille, P. Characterization of photoinduced isomerization and back-isomerization of the cyanine dye Cy5 by fluorescence correlation spectroscopy. *The Journal of Physical Chemistry A* **104**, 6416-6428 (2000).
86 Widengren, J., Mets, Ü. & Rigler, R. Photodynamic properties of green fluorescent proteins investigated by fluorescence correlation spectroscopy. *Chemical Physics* **250**, 171-186 (1999).
87 Schwille, P., Kummer, S., Heikal, A. A., Moerner, W. & Webb, W. W. Fluorescence correlation spectroscopy reveals fast optical excitation-driven intramolecular dynamics of yellow fluorescent proteins. *Proceedings of the National Academy of Sciences* **97**, 151-156 (2000).
88 Nienhaus, K. & Nienhaus, G. U. Chromophore photophysics and dynamics in fluorescent proteins of the GFP family. *Journal of Physics: Condensed Matter* **28**, 443001 (2016).
89 Widengren, J. 13 Photophysical Aspects of FCS Measurements. *Fluorescence correlation spectroscopy: theory and applications* **65**, 276 (2001).
90 Widengren, J., Mets, U. & Rigler, R. Fluorescence correlation spectroscopy of triplet states in solution: a theoretical and experimental study. *The Journal of Physical Chemistry* **99**, 13368-13379 (1995).
91 Doose, S., Neuweiler, H. & Sauer, M. Fluorescence quenching by photoinduced electron transfer: a reporter for conformational dynamics of macromolecules. *ChemPhysChem* **10**, 1389-1398 (2009).
92 Kask, P., Piksarv, P., Pooga, M., Mets, Ü. & Lippmaa, E. Separation of the rotational contribution in fluorescence correlation experiments. *Biophysical journal* **55**, 213-220 (1989).
93 Rigler, R., Elson, E. S. & Mets, Ü. Antibunching and rotational diffusion in FCS. *Fluorescence correlation spectroscopy: theory and applications*, 346-359 (2001).
94 Oura, M. *et al.* Polarization-dependent fluorescence correlation spectroscopy for studying structural properties of proteins in living cell. *Sci. Rep.* **6**, 31091 (2016).
95 Aragon, S. & Pecora, R. Fluorescence correlation spectroscopy and Brownian rotational diffusion. *Biopolymers: Original Research on Biomolecules* **14**, 119-137 (1975).
96 Loman, A., Gregor, I., Stutz, C., Mund, M. & Enderlein, J. Measuring rotational diffusion of macromolecules by fluorescence correlation spectroscopy. *Photochemical & photobiological sciences* **9**, 627-636 (2010).
97 Jain, R. & Sebastian, K. Diffusing diffusivity: Rotational diffusion in two and three dimensions. *The Journal of chemical physics* **146** (2017).
98 Debye, P. Polar Molecules, Dover, New York. (1929).

99 Grußmayer, K. S. & Herten, D.-P. Photon antibunching in single molecule fluorescence spectroscopy. *Advanced Photon Counting: Applications, Methods, Instrumentation*, 159-190 (2015).
100 Lamb, D., Muller, B. & Brauchle, C. Enhancing the sensitivity of fluorescence correlation spectroscopy by using time-correlated single photon counting. *Current pharmaceutical biotechnology* **6**, 405-414 (2005).
101 Müller, B. K., Zaychikov, E., Bräuchle, C. & Lamb, D. C. Pulsed interleaved excitation. *Biophysical journal* **89**, 3508-3522 (2005).
102 Schwille, P. Fluorescence correlation spectroscopy and its potential for intracellular applications. *Cell biochemistry and biophysics* **34**, 383-408 (2001).
103 Ackers, I. & Malgor, R. Interrelationship of canonical and non-canonical Wnt signalling pathways in chronic metabolic diseases. *Diabetes and Vascular Disease Research* **15**, 3-13 (2018).
104 Fernandez, A. *et al.* The WNT receptor FZD7 is required for maintenance of the pluripotent state in human embryonic stem cells. *Proceedings of the National Academy of Sciences* **111**, 1409-1414 (2014).
105 Rao, T. P. & Kühl, M. An updated overview on Wnt signaling pathways: a prelude for more. *Circulation research* **106**, 1798-1806 (2010).
106 Lorenowicz, M. J. & Korswagen, H. C. Sailing with the Wnt: charting the Wnt processing and secretion route. *Experimental cell research* **315**, 2683-2689 (2009).
107 Takada, S., Fujimori, S., Shinozuka, T., Takada, R. & Mii, Y. Differences in the secretion and transport of Wnt proteins. *The journal of biochemistry* **161**, 1-7 (2017).
108 Mii, Y. & Takada, S. Heparan sulfate proteoglycan clustering in Wnt signaling and dispersal. *Frontiers in Cell and Developmental Biology* **8**, 631 (2020).
109 Mii, Y. & Taira, M. Secreted Wnt "inhibitors" are not just inhibitors: Regulation of extracellular Wnt by secreted Frizzled-related proteins. *Development, growth & differentiation* **53**, 911-923 (2011).
110 Gorny, A.-K., Kaufmann, L. T., Swain, R. K. & Steinbeisser, H. A secreted splice variant of the Xenopus frizzled-4 receptor is a biphasic modulator of Wnt signalling. *Cell Communication and Signaling* **11**, 1-6 (2013).
111 Stanganello, E. & Scholpp, S. Role of cytonemes in Wnt transport. *Journal of cell science* **129**, 665-672 (2016).
112 Stetefeld, J., McKenna, S. A. & Patel, T. R. Dynamic light scattering: a practical guide and applications in biomedical sciences. *Biophysical reviews* **8**, 409-427 (2016).
113 Swinehart, D. F. The beer-lambert law. *Journal of chemical education* **39**, 333 (1962).
114 Gill, S. C. & Von Hippel, P. H. Calculation of protein extinction coefficients from amino acid sequence data. *Analytical biochemistry* **182**, 319-326 (1989).
115 Petrášek, Z. & Schwille, P. Precise measurement of diffusion coefficients using scanning fluorescence correlation spectroscopy. *Biophysical journal* **94**, 1437-1448 (2008).
116 Trullo, A., Corti, V., Arza, E., Caiolfa, V. R. & Zamai, M. Application limits and data correction in number of molecules and brightness analysis. *Microscopy research and technique* **76**, 1135-1146 (2013).
117 Hellriegel, C., Caiolfa, V. R., Corti, V., Sidenius, N. & Zamai, M. Number and brightness image analysis reveals ATF-induced dimerization kinetics of uPAR in the cell membrane. *The FASEB Journal* **25**, 2883 (2011).
118 DeLuca, M. A. & McElroy, W. D. *Bioluminescence and chemiluminescence: basic chemistry and analytical applications*. (Academic Press, 2013).
119 Topell, S., Hennecke, J. & Glockshuber, R. Circularly permuted variants of the green fluorescent protein. *FEBS letters* **457**, 283-289 (1999).

120 Ward, W. W. in *Green fluorescent protein: properties, applications, and protocols* 39-65 (John Wiley & Sons, 2005).
121 Khan, K., Rehman, S. U., Aziz, K., Fong, S. & Sarasvady, S. in *The fifth international conference on the applications of digital information and web technologies (ICADIWT 2014).* 232-238 (IEEE).
122 Schubert, E., Sander, J., Ester, M., Kriegel, H. P. & Xu, X. DBSCAN revisited, revisited: why and how you should (still) use DBSCAN. *ACM Transactions on Database Systems (TODS)* **42**, 1-21 (2017).
123 Pedregosa, F. *et al.* Scikit-learn: Machine learning in Python. *the Journal of machine Learning research* **12**, 2825-2830 (2011).
124 Nederveen-Schippers, L. M. *et al.* Combined fcs and pch analysis to quantify protein dimerization in living cells. *International Journal of Molecular Sciences* **22**, 7300 (2021).
125 Schatzel, K. Noise on photon correlation data. I. Autocorrelation functions. *Quantum Optics: Journal of the European Optical Society Part B* **2**, 287 (1990).
126 Sankaran, J., Shi, X., Ho, L. Y., Stelzer, E. H. & Wohland, T. ImFCS: a software for imaging FCS data analysis and visualization. *Optics express* **18**, 25468-25481 (2010).
127 Schätzel, K., Drewel, M. & Stimac, S. Photon correlation measurements at large lag times: improving statistical accuracy. *Journal of Modern Optics* **35**, 711-718 (1988).
128 Wahl, M., Gregor, I., Patting, M. & Enderlein, J. Fast calculation of fluorescence correlation data with asynchronous time-correlated single-photon counting. *Optics express* **11**, 3583-3591 (2003).
129 Magatti, D. & Ferri, F. Fast multi-tau real-time software correlator for dynamic light scattering. *Appl. Opt.* **40**, 4011-4021 (2001).
130 Leys, C., Ley, C., Klein, O., Bernard, P. & Licata, L. Detecting outliers: Do not use standard deviation around the mean, use absolute deviation around the median. *Journal of experimental social psychology* **49**, 764-766 (2013).
131 Huber, P. J. in *International Encyclopedia of Statistical Science* (ed M. Lovric) 1248-1251 (Springer Berlin Heidelberg, 2011).
132 Luz, M. *et al.* Dynamic association with donor cell filopodia and lipid-modification are essential features of Wnt8a during patterning of the zebrafish neuroectoderm. *PloS one* **9**, e84922 (2014).
133 Rhinn, M., Lun, K., Luz, M., Werner, M. & Brand, M. Positioning of the midbrain-hindbrain boundary organizer through global posteriorization of the neuroectoderm mediated by Wnt8 signaling. (2005).
134 Holzer, T. *et al.* Live imaging of active fluorophore labelled Wnt proteins. *FEBS letters* **586**, 1638-1644 (2012).
135 Wallkamm, V. *et al.* Live imaging of Xwnt5A-ROR2 complexes. *PloS one* **9**, e109428 (2014).
136 Mii, Y. *et al.* Quantitative analyses reveal extracellular dynamics of Wnt ligands in Xenopus embryos. *Elife* **10**, e55108 (2021).
137 Wesslowski, J. *et al.* eGFP-tagged Wnt-3a enables functional analysis of Wnt trafficking and signaling and kinetic assessment of Wnt binding to full-length Frizzled. *Journal of Biological Chemistry* **295**, 8759-8774 (2020).
138 Galli, L. M. *et al.* Direct visualization of the Wntless-induced redistribution of WNT1 in developing chick embryos. *Developmental biology* **439**, 53-64 (2018).
139 ASSA, T. Luciferase reporter assays: powerful, adaptable tools for cell biology research. *Cell Notes* **21** (2008).
140 Bartscherer, K. & Boutros, M. Regulation of Wnt protein secretion and its role in gradient formation. *EMBO reports* **9**, 977-982 (2008).

141 Zhang, L. & Wrana, J. L. The emerging role of exosomes in Wnt secretion and transport. *Current opinion in genetics & development* **27**, 14-19 (2014).
142 Demir, K. *et al.* RAB8B is required for activity and caveolar endocytosis of LRP6. *Cell Rep.* **4**, 1224-1234 (2013).
143 Sha, L., Ma, D. & Chen, C. Exosome-mediated Hic-5 regulates proliferation and apoptosis of osteosarcoma via Wnt/β-catenin signal pathway. *Aging (Albany NY)* **12**, 23598 (2020).
144 Ishitani, T. *et al.* The TAK1-NLK mitogen-activated protein kinase cascade functions in the Wnt-5a/Ca2+ pathway to antagonize Wnt/β-catenin signaling. *Molecular and cellular biology* **23**, 131-139 (2003).
145 Lai, K. K. *et al.* Convergence of canonical and non-canonical Wnt signal: differential Kat3 coactivator usage. *Current molecular pharmacology* **12**, 167-183 (2019).
146 Torres, M. A. *et al.* Activities of the Wnt-1 class of secreted signaling factors are antagonized by the Wnt-5A class and by a dominant negative cadherin in early Xenopus development. *The Journal of cell biology* **133**, 1123-1137 (1996).
147 Yuzugullu, H. *et al.* Canonical Wnt signaling is antagonized by noncanonical Wnt5a in hepatocellular carcinoma cells. *Molecular cancer* **8**, 1-20 (2009).
148 Gardiner, C. *et al.* Measurement of refractive index by nanoparticle tracking analysis reveals heterogeneity in extracellular vesicles. *Journal of extracellular vesicles* **3**, 25361 (2014).
149 Bhattacharjee, S. DLS and zeta potential–what they are and what they are not? *Journal of controlled release* **235**, 337-351 (2016).
150 Zhang, H. *et al.* Identification of distinct nanoparticles and subsets of extracellular vesicles by asymmetric flow field-flow fractionation. *Nature cell biology* **20**, 332-343 (2018).
151 Zhang, Q. *et al.* Supermeres are functional extracellular nanoparticles replete with disease biomarkers and therapeutic targets. *Nature cell biology* **23**, 1240-1254 (2021).
152 Cha, S.-W., Tadjuidje, E., Tao, Q., Wylie, C. & Heasman, J. Wnt5a and Wnt11 interact in a maternal Dkk1-regulated fashion to activate both canonical and non-canonical signaling in Xenopus axis formation. (2008).
153 Shen, Y., Chen, Y., Wu, J., Shaner, N. C. & Campbell, R. E. Engineering of mCherry variants with long Stokes shift, red-shifted fluorescence, and low cytotoxicity. *PLoS One* **12**, e0171257 (2017).
154 Bindels, D. S. *et al.* mScarlet: a bright monomeric red fluorescent protein for cellular imaging. *Nature methods* **14**, 53-56 (2017).
155 Prangsma, J. C. *et al.* Quantitative determination of dark chromophore population explains the apparent low quantum yield of red fluorescent proteins. *The Journal of Physical Chemistry B* **124**, 1383-1391 (2020).
156 Schubert, A. *et al.* WNT5a export onto extracellular vesicles studied at single-molecule and single-vesicle resolution. *The FEBS Journal* (2025) - *accepted*.
157 Wyss, R. *et al.* Molecular and dimensional profiling of highly purified extracellular vesicles by fluorescence fluctuation spectroscopy. *Analytical chemistry* **86**, 7229-7233 (2014).
158 Burrus, L. W. & McMahon, A. P. Biochemical analysis of murine Wnt proteins reveals both shared and distinct properties. *Experimental cell research* **220**, 363-373 (1995).
159 Hirai, H., Matoba, K., Mihara, E., Arimori, T. & Takagi, J. Crystal structure of a mammalian Wnt–frizzled complex. *Nature structural & molecular biology* **26**, 372-379 (2019).
160 Hu, Y.-B. *et al.* Exosomal Wnt-induced dedifferentiation of colorectal cancer cells contributes to chemotherapy resistance. *Oncogene* **38**, 1951-1965 (2019).

161 Haupts, U., Maiti, S., Schwille, P. & Webb, W. W. Dynamics of fluorescence fluctuations in green fluorescent protein observed by fluorescence correlation spectroscopy. *Proceedings of the National Academy of Sciences* **95**, 13573-13578 (1998).
162 Heikal, A. A., Hess, S. T., Baird, G. S., Tsien, R. Y. & Webb, W. W. Molecular spectroscopy and dynamics of intrinsically fluorescent proteins: coral red (dsRed) and yellow (Citrine). *Proceedings of the National Academy of Sciences* **97**, 11996-12001 (2000).
163 Schenk, A., Ivanchenko, S., Röcker, C., Wiedenmann, J. & Nienhaus, G. U. Photodynamics of red fluorescent proteins studied by fluorescence correlation spectroscopy. *Biophysical journal* **86**, 384-394 (2004).
164 Malvezzi-Campeggi, F., Jahnz, M., Heinze, K. G., Dittrich, P. & Schwille, P. Light-induced flickering of DsRed provides evidence for distinct and interconvertible fluorescent states. *Biophysical journal* **81**, 1776-1785 (2001).
165 Dickson, R. M., Cubitt, A. B., Tsien, R. Y. & Moerner, W. E. On/off blinking and switching behaviour of single molecules of green fluorescent protein. *Nature* **388**, 355-358 (1997).
166 Garcia-Parajo, M., Segers-Nolten, G. M., Veerman, J.-A., Greve, J. & Van Hulst, N. Real-time light-driven dynamics of the fluorescence emission in single green fluorescent protein molecules. *Proceedings of the National Academy of Sciences* **97**, 7237-7242 (2000).
167 Sadovsky, R. G., Brielle, S., Kaganovich, D. & England, J. L. Measurement of rapid protein diffusion in the cytoplasm by photo-converted intensity profile expansion. *Cell Rep.* **18**, 2795-2806 (2017).
168 Meseth, U., Wohland, T., Rigler, R. & Vogel, H. Resolution of fluorescence correlation measurements. *Biophysical journal* **76**, 1619-1631 (1999).
169 Swaminathan, R., Hoang, C. P. & Verkman, A. Photobleaching recovery and anisotropy decay of green fluorescent protein GFP-S65T in solution and cells: cytoplasmic viscosity probed by green fluorescent protein translational and rotational diffusion. *Biophysical journal* **72**, 1900-1907 (1997).
170 Corso, G. *et al.* Systematic characterization of extracellular vesicle sorting domains and quantification at the single molecule–single vesicle level by fluorescence correlation spectroscopy and single particle imaging. *Journal of extracellular vesicles* **8**, 1663043 (2019).
171 Fu, X. *et al.* High-throughput fluorescence correlation spectroscopy enables analysis of surface components of cell-derived vesicles. *Analytical and bioanalytical chemistry* **412**, 2589-2597 (2020).
172 Montis, C. *et al.* Size distribution of extracellular vesicles by optical correlation techniques. *Colloids and Surfaces B: Biointerfaces* **158**, 331-338 (2017).
173 Nordin, J. Z. *et al.* Ultrafiltration with size-exclusion liquid chromatography for high yield isolation of extracellular vesicles preserving intact biophysical and functional properties. *Nanomedicine: Nanotechnology, Biology and Medicine* **11**, 879-883 (2015).
174 Koynov, K. & Butt, H.-J. Fluorescence correlation spectroscopy in colloid and interface science. *Current Opinion in Colloid & Interface Science* **17**, 377-387 (2012).
175 Starchev, K., Zhang, J. & Buffle, J. Applications of fluorescence correlation spectroscopy—particle size effect. *Journal of colloid and interface science* **203**, 189-196 (1998).
176 Brennan, K. *et al.* A comparison of methods for the isolation and separation of extracellular vesicles from protein and lipid particles in human serum. *Sci. Rep.* **10**, 1039 (2020).

177 Dieplinger, H. & Dieplinger, B. Afamin—A pleiotropic glycoprotein involved in various disease states. *Clinica Chimica Acta* **446**, 105-110 (2015).
178 James, I. *et al.* FrzB-2: a human secreted frizzled-related protein with a potential role in chondrocyte apoptosis. *Osteoarthritis and Cartilage* **8**, 452-463 (2000).
179 Pera, E. M. & De Robertis, E. A direct screen for secreted proteins in Xenopus embryos identifies distinct activities for the Wnt antagonists Crescent and Frzb-1. *Mechanisms of development* **96**, 183-195 (2000).
180 Weissman, M., Schindler, H. & Feher, G. Determination of molecular weights by fluctuation spectroscopy: application to DNA. *Proceedings of the National Academy of Sciences* **73**, 2776-2780 (1976).
181 Berland, K. M., So, P. & Gratton, E. Two-photon fluorescence correlation spectroscopy: method and application to the intracellular environment. *Biophysical journal* **68**, 694-701 (1995).
182 Levi, V., Ruan, Q., Kis-Petikova, K. & Gratton, E. (Portland Press Ltd., 2003).
183 Willert, K. H. Isolation and application of bioactive Wnt proteins. *Wnt Signaling: Pathway Methods and Mammalian Models*, 17-29 (2008).
184 Tüysüz, N. *et al.* Lipid-mediated Wnt protein stabilization enables serum-free culture of human organ stem cells. *Nature communications* **8**, 14578 (2017).
185 Matera, R., Horvath, K. V., Nair, H., Schaefer, E. J. & Asztalos, B. F. HDL particle measurement: comparison of 5 methods. *Clinical Chemistry* **64**, 492-500 (2018).
186 López, C. A., de Vries, A. H. & Marrink, S. J. Molecular mechanism of cyclodextrin mediated cholesterol extraction. *PLoS computational biology* **7**, e1002020 (2011).
187 Abe, M. & Kobayashi, T. Imaging cholesterol depletion at the plasma membrane by methyl-β-cyclodextrin. *Journal of Lipid Research* **62** (2021).
188 Mahammad, S. & Parmryd, I. Cholesterol depletion using methyl-β-cyclodextrin. *Methods in membrane lipids*, 91-102 (2015).
189 Beseničar, M. P., Bavdek, A., Kladnik, A., Maček, P. & Anderluh, G. Kinetics of cholesterol extraction from lipid membranes by methyl-β-cyclodextrin—A surface plasmon resonance approach. *Biochimica et Biophysica Acta (BBA)-Biomembranes* **1778**, 175-184 (2008).
190 Sanchez, S. A., Gunther, G., Tricerri, M. A. & Gratton, E. Methyl-β-cyclodextrins preferentially remove cholesterol from the liquid disordered phase in giant unilamellar vesicles. *The Journal of membrane biology* **241**, 1-10 (2011).
191 Catapano, A. L., Pirillo, A., Bonacina, F. & Norata, G. D. HDL in innate and adaptive immunity. *Cardiovascular research* **103**, 372-383 (2014).
192 Kontush, A. *et al.* Structure of HDL: particle subclasses and molecular components. *High Density Lipoproteins: From Biological Understanding to Clinical Exploitation*, 3-51 (2015).
193 Landa, S. *et al.* Extracellular particles as carriers of cholesterol not associated with lipoproteins. *Membranes* **12**, 618 (2022).
194 Jarmoskaite, I., AlSadhan, I., Vaidyanathan, P. P. & Herschlag, D. How to measure and evaluate binding affinities. *Elife* **9**, e57264 (2020).
195 Kohler, J., Hur, K.-H. & Mueller, J. D. Autocorrelation function of finite-length data in fluorescence correlation spectroscopy. *Biophysical journal* **122**, 241-253 (2023).
196 Nickles, D., Falschlehner, C., Metzig, M. & Boutros, M. A genome-wide RNA interference screen identifies caspase 4 as a factor required for tumor necrosis factor alpha signaling. *Molecular and cellular biology* (2012).
197 Patterson, G. H., Knobel, S. M., Sharif, W. D., Kain, S. R. & Piston, D. W. Use of the green fluorescent protein and its mutants in quantitative fluorescence microscopy. *Biophysical Journal* **73**, 2782-2790 (1997).

198 Costantini, L. M. *et al.* A palette of fluorescent proteins optimized for diverse cellular environments. *Nature communications* **6**, 7670 (2015).
199 Shaner, N. C. *et al.* Improved monomeric red, orange and yellow fluorescent proteins derived from Discosoma sp. red fluorescent protein. *Nature biotechnology* **22**, 1567-1572 (2004).
200 Mukherjee, S. *et al.* Directed evolution of a bright variant of mCherry: suppression of nonradiative decay by fluorescence lifetime selections. *The Journal of Physical Chemistry B* **126**, 4659-4668 (2022).

Appendix A

Supporting Information for Chapter 3: Materials and Methods

A.1 Materials and Equipment

Table A.1. List of Chemicals

Chemical	Abbreviation	Company	Detail
Alexa Fluor 546		Thermo Fisher Scientific, Waltham, MA	
CoraLite Plus 488-conjugated Apolipoprotein AI antibody	AB-CoraLite 488	Proteintech/Thermo Fisher Scientific	monoclonal
Dulbecco's modified Eagle medium	DMEM	Thermo Fisher Scientific	
Dulbecco's Phosphate-Buffered Saline	DPBS	Gibco/BRL, Grand Island, NY, USA	No calcium, no magnesium
Exosome-depleted fetal bovine serum	Exo-depleted FBS	Thermo Fisher Scientific	
Fetal bovine serum	FBS	Thermo Fisher Scientific	
Geneticin G418	G418	Merck, Germany	
Methyl-β-cyclodextrin	MβCD	Sigma-Aldrich, St Louis, MO	C4555
Nano-Glo Dual Luciferase Reporter Assay system		Promega, Madison, WI	N1610
Recombinant mouse Wnt3a	rc mWnt3a	PeproTech, Germany	315-20
Recombinant WNT3a	rc WNT3a	R&D system, Minneapolis, MN	5036-WN/CF
RFP-catcher		Antibodies-online, Germany	ABIN5311510
Roswell Park Memorial Institute 1640 medium	RMPI-1640	Thermo Fisher Scientific	
Sodium pyruvate	SP	Thermo Fisher Scientific	
TransIT LT1 transfection reagent		Mirus Bio, Madison, WI	
Xfect™ protein transfection reagent	Xfect	Takara Bio, Japan	

Table A.2. List of Plasmids

Plasmid	Details	Source
pcDNA	pcDNA3.2/V5-DEST	Invitrogen, Carlsbad, CA
mScarlet-WNT5a	pcDNA WNT5a LONG-mScarlet	A. Schubert (Boutros laboratory, Universität Heidelberg)
Renilla luciferase	pAct-RL, Renilla luciferase	D. Nickels (Boutros laboratory, Universität Heidelberg) [196]
Flyfire lucifease	pGL4.54[luc2P/TK], E506A	Promega
mCherry2	mCherry2-N1, #54517	Addgene, Cambridge, MA
mScarlet	pmScarlet_C1, #85042	Addgene
TCF4/WNT firefly luciferase	6xKD; pGL4.26 6xTcf-Firefly luciferase	K. Demir (Boutros laboratory, Universität Heidelberg) [142]
TCF/WNT NanoLuc luciferase	pNL[NLucP/TCF/LEF-RE/Hygro], #CS181801	Promega
WNT3a	pcDNA-WNT5a, #35908	Addgene
WNT5a	pcDNA-WNT5a, #35911	Addgene
WNT11	pcDNA-WNT11, #35922	Addgene

Table A.3. List of Materials

Material	Company	Detail
8-well chambered cover glass with #1 high performance cover glass	Nunc, Rochester, NY, USA	
96-well plate	Greiner, Germany	White, flat bottom, polystyrene
384-well plate	Greiner, Germany	Flat-bottom polystyrene plate
Coverslips, 18 × 18 mm^2	Hirschmann Laborgeräte, Germany	
Exo-spin mini size-exclusion column	Cell Guidance System, UK	EX03
Nanosep device	Pall, Ann Arbor, MI, USA	Omega membrane, 300 kDa MWCO
Open-top thinwall ultra-clear centrifuge tubes	Beckman Coulter, Fullerton, CA, USA	Cat # 344058
Polycarbonate ultracentrifugation tubes	Beckman Coulter	Cat # 355631
Polystyrene beads, 200 nm	Polysciences Inc, Warrington, PA, USA	Cat # 19402-15
Vivaspin 20 centrifugal device	Cytiva, Marlborough, MA	Polyethersulfone membrane, 50 kDa MWCO

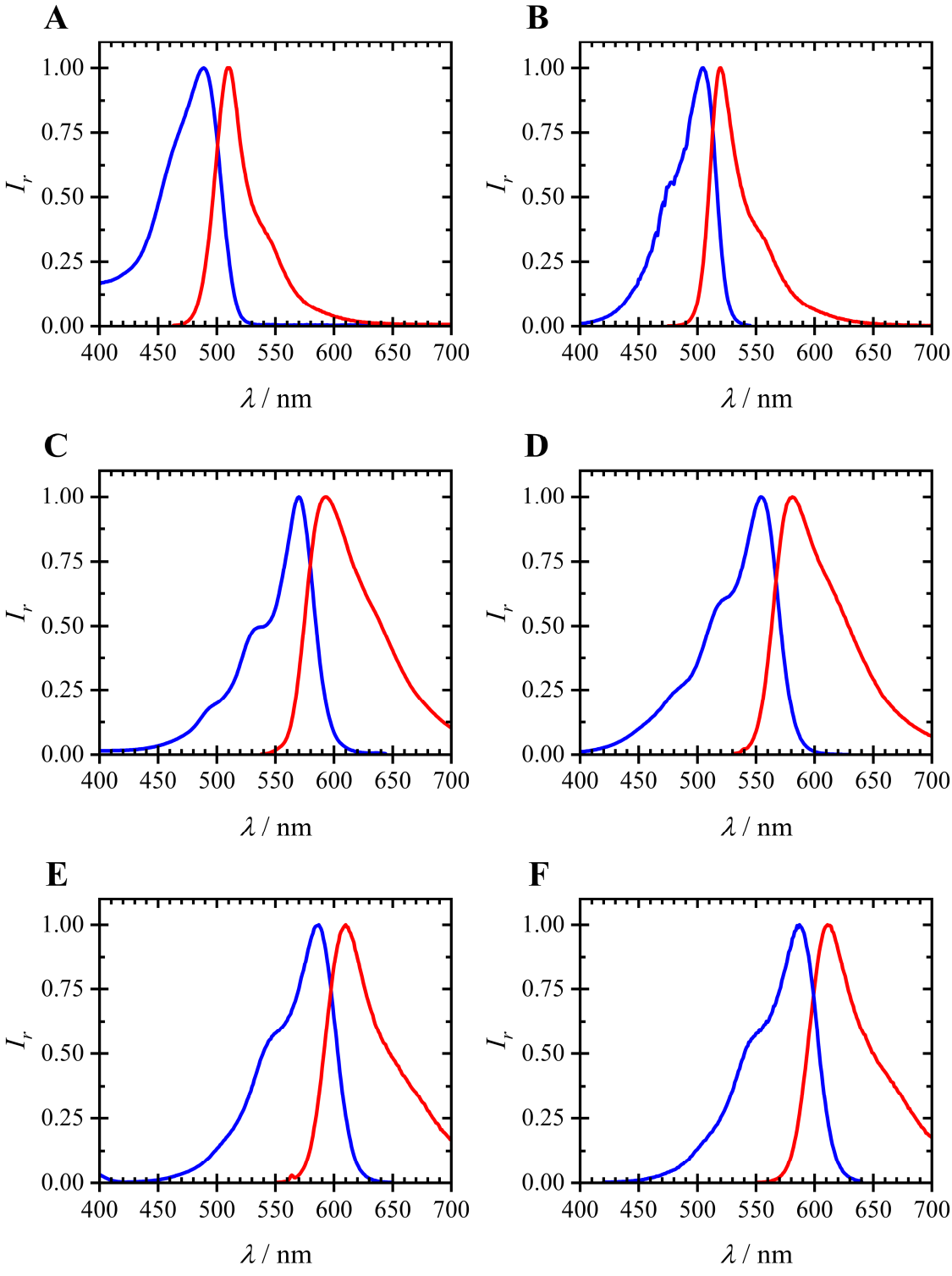

Figure A.1. Excitation and Emission Spectra of Fluorescent Proteins Used in This Research. Each graph displays the excitation (blue) and emission (red) spectra of eGFP[55] (A), moxNeonGreen (B), mScarlet[55] (C), tdTomato[55] (D), mCherry[55] (E), and mCherry2 (F). Lines: Intensity normalized at the maximum excitation/emission (I_r). The spectra of moxNeonGreen and mCherry2 were measured using the Fluorolog-3 spectrofluorometer.

Table A.4. List and Characteristics of Fluorescent Proteins Used in this Research. Unless specific citations are given, the information was obtained from Reference [55].

Fluorescent Protein	λ_{ex} / nm	λ_{em} / nm	$\varepsilon_{\lambda_{ex}}$ / mol^{-1} cm^{-1}	Φ_F	Brightness (×10^3) / mol^{-1} cm^{-1}	Lifetime / ns	M_M / kDa
eGFP	488	507	55,300 [197]	0.60 [197]	33.2	2.6	26.9
moxNeonGreen	505	520	111,000 [198]	0.74 [198]	82.1	-	26.6
mCherry	587	610	72,000 [199]	0.22 [199]	15.8	1.4	26.7
mCherry2	589	610	79,400 [153]	0.22 [153]	17.5	-	26.7
mScarlet	569	594	100,000 [154]	0.70 [154]	70	3.9	26.4
tdTomato	554	581	138,000 [199]	0.69 [199]	95.2	-	54.2

Table A.5. List of Equipment

Equipment	Detail	Company
In the M2 Microscope		
470 nm laser	LDH-P-C-470B	PicoQuant, Germany
561 nm laser	gem 561	Laser Quantum, Germany
APD	COUNT-T100	Laser Components, Germany
CO_2 mixing system	CO_2 Gas Controller Systems	MicroscopeHeaters.com, UK
Galvo scanner	Yanus IV	TILL Photonics, Germany
Incubation chamber	Custom-built	-
Inverted epi-fluorescence microscope	DMi8	Leica Microsystems, Germany
Objective	Water immersion, HCX PL APO W CORR CS2 63x/1.2	Leica Microsystems, Germany
Piezo scanner	M-122	Physik Instrumente, Germany
Quad-band dichroic beamsplitter	R405/488/561/635 lambda/5	AHF Analysentechnik, Germany
Time-correlated single photon counting card	SPC-150	Becker & Hickl, Germany
In the MicroTime 200 Microscope		
485 nm laser	LDH-D-C-485	PicoQuant
560 nm laser	LDH-D-TA-560B	PicoQuant
λ/2 wave plate	400 – 800 nm ACHROMATIC	Thorlabs, Newton, NJ
λ/4 wave plate	450 – 800 nm ACHROMATIC	Thorlabs
APD	SPCM-AQR-13	Perkin Elmer, Germany
CO_2 mixing system	CO_2 O_2 unit BL-CP2	Okolab, Italy
Galvo scanner	FLIMbee	PicoQuant
Incubation chamber	H301-T-UNIT-BL-PLUS	Okolab
Inverted epi-fluorescence microscope	Olympus IX73	Olympus, Japan
MicroTime 200 microscopy system		PicoQuant, Germany
Objective	Water immersion, UPLSAPO 60XW	Olympus
Polarizer	WP25M-VIS	Thorlabs
Polarizing beam splitter	PBS201	Thorlabs

Equipment	Detail	Company
Quad-band dichroic beamsplitter	ZT405/488/561/640rpc, Chroma	
Time-correlated single photon counting card	HydraHarp 400	PicoQuant
Optics		
Bandpass filter	525/50 nm (center/width) Brightline HC	AHF Analysentechnik
Bandpass filter	600/37 nm (center/width) Brightline HC	AHF Analysentechnik
Bandpass filter	609/62 nm (center/width) Brightline HC	AHF Analysentechnik
Others		
Cary-100 spectrophotometer		Agilent Technologies, Santa Clara, CA
Cuvette	Article # 105 – 251 – 15 – 40, Light path 3 mm, Center 15 mm	Hellma Analytics, Germany
Fluorolog-3 spectrofluorometer		HORIBA Jobin Yvon, Edison, NJ
Glo Max navigator system	GM2010	Promega
Optima L80M ultracentrifuge		Beckman Coulter
Optima L90K ultracentrifuge		Beckman Coulter
Mithras reader LB940		Berthold Technologies, Germany
SW28 ultracentrifuge rotor	#14011783	Beckman Coulter
SW32Ti ultracentrifuge rotor	#369650	Beckman Coulter
Vivaspin 20 centrifugal device	Polyethersulfone membrane, 50 kDa MWCO	Cytiva, Marlborough, MA, USA
Zetasizer Nano-ZS instrument		Malvern Instruments, UK

A.2 Protocols for Cell Culture and Sample Preparation

A.2.1 Cell Handling

Cell Culture

Human embryonic kidney HEK293T cells, except those stably expressing mScarlet-WNT5a, were maintained in DMEM (without phenol red) with 10% FBS and 1% SP. HEK293T cells expressing mScarlet-WNT5a were cultured in DMEM supplemented with 10% FBS. Human

lung cancer NCI-H1703 cells were maintained in RMPI-1640 medium supplemented with 1% sodium pyruvate and 10% FBS. The cells were all kept at 37°C and 5% CO_2.

Transfection

Transfections were carried out using Xfect™ Protein Transfection Reagent following the manufacturer's instructions. Unless stated otherwise, cells were transfected 1–3 h after cell seeding.

Stable Cell Line Maintenance

The expression levels of mCherry2/mScarlet-WNT3a/5a/11 in HEK293T cells were evaluated weekly by measuring the emission intensity. If the proportion of cells expressing fluorescence was below 80%, G418 was administered to the cells. To minimize the impact of G418 on the conditioned medium, cells were allowed to grow for at least one generation post G418 treatment before collecting the conditioned medium.

Sample Storage

All samples were stored at 4°C for maximum of 30 d in total. For longer storage, they were kept at –20°C or –80°C.

A.2.2 Sample Preparation for Fluorescence Microscopy Measurements

The wells of an 8-well chambered cover glass with #1 high performance cover glass were incubated with 200 µL of 10 mg/ml (0.15 mM) BSA for at least 1 h before being rinsed five times with DPBS or buffer (40 mM Na-phosphate, 300 mM NaCl, pH 7.4). Then, 100 – 200 µL of sample solution were added to each pre-treated well. Each pre-treated well received 100–200 µL of sample solution.

To accommodate samples of small volume, a sample holder was constructed using two coverslips (18 × 18 mm^2), with an 0.8-mm thick aluminum washer (with a 12 mm interior diameter) separating them. Prior to incubation with BSA, the coverslips were briefly torched to eliminate fluorescent impurities. 20-30 µl of sample solution was inserted between two coverslips.

A.2.3 Extraction of mScarlet-WNT3a by RFP-Catcher

50 µl of RFP-catcher was added to 35 ml of the non-EV fraction of conditioned medium gathered from cells expressing mScarlet-WNT3a. The mixture was incubated overnight before being centrifuged at 1,000 × g for 1 min to pellet the agarose resin.

A.3 Functionality Tests via Dual-Luciferase Reporter Assay

A.3.1 Qualitative Functionality Tests for mCherry2-WNT3a/5a/11 and mScarlet-WNT3a/11

NCI-H1703 cells were seeded at a density of 150,000 cells per well into 96-well plates and maintained in RPMI supplemented with 10% FBS. After a 7-h incubation period, cells were co-transfected with 250 ng of the NLucP/TCF/LEF-RE/Hygro vector and 100 ng of the pGL4.54 control Firefly Luciferase vector using Xfect, following the manufacturer's protocol. Following a 24-h incubation period, the cell culture medium was replaced with mScarlet/mCherry2-WNT3A conditioned medium, mCherry2-WNT5A conditioned medium, mScarlet/mCherry2-WNT11 conditioned medium, control (pcDNA) conditioned medium and/or rc WNT dissolved in1 mg/ml (15 nM) BSA. The ability of WNT5a and WNT11 to inhibit canonical Wnt signaling induced by 100 ng/ml rc WNT3A was evaluated. After 14 h, cell lysates were collected using the Nano-Glo® Luciferase Assay System. Bioluciferase readout was performed on the cell lysates using the Glo Max Navigator System.

A.3.2 Qualitative Functionality Test for mScarlet-WNT5a

7,500 HEK293T cells were seeded in DMEM with 10% FBS into each well of a 384-well plate. After 24 h, cells were transfected with 20 ng of TCF4/WNT firefly luciferase reporter and 10 ng of control actin-Renilla luciferase reporter. Concurrently, cells were transfected with 20 ng of the respective WNT or control (pcDNA) plasmids using the TransIT LT1 Transfection Reagent. 24 h post-transfection, canonical Wnt signaling was induced by adding rc mouse WNT3a at a concentration of 100 ng/ml. Luminescence was measured 16 h later using the Mithras reader LB940.

A.3.3 Comparison of Canonical Wnt Signaling Activities Induced by mCherry2-WNT3a in Non-EV, Small-EV, and Large-EV Fractions

The concentrations of mCherry2-WNT3a in the non-EV, small-EV, and large-EV fractions isolated from conditioned medium from HEK293T cells expressing mCherry2-WNT3a were determined based on their emission spectra (Section 3.3.4). All samples were diluted to a final (mature) mCherry2 concentration of 2.5 nM. Equivalent control samples were prepared from HEK293T cells transfected with pcDNA, diluted using the average dilution factor of mCherry2-WNT3a samples.

NCI-H1703 cells in RPMI with 10% FBS were seeded into a 96-well plate (150,000 cells/well). After 7 h, cells were co-transfected with 250 ng of NLucP/TCF/LEF-RE/Hygro vector and 100 ng of pGL4.54 control Firefly Luciferase vector using Xfect. Following a 24-h incubation, the cell culture medium in each well was replaced with non/EV, small-EV, or large-EV samples. After an additional 14-h incubation, cell lysates were collected using the Nano-Glo® Luciferase Assay System. Bioluciferase readout was performed using the Glo Max Navigator System.

A.4 Number of Measurements and Samples

Table A.6. Number of Samples Used in the Qualitative Functionality Test of mCherry2/mScarlet-WNT Proteins via Dual-Luciferase Reporter Assays

Sample type	# samples	# wells / sample	Note
Functionality Test for mCherry2/mScarlet-WNT5a			
mCherry2-WNT3a	3	3	
mScarlet-WNT3a	3	3	
Control (pcDNA)	3	3	
Functionality Test for mCherry2-WNT5a, mCherry2/mScarlet-WNT11			
mCherry2-WNT5a	3	3	+ rc WNT3a
mCherry2-WNT11	3	3	+ rc WNT3a
mScarlet-WNT11	3	3	+ rc WNT3a
Control (pcDNA)	3	3	
Control (pcDNA)	3	3	+ rc WNT3a
Functionality Test for mScarlet-WNT5a			
mScarlet-WNT5a	3	1	+ rc mWnt3a
Control (pcDNA)	3	1	
Control (pcDNA)	3	1	+ rc mWnt3a

Table A.7. Number of Measurements and Samples Used for Determining the Radius Distributions of Particles in Non-EV, Small-EV, and Large-EV Fractions via Dynamic Light Scattering

Sample Type	Fraction	# Samples	# Measurements / Sample
mCherry2-WNT3a	Non-EV	4	10
mScarlet-WNT3a	Small-EV	5	10
mScarlet-WNT3a	Large-EV	3	10
mCherry2-WNT5a	Non-EV	4	10
mScarlet-WNT5a	Small-EV	3	10
mScarlet-WNT5a	Large-EV	3	5–10
mCherry2-WNT11	Non-EV	4	10
mScarlet-WNT11	Small-EV	5	10
mScarlet-WNT11	Large-EV	3	10
Control (pcDNA)	Non-EV	4	10
Control (pcDNA)	Small-EV	3	10
Control (pcDNA)	Large-EV	3	10

Table A.8. Number of Measurements and Samples Used for Determining the Relative mCherry2/mScarlet-Wnt Concentrations in Non-EV, Small-EV, and Large-EV Fractions

Sample Type	# Conditioned Medium Samples	# Measurements / Sample
mCherry2-WNT3a	3	1
mScarlet-WNT3a	3	1
mCherry2-WNT5a	3	1
mScarlet-WNT5a	3	1
mCherry2-WNT11	4	1
mScarlet-WNT11	3	1
Control (pcDNA) with Phenol Red	3	1
Control (pcDNA) without Phenol Red	3	1

Table A.9. Number of Samples Used for Comparing the Canonical Wnt Signaling Activities Induced by mCherry2-WNT3a in Non-EV, Small-EV, and Large-EV Fractions Using Dual-Luciferase Reporter Assays

Sample Type	Fraction	# Samples	# Wells / Sample
mCherry2-WNT3a	Non-EV	4	1
	Small-EV	4	1
	Large-EV	4	1
Control (pcDNA)	Non-EV	4	1
	Small-EV	4	1
	Large-EV	4	1

Table A.10. Number of Cells Used for Determining the Maturation Efficiencies of mCherry2 and mScarlet Expressed in Cytosol

Fluorescent Protein	# Cell Generations	# Cells Measured		
		Monomeric	Dimeric	Trimeric
mCherry2	4	55	52	-
mScarlet	3	40	49	69

Table A.11. Number of Measurements and Samples Used for Determining the Maturation Efficiencies of mCherry2 and mScarlet Purified from E. coli Using the Base-Denaturation Approach

Fluorescent Protein	# Stock Solution	# Dilution Samples		# Measurements / Sample
		pH 7.4	pH 13	
eGFP	1	4	3	1
moxNeonGreen	1	4	4	1
mCherry	1	4	4	1
mCherry2	1	4	4	1
mScarlet	1	4	4	1

Table A.12. Number of Measurements and Samples Used to Determine the Molecular Brightness of EVs Carrying mScarlet-WNT

Sample type	Fraction	# Samples	# Measurements / Sample
mScarlet-WNT3a	Small EVs	6	6–8
	Large EVs	4	5
mScarlet-WNT5a	Small EVs	4	12–15
	Large EVs	3	5
mScarlet	-	4	3
Background, 0.7 kW cm^{-2}	-	7	1
Background, 1.4 kW cm^{-2}	-	10	1–2

Table A.13. Number of Measurements and Samples Used to Determine the Hydrodynamic Radii of Non-EV-Bound mCherry2-WNT3a/5a/11 Units via Translational Diffusion

Sample Type	# Samples	# Measurements / Sample		
		0.65 kW cm^{-2} (100 s / Measurement)	**1.30 kW cm^{-2}** (50 s / Measurement)	**1.95 kW cm^{-2}** (50 s / Measurement)
mCherry2-WNT3a	6	18	18	12
mCherry2-WNT5a	3	18	18	12
mCherry2-WNT11	3	18	18	12
mCherry2	3	18	18	12

Table A.14. Number of Samples Used to Characterize the Rotational Brownian Motion of Non-EV-Bound mCherry2-WNT3a/5a/11 Units

Sample Type	# Samples
mCherry2-WNT3a	3
mCherry2-WNT5a	4
mCherry2-WNT11	4
mCherry2	4

Table A.15. Number of Samples Used to Determine the Hydrodynamic Radii of Small and Large EVs Transporting mScarlet-WNT3a/5a/11

Sample Type	Fraction	# Samples
mScarlet-WNT3a	Small-EV	6
	Large-EV	4
mScarlet-WNT5a	Small-EV	4
	Large-EV	3

Table A.16. Number of Samples and Measurements Used to Investigate the Effect of MβCD on the Diffusion Coefficients of Non-EV-Bound mCherry2-WNT3a/5a/11

Sample Type	# Samples	# Measurements / Sample	Measurement Time per Sample / min		
			40 mM MβCD	10 mM MβCD	DPBS
mCherry2-WNT3a	4	1	120	120	60
mCherry2-WNT5a	4	1	120	120	60
mCherry2-WNT11	4	1	120	120	60
mCherry2	4	1	60	60	60

Table A.17. Number of Samples and Measurements Used in Dual-Color Fluorescence Cross-Correlation Spectroscopy Measurements of Non-EV-Bound mCherry2-WNT3a/5a/11 Incubated with AB-CoraLite 488

Sample Type	# Samples	# Measurements
mCherry2-WNT3a	3	1
mCherry2-WNT5a	3	1
mCherry2-WNT11	3	1
mCherry2	3	1

Table A.18. Number of Samples and Measurements Used in Dual-Color Fluorescence Cross-Correlation Spectroscopy Measurements of WNT3a Proteins Co-Diffusing with AFAMIN

Sample Type	# Samples	# Measurements
mCherry2-WNT3a	3	1
mCherry2	3	1

Appendix B

Supporting Information for Chapter 4: General Characterization of WNT Proteins Secreted Externally by Living Cells

Table B.1. Results of Individual Samples from Qualitative Functionality Tests Conducted Using Dual-Luciferase Reporter Assays

Sample Type	Activity			
	Sample 1	Sample 2	Sample 3	Mean
Functionality Test for mCherry2/mScarlet-WNT3a				
mCherry2-WNT3a	21.4 ± 5.0	23.5 ± 3.5	15.5 ± 2.0	20.2 ± 2.4
mScarlet-WNT3a	6.0 ± 0.7	6.3 ± 0.4	5.2 ± 1.0	5.8 ± 0.3
Control (pcDNA)	0.7 ± 0.1	1.9 ± 1.0	0.6 ± 0.1	1.1 ± 0.4
Functionality Test for mCherry2-WNT5a, mCherry2/mScarlet-WNT11				
mCherry2-WNT5a + rc WNT3a	13.0 ± 0.1	8.2 ± 0.1	9.6 ± 0.1	10.2 ± 1.4
mCherry2-WNT11 + rc WNT 3a	12.4 ± 0.1	9.7 ± 0.1	6.6 ± 0.1	9.6 ± 1.7
mScarlet-WNT11 + rc WNT3a	14.2 ± 0.1	9.3 ± 0.1	7.4 ± 0.1	10.3 ± 2.0
Control (pcDNA)	1.4 ± 0.1	0.8 ± 0.1	0.6 ± 0.1	0.9 ± 0.2
Control (pcDNA) + rc WNT3a	29.3 ± 0.3	29.7 ± 1.0	35.4 ± 1.2	31.5 ± 2.0
Functionality Test for mScarlet-WNT5a				
mScarlet-WNT5a + rc mWnt3a	2.3 ± 0.5	9.1 ± 1.8	7.2 ± 1.4	5.6 ± 1.4
Control (pcDNA)	7.4 ± 1.5	6.6 ± 1.3	3.0 ± 0.6	6.2 ± 2.0
Control (pcDNA) + rc mWnt3a	24.4 ± 4.9	25.3 ± 5.1	31.8 ± 6.4	27.2 ± 2.3

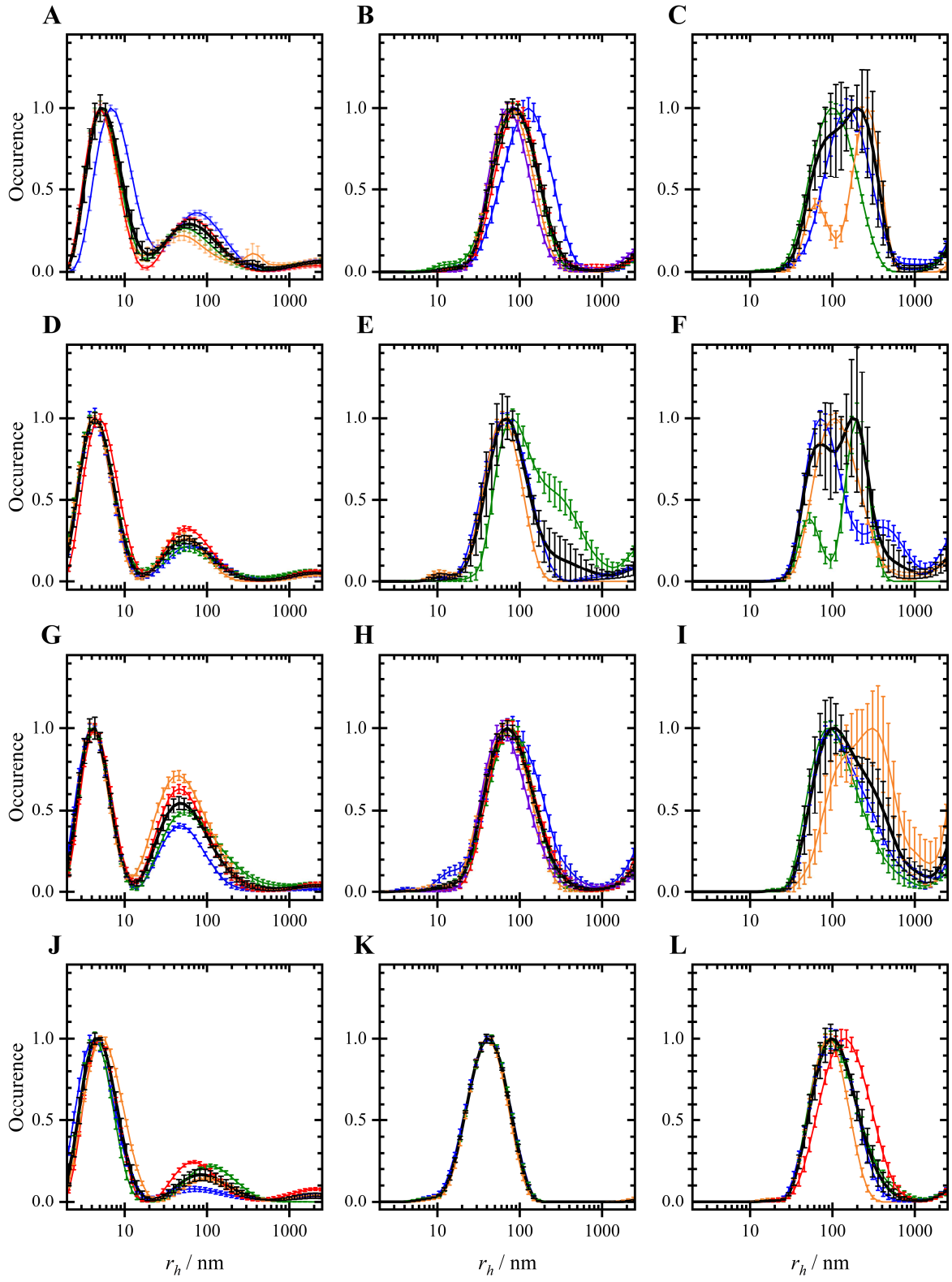

Figure B.1. Results of Individual Samples from Radius (r_h) Distributions of Particles in Non-EV, Small-EV, and Large-EV Fractions Determined Using Dynamic Light Scattering

Left column: Non-EV fraction; Middle column: Small-EV fraction; Right column: Large-EV fraction

A–C: WNT3a; D–F: WNT5a; G–I: WNT11; J–L: Control (pcDNA)

Table B.2. Results of Individual Samples from Relative mCherry2/mScarlet-Wnt Concentrations in Non-EV, Small-EV, and Large-EV Fractions. The values reported are the mean ± *SEM*. The values in the 'Mean' row are calculated using 1/*SEM* as the weight.

Sample Type	Sample	Percentage		
		Non-EV	Small EV	Large EV
mCherry2-WNT3a	1	95.2 ± 0.7%	4.7 ± 0.2%	0.2 ± 0.1%
	2	96.8 ± 0.6%	3.0 ± 0.1%	0.2 ± 0.1%
	3	94.9 ± 0.7%	4.9 ± 0.2%	0.2 ± 0.1%
	Mean	95.5 ± 0.6%	4.3 ± 0.6%	0.2 ± 0.1%
mScarlet-WNT3a	1	97.7 ± 0.5%	2.1 ± 0.1%	0.2 ± 0.1%
	2	97.9 ± 0.5%	1.9 ± 0.1%	0.2 ± 0.1%
	3	98.8 ± 0.4%	1.0 ± 0.1%	0.2 ± 0.1%
	Mean	98.3 ± 0.3%	1.6 ± 0.2%	0.1 ± 0.1%
mCherry2-WNT5a	1	97.6 ± 0.5%	2.2 ± 0.1%	0.2 ± 0.1%
	2	96.7 ± 0.6%	3.2 ± 0.1%	0.1 ± 0.1%
	3	97.4 ± 0.5%	2.0 ± 0.1%	0.2 ± 0.1%
	Mean	97.3 ± 0.9%	2.0 ± 0.9%	0.7 ± 0.4%
mScarlet-WNT5a	1	93.6 ± 4.3%	5.7 ± 3.8%	0.8 ± 0.5%
	2	94.6 ± 3.4%	4.1 ± 2.8%	1.3 ± 0.9%
	3	97.9 ± 1.5%	1.2 ± 0.9%	0.9 ± 0.6%
	Mean	95.3 ± 3.2%	3.7 ± 2.5%	1.0 ± 0.7%
mScarlet-WNT11	1	97.3 ± 0.5%	1.8 ± 0.1%	0.8 ± 0.1%
	2	96.9 ± 0.5%	1.1 ± 0.1%	2.0 ± 0.1%
	3	97.0 ± 0.5%	1.3 ± 0.1%	1.7 ± 0.1%
	Mean	97.7 ± 0.3%	1.2 ± 0.2%	1.1 ± 0.3%

Table B.3. Results of Individual Samples from the Comparison of Canonical Wnt Signaling Activities Induced by mCherry2-WNT3a in Non-EV, Small-EV, and Large-EV Fractions Using Dual-Luciferase Reporter Assays

Sample type	Fraction	Activity				
		Sample 1	Sample 2	Sample 3	Sample 4	Mean ± *SEM*
mCherry2-WNT3a	Non-EV	39.1	23.0	16.0	33.9	28 ± 5
	Small-EV	58.8	(36.4)*	60.7	66.0	62 ± 2
	Large-EV	34.2	(71.9)*	44.4	33.2	37 ± 4
Control (pcDNA)	Non-EV	0.6	0.9	0.7	0.7	0.7 ± 0.1
	Small-EV	0.5	0.7	0.9	0.6	0.7 ± 0.1
	Large-EV	0.5	0.7	0.5	0.4	0.5 ± 0.1

* Outlier (further from the median more than 3 *scaled MAD*)

Appendix C

Supporting Information for Chapter 5: Determination of Wnt Protein Numbers per Particle

C.1 Additional Analysis and Results on the Apparent Fluorescence Probability of mCherry2 and mScarlet Expressed in the Cytosol of Living Cells

Table C.1. Background and Monomeric Reference Molecular Brightness Values Used in the Individual Analysis Determined by N&B Analysis

Measurement date	I_{BG} / Hz	$\langle \varepsilon_1 \rangle$ / Hz
mCherry2		
23.07.2022	456	370
24.07.2022	456*	485
28.07.2022	511	513
29.07.2022	517	408
mScarlet		
18.02.2022	590	557
19.02.2022	513	626
03.04.2022	463	398

* The background intensity was determined using the value measured on 23.07.2022, as the microscope was operated overnight without any changes to its alignment.

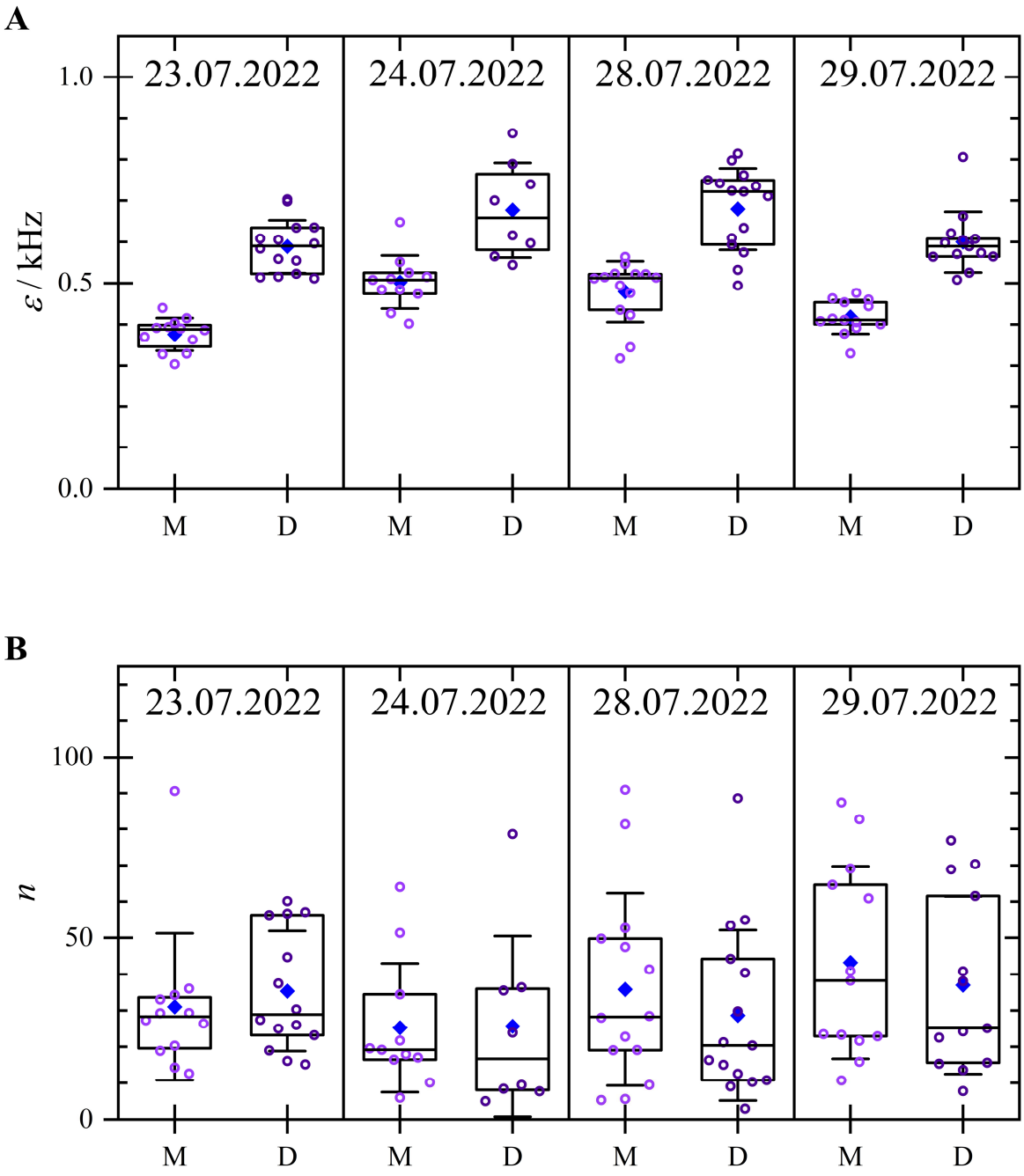

Figure C.1. Molecular Brightness (ε) and Particle Number (n) of Oligomeric mCherry2, Categorized by Measurement Date. On the horizontal axis, M and D denote monomer and dimer, respectively. Each data point represents a single measurement. Boxes represent data points within the 25th to 75th percentile range, blue diamonds: mean, middle line: median, and whisker: *SD*.

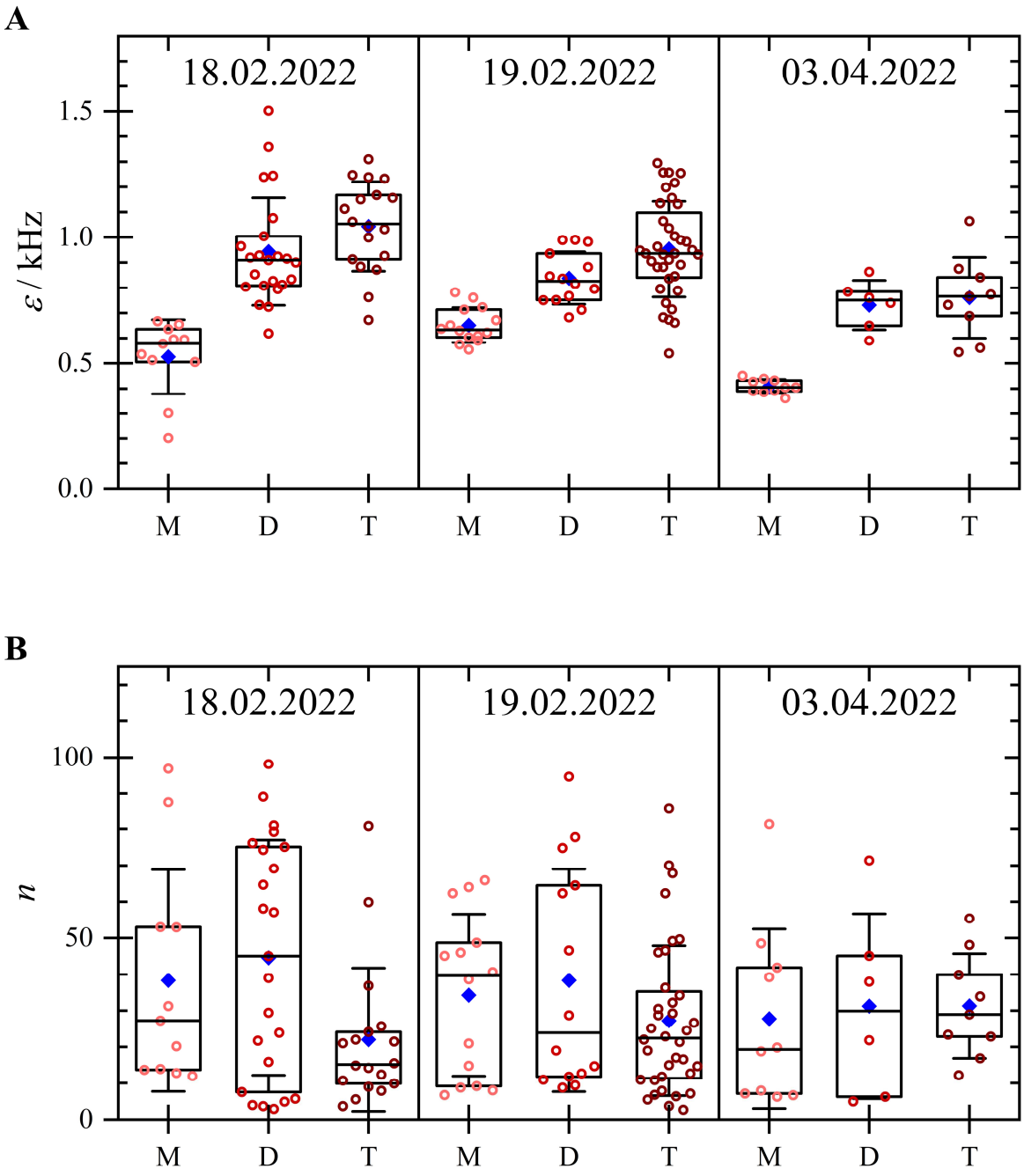

Figure C.2. Molecular Brightness (ε) and Particle Number (n) of Oligomeric mScarlet, Categorized by Measurement Date. On the horizontal axis, M, D, and T denote monomer, dimer, and trimer, respectively. Each data point represents a single measurement. Boxes represent data points within the 25th to 75th percentile range, blue diamonds: mean, middle line: median, and whisker: *SD*.

Table C.2. Comparison of Molecular Brightness and Apparent Fluorescence Probability: Full Dataset versus Data with $n > 100$. The number of data points is indicated by '# data points.' The values of ε_r and p_f are reported as median ± *MAD*.

Oligomer	All Data			Data Excluding Points where $n > 100$		
	# Data Points	ε_r	p_f / %	# Data Points	ε_r	p_f / %
mCherry2						
Monomer	55	1.00 ± 0.07	44 ± 15	47	1.00 ± 0.05	43 ± 11
Dimer	52	1.44 ± 0.14		49	1.43 ± 0.11	
mScarlet						
Monomer	40	1.00 ± 0.08	47 ± 18	33	1.00 ± 0.07	48 ± 15
Dimer	49	1.47 ± 0.18		41	1.48 ± 0.14	
Trimer	69	1.63 ± 0.27		63	**8.58 0.25**	

C.2 Maturation Efficiencies of Fluorescent Proteins Determined by the Base-Denaturation Approach

The maturation efficiencies of eGFP, moxNeonGreen, and mCherry purified from *E. Coli* were evaluated following the procedure outlines in Section 3.6. The emission spectra obtained from these fluorescent proteins are displayed in Figure E.1. The determined maturation efficiencies for eGFP, moxNeonGreen, and mCherry are 73 ± 2%, 57 ± 5%, and 31 ± 1% (mean ± *SD*), respectively.

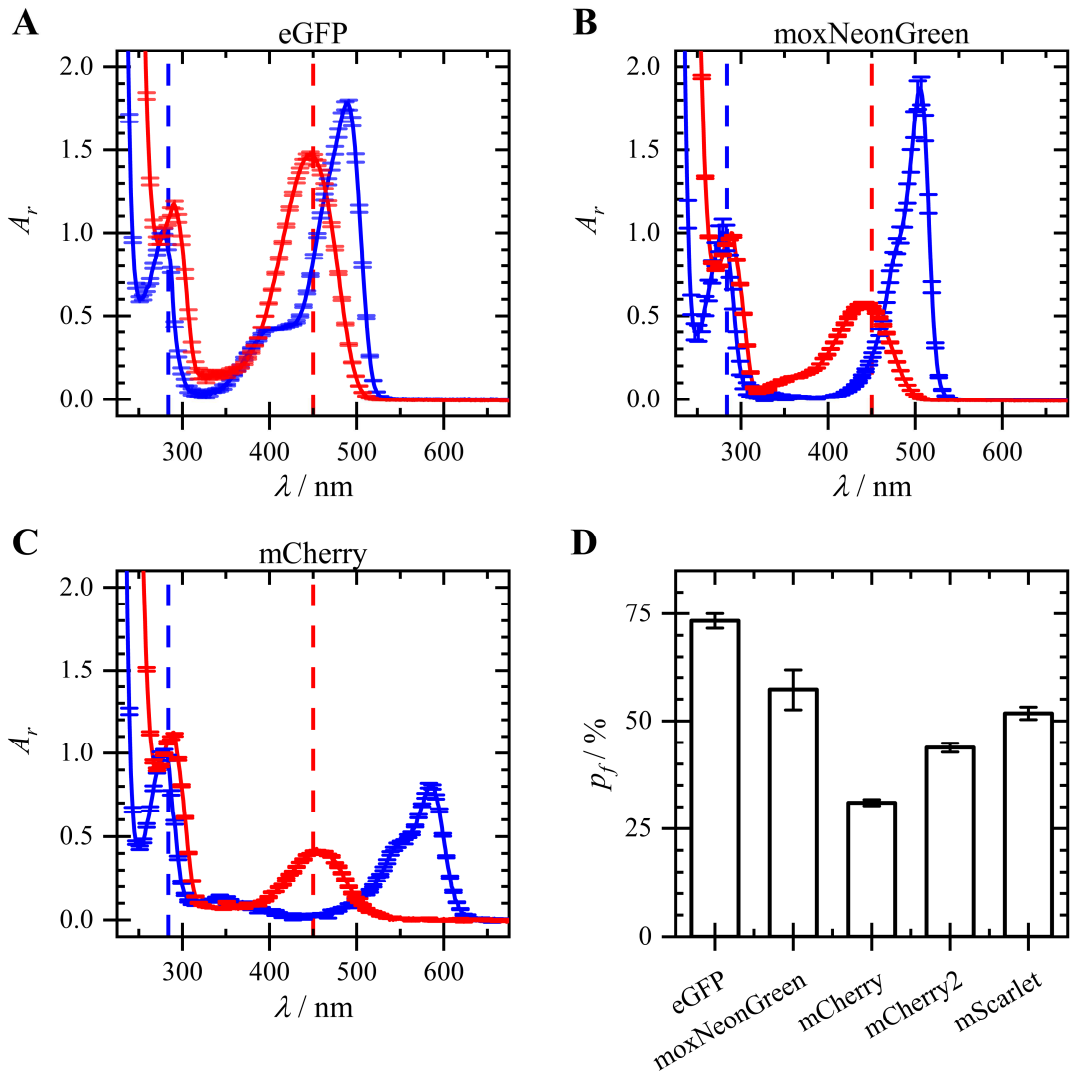

Figure C.3. Determination of Maturation Efficiencies via the Base-Denaturation Approach

A–C: Absorption spectra of eGFP (A), moxNeonGreen (B), and mCherry (C) at pH 7.4 (blue) and pH 13 (red). Each graph displays the mean relative absorption (A_r), with error bars representing *SEM*, of absorbance from 4 samples diluted from the same stock solution. The vertical dashed blue and red lines indicate wavelengths of 280 nm and 447 nm, respectively.

D: Comparison of maturation efficiencies of different fluorescent proteins. The bars represent mean, and the error bars represent *SD*.

C.3 Control Measurements and Additional Analysis Details on the Determination of Molecular Brightness of Non-EV-Bound mScarlet-WNT Units

C.3.1 Control Measurements

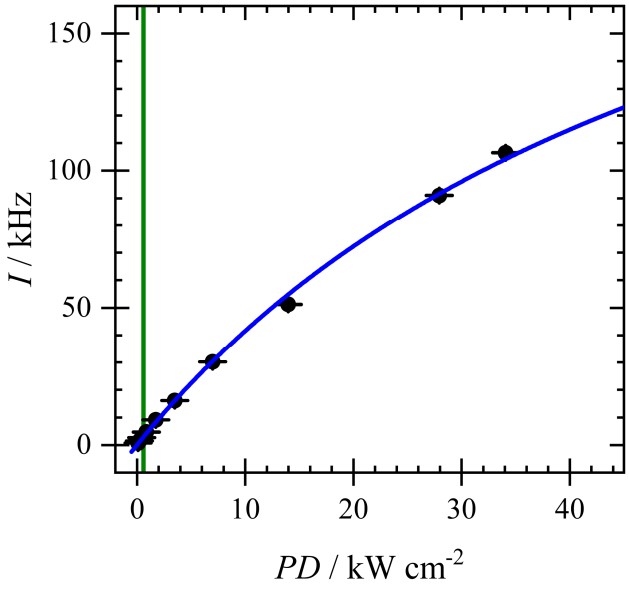

Figure C.4. Intensity (*I*) versus Power Density (*PD*) for Determining the Molecular Brightness of Non-EV-Bound mScarlet-WNT3a/5a/11 Units. The data points were taken from non-EV-bound mScarlet-WNT5a (the same measurement as Figure 5.6B). The fits with Equation (2.2) yield PD_{sat} = 27 ± 4 kW cm^{-2} I_{sat} = 151 ± 16 kHz, and R^2 = 1.0. The green, vertical line show the maximum power used, which is 0.6 kW cm^{-2}.

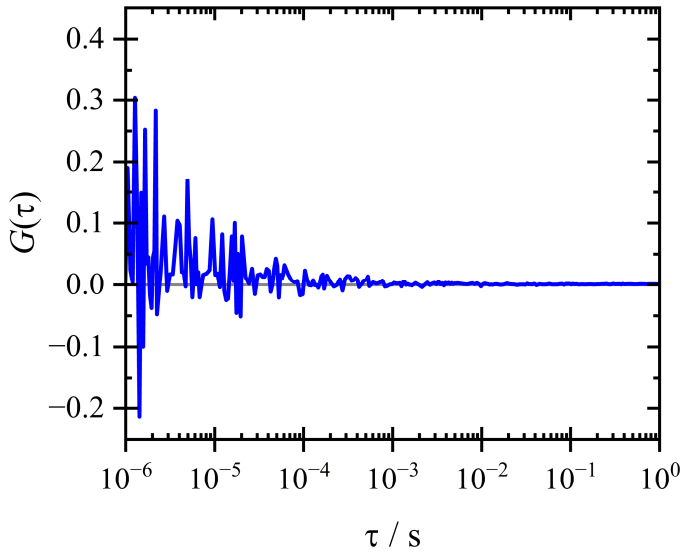

Figure C.5. Autocorrelation function ($G(\tau)$) of the background measured on the non-EV fraction of conditioned medium gathered from cells transfected with pcDNA. The measurement was performed with a laser power density of 0.7 kW cm^{-2} for 300 s. The background was estimated to be uncorrelated and constant, allowing the use of Equations (2.12)–(2.13) for background correction.

C.3.2 Parameters and Results of N&B Analysis

Table C.3. Parameters of N&B Analysis and Results of Individual Samples for the Number of Particles and Molecular Brightness of Non-EV-Bound mScarlet-WNT3a and Non-EV-Bound mScarlet-WNT11. Background intensities are reported as mean ± *SD*, while all other values are reported as median ± *MAD*.

Sample	Date	I_{BG} / Hz	$\langle\varepsilon_1\rangle$ / kHz	n	ε / kHz
mScarlet-WNT3a					
1	14.09.23	235 ± 9	3.55 ± 0.10	1.51 ± 0.09	3.41 ± 0.07
2	14.09.23	235 ± 9	3.55 ± 0.10	2.23 ± 0.12	3.39 ± 0.07
3	14.09.23	235 ± 9	3.55 ± 0.10	2.06 ± 0.11	3.59 ± 0.07
4	14.09.23	235 ± 9	3.55 ± 0.10	2.25 ± 0.13	3.41 ± 0.07
mScarlet-WNT11					
1	14.09.23	235 ± 9	3.55 ± 0.10	0.31 ± 0.03	3.75 ± 0.08
2	14.09.23	235 ± 9	3.55 ± 0.10	0.46 ± 0.04	3.70 ± 0.07
3	14.09.23	235 ± 9	3.55 ± 0.10	0.42 ± 0.05	3.54 ± 0.24
4	14.09.23	235 ± 9	3.55 ± 0.10	0.43 ± 0.04	3.80 ± 0.09
mScarlet					
1	14.09.23	235 ± 9	3.55 ± 0.10	0.70 ± 0.04	3.61 ± 0.02
2	14.09.23	235 ± 9	3.55 ± 0.10	0.74 ± 0.05	3.42 ± 0.14
3	14.09.23	235 ± 9	3.55 ± 0.10	0.68 ± 0.05	3.55 ± 0.09
4	14.09.23	235 ± 9	3.55 ± 0.10	0.64 ± 0.05	3.51 ± 0.09

Table C.4. Parameters of N&B Analysis and Results of Individual Samples for the Number of Particles and Molecular Brightness of Non-EV-Bound mScarlet-WNT5a. Background intensities are reported as mean ± *SD*, while all other values are reported as median ± *MAD*.

Sample	Date	I_{BG} / Hz	$\langle\varepsilon_1\rangle$ / kHz	n	ε / kHz
mScarlet-WNT5a					
1	03.05.22	240 ± 40	0.87 ± 0.03	3.46 ± 0.08	1.00 ± 0.01
2	03.05.22	240 ± 40	0.87 ± 0.03	3.19 ± 0.17	1.00 ± 0.02
3	03.05.22	240 ± 40	0.87 ± 0.03	3.08 ± 0.10	0.89 ± 0.01
4	03.05.22	240 ± 40	0.87 ± 0.03	0.75 ± 0.03	0.75 ± 0.03
mScarlet					
1	03.05.22	240 ± 40	0.87 ± 0.03	2.03 ± 0.01	0.87 ± 0.03
2	03.05.22	240 ± 40	0.87 ± 0.03	3.85 ± 0.45	0.62 ± 0.03
3	03.05.22	240 ± 40	0.87 ± 0.03	2.12 ± 0.09	0.95 ± 0.04
4	03.05.22	240 ± 40	0.87 ± 0.03	2.66 ± 0.04	0.85 ± 0.01

C.4 Control Measurements and Additional Analysis Details on the Determination of Molecular Brightness of EVs

C.4.1 Control and Calibration Measurements

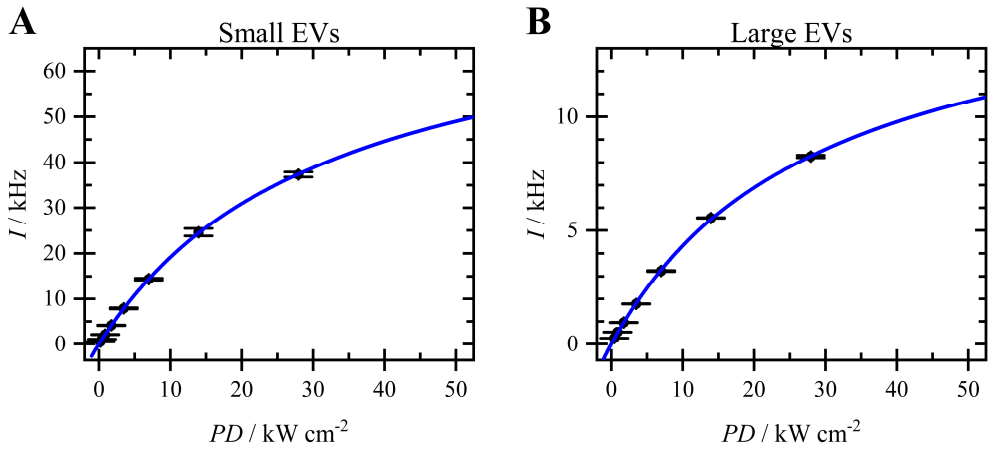

Figure C.6. Intensity (*I*) versus Power Density (*PD*) for Determining the ... (Continued on next page)
(Continued from previous page) **... Molecular Brightness of EVs.** The data points were taken from non-EV-bound mScarlet-WNT5a (the same measurement as Figure 5.8). The fits with Equation (2.2) yield (mean ± *SD*)
A: PD_{sat} = 32 ± 1 kW cm^{-2}, I_{sat} = 80 ± 1 kHz, R^2 = 1.0
B: PD_{sat}= 29 ± 1 kW cm^{-2}, I_{sat} = 17 ± 1 kHz, R^2 = 1.0

Table C.5. Parameters Describing the Observation Volume Obtained from Calibration Measurements on Alexa Fluor 546. The values of w_0, V_{eff}, and ε_{A546} are reported as mean ± *SD*.

Date	w_0 / nm	ε_{A546} / kHz	$a_1{}^*$	$a_2{}^*$	$a_3{}^*$	$B_0{}^*$	R^2
Calibration for small EVs carrying mScarlet-WNT3a							
03.08.23	336 ± 3	3.79 ± 0.02	9.4 ± 1.1	–9.1 ± 1.1	1.49 ± 0.19	1.37 ± 0.13	1.0000
04.08.23	350 ± 3	3.94 ± 0.02	9.2 ± 1.1	–8.9 ± 1.1	1.45 ± 0.19	1.38 ± 0.13	1.0000
22.08.23	338 ± 6	2.06 ± 0.02	5.3 ± 1.1	–5.1 ± 1.1	0.80 ± 0.19	1.77 ± 0.13	1.0000
13.09.23	328 ± 6	2.52 ± 0.03	6.6 ± 1.1	–6.3 ± 1.1	1.00 ± 0.19	1.61 ± 0.13	1.0000
Calibration for small EVs carrying mScarlet-WNT5a							
08.04.22	293 ± 2	3.28 ± 0.01	10.0 ± 1.1	–9.7 ± 1.1	1.58 ± 0.19	1.33 ± 0.13	1.0000
11.04.22	311 ± 1	3.66 ± 0.01	10.0 ± 1.1	–9.7 ± 1.1	1.58 ± 0.19	1.33 ± 0.13	1.0000
Calibration for large EVs carrying mScarlet-WNT3a							
17.04.23	280 ± 2	2.10 ± 0.01	4.6 ± 1.1	–4.3 ± 1.1	0.67 ± 0.19	1.89 ± 0.13	1.0000
18.04.23	273 ± 2	3.09 ± 0.02	8.9 ± 1.1	–8.6 ± 1.1	1.39 ± 0.19	1.40 ± 0.13	1.0000
Calibration for large EVs carrying mScarlet-WNT5a							
03.11.21	303 ± 1	4.54 ± 0.02	10.0 ± 1.1	–9.7 ± 1.1	1.59 ± 0.19	1.33 ± 0.13	0.9999
05.05.23	292 ± 2	2.37 ± 0.01	8.5 ± 1.1	–8.2 ± 1.1	1.33 ± 0.19	1.43 ± 0.13	1.0000
Calibration for purified mScarlet							
03.08.23	336 ± 3	3.79 ± 0.02	9.4 ± 1.1	–9.1 ± 1.1	1.49 ± 0.19	1.37 ± 0.13	1.0000
04.08.23	350 ± 3	3.94 ± 0.02	9.2 ± 1.1	–8.9 ± 1.1	1.45 ± 0.19	1.38 ± 0.13	1.0000
13.09.23	328 ± 6	2.52 ± 0.03	6.6 ± 1.1	–6.3 ± 1.1	1.00 ± 0.19	1.61 ± 0.13	1.0000

* Values were obtained by fitting the data with a fixed background signal of 0.2 kHz. Uncertainties were estimated as the average of half the differences between the values measured on consecutive days.
Abbreviation: Molecular brightness of Alexa Fluor 546 is abbreviated as ε_{A546} in this table.

C.4.2 Background Signal and Molecular Brightness of Purified mScarlet

Table C.6. Background Signal with Respect to the Excitation Power Density and Emission Filter Used in the Setup

Measurement Condition	PD / kW cm^{-2}	Emission Filter (Center/Width) / nm	I_{BG} / kHz
1 (dark count)	0	-	0.2 ± 0.1*
2	0.7	600/37	0.3 ± 0.1†
3	1.4	600/37	0.4 ± 0.2‡
4	0.7	609/62	0.4 ± 0.2×
5	2.0	609/62	0.8 ± 0.4×

* Values were observed consistently throughout all measurements and agree with the y-intercept obtained from linear regression of measurement conditions 2 and 3.

† Data were obtained from raw measurements on 08.04.22, 05.05.23, 22.08.23, and 19.09.23. The values are reported as mean ± *SEM*.

‡ Data were obtained from raw measurements on 03.08.23, 04.08.23, 06–08.09.23, 13.09.23, and 21.11.03. The values are reported as mean ± *SEM*.

× Calculated as the sum of the dark count and the scattering signal estimated from measurement condition 2, with adjustments for excitation power density and an emission filter correction factor of 1.4.

Table C.7. Molecular Brightness of mScarlet Obtained by N&B and FIDA. For reference, the molecular brightness of Alexa Fluor 546, measured on the same day, is also provided. The values are reported as mean ± *SD*.

Sample	Date	N&B	FIDA		ε_{A546} / kHz
		ε / kHz	ε / kHz	R^2	
1	03.08.23	5.76 ± 0.65	5.78 ± 0.57	0.9999	3.79 ± 0.02
2	03.08.23	5.67 ± 0.24	5.75 ± 0.09	0.9999	3.79 ± 0.02
3	04.08.23	6.00 ± 0.11	6.12 ± 0.12	0.9998	3.94 ± 0.02
4	13.09.23	3.98 ± 0.15	4.06 ± 0.15	0.9999	2.52 ± 0.03

C.4.3 Concentration of Individual Brightness Components of EVs

Table C.8. Concentration of Individual Brightness Components of Small EVs Carrying mScarlet-WNT3a. All parameters are reported as mean ± *SEM*, except the molecular brightness of mScarlet (ε_{Sc}) which is reported as mean ± *SD*.

Parameter	ε_r	Sample 1	Sample 2	Sample 3	Sample 4	Sample 5	Sample 6
ε_{Sc}* / kHz	1	5.80 ± 0.16	5.80 ± 0.16	6.03 ± 0.16	1.57 ± 0.04	1.57 ± 0.04	3.85 ± 0.11
c_1 / nM	1	17 ± 3	11 ± 1	6.16 ± 0.09	6.2 ± 0.3	5.8 ± 0.2	4.8 ± 0.2
c_2 / pM	20	36 ± 9	42 ± 7	30.7 ± 0.6	54 ± 6	21 ± 1	14 ± 2
c_3 / pM	60	0.46 ± 0.05	2.2 ± 0.4	0.75 ± 0.02	3.1 ± 0.2	0.06 ± 0.01	0.068 ± 0.005
c_4 / fM	150	11 ± 4	80 ± 30	84 ± 4	490 ± 50	82 ± 5	12 ± 2
c_5 / fM	300	0.7 ± 0.2	0.7 ± 0.3	0.7 ± 0.2	4.0 ± 0.7	1.8 ± 0.1	0.8 ± 0.4
c_6 / fM	600	-	-	-	-	-	-
R^2		0.9999	1.0000	0.9999	1.0000	1.0000	1.0000
$\langle \varepsilon_r \rangle_{1-5}$		1.04 ± 0.21	1.09 ± 0.20	1.10 ± 0.02	1.21 ± 0.09	1.07 ± 0.04	1.06 ± 0.08
$\langle \varepsilon_r \rangle_{2-5}$		21 ± 7	22 ± 5	21 ± 1	23 ± 3	21 ± 2	20 ± 4

* Fixed parameters (uncertainties not included). The molecular brightness of mScarlet was estimated from the N&B measurements reported in Table C.7. The values were adjusted for excitation power density, emission filter, and microscope detection efficiency (calibrated using the molecular brightness of Alexa Fluor 546).

Table C.9. Concentration of Individual Brightness Components of Small EVs Carrying mScarlet-WNT5a. All parameters are reported as mean ± *SEM*, except the molecular brightness of mScarlet (ε_{Sc}) which is reported as mean ± *SD*.

Parameter	ε_r	Sample 1	Sample 2	Sample 3	Sample 4
ε_{Sc}* / kHz	1	1.73 ± 0.05	2.85 ± 0.08	2.85 ± 0.08	2.85 ± 0.08
c_1 / nM	1	0.97 ± 0.07	1.31 ± 0.01	2.7 ± 0.3	16 ± 2
c_2 / pM	20	0.5 ± 0.2	5.4 ± 0.3	6.9 ± 0.2	47 ± 7
c_3 / pM	60	0.33 ± 0.09	0.33 ± 0.02	0.5 ± 0.1	1.6 ± 0.8
c_4 / fM	150	10 ± 1	11 ± 2	30 ± 2	90 ± 10
c_5 / fM	300	4 ± 1	1.3 ± 0.6	3 ± 2	2 ± 1
c_6 / fM	600	-	-	-	-
R^2		1.0000	1.0000	1.0000	1.0000
$\langle \varepsilon_r \rangle_{1-5}$		1.03 ± 0.11	1.09 ± 0.02	1.06 ± 0.19	1.06 ± 0.21
$\langle \varepsilon_r \rangle_{2-5}$		39 ± 21	23 ± 2	24 ± 2	22 ± 5

* Fixed parameters (uncertainties not included). The molecular brightness of mScarlet was estimated from the N&B measurements reported in Table C.7. The values were adjusted for excitation power density, emission filter, and microscope detection efficiency (calibrated using the molecular brightness of Alexa Fluor 546).

Table C.10. Concentration of Individual Brightness Components of Large EVs Carrying mScarlet-WNT3a. All parameters are reported as mean ± *SEM*, except the molecular brightness of mScarlet (ε_{Sc}) which is reported as mean ± *SD*.

Parameter	ε_r	Sample 1	Sample 2	Sample 3	Sample 4
ε_{Sc}* / kHz	1	6.70 ± 0.17	6.70 ± 0.17	6.85 ± 0.18	6.85 ± 0.18
c_1 / nM	1	5.9 ± 0.5	3.0 ± 0.1	6.2 ± 0.8	2.9 ± 0.2
c_2 / pM	20	12.6 ± 0.9	9.7 ± 0.9	3.2 ± 0.5	8.8 ± 0.5
c_3 / pM	60	2.1 ± 0.1	1.1 ± 0.2	0.89 ± 0.06	1.10 ± 0.05
c_4 / pM	150	0.16 ± 0.02	0.22 ± 0.09	0.08 ± 0.01	0.20 ± 0.01
c_5 / fM	300	10 ± 2	30 ± 20	16 ± 2	13 ± 2
c_6 / fM	600	8 ± 1	13 ± 4	3.5 ± 0.7	7 ± 1
R^2		0.9963	0.9998	0.9994	0.9999
$\langle \varepsilon_r \rangle_{1-5}$		1.07 ± 0.12	1.10 ± 0.07	1.02 ± 0.18	1.09 ± 0.10
$\langle \varepsilon_r \rangle_{2-5}$		27 ± 3	28 ± 5	33 ± 6	28 ± 2

* Fixed parameters (uncertainties not included). The molecular brightness of mScarlet was estimated from the N&B measurements reported in Table C.7. The values were adjusted for excitation power density, emission filter, and microscope detection efficiency (calibrated using the molecular brightness of Alexa Fluor 546).

Table C.11. Concentration of Individual Brightness Components of Large EVs Carrying mScarlet-WNT5a. All parameters are reported as mean ± *SEM*, except the molecular brightness of mScarlet (ε_{Sc}) which is reported as mean ± *SD*.

Parameter	ε_r	Sample 1	Sample 2	Sample 3
ε_{Sc}* / kHz	1	4.82 ± 0.13	4.82 ± 0.13	1.80 ± 0.05
c_1 / nM	1	1.0 ± 0.6	0.4 ± 0.1	6.0 ± 0.7
c_2 / pM	20	2.9 ± 0.7	3.1 ± 0.2	2 ± 2
c_3 / pM	60	0.4 ± 0.1	0.53 ± 0.03	0.7 ± 0.1
c_4 / pM	150	0.10 ± 0.02	0.096 ± 0.005	0.07 ± 0.01
c_5 / fM	300	14 ± 6	23 ± 3	11 ± 3
c_6 / fM	600	5 ± 1	6 ± 2	1.9 ± 0.3
R^2		1.0000	1.0000	1.0000
$\langle \varepsilon_r \rangle_{1-5}$		1.09 ± 0.87	1.32 ± 0.69	1.02 ± 0.17
$\langle \varepsilon_r \rangle_{2-5}$		30 ± 12	32 ± 3	35 ± 31

* Fixed parameters (uncertainties not included). The molecular brightness of mScarlet was estimated from the N&B measurements reported in Table C.7. The values were adjusted for excitation power density, emission filter, and microscope detection efficiency (calibrated using the molecular brightness of Alexa Fluor 546).

Appendix D

Supporting Information for Chapter 6: Hydrodynamic Radii of Secreted Wnt Particles

D.1 Fit Parameters for the Autocorrelation Functions of mCherry2 and mScarlet Obtained Using the Pure Diffusion model (Figure 6.1)

Table D.1. Fit Parameters Corresponding to Figure 6.1A–B. Values are reported as mean ± *SD*.

Fluorescent protein	PD / kW cm^{-2}	N	D / µm^2 s^{-1}	$w_0{}^*$ / nm	χ^2_μ	R^2
mCherry2	0.7	0.98 ± 0.01	113 ± 2	337 ± 1	9.9×10^{-4}	0.997
	2.0	1.02 ± 0.01	126 ± 2	337 ± 1		0.997
mScarlet	0.6	0.99 ± 0.01	145 ± 3	286 ± 1	1.2×10^{-3}	0.993
	1.8	0.98 ± 0.01	214 ± 4	286 ± 1		0.997

* Fixed parameters (uncertainties not included)

Table D.2. Fit Parameters for the Apparent Diffusion Coefficient of mCherry2, Corresponding to Figure 6.1C. Values are reported as mean ± *SD*.

Sample	PD / kW cm^{-2}	N	D / µm^2 s^{-1}	$w_0{}^*$ / nm	χ_μ^2	R^2
1	0.7	10.2 ± 0.04	115 ± 2	337 ± 1	2.2×10^{-6}	0.997
	1.3	9.7 ± 0.03	129 ± 2			0.998
	2.0	9.5 ± 0.03	138 ± 2			0.999
2	0.7	14.7 ± 0.07	113 ± 2	335 ± 1		0.996
	1.3	14.3 ± 0.07	123 ± 3			0.998
	2.0	14.1 ± 0.07	135 ± 3			0.998
3	0.7	14.1 ± 0.07	117 ± 2	335 ± 1		0.996
	1.3	13.4 ± 0.06	126 ± 2			0.998
	2.0	12.9 ± 0.06	143 ± 3			0.998

* Fixed parameters (uncertainties not included)

Table D.3. Fit Parameters for the Apparent Diffusion Coefficient of mScarlet, Corresponding to Figure 6.1C. Values are reported as mean ± *SD*.

PD / kW cm^{-2}	N	D / µm^2 s^{-1}	$w_0{}^*$ / nm	χ_μ^2	R^2
0.6	1.97 ± 0.01	140 ± 4	286 ± 1	1.7×10^{-4}	0.991
1.0	1.63 ± 0.01	167 ± 4			0.997
1.4	1.47 ± 0.01	190 ± 4			0.997
1.8	1.39 ± 0.01	202 ± 4			0.998

* Fixed parameters (uncertainties not included)

D.2 Fit Parameters for the Autocorrelation Functions of mCherry2 and mScarlet Obtained Using the Diffusion-Flickering Model

D.2.1 Global Fitting of Autocorrelation Functions with Shared Diffusion Coefficients

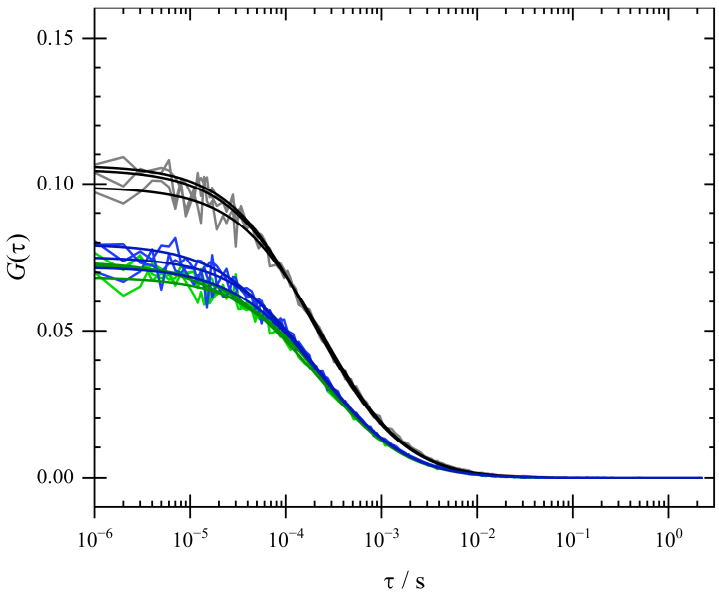

Figure D.1. Fitted Autocorrelation Functions ($G(\tau)$) for the Diffusion Coefficient of Purified mCherry2. The autocorrelation functions were globally fitted using a shared diffusion coefficient. The different colors representing autocorrelation functions from distinct samples.

Table D.4. Global Fit Parameters for the Diffusion Coefficient of Purified mCherry2, Corresponding to Figure D.1. Values are reported as mean ± *SD*.

Sample	PD / kW cm^{-2}	N	$D^{\dagger}$ / µm^2 s^{-1}	$w_0{}^{*}$ / nm	f_F	τ_F / µs	χ^2_μ	R^2
1	0.7	10.7 ± 0.2	105 ± 2	337 ± 1	0.05 ± 0.01	67 ± 30	1.9 × 10^{-6}	0.997
	1.3	10.8 ± 0.2			0.12 ± 0.01	67 ± 13		0.999
	2.0	11.2 ± 0.2			0.16 ± 0.01	94 ± 14		0.999
2	0.7	15.4 ± 0.3		335 ± 1	0.05 ± 0.02	97 ± 75		0.996
	1.3	15.2 ± 0.2			0.11 ± 0.01	16 ± 4		0.998
	2.0	15.9 ± 0.3			0.14 ± 0.01	54 ± 12		0.998
3	0.7	14.8 ± 0.2		335 ± 1	0.06 ± 0.01	46 ± 23		0.996
	1.3	14.9 ± 0.3			0.11 ± 0.02	93 ± 28		0.998
	2.0	15.1 ± 0.3			0.17 ± 0.01	59 ± 10		0.999

* Fixed parameters (uncertainties not included)

† Global parameters (shared across the simultaneous fit for all power densities of the same sample)

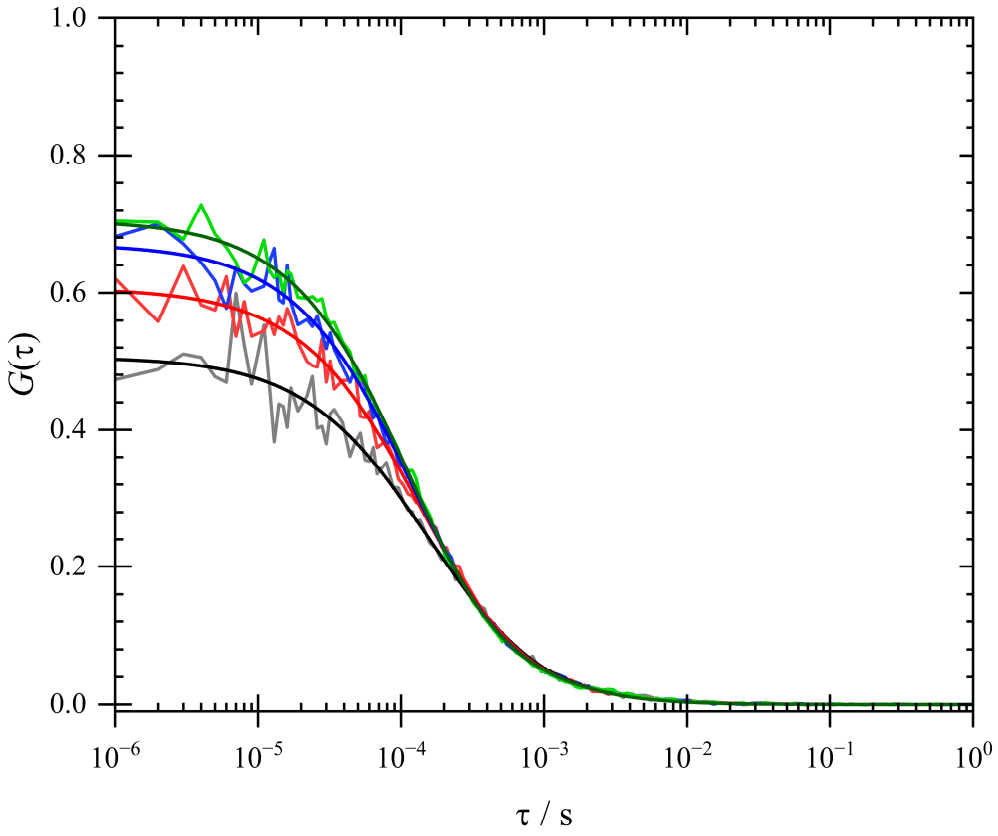

Figure D.2. Fitted Autocorrelation Functions ($G(\tau)$) for the Diffusion Coefficient of Purified mScarlet. The autocorrelation functions were globally fitted using a shared diffusion coefficient. The different colors representing autocorrelation functions from distinct samples.

Table D.5. Global Fit Parameters for the Diffusion Coefficient of Purified mScarlet, Corresponding to Figure D.2. Values are reported as mean ± *SD*.

PD / kW cm^{-2}	$N^{\dagger}$	$D^{\dagger}$ / µm^2 s^{-1}	$w_0{}^{*}$ / nm	f_F	τ_F / µs	χ^2_μ	R^2
0.6	2.5 ± 0.1	128 ± 9	286 ± 1	0.20 ± 0.05	810 ± 620	1.6×10^{-4}	0.991
1.0				0.33 ± 0.04	360 ± 90		0.997
1.4				0.39 ± 0.04	240 ± 40		0.998
1.8				0.42 ± 0.03	220 ± 30		0.999

* Fixed parameters (uncertainties not included)

† Global parameters (shared across the simultaneous fit for all power densities)

D.2.2 Individual Fitting of Autocorrelation Functions with a Fixed Diffusion Coefficient (Figure 6.2)

Table D.6. Fit Parameters for Flickering Parameters, Corresponding to Figure 6.2A–B. Values are reported as mean ± *SD*.

Sample	N	D^{*} / µm^2 s^{-1}	$w_0{}^{*}$ / nm	f_F	τ_F / µs	χ^2_μ	R^2
mCherry2	1.2 ± 0.1	102	337 ± 1	0.18 ± 0.01	101 ± 11	1.3×10^{-4}	0.999
mScarlet	2.1 ± 0.1		286 ± 1	0.54 ± 0.02	191 ± 12	1.6×10^{-4}	0.999

* Fixed parameters (uncertainties not included)

Table D.7. Fit Parameters for Flickering Parameters, Corresponding to Figure 6.2C–D. Values are reported as mean ± *SD*.

Sample	PD / kW cm^{-2}	$N^{\dagger}$	D^{*} / µm^2 s^{-1}	$w_0{}^{*}$ / nm	f_F	τ_F / µs	χ^2_μ	R^2
mCherry2								
1	0.7	11.2 ± 0.1	102	337 ± 1	0.09 ± 0.01	150 ± 50	8.6×10^{-5}	0.995
	1.3				0.14 ± 0.01	90 ± 20		0.998
	2.0				0.16 ± 0.01	80 ± 10		0.998
2	0.7	16.0 ± 0.1		335 ± 1	0.08 ± 0.01	210 ± 80	6.3×10^{-5}	0.997
	1.3				0.12 ± 0.01	80 ± 20		0.997
	2.0				0.14 ± 0.01	50 ± 10		0.997
3	0.7	15.4 ± 0.1		335 ± 1	0.09 ± 0.01	130 ± 50	8.6×10^{-5}	0.996
	1.3				0.14 ± 0.01	120 ± 30		0.998
	2.0				0.18 ± 0.01	60 ± 10		0.998
Mean	0.7	-	-	-	0.09 ± 0.01	170 ± 40	-	-
	1.3	-	-	-	0.13 ± 0.01	100 ± 20	-	-
	2.0	-	-	-	0.16 ± 0.02	70 ± 20	-	-

Sample	PD / kW cm^{-2}	$N^{\dagger}$	D^{*} / µm^2 s^{-1}	$w_0{}^{*}$ / nm	f_F	τ_F / µs	χ^2_μ	R^2
mScarlet								
-	0.6	2.9 ± 0.1	102	286 ± 1	0.32 ± 0.02	310 ± 50	1.6×10^{-4}	0.991
	1.0				0.43 ± 0.02	240 ± 20		0.997
	1.4				0.49 ± 0.01	190 ± 10		0.998
	1.8				0.51 ± 0.01	180 ± 10		0.999

* Fixed parameters (uncertainties not included)

† Global parameters (shared across the simultaneous fit for all power densities within each sample)

D.3 Fit Parameters for Determining the Hydrodynamic Radii of Non-EV-Bound mCherry2-WNT3a/5a/11 Units via Translational Diffusion

Table D.8. Fit Parameters from the Analysis of a Representative Sample for Each Sample Type, Corresponding to Figure 6.3. Values are reported as mean ± *SD*.

Sample	N	D / µm^2 s^{-1}	$w_0{}^{*}$ / nm	f_F	τ_F / µs	χ^2_μ	R^2
mCherry2	1.2 ± 0.2	91 ± 26	341 ± 5	0.16 ± 0.17	133 ± 94	1.4×10^{-3}	0.997
Ch2-WNT3a	1.3 ± 0.2	43 ± 8	349 ± 2	0.25 ± 0.09	171 ± 60		0.985
Ch2-WNT5a	1.4 ± 0.2	41 ± 9	337 ± 3	0.30 ± 0.10	182 ± 52		0.998
Ch2-WNT11	1.4 ± 0.3	50 ± 14	337 ± 31	0.30 ± 0.14	203 ± 62		0.983

* Fixed parameters (uncertainties not included)

Abbreviation: *mCherry2* is abbreviated as *Ch2* in this table.

Table D.9. Fit Parameters for the Diffusion Coefficient of Purified mCherry2, Derived from Simultaneous Fitting of Autocorrelation Functions at All Power Densities for Each Sample. Values are reported as mean ± *SD*.

Sample	PD / kW cm^{-2}	N	$D^{\dagger}$ / µm^2 s^{-1}	$w_0{}^{*}$ / nm	f_F / × 10^{-2}	τ_F / µs	χ^2_μ	R^2
1	0.65	10.6 ± 0.2	111 ± 3	341 ± 5	5 ± 2	94 ± 69	8.5 × 10^{-5}	0.995
	1.30				10 ± 2	61 ± 21		0.998
	1.95				12 ± 2	60 ± 18		0.998
2	0.65	14.8 ± 0.1	114 ± 2	334 ± 1	2 ± 2	7 ± 9¥	1.7 × 10^{-6}	0.996
	1.30				9 ± 1	10 ± 3		0.998
	1.95				8 ± 1	16 ± 4		0.998
3	0.65	14.7 ± 0.3	108 ± 3	334 ± 1	5 ± 2	47 ± 38	6.1 × 10^{-5}	0.996
	1.30				9 ± 2	92 ± 30		0.998
	1.95				14 ± 2	45 ± 11		0.998
Mean			111 ± 3	-	-	-		-

* Fixed parameters (uncertainties not included)

† Global parameters (shared across the simultaneous fit for all power densities and all samples)

¥ The large *SD* can be attributed to the low flickering contribution at this excitation power.

Table D.10. Fit Parameters for the Diffusion Coefficient of Non-EV-Bound mCherry2-WNT3a, Derived from Simultaneous Fitting of Autocorrelation Functions at All Power Densities for Each Sample. Values are reported as mean ± *SD*.

Sample	PD / kW cm^{-2}	N	$D^{\dagger}$ / µm^2 s^{-1}	$w_0{}^{*}$ / nm	f_F / × 10^{-2}	τ_F / µs	χ^2_μ	R^2
1	0.65	10.5 ± 0.6	38 ± 4	349 ± 2	31 ± 4	221 ± 32	2.8 × 10^{-5}	0.985
	1.30				36 ± 4	155 ± 21		0.993
	1.95				38 ± 3	116 ± 16		0.995
2	0.65	3.6 ± 0.2	50 ± 3	337 ± 3	30 ± 3	90 ± 19	1.3 × 10^{-3}	0.988
	1.30				35 ± 3	165 ± 23		0.990
	1.95				34 ± 3	154 ± 23		0.993
3	0.65	8.8 ± 0.2	39 ± 1	344 ± 3	29 ± 2	164 ± 22	2.9 × 10^{-4}	0.994
	1.30				34 ± 2	118 ± 13		0.996
	1.95				32 ± 2	97 ± 12		0.995
4	0.65	30.8 ± 1.0	25 ± 1	327 ± 2	46 ± 2	230 ± 26	6.1 × 10^{-1}	0.981
	1.30				46 ± 2	348 ± 30		0.995
	1.95				47 ± 2	341 ± 21		0.996
5	0.65	26.2 ± 0.8	33 ± 1	327 ± 2	41 ± 2	181 ± 14	7.5 × 10^{-5}	0.995
	1.30				41 ± 2	206 ± 16		0.996
	1.95				41 ± 2	194 ± 15		0.998
6	0.65	23.9 ± 0.3	40 ± 1	331 ± 2	39 ± 1	128 ± 10	6.6 × 10^{-5}	0.996
	1.30				39 ± 1	147 ± 11		0.997
	1.95				39 ± 1	121 ± 9		0.998
Mean			38 ± 8	-	-	-		-

* Fixed parameters (uncertainties not included)

† Global parameters (shared across the simultaneous fit for all power densities and all samples)

Table D.11. Fit Parameters for the Diffusion Coefficient of Non-EV-Bound mCherry2-WNT5a, Derived from Simultaneous Fitting of Autocorrelation Functions at All Power Densities for Each Sample. Values are reported as mean ± *SD*.

Sample	PD / kW cm^{-2}	N	$D^{\dagger}$ / µm^2 s^{-1}	$w_0{}^{*}$ / nm	f_F / × 10^{-2}	τ_F / µs	χ^2_μ	R^2
1	0.65	7.1 ± 0.2	48 ± 1	337 ± 3	23 ± 2	161 ± 22	1.9 × 10^{-4}	0.998
	1.30				30 ± 2	118 ± 12		0.997
	1.95				32 ± 1	102 ± 10		0.996
2	0.65	4.8 ± 0.1	43 ± 1	335 ± 2	14 ± 2	56 ± 17	3.8 × 10^{-4}	0.991
	1.30				20 ± 1	111 ± 19		0.997
	1.95				23 ± 1	77 ± 12		0.998
3	0.65	4.7 ± 0.1	27 ± 1	335 ± 2	33 ± 1	353 ± 32	4.2 × 10^{-4}	0.995
	1.30				32 ± 1	163 ± 17		0.998
	1.95				30 ± 2	112 ± 14		0.996
Mean			39 ± 11	-	-	-	-	-

* Fixed parameters (uncertainties not included)

† Global parameters (shared across the simultaneous fit for all power densities and all samples)

Table D.12. Fit Parameters for the Diffusion Coefficient of Non-EV-Bound mCherry2-WNT11, Derived from Simultaneous Fitting of Autocorrelation Functions at All Power Densities for Each Sample. Values are reported as mean ± *SD*.

Sample	PD / kW cm^{-2}	N	$D^{\dagger}$ / µm^2 s^{-1}	$w_0{}^{*}$ / nm	f_F / × 10^{-2}	τ_F / µs	χ^2_μ	R^2
1	0.65	3.8 ± 0.2	59 ± 3	337 ± 3	17 ± 4	110 ± 43	1.0 × 10^{-3}	0.990
	1.30				24 ± 3	145 ± 32		0.991
	1.95				31 ± 3	105 ± 19		0.992
2	0.65	3.1 ± 0.1	60 ± 3	337 ± 3	36 ± 2	112 ± 13	1.1 × 10^{-3}	0.994
	1.30				24 ± 3	107 ± 23		0.990
	1.95				24 ± 3	82 ± 19		0.994
3	0.65	4.4 ± 0.3	60 ± 5	349 ± 2	24 ± 5	180 ± 49	1.2 × 10^{-3}	0.983
	1.30				26 ± 4	178 ± 44		0.988
	1.95				35 ± 4	121 ± 23		0.993
Mean			60 ± 1	-	-	-	-	-

* Fixed parameters (uncertainties not included)

† Global parameters (shared across the simultaneous fit for all power densities and all samples)

D.4 Control Measurement and Analysis Details for the Rotational Correlation Times of mCherry2 and Non-EV-Bound mCherry2-WNT Units

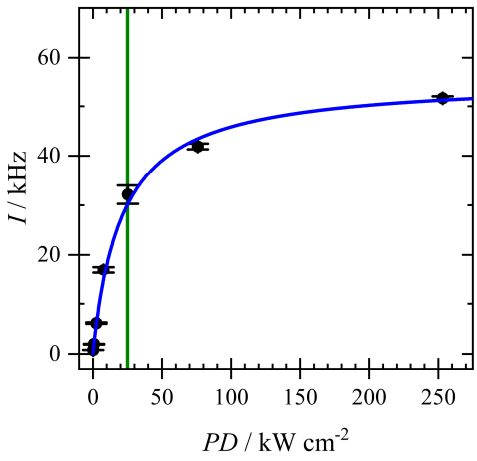

Figure D.3. Intensity (*I*) versus Power Density (*PD*) from Non-EV-Bound mCherry2-WNT3a Units. Data points and error bars show mean and *SEM* of *I* with respect to *PD*. The line of best fit was obtained through fitting with Equation (2.2), yielding PD_{sat} = 21 ± 1 kW cm^{-2} and I_{sat} = 44 ± 1 kHz, and R^2 = 1.0. The green, vertical blue line show the excitation power density of 25 kW cm^{-2} used in polarization-dependent FCS measurements.

Table D.13. Fit Parameters Obtained from Fitting the Autocorrelation Functions with a Model Incorporating a Single Exponential Term to Describe Rotational Diffusion, Corresponding to Figure 6.6. Values are reported as mean ± *SD*.

Parameter	mCherry2	mCherry2-WNT3a	mCherry2-WNT5a	mCherry2-WNT11
N	1.9 ± 0.1	2.2 ± 0.1	2.1 ± 0.1	2.1 ± 0.1
f_A	1.18 ± 0.04	1.09 ± 0.05	1.06 ± 0.05	1.11 ± 0.04
f_R	1.97 ± 0.11	1.57 ± 0.08	1.63 ± 0.08	1.76 ± 0.09
f_F	0.51 ± 0.03	0.59 ± 0.02	0.58 ± 0.02	0.58 ± 0.03
τ_A† / ns	1.9 ± 0.1			
τ_R / ns	15 ± 1	26 ± 2	21 ± 2	19 ± 2
τ_F† / µs	18 ± 1			
D / µm^2 s^{-1}	139 ± 16	85 ± 10	89 ± 10	108 ± 13
w_0* / nm	360‡			
χ^2_μ	8.1 × 10^{-3}			
R^2	0.986	0.990	0.986	0.993

* Fixed parameters (uncertainties not included)

† Global parameters (shared across the simultaneous fit for all sample types)

‡ At this laser power, the signal from Alexa Fluor 546 is excessively high, resulting in detector saturation and making the calibration of w_0 impossible. The value provided is therefore an estimation. However, this value influences only the translational diffusion coefficient, which is not further utilized in the analysis.

Table D.14. Fit Parameters Obtained from Fitting the Autocorrelation Functions with a Model Incorporating Two Exponential Terms to Describe Rotational Diffusion, Corresponding to Figure 6.5–Figure 6.6

Parameter	mCherry2	mCherry2-WNT3a	mCherry2-WNT5a	mCherry2-WNT11
N	2.0 ± 0.1	2.3 ± 0.1	2.1 ± 0.1	2.2 ± 0.1
f_A	1.13 ± 0.04	1.09± 0.04	1.03 ± 0.04	1.06 ± 0.04
f_R	1.75 ± 0.10	1.65 ± 0.09	1.62 ± 0.09	1.64 ± 0.08
f_F	0.54 ± 0.03	0.58 ± 0.03	0.57 ± 0.03	0.59 ± 0.03
$C^{\dagger}$	4.9 ± 1.0			
$\tau_A{}^{\dagger}$ / ns	1.9 ± 0.1			
$\tau_{R1}{}^{*}$ / ns	15 ± 1			
τ_{R2} / ns	18 ± 6	225 ± 86	190 ± 72	99 ± 35
$\tau_F{}^{\dagger}$ / µs	22 ± 2			
D / µm^2 s^{-1}	126 ± 15	81 ± 9	85 ± 10	101 ± 12
$w_0{}^{*}$ / nm	360‡			
χ^2_μ	7.6×10^{-3}			
R^2	0.986	0.991	0.987	0.994

All values are reported as mean ± *SD*.

* Fixed parameters (uncertainties not included)

† Global parameters (shared across the simultaneous fit for all sample types)

‡ At this laser power, the signal from Alexa Fluor 546 is excessively high, resulting in detector saturation and making the calibration of w_0 impossible. The value provided is therefore an estimation. However, this value influences only the translational diffusion coefficient, which is not further utilized in the analysis.

D.5 Fluorescence Lifetime of mCherry2

The fluorescence lifetime of mCherry2 was assessed using five samples of purified mCherry2, each diluted in a buffer solution (40mM Na-PO_4, 300 mM NaCl). Pulsed excitation at 560 nm with an intensity of 1.6 kW cm^{-2} was applied for 300 s per sample. Photon sorting was conducted with a time bin of 16 ps. A histogram depicting the time difference between photon detection and the preceding laser pulse, denoted as t, was constructed, as illustrated in Figure D.4.

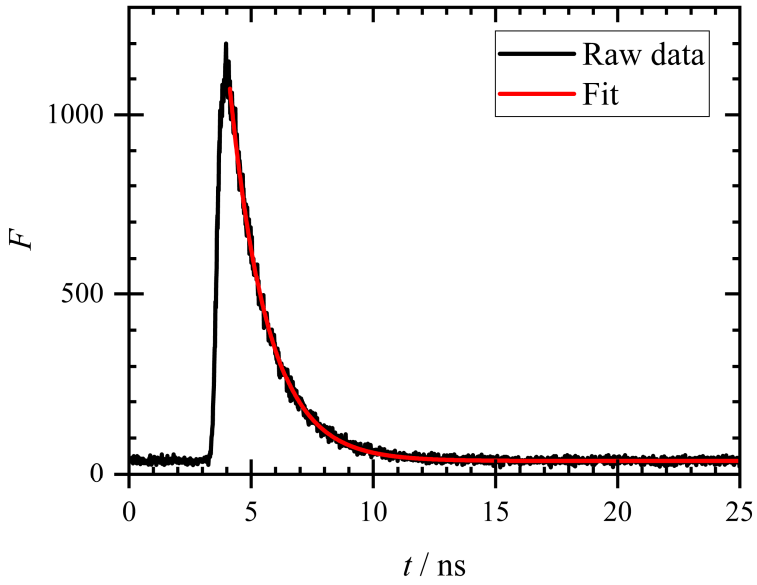

Figure D.4. Fluorescence Decay Time Histogram from purified mCherry2 in buffer. The vertical axis shows the number of photons (F), and the horizontal axis shows the decay time (t).

The histogram data were fitted utilizing a single-exponential decay equation:

$$F(t) = F_0 e^{-(t/\tau_F)},$$

where F_o represents the initial intensity and τ_F denotes the fluorescence lifetime. The analysis yielded an average lifetime of 1.6 ± 0.1 ns (mean ± *SEM*), similar to the published fluorescence lifetime of mCherry (1.6 ns)[200].

D.6 Analysis Details and Fit Parameters for the Hydrodynamic Radii of Small and Large EVs

D.6.1 Fitting with the Pure Diffusion Model

Table D.15. Fit Parameters for the Autocorrelation Functions of Small EVs Carrying mScarlet-WNT3a, Obtained by Fitting with the Pure Diffusion Model

Parameter	Statistics	Sample 1	Sample 2	Sample 3	Sample 4	Sample 5	Sample 6
# segments	Total	62	60	60	60	60	60
	1 species	59	57	59	59	58	60
	2 species	3	0	0	1	0	0
	Discarded	0	3	1	0	2	0
N	Median	14.5	6.1	4.7	8.6	5.7	3.7
	MAD	2.8	2.4	0.8	4.1	0.4	0.3
τ_D / ms	Median	9.0	34.3	7.1	20.8	4.0	4.1
	MAD	3.6	17.7	2.2	10.3	1.1	0.8
w_0 / nm	Mean	336	336	350	338	338	328
	SD	3	3	3	6	6	6
r_h / nm (not corrected)	Median	78	298	57	178	34	37
	MAD	31	154	18	89	10	7
r_h / nm (corrected)	Median	75	213	55	149	34	37
	MAD	27	73	17	53	10	7
χ^2_μ	Minimum	1.2×10^{-6}	1.3×10^{-5}	8.4×10^{-6}	1.5×10^{-6}	1.1×10^{-5}	2.2×10^{-5}
	Median	8.6×10^{-6}	5.9×10^{-5}	4.3×10^{-5}	2.7×10^{-5}	3.8×10^{-5}	4.8×10^{-5}
	Maximum	1.2×10^{-2}	1.1×10^{-2}	6.1×10^{-2}	1.9×10^{-2}	5.4×10^{-2}	6.6×10^{-3}
R^2	Minimum	0.920	0.907	0.934	0.901	0.907	0.946
	Median	0.982	0.977	0.987	0.982	0.980	0.990
	Maximum	0.996	0.996	0.996	0.997	0.992	0.995

Table D.16. Fit Parameters for the Autocorrelation Functions of Small EVs Carrying mScarlet-WNT5a, Obtained by Fitting with the Pure Diffusion Model

Parameter	Statistics	Sample 1	Sample 2	Sample 3	Sample 4
# segments	Total	50	50	50	50
	1 species	49	50	50	49
	2 species	1	0	0	1
	Discarded	0	0	0	0
N	Median	1.6	1.2	3.6	13.2
	MAD	0.5	0.3	0.8	2.6

Parameter	Statistics	Sample 1	Sample 2	Sample 3	Sample 4
τ_D / ms	Median	6.6	11.4	7.1	10.0
	MAD	2.3	3.5	2.1	4.3
w_0/ nm	Mean	293	311	311	311
	SD	2	1	1	1
r_h / nm (not corrected)	Median	66	105	66	92
	MAD	24	32	19	40
r_h / nm (corrected)	Median	63	96	63	86
	MAD	21	26	16	33
χ^2_μ	Minimum	1.0×10^{-4}	1.5×10^{-4}	1.6×10^{-5}	1.3×10^{-6}
	Median	4.7×10^{-4}	9.3×10^{-4}	8.8×10^{-5}	6.4×10^{-6}
	Maximum	3.6×10^{-2}	1.3×10^{-1}	1.2×10^{-2}	3.0×10^{-2}
R^2	Minimum	0.944	0.928	0.914	0.910
	Median	0.982	0.986	0.989	0.989
	Maximum	0.995	0.997	0.996	0.998

Table D.17. Fit Parameters for the Autocorrelation Functions of Large EVs Carrying mScarlet-WNT3a, Obtained by Fitting with the Pure Diffusion Model

Parameter	Statistics	Sample 1	Sample 2	Sample 3	Sample 4
# segments	Total	20	20	20	20
	1 species	15	19	17	14
	2 species	5	1	3	3
	Discarded	0	0	0	3
N	Median	6.0	2.1	3.4	11.1
	MAD	3.3	1.4	0.9	3.4
τ_D / ms	Median	25.9	20.5	12.2	30.9
	MAD	17.9	16.9	8.6	27.1
w_0 / nm	Mean	280	280	273	273
	SD	2	2	2	2
r_h / nm (not corrected)	Median	324	257	162	409
	MAD	224	212	114	358
r_h / nm (corrected)	Median	208	181	131	235
	MAD	91	124	74	154
χ^2_μ	Minimum	6.1×10^{-6}	3.4×10^{-5}	3.3×10^{-5}	7.1×10^{-6}
	Median	6.6×10^{-5}	9.4×10^{-4}	1.8×10^{-4}	2.5×10^{-5}
	Maximum	1.2×10^{-2}	3.2×10^{-2}	2.5×10^{-1}	3.6×10^{-3}
R^2	Minimum	0.941	0.902	0.930	0.913
	Median	0.970	0.965	0.973	0.933
	Maximum	0.993	0.987	0.994	0.984

Table D.18. Fit Parameters for the Autocorrelation Functions of Large EVs Carrying mScarlet-WNT5a, Obtained by Fitting with the Pure Diffusion Model

Parameter	Statistics	Sample 1	Sample 2	Sample 3
# segments	Total	40	10	50
	1 species	36	10	30
	2 species	4	10	19
	Discarded	0	0	1
N	Median	7.6	1.0	35.8
	MAD	1.6	0.7	28.4
τ_D / ms	Median	4.6	19.7	231.4
	MAD	2.9	12.9	154.7
w_0 / nm	Mean	303	303	292
	SD	1	1	2
r_h / nm (not corrected)	Median	43	186	2,677
	MAD	27	122	1,790
r_h / nm (corrected)	Median	42	142	565
	MAD	26	80	171
χ^2_μ	Minimum	9.7×10^{-6}	5.1×10^{-4}	4.4×10^{-8}
	Median	3.1×10^{-5}	3.6×10^{-3}	1.7×10^{-6}
	Maximum	7.2×10^{-2}	3.1×10^{-1}	1.3×10^{-4}
R^2	Minimum	0.918	0.944	0.907
	Median	0.968	0.978	0.960
	Maximum	0.990	0.994	0.996

D.6.2 Fitting with the Diffusion-Flickering Model

Table D.19. Fit Parameters for the Autocorrelation Functions of Small EVs Carrying mScarlet-WNT3a, Obtained by Fitting with the Diffusion-Flickering Model

Parameter	Statistics	Sample 1	Sample 2	Sample 3	Sample 4	Sample 5	Sample 6
# segments	Total	62	60	60	60	60	60
	1 species	62	60	60	49	59	60
	2 species	0	0	0	0	0	0
	Discarded	0	0	0	11	1	0
N	Median	14.7	6.1	4.8	6.5	6.3	3.7
	MAD	3.0	2.5	1.0	4.2	0.6	0.5
f_F	Median	0.48	0.38	0.46	0.35	0.58	0.46
	MAD	0.04	0.09	0.05	0.10	0.04	0.04
τ_D / ms	Median	9.2	36.7	7.3	21.5	4.7	4.3
	MAD	3.4	18.3	2.2	9.9	1.2	0.9
$\tau_F{}^*$ / µs	Mean	309	309	309	309	309	309
	SD	46	46	46	46	46	46
$w_0{}^*$ / nm	Mean	336	336	350	338	338	328
	SD	3	3	3	6	6	6

Parameter	Statistics	Sample 1	Sample 2	Sample 3	Sample 4	Sample 5	Sample 6
r_h / nm (not corrected)	Median	80	319	59	184	41	39
	MAD	30	159	18	85	10	8
r_h / nm (corrected)	Median	76	222	57	153	40	38
	MAD	26	69	17	50	10	8
χ^2_μ	Minimum	1.2×10^{-5}	3.5×10^{-5}	4.2×10^{-5}	7.9×10^{-5}	3.8×10^{-4}	5.2×10^{-4}
	Median	2.1×10^{-5}	7.7×10^{-5}	2.0×10^{-4}	3.2×10^{-4}	7.7×10^{-4}	9.2×10^{-4}
	Maximum	8.4×10^{-4}	6.7×10^{-3}	4.0×10^{-2}	1.3×10^{-2}	6.3×10^{-3}	4.7×10^{-3}
R^2	Minimum	0.929	0.941	0.953	0.902	0.922	0.939
	Median	0.990	0.987	0.989	0.955	0.959	0.973
	Maximum	0.996	0.994	0.996	0.990	0.988	0.988

* Fixed parameters (uncertainties not included)

Table D.20. Fit Parameters for the Autocorrelation Functions of Small EVs Carrying mScarlet-WNT5a, Obtained by Fitting with the Diffusion-Flickering Model

Parameter	Statistics	Sample 1	Sample 2	Sample 3	Sample 4
# segments	Total	50	50	50	50
	1 species	39	50	50	50
	2 species	0	0	0	0
	Discarded	11	0	0	0
N	Median	1.4	1.2	3.6	13.1
	MAD	0.3	0.3	0.9	2.8
f_F	Median	0.23	0.29	0.40	0.35
	MAD	0.05	0.05	0.05	0.03
τ_D / ms	Median	6.6	10.7	7.2	9.9
	MAD	1.9	3.2	1.8	4.1
$\tau_F{}^*$ / µs	Mean	309	309	309	309
	SD	46	46	46	46
$w_0{}^*$ / nm	Mean	293	311	311	311
	SD	2	1	1	1
r_h / nm (not corrected)	Median	66	98	66	91
	MAD	19	29	17	38
r_h / nm (corrected)	Median	63	90	63	85
	MAD	17	24	15	31
χ^2_μ	Minimum	3.2×10^{-3}	1.4×10^{-3}	2.2×10^{-4}	9.0×10^{-6}
	Median	6.6×10^{-3}	3.2×10^{-3}	5.4×10^{-4}	1.9×10^{-5}
	Maximum	3.6×10^{-2}	8.8×10^{-2}	9.0×10^{-3}	1.9×10^{-2}
R^2	Minimum	0.907	0.943	0.951	0.939
	Median	0.950	0.983	0.986	0.989
	Maximum	0.986	0.994	0.994	0.995

* Fixed parameters (uncertainties not included)

Table D.21. Fit Parameters for the Autocorrelation Functions of Large EVs Carrying mScarlet-WNT3a, Obtained by Fitting with the Diffusion-Flickering Model

Parameter	Statistics	Sample 1	Sample 2	Sample 3	Sample 4
# segments	Total	20	20	20	20
	1 species	20	20	20	14
	2 species	0	0	0	0
	Discarded	0	0	0	6
N	Median	6.2	2.1	3.9	8.4
	MAD	4.1	1.4	1.3	4.8
f_F	Median	0.51	0.44	0.66	0.53
	MAD	0.15	0.19	0.08	0.22
τ_D / ms	Median	19.1	17.5	8.7	33.1
	MAD	10.1	11.6	4.5	32.9
$\tau_F{}^*$ / µs	Mean	235	235	235	235
	SD	21	21	21	21
$w_0{}^*$ / nm	Mean	280	280	275	275
	SD	2	2	2	2
r_h / nm (not corrected)	Median	239	219	114	438
	MAD	127	145	60	436
r_h / nm (corrected)	Median	172	162	100	243
	MAD	73	89	46	188
χ^2_μ	Minimum	1.7×10^{-4}	7.3×10^{-4}	9.9×10^{-4}	1.8×10^{-4}
	Median	3.5×10^{-4}	1.7×10^{-3}	1.9×10^{-3}	3.7×10^{-4}
	Maximum	9.0×10^{-3}	2.5×10^{-2}	1.7×10^{-1}	2.5×10^{-2}
R^2	Minimum	0.914	0.936	0.945	0.912
	Median	0.964	0.962	0.970	0.942
	Maximum	0.990	0.988	0.995	0.987

* Fixed parameters (uncertainties not included)

Table D.22. Fit Parameters for the Autocorrelation Functions of Large EVs Carrying mScarlet-WNT5a, Obtained by Fitting with the Diffusion-Flickering Model

Parameter	Statistics	Sample 1	Sample 2	Sample 3
# segments	Total	40	10	50
	1 species	40	10	49
	2 species	0	0	0
	Discarded	0	0	1
N	Median	6.6	0.9	41.2
	MAD	1.0	0.6	37.7
f_F	Median	0.62	0.40	0.51
	MAD	0.05	0.17	0.32
τ_D / ms	Median	3.2	17.1	146.0
	MAD	2.0	12.3	141.4
$\tau_F{}^*$ / µs	Mean	188	188	188
	SD	13	13	13
$w_0{}^*$ / nm	Mean	303	303	292
	SD	1	1	2

Parameter	Statistics	Sample 1	Sample 2	Sample 3
r_h / nm (not corrected)	Median	30	161	1,689
	MAD	19	116	1,636
r_h / nm (corrected)	Median	30	127	470
	MAD	18	83	212
χ^2_μ	Minimum	1.8×10^{-4}	5.9×10^{-3}	1.6×10^{-6}
	Median	4.2×10^{-4}	9.1×10^{-3}	4.4×10^{-6}
	Maximum	5.3×10^{-2}	2.1×10^{-1}	9.5×10^{-5}
R^2	Minimum	0.913	0.947	0.904
	Median	0.978	0.977	0.973
	Maximum	0.989	0.995	0.996

* Fixed parameters (uncertainties not included)

Appendix E

Supporting Information for Chapter 7: Investigation of Co-Migrating Structures of Non-EV-Bound Wnt Units

E.1 Individual Results and Fit Parameters in Investigating the Effects of MβCD Applications on Conditioned Medium and Non-EV-Bound mCherry2-WNT3a/5a

E.1.1 Purified mCherry2

Table E.1. Fit Parameters Obtained from Fitting the Autocorrelation Functions of Purified mCherry2 Mixed with DPBS (0 mM MβCD). The autocorrelation functions were fitted with Equation (7.1). All values are reported as mean ± *SD*.

Parameter	Value
N	10.6 ± 0.9
D / μm^2 s^{-1}	56 ± 7
f_F†	0.19 ± 0.06
τ_F† / μs	82 ± 8
χ^2_μ	9.0×10^{-6}
R^2	0.999

† Global parameters (shared across the simultaneous fit for all samples)

Table E.2. Fit Parameters Obtained from Fitting the Autocorrelation Functions of Purified mCherry2 Mixed with 10 mM MβCD. The autocorrelation functions were fitted with Equation (7.1). All values are reported as mean ± *SD*.

Parameter	Sample 1	Sample 2	Sample 3
N	6.19 ± 0.17	3.38 ± 0.09	6.25 ± 0.17
τ_D / µs	305 ± 13	295 ± 12	309 ± 14
f_F†	0.21 ± 0.02		
τ_F† / µs	92 ± 8		
χ^2_μ	9.8×10^{-6}		
R^2	1.000	0.999	0.999

† Global parameters (shared across the simultaneous fit for all samples)

Table E.3. Fit Parameters Obtained from Fitting the Autocorrelation Functions of Purified mCherry2 Mixed with 40 mM MβCD. The autocorrelation functions were fitted with Equation (7.1). All values are reported as mean ± *SD*.

Parameter	Sample 1	Sample 2	Sample 3
N	5.06 ± 0.10	3.34 ± 0.06	5.87 ± 0.11
τ_D / µs	331 ± 11	314 ± 9	323 ± 11
f_F†	0.20 ± 0.01		
τ_F† / µs	80 ± 6		
χ^2_μ	8.4×10^{-6}		
R^2	0.999	0.999	1.000

† Global parameters (shared across the simultaneous fit for all samples)

Table E.4. Individual Results for the Diffusional Correlation Times of Purified mCherry2 and Their Normalized Values (Normalized to Those Measured from Samples with 0 mM MβCD) as a Function of MβCD Concentration. Values for individual samples are reported as mean ± *SD*.

$C_{M\beta CD}$	τ_D / µs			$\tilde{\tau}_D$			
/ mM	Sample 1	Sample 2	Sample 3	Sample 1	Sample 2	Sample 3	Mean ± *SD*
0	279 ± 11	277 ± 10	269 ± 10	1.00 ± 0.05	1.00 ± 0.05	1.00 ± 0.05	1.00 ± 0.05¥
10	305 ± 13	295 ± 12	309 ± 14	1.10 ± 0.06	1.06 ± 0.06	1.15 ± 0.07	1.10 ± 0.04
40	331 ± 11	314 ± 9	323 ± 11	1.19 ± 0.06	1.13 ± 0.05	1.20 ± 0.06	1.17 ± 0.04

¥ *SD* was taken as the average *SD* from the fits of individual samples

E.1.2 Non-EV-Bound mCherry2-WNT3a

Table E.5. Fit Parameters Obtained from Fitting the Autocorrelation Functions of Non-EV-Bound mCherry2-WNT3a Mixed with DPBS (0 mM MβCD). The autocorrelation functions were fitted with Equation (7.1). All values are reported as mean ± *SD*.

Parameter	Sample 1	Sample 2	Sample 3
N	6.48 ± 0.05	6.35 ± 0.05	6.07 ± 0.05
τ_D / µs	892 ± 16	869 ± 16	918 ± 17
f_F†	0.30 ± 0.01		
τ_F† / µs	109 ± 3		
χ_μ^2	5.6×10^{-4}		
R^2	0.999	1.000	0.999

† Global parameters (shared across the simultaneous fit for all samples)

Table E.6. Fit Parameters Obtained from Fitting the Autocorrelation Functions of Non-EV-Bound mCherry2-WNT3a Mixed with 10 mM MβCD. The autocorrelation functions were fitted with Equation (7.1). All values are reported as mean ± *SD*. The time label corresponds to the middle of the time range in which the data were taken.

Parameter	11 min	31 min	51 min	71 min	91 min	111 min
Sample 1						
N	6.17 ± 0.05	6.37 ± 0.05	6.36 ± 0.05	6.41 ± 0.05	6.30 ± 0.05	6.33 ± 0.05
τ_D / µs	913 ± 22	893 ± 21	848 ± 20	879 ± 21	822 ± 20	847 ± 20
f_F†	0.31 ± 0.01					
τ_F† / µs	113 ± 3					
χ_μ^2	1.5×10^{-5}					
R^2	0.998	0.998	0.997	0.998	0.999	0.998
Sample 2						
N	6.86 ± 0.06	6.76 ± 0.05	6.80 ± 0.05	6.82 ± 0.06	7.24 ± 0.06	6.79 ± 0.05
τ_D / µs	895 ± 23	896 ± 22	878 ± 22	856 ± 22	874 ± 23	866 ± 22
f_F†	0.31 ± 0.01					
τ_F† / µs	113 ± 3					
χ_μ^2	1.5×10^{-5}					
R^2	0.998	0.999	0.998	0.998	0.993	0.997
Sample 3						
N	6.25 ± 0.05	6.03 ± 0.05	6.02 ± 0.05	6.08 ± 0.05	6.14 ± 0.05	6.12 ± 0.05
τ_D / µs	931 ± 22	909 ± 21	873 ± 20	877 ± 20	854 ± 20	893 ± 21
f_F†	0.31 ± 0.01					
τ_F† / µs	113 ± 3					
χ_μ^2	1.5×10^{-5}					
R^2	0.998	0.998	0.998	0.998	0.998	0.999

† Global parameters (shared across the simultaneous fit for all samples)

Table E.7. Fit Parameters Obtained from Fitting the Autocorrelation Functions of Non-EV-Bound mCherry2-WNT3a Mixed with 40 mM MβCD. The autocorrelation functions were fitted with Equation (7.1). All values are reported as mean ± *SD*. The time label corresponds to the middle of the time range in which the data were taken.

Parameter	11 min	31 min	51 min	71 min	91 min	111 min
Sample 1						
N	5.74 ± 0.04	5.73 ± 0.04	5.78 ± 0.04	5.84 ± 0.04	5.81 ± 0.04	5.88 ± 0.05
τ_D / µs	902 ± 22	855 ± 21	849 ± 21	812 ± 20	827 ± 20	815 ± 20
f_F†	0.31 ± 0.01					
τ_F† / µs	109 ± 2					
χ^2_μ	2.0×10^{-5}					
R^2	0.998	0.999	0.999	0.998	0.998	0.998
Sample 2						
N	3.52 ± 0.02	3.88 ± 0.03	4.00 ± 0.03	4.21 ± 0.03	4.36 ± 0.03	4.42 ± 0.03
τ_D / µs	878 ± 16	808 ± 15	781 ± 15	800 ± 16	761 ± 15	774 ± 16
f_F†	0.31 ± 0.01					
τ_F† / µs	109 ± 2					
χ^2_μ	2.0×10^{-5}					
R^2	0.998	0.999	0.998	0.999	0.998	0.998
Sample 3						
N	6.00 ± 0.05	5.86 ± 0.04	5.93 ± 0.05	5.99 ± 0.05	5.97 ± 0.05	6.11 ± 0.05
τ_D / µs	933 ± 24	887 ± 22	878 ± 22	883 ± 22	838 ± 21	878 ± 23
f_F†	0.31 ± 0.01					
τ_F† / µs	109 ± 2					
χ^2_μ	2.0×10^{-5}					
R^2	0.998	0.998	0.999	0.998	0.998	0.998

† Global parameters (shared across the simultaneous fit for all sample types)

Table E.8. Normalized Diffusional Correlation Times of Individual Samples of Non-EV-Bound mCherry2-WNT3a After MβCD Applications. All values are reported as mean ± *SD*. The time label corresponds to the middle of the time range in which the data were taken.

$C_{\mathrm{M\beta CD}}$ / mM	t / min	Sample 1	Sample 2	Sample 3	Mean
10	0	1.00 ± 0.06	1.00 ± 0.06	1.00 ± 0.06	1.00 ± 0.06¥
	11	0.93 ± 0.04	0.93 ± 0.05	0.92 ± 0.04	0.93 ± 0.01
	31	0.91 ± 0.04	0.94 ± 0.05	0.90 ± 0.04	0.91 ± 0.02
	51	0.86 ± 0.04	0.92 ± 0.04	0.86 ± 0.04	0.88 ± 0.03
	71	0.89 ± 0.04	0.89 ± 0.04	0.87 ± 0.04	0.88 ± 0.02
	91	0.84 ± 0.04	0.91 ± 0.05	0.84 ± 0.04	0.86 ± 0.04
	111	0.86 ± 0.04	0.90 ± 0.04	0.88 ± 0.04	0.88 ± 0.02

$C_{\mathrm{M\beta CD}}$ / mM	t / min	Sample 1	Sample 2	Sample 3	Mean
40	0	1.00 ± 0.05	1.00 ± 0.05	1.00 ± 0.05	1.00 ± 0.05¥
	11	0.86 ± 0.04	0.86 ± 0.04	0.87 ± 0.04	0.86 ± 0.00
	31	0.82 ± 0.04	0.79 ± 0.03	0.82 ± 0.04	0.81 ± 0.02
	51	0.81 ± 0.04	0.77 ± 0.03	0.81 ± 0.04	0.80 ± 0.03
	71	0.78 ± 0.03	0.78 ± 0.03	0.82 ± 0.04	0.79 ± 0.02
	91	0.79 ± 0.04	0.75 ± 0.03	0.78 ± 0.03	0.77 ± 0.02
	111	0.78 ± 0.03	0.76 ± 0.03	0.81 ± 0.04	0.78 ± 0.03

¥ *SD* was taken as the average *SD* from the fits of individual samples
Abbreviation: Concentration of MβCD is abbreviated as $C_{\mathrm{M\beta CD}}$ in this table.

E.1.3 Non-EV-bound mCherry2-WNT5a

Table E.9. Fit Parameters Obtained from Fitting the Autocorrelation Functions of Non-EV-Bound mCherry2-WNT5a Mixed with DPBS (0 mM MβCD). The autocorrelation functions were fitted with Equation (7.1). All values are reported as mean ± *SD*.

Parameter	Sample 1	Sample 2	Sample 3	Sample 4
N	5.45 ± 0.04	5.50 ± 0.04	5.32 ± 0.04	6.21 ± 0.05
τ_D / µs	967 ± 17	935 ± 16	983 ± 17	1120 ± 21
f_F†	0.29 ± 0.01			
τ_F† / µs	110 ± 3			
χ^2_μ	5.7×10^{-6}			
R^2	0.999	0.999	0.999	0.999

† Global parameters (shared across the simultaneous fit for all samples)

Table E.10. Fit Parameters Obtained from Fitting the Autocorrelation Functions of Non-EV-Bound mCherry2-WNT5a Mixed with 10 mM MβCD. The autocorrelation functions were fitted with Equation (7.1). All values are reported as mean ± *SD*. The time label corresponds to the middle of the time range in which the data were taken.

Parameter	11 min	31 min	51 min	71 min	91 min	111 min
Sample 1						
N	5.55 ± 0.04	5.65 ± 0.04	5.78 ± 0.04	5.77 ± 0.04	5.89 ± 0.04	5.82 ± 0.04
τ_D / µs	971 ± 24	966 ± 24	919 ± 24	916 ± 23	934 ± 24	875 ± 23
f_F†	0.30 ± 0.01					
τ_F† / µs	110 ± 2					
χ^2_μ	2.3×10^{-5}					
R^2	0.998	0.998	0.998	0.997	0.998	0.998
Sample 2						
N	5.43 ± 0.04	5.39 ± 0.04	5.40 ± 0.04	5.58 ± 0.04	5.57 ± 0.04	5.65 ± 0.04
τ_D / µs	987 ± 24	934 ± 23	894 ± 22	876 ± 22	894 ± 22	876 ± 22
f_F†	0.30 ± 0.01					
τ_F† / µs	110 ± 2					

Parameter	11 min	31 min	51 min	71 min	91 min	111 min
χ_μ^2	2.3×10^{-5}					
R^2	0.998	0.998	0.998	0.997	0.998	0.998
Sample 2						
N	5.43 ± 0.04	5.39 ± 0.04	5.40 ± 0.04	5.58 ± 0.04	5.57 ± 0.04	5.65 ± 0.04
τ_D / µs	987 ± 24	934 ± 23	894 ± 22	876 ± 22	894 ± 22	876 ± 22
$f_F{}^\dagger$	0.30 ± 0.01					
$\tau_F{}^\dagger$ / µs	110 ± 2					
χ_μ^2	2.3×10^{-5}					
R^2	0.999	0.998	0.998	0.998	0.998	0.998
Sample 3						
N	5.57 ± 0.04	5.67 ± 0.04	5.73 ± 0.04	5.64 ± 0.04	5.81 ± 0.04	5.70 ± 0.04
τ_D / µs	973 ± 24	942 ± 24	899 ± 23	866 ± 22	863 ± 22	790 ± 20
$f_F{}^\dagger$	0.30 ± 0.01					
$\tau_F{}^\dagger$ / µs	110 ± 2					
χ_μ^2	2.3×10^{-5}					
R^2	0.998	0.998	0.998	0.997	0.998	0.992
Sample 4						
N	5.60 ± 0.04	5.50 ± 0.04	5.61 ± 0.04	5.53 ± 0.04	5.67 ± 0.04	5.57 ± 0.04
τ_D / µs	1,072 ± 27	991 ± 25	984 ± 25	984 ± 24	982 ± 25	917 ± 23
$f_F{}^\dagger$	0.30 ± 0.01					
$\tau_F{}^\dagger$ / µs	110 ± 2					
χ_μ^2	2.3×10^{-5}					
R^2	0.997	0.997	0.998	0.997	0.996	0.998

† Global parameters (shared across the simultaneous fit for all samples)

Table E.11. Fit Parameters Obtained from Fitting the Autocorrelation Functions of Non-EV-Bound mCherry2-WNT5a Mixed with 40 mM MβCD. The autocorrelation functions were fitted with Equation (7.1). All values are reported as mean ± *SD*. The time label corresponds to the middle of the time range in which the data were taken.

Parameter	11 min	31 min	51 min	71 min	91 min	111 min
Sample 1						
N	5.40 ± 0.04	5.52 ± 0.05	5.68 ± 0.05	5.68 ± 0.05	5.66 ± 0.05	5.68 ± 0.05
τ_D / µs	925 ± 25	847 ± 23	851 ± 24	814 ± 23	838 ± 23	814 ± 23
$f_F{}^\dagger$	0.30 ± 0.01					
$\tau_F{}^\dagger$ / µs	107 ± 3					
χ_μ^2	2.8×10^{-5}					
R^2	0.998	0.998	0.998	0.999	0.997	0.998
Sample 2						
N	5.54 ± 0.04	5.37 ± 0.04	5.36 ± 0.04	5.36 ± 0.04	5.37 ± 0.04	5.71 ± 0.05
τ_D / µs	967 ± 27	883 ± 24	826 ± 22	815 ± 22	823 ± 22	921 ± 26
$f_F{}^\dagger$	0.30 ± 0.01					

Parameter	11 min	31 min	51 min	71 min	91 min	111 min
τ_F† / µs	107 ± 3					
χ^2_μ	2.8×10^{-5}					
R^2	0.997	0.998	0.998	0.998	0.998	0.993
Sample 3						
N	5.71 ± 0.05	5.80 ± 0.05	5.83 ± 0.05	5.98 ± 0.05	5.98 ± 0.05	5.88 ± 0.05
τ_D / µs	920 ± 26	818 ± 23	799 ± 23	816 ± 24	804 ± 23	769 ± 22
f_F†	0.30 ± 0.01					
τ_F† / µs	107 ± 3					
χ^2_μ	2.8×10^{-5}					
R^2	0.998	0.999	0.998	0.998	0.997	0.997
Sample 4						
N	4.37 ± 0.03	4.46 ± 0.03	4.62 ± 0.04	4.77 ± 0.04	4.72 ± 0.04	4.81 ± 0.04
τ_D / µs	942 ± 22	847 ± 20	805 ± 19	842 ± 21	737 ± 18	772 ± 19
f_F†	0.30 ± 0.01					
τ_F† / µs	107 ± 3					
χ^2_μ	2.8×10^{-5}					
R^2	0.997	0.995	0.997	0.995	0.997	0.997

† Global parameters (shared across the simultaneous fit for all samples)

Table E.12. Normalized Diffusional Correlation Times of Individual Samples of Non-EV-Bound mCherry2-WNT5a After MβCD Applications. All values are reported as mean ± *SD*. The time label corresponds to the middle of the time range in which the data were taken.

$C_{\mathrm{M\beta CD}}$ / mM	t / min	Sample 1	Sample 2	Sample 3	Sample 4	Mean
10	0	1.00 ± 0.06	1.00 ± 0.06	1.00 ± 0.06	1.00 ± 0.06	1.00 ± 0.06¥
	11	0.91 ± 0.04	0.96 ± 0.05	0.90 ± 0.04	0.87 ± 0.04	0.91 ± 0.04
	31	0.91 ± 0.04	0.91 ± 0.04	0.87 ± 0.04	0.80 ± 0.04	0.87 ± 0.05
	51	0.86 ± 0.04	0.87 ± 0.04	0.83 ± 0.04	0.80 ± 0.04	0.84 ± 0.03
	71	0.86 ± 0.04	0.85 ± 0.04	0.80 ± 0.04	0.80 ± 0.04	0.83 ± 0.03
	91	0.88 ± 0.04	0.87 ± 0.04	0.80 ± 0.04	0.80 ± 0.04	0.83 ± 0.04
	111	0.82 ± 0.04	0.85 ± 0.04	0.73 ± 0.04	0.74 ± 0.04	0.79 ± 0.06
40	0	1.00 ± 0.05	1.00 ± 0.05	1.00 ± 0.05	1.00 ± 0.05	1.00 ± 0.05¥
	11	0.81 ± 0.04	0.88 ± 0.04	0.80 ± 0.04	0.72 ± 0.03	0.80 ± 0.07
	31	0.75 ± 0.03	0.80 ± 0.04	0.71 ± 0.03	0.64 ± 0.03	0.73 ± 0.07
	51	0.75 ± 0.03	0.75 ± 0.03	0.69 ± 0.03	0.61 ± 0.03	0.70 ± 0.07
	71	0.72 ± 0.03	0.74 ± 0.03	0.71 ± 0.03	0.64 ± 0.03	0.70 ± 0.04
	91	0.74 ± 0.03	0.75 ± 0.03	0.70 ± 0.03	0.56 ± 0.02	0.69 ± 0.09
	111	0.72 ± 0.03	0.84 ± 0.04	0.67 ± 0.03	0.59 ± 0.03	0.70 ± 0.11

¥ *SD* was taken as the average *SD* from the fits of individual samples

Abbreviation: Concentration of MβCD is abbreviated as $C_{\mathrm{M\beta CD}}$ in this table.

E.2 Positive Control for Dual-Color Fluorescence Cross-Correlation Spectroscopy

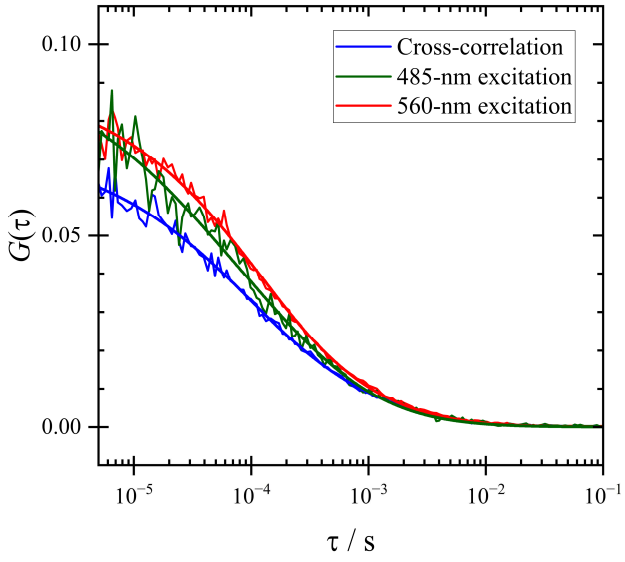

Figure E.1. Positive Control Demonstrating the Laser Focus Overlap for Dual-Color Fluorescence Cross-Correlation Spectroscopy Measurement. The figure shows individual autocorrelation functions ($G(\tau)$) from the 485-nm and 560-nm excitations, along with cross-correlation function from the signals from both excitations of purified tdTomato, which could be excited at both 485 nm and 560 nm (see the excitation spectrum in Appendix A).

E.3 Results of Individual Samples from Dual-Color Measurements with AB-CoralLite

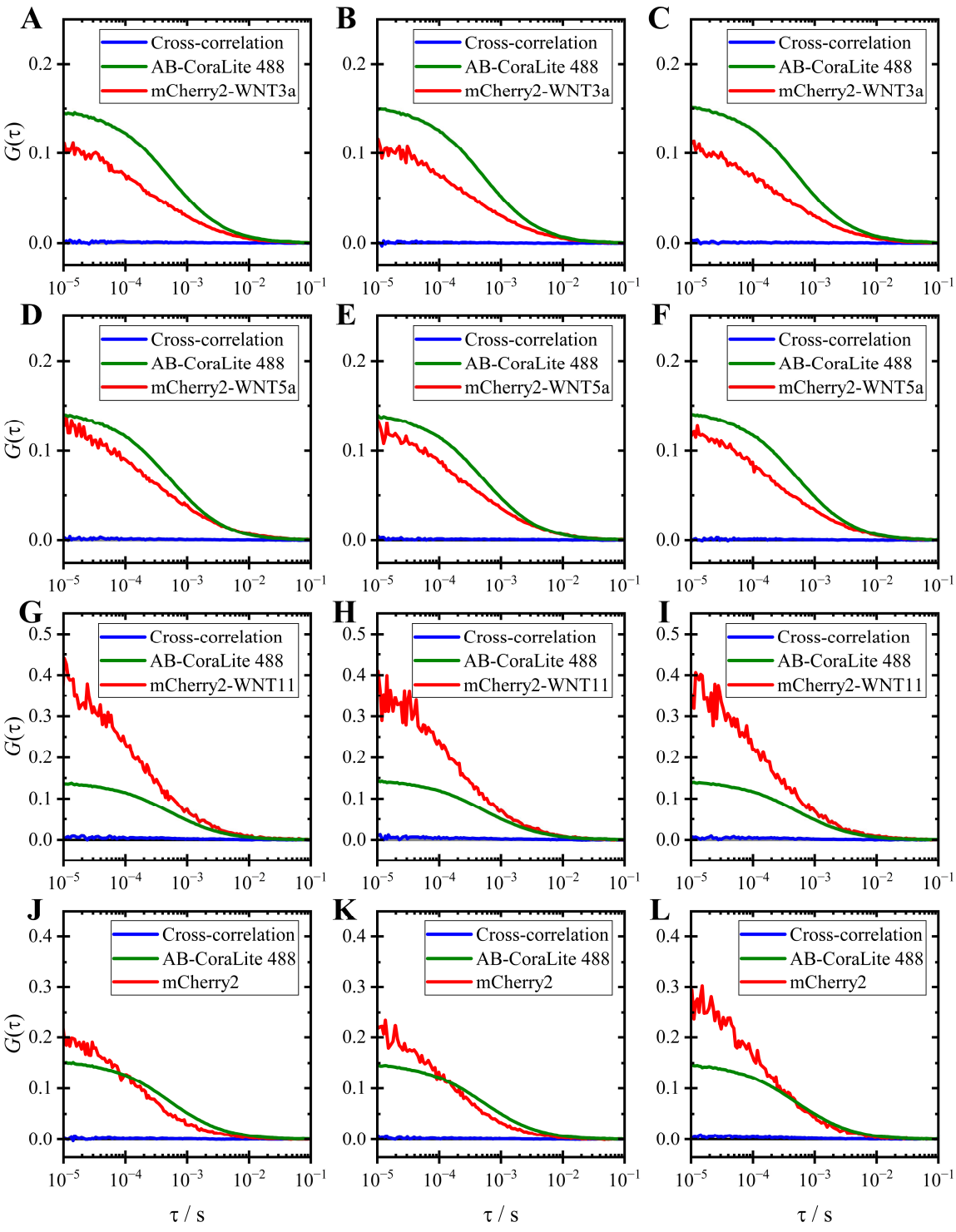

Figure E.2. Results of Individual Samples from Dual-Color Fluorescence Cross-Correlation Spectroscopy Measurements on Non-EV-Bound mCherry2-WNT3a/5a/11 Incubated with AB-CoraLite 488. A–C: mCherry2-WNT3a. D–F: mCherry2-WNT5a. G–I: mCherry2-WNT11. J–L: Purified mCherry2.

E.4 Individual Results and Fit Parameters from Dual-Color Measurements with AFAMIN-eGFP

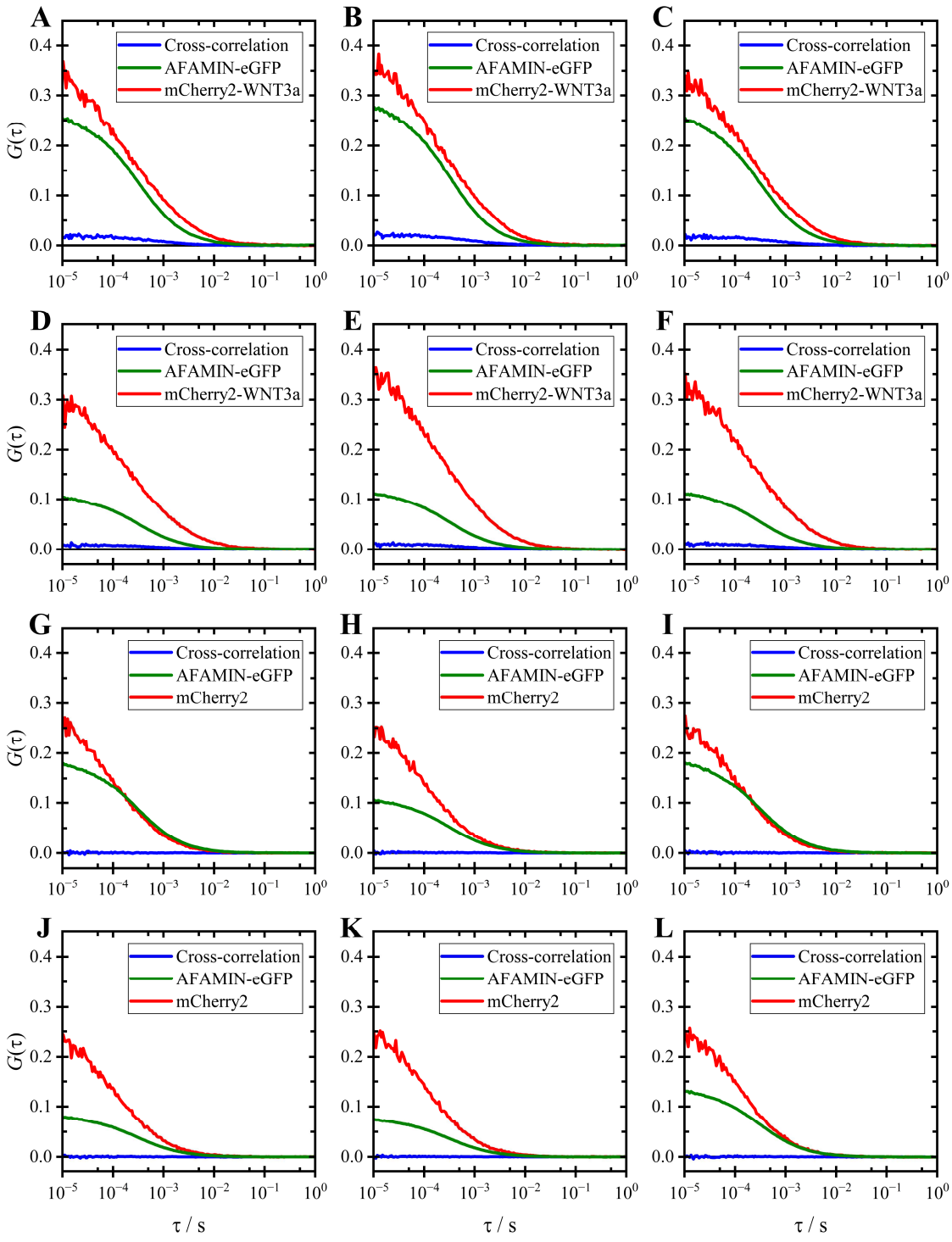

Figure E.3. Results of Individual Samples from Dual-Color Fluorescence Cross-Correlation Spectroscopy Measurements on WNT3a Proteins Co-Diffusing with AFAMIN (Continued on next page)

(Continued from previous page)

A–F: Cross-correlation functions ($G(\tau)$) obtained from conditioned medium collected from cells expressing mCherry2-WNT3a transfected with 0.75 µg (A–C) and 1.5 µg (D–F) AFAMIN-eGFP, compared to autocorrelation functions of each channel

G–L: Cross-correlation functions obtained from purified mCherry2 diluted in the negative control conditioned medium gathered from cells transfected and with 0.75 µg (A–C) and 1.5 µg (D–F) AFAMIN-eGFP, compared to autocorrelation functions of each channel.

Table E.13. Fit Parameters Obtained from Fitting the Autocorrelation and Cross-Correlation Functions of purified mCherry2 and AFAMIN-eGFP. The autocorrelation functions were fitted with Equation (6.2), and the cross-correlation functions were fitted with Equation (6.1). All values are reported as mean ± *SD*.

Plasmid / µg	Sample	N	D / µm² s⁻¹	w_0 / nm	f_F	τ_F † / µs	χ^2_μ	R^2
AFAMIN-eGFP								
0.75	1	6.23 ± 0.02	60.7 ± 0.4†	309 ± 11*	0.131 ± 0.003	74 ± 2	3.2 × 10⁻⁷	0.9999
	2	10.47 ± 0.04			0.120 ± 0.004			0.9999
	3	6.20 ± 0.02			0.136 ± 0.003			0.9998
1.5	1	14.21 ± 0.06			0.144 ± 0.004			0.9999
	2	14.95 ± 0.06			0.127 ± 0.005			0.9999
	3	8.49 ± 0.03			0.129 ± 0.003			0.9999
Purified mCherry2								
0.75	1	6.12 ± 0.05	102‡	355 ± 15*	0.416 ± 0.007	69 ± 2	1.5 × 10⁻⁵	0.9980
	2	6.24 ± 0.06			0.401 ± 0.007			0.9976
	3	5.89 ± 0.05			0.376 ± 0.007			0.9973
1.5	1	6.60 ± 0.06			0.400 ± 0.007			0.9977
	2	6.18 ± 0.05			0.391 ± 0.007			0.9976
	3	5.76 ± 0.05			0.349 ± 0.007			0.9976
Cross-Correlation								
0.75	1	1,406 ± 309	(0.7 ± 0.6) × 10⁶	333 ± 25**	-	-	4.7 × 10⁻⁷	0.0595
	2	950 ± 107	(0.2 ± 0.1) × 10⁶		-			0.2897
	3	371 ± 99	(10.2 ± 5.4) × 10⁶		-			0.2273
1.5	1	1,911 ± 433	(0.2 ± 0.2) × 10⁶		-			0.1033
	2	1,415 ± 229	(0.2 ± 0.1) × 10⁶		-			0.1868
	3	2,025 ± 408	(0.1 ± 0.1) × 10⁶		-			0.0983

* Fixed parameter (uncertainties not included), obtained from calibration measurements on tdTomato (based on the estimated diffusion coefficient of 81 µm² s⁻¹, calculated from the molecular mass of tdTomato and the diffusion coefficient of GFP-like fluorescent protein at 25°C)

** Fixed parameter (uncertainties not included), obtained from the the root mean square of w_0 of both lasers

† Global parameters (shared across the simultaneous fit for all samples)

‡ Fixed parameter, calculated based on the reported value of 95 µm² s⁻¹ at 22.5 ± 0.5°C [115,163,167] (see Section 6.1)

Table E.14. Fit Parameters Obtained from Fitting the Autocorrelation and Cross-Correlation Functions of Non-EV-Bound mCherry2-WNT3a and AFAMIN-eGFP. The autocorrelation functions were fitted with Equation (6.2), and the cross-correlation functions were fitted with Equation (6.1). All values are reported as mean ± *SD*.

Plasmid / µg	Sample	N	D / µm² s⁻¹	w_0 / nm	f_F	τ_F† / µs	χ^2_μ	R^2
AFAMIN-eGFP								
0.75	1	4.36 ± 0.02	58.8 ± 0.5	309 ± 11*	0.128 ± 0.004	66 ± 2	7.7 × 10⁻⁷	0.9998
	2	3.97 ± 0.02	59.6 ± 0.4		0.121 ± 0.004			0.9999
	3	4.36 ± 0.02	61.3 ± 0.5		0.126 ± 0.004			0.9999
1.5	1	10.58 ± 0.08	62.0 ± 1.1		0.117 ± 0.009			0.9998
	2	9.95 ± 0.07	60.2 ± 1.0		0.127 ± 0.008			0.9999
	3	9.95 ± 0.07	59.7 ± 1.0		0.131 ± 0.008			0.9999
mCherry2-WNT3a								
0.75	1	4.80 ± 0.08	35.9 ± 1.4	355 ± 15*	0.413 ± 0.010	81 ± 2	3.0 × 10⁻⁵	0.9977
	2	4.28 ± 0.06	39.5 ± 1.4		0.382 ± 0.010			0.9981
	3	4.68 ± 0.08	43.4 ± 1.8		0.383 ± 0.012			0.9977
1.5	1	5.38 ± 0.10	41.1 ± 1.9		0.401 ± 0.013			0.9968
	2	4.56 ± 0.07	40.2 ± 1.6		0.408 ± 0.011			0.9978
	3	4.87 ± 0.08	40.5 ± 1.7		0.402 ± 0.011			0.9975
Cross-Correlation								
0.75	1	54.0 ± 0.6	39.0 ± 1.8	333 ± 25**	-	-	9.8 × 10⁻⁷	0.9740
	2	47.9 ± 0.4	36.1 ± 1.4		-			0.9807
	3	58.0 ± 0.7	41.6 ± 2.0		-			0.9687
1.5	1	116.5 ± 2.5	34.7 ± 3.3		-			0.9501
	2	98.2 ± 1.9	40.5 ± 3.3		-			0.9596
	3	94.5 ± 1.7	39.2 ± 3.1		-			0.9694

* Fixed parameter (uncertainties not included), obtained from calibration measurements on tdTomato (based on the estimated diffusion coefficient of 81 µm² s⁻¹, calculated from the molecular mass of tdTomato and the diffusion coefficient of GFP-like fluorescent protein at 25°C)

** Fixed parameter (uncertainties not included), obtained from the the root mean square of w_0 of both lasers

† Global parameters (shared across the simultaneous fit for all samples)

Table E.15. Concentration of Individual and Bound Fractions in Individual Samples. All values are reported as mean ± *SD*.

Sample	Concentration / nm			Bound Fraction / %
	AFAMIN-eGFP	mCherry2(-WNT3a)	Bound Species[†]	
mCherry2-WNT3a and AFAMIN-eGFP (0.75 µg)				
1	8.8 ± 0.5	6.4 ± 0.5	0.63 ± 0.08	9.8 ± 1.5
2	8.0 ± 0.5	5.7 ± 0.4	0.57 ± 0.08	10.0 ± 1.5
3	8.8 ± 0.5	6.3 ± 0.5	0.57 ± 0.08	9.1 ± 1.4
			Average[*]	9.6 ± 0.4
mCherry2-WNT3a and AFAMIN-eGFP (1.5 µg)				
1	21.4 ± 1.3	7.2 ± 0.5	0.79 ± 0.11	11.0 ± 1.7
2	20.1 ± 1.2	6.1 ± 0.4	0.75 ± 0.10	12.3 ± 1.9
3	20.1 ± 1.2	6.5 ± 0.5	0.83 ± 0.11	12.8 ± 2.0
			Average[*]	12.0 ± 0.7
Purified mCherry2 and AFAMIN-eGFP (0.75 µg)				
1	12.6 ± 0.8	8.2 ± 0.6	0.04 ± 0.01	0.5 ± 0.1
2	21.1 ± 1.3	8.3 ± 0.6	0.11 ± 0.02	1.3 ± 0.3
3	12.5 ± 0.8	7.9 ± 0.6	0.16 ± 0.05	2.0 ± 0.6
			Average[*]	1.0 ± 1.3
Purified mCherry2 and AFAMIN-eGFP (1.5 µg)				
1	28.7 ± 1.8	8.2 ± 0.6	0.08 ± 0.02	0.9 ± 0.2
2	30.2 ± 1.9	8.3 ± 0.6	0.11 ± 0.02	1.3 ± 0.3
3	17.1 ± 1.1	7.9 ± 0.6	0.04 ± 0.01	0.5 ± 0.1
			Average[*]	0.8 ± 0.9

[†] Calculated using Equation (2.42)

* Calculated using 1/*SD* of individual samples as the weight

Appendix F

Custom Programming Scripts

F.1 MATLAB script for reading data from Time-Correlated Single Photon Counting Card SPC-150

```
function [valid_Time] = getTime(Data,MT_unit)

        bINV = 7;
        bFLAG = 4;
        bMTOV = 6;
        bFR = 22;
        bLN = 21;
        bPX = 20;

        phIdx = uint32(find(bitand(Data,pow2(bFLAG),'uint32') == 0)); % all photons
        phIdxV = uint32(find(bitand(Data,pow2(bINV) + pow2(bFLAG),'uint32') == 0)); % all
valid photons

        pxIdx = uint32(find(bitand(Data,pow2(bFLAG),'uint32') &
bitand(Data,pow2(bPX),'uint32'))); % pixel marker
        frIdx = uint32(find(bitand(Data,pow2(bFLAG),'uint32') &
bitand(Data,pow2(bFR),'uint32'))); % frame marker

        % Micro Time (bhmtcalc)
        MicT = pow2(12) - 1 - bitshift(bitand(Data, pow2(4)-1),8) - bitand(bitshift(Data,-
8), pow2(8)-1);

        % Macro Time
        b_inv = bitand(bitshift(Data,-bINV),1,'uint32');
        b_ov = bitand(bitshift(Data,-bMTOV),1,'uint32');
        b_fl = bitand(bitshift(Data,-bFLAG),1,'uint32');

        d_l = bitshift(bitand(bitshift(Data, -16), pow2(4)-1, 'uint32'),8); %calc bits 9:12
        d_h = bitand(bitshift(Data,-24), pow2(8)-1, 'uint32'); %calc bits 1:8



        % single overflow MTOV = 1 with FLAG = 1
        mt_sovf = b_inv.*b_ov.*b_fl.*pow2(12);
        mt_ov = cumsum(uint64(b_ov).*(uint64(mt_sov) + uint64(mt_mov) + uint64(mt_sovf)));
```

```
        %MT = uint32(mt_nov + mt_sov + mt_mov + mt_sovf);
        MT = uint64(mt_nov) + mt_ov;

        % Use this one if want to crop the peak
        bph = find(b_inv == 0 & b_fl == 0); % The valid photons... checked with the BKHK
and correct

        valid_MT = MT(bph); % Macro time for all valid photons
        valid_MT = round(valid_MT);
        valid_MT = double(valid_MT);
        valid_MT = valid_MT.*MT_unit; %in s


        valid_MicT = MicT(bph).*MT_unit./4095/1e-9; % Micro time for all valid photons in
ns
        valid_MicT = double(valid_MicT);

        % Output
        % Column 1 = macrotime (s)
        % Column 2 = microtime (ns)
        % Column 3 = position of the event
        valid_Time = [valid_MT, valid_MicT, bph];

end
```

F.2 MATLAB script for reading data from Time-Correlated Single Photon Counting Card HydraHarp 400

```
function [MT_photon_Det1, MicT_photon_Det1, MT_photon_Det2, MicT_photon_Det2, MT_marker_s,
Channel_marker] = Read_PTU(pathname,filename)

    % some constants
    tyEmpty8      = hex2dec('FFFF0008');
    tyBool8       = hex2dec('00000008');
    tyInt8        = hex2dec('10000008');
    tyBitSet64    = hex2dec('11000008');
    tyColor8      = hex2dec('12000008');
    tyFloat8      = hex2dec('20000008');
    tyTDateTime   = hex2dec('21000008');
    tyFloat8Array = hex2dec('2001FFFF');
    tyAnsiString  = hex2dec('4001FFFF');
    tyWideString  = hex2dec('4002FFFF');
    tyBinaryBlob  = hex2dec('FFFFFFFF');
    % RecordTypes
    rtPicoHarpT3     = hex2dec('00010303');% (SubID = $00 ,RecFmt: $01) (V1), T-Mode: $03
(T3), HW: $03 (PicoHarp)
    rtPicoHarpT2     = hex2dec('00010203');% (SubID = $00 ,RecFmt: $01) (V1), T-Mode: $02
(T2), HW: $03 (PicoHarp)
    rtHydraHarpT3    = hex2dec('00010304');% (SubID = $00 ,RecFmt: $01) (V1), T-Mode: $03
(T3), HW: $04 (HydraHarp)
    rtHydraHarpT2    = hex2dec('00010204');% (SubID = $00 ,RecFmt: $01) (V1), T-Mode: $02
(T2), HW: $04 (HydraHarp)
```

```
    rtHydraHarp2T3   = hex2dec('01010304');% (SubID = $01 ,RecFmt: $01) (V2), T-Mode: $03
(T3), HW: $04 (HydraHarp)
    rtHydraHarp2T2   = hex2dec('01010204');% (SubID = $01 ,RecFmt: $01) (V2), T-Mode: $02
(T2), HW: $04 (HydraHarp)
    rtTimeHarp260NT3 = hex2dec('00010305');% (SubID = $00 ,RecFmt: $01) (V1), T-Mode: $03
(T3), HW: $05 (TimeHarp260N)
    rtTimeHarp260NT2 = hex2dec('00010205');% (SubID = $00 ,RecFmt: $01) (V1), T-Mode: $02
(T2), HW: $05 (TimeHarp260N)
    rtTimeHarp260PT3 = hex2dec('00010306');% (SubID = $00 ,RecFmt: $01) (V1), T-Mode: $03
(T3), HW: $06 (TimeHarp260P)
    rtTimeHarp260PT2 = hex2dec('00010206');% (SubID = $00 ,RecFmt: $01) (V1), T-Mode: $02
(T2), HW: $06 (TimeHarp260P)
    rtMultiHarpT3    = hex2dec('00010307');% (SubID = $00 ,RecFmt: $01) (V1), T-Mode: $03
(T3), HW: $07 (MultiHarp)
    rtMultiHarpT2    = hex2dec('00010207');% (SubID = $00 ,RecFmt: $01) (V1), T-Mode: $02
(T2), HW: $07 (MultiHarp)

    % Globals for subroutines
    global fid
    global TTResultFormat_TTTRRecType;
    global TTResult_NumberOfRecords; % Number of TTTR Records in the File;
    global MeasDesc_Resolution;      % Resolution for the Dtime (T3 Only)
    global MeasDesc_GlobalResolution;

    TTResultFormat_TTTRRecType = 0;
    TTResult_NumberOfRecords = 0;
    MeasDesc_Resolution = 0;
    MeasDesc_GlobalResolution = 0;


    file2read = strcat(pathname,filename);
    fid=fopen(file2read);
    % Only to check whetehr the file exists - AM - seems to need this to read the file
header
    fprintf(1,'\n');
    Magic = fread(fid, 8, '*char');
    if not(strcmp(Magic(Magic~=0)','PQTTTR'))
        error('Magic invalid, this is not an PTU file.');
    end;


    % Check version = 1
    Version = fread(fid, 8, '*char');
    fprintf(1,'Tag Version: %s\n', Version);

    % there is no repeat.. until (or do..while) construct in matlab so we use
    % while 1 ... if (expr) break; end; end;
    while 1
        % read Tag Head
        TagIdent = fread(fid, 32, '*char'); % TagHead.Ident
        TagIdent = (TagIdent(TagIdent ~= 0))'; % remove #0 and more more readable
        TagIdx = fread(fid, 1, 'int32');    % TagHead.Idx
        TagTyp = fread(fid, 1, 'uint32');   % TagHead.Typ
                                            % TagHead.Value will be read in the
                                            % right type function
        TagIdent = genvarname(TagIdent);    % remove all illegal characters
        if TagIdx > -1
          EvalName = [TagIdent '(' int2str(TagIdx + 1) ')'];
        else
          EvalName = TagIdent;
        end
        fprintf(1,'\n   %-40s', EvalName);
        % check Typ of Header
        switch TagTyp
            case tyEmpty8
                fread(fid, 1, 'int64');
```

```
                %fprintf(1,'<Empty>');
            case tyBool8
                TagInt = fread(fid, 1, 'int64');
                if TagInt==0
                    %fprintf(1,'FALSE');
                    eval([EvalName '=false;']);
                else
                    %fprintf(1,'TRUE');
                    eval([EvalName '=true;']);
                end
            case tyInt8
                TagInt = fread(fid, 1, 'int64');
                %fprintf(1,'%d', TagInt);
                eval([EvalName '=TagInt;']);
            case tyBitSet64
                TagInt = fread(fid, 1, 'int64');
                %fprintf(1,'%X', TagInt);
                eval([EvalName '=TagInt;']);
            case tyColor8
                TagInt = fread(fid, 1, 'int64');
                %fprintf(1,'%X', TagInt);
                eval([EvalName '=TagInt;']);
            case tyFloat8
                TagFloat = fread(fid, 1, 'double');
                %fprintf(1, '%e', TagFloat);
                eval([EvalName '=TagFloat;']);
            case tyFloat8Array
                TagInt = fread(fid, 1, 'int64');
                %fprintf(1,'<Float array with %d Entries>', TagInt / 8);
                fseek(fid, TagInt, 'cof');
            case tyTDateTime
                TagFloat = fread(fid, 1, 'double');
                %fprintf(1, '%s', datestr(datenum(1899,12,30)+TagFloat)); % display as
Matlab Date String
                eval([EvalName '=datenum(1899,12,30)+TagFloat;']); % but keep in memory as
Matlab Date Number
            case tyAnsiString
                TagInt = fread(fid, 1, 'int64');
                TagString = fread(fid, TagInt, '*char');
                TagString = (TagString(TagString ~= 0))';
                %fprintf(1, '%s', TagString);
                if TagIdx > -1
                   EvalName = [TagIdent '{' int2str(TagIdx + 1) '}'];
                end;
                eval([EvalName '=[TagString];']);
            case tyWideString
                % Matlab does not support Widestrings at all, just read and
                % remove the 0's (up to current (2012))
                TagInt = fread(fid, 1, 'int64');
                TagString = fread(fid, TagInt, '*char');
                TagString = (TagString(TagString ~= 0))';
                %fprintf(1, '%s', TagString);
                if TagIdx > -1
                   EvalName = [TagIdent '{' int2str(TagIdx + 1) '}'];
                end;
                eval([EvalName '=[TagString];']);
            case tyBinaryBlob
                TagInt = fread(fid, 1, 'int64');
                %fprintf(1,'<Binary Blob with %d Bytes>', TagInt);
                fseek(fid, TagInt, 'cof');
            otherwise
                error('Illegal Type identifier found! Broken file?');
        end;
        if strcmp(TagIdent, 'Header_End')
            break
        end
```

```
    end


    global isT2;
    isT2 = false;


    fprintf('\n\n Start reading event data \n');
    tic;
    %% AM - Decode function
    global RecNum;
    T3WRAPAROUND = 1024;

    % AM - Let's try to make it fast
    % Read all data at once
    data = fread(fid,'ubit32');

    % Remove overflow
    index_NotOV = find(data ~= 4261412864); % Index of either photon or marker
    data_NotOV = data(data~= 4261412864); % Data of either photon or marker
    data_NotOV_bin =flip(de2bi(data_NotOV,32),2); % Convert data to binary

    % Find macrotime (nsync (Bit 23-32) + overflow correction(overflow
    % number x T3WRAPAROUND)) of both photons and markers
    pos_index_NotOV = 1:length(index_NotOV); pos_index_NotOV = pos_index_NotOV.';
    num_OV = index_NotOV - pos_index_NotOV; % Number of overflow before that photon/marker
= index of that photon/marker - number of photons/markers before that one
    MT = bi2de(data_NotOV_bin(:,23:32),'left-msb') + (num_OV*T3WRAPAROUND);

    % Find detector channel (detector 1 = channel 0, detector 2 = channel 1)
    Det = data_NotOV_bin(:,7)+1;

    % Find microtime channel (Bit 8-22)
    MicT = bi2de(data_NotOV_bin(:,8:22),'left-msb');

    % Select photon data and change unit to s
    Check_marker = data_NotOV_bin(:,1);
    pos_marker = find(Check_marker > 0);
    MT_photon = MT; MT_photon(pos_marker,:) = [];
    MT_photon_s = (MT_photon-1)*MeasDesc_GlobalResolution; % in s
    MicT_photon = MicT; MicT_photon(pos_marker,:) = [];
    MicT_photon_s = MicT_photon*MeasDesc_Resolution;
    Det_photon = Det; Det(pos_marker,:) = [];

    % Separate photons into 2 detector channels -- High resolution = 16 ps
    MicT_photon_s_Det1 = MicT_photon_s(Det_photon==1); MicT_photon_s_Det2 =
MicT_photon_s(Det_photon==2);
    MT_photon_Det1 = MT_photon_s(Det_photon==1); MicT_photon_Det1 =
MicT_photon(Det_photon==1);
    MT_photon_Det2 = MT_photon_s(Det_photon==2); MicT_photon_Det2 =
MicT_photon(Det_photon==2);
    MT_photon_Det1 = MT_photon_Det1 + MicT_photon_s_Det1;
    MT_photon_Det2 = MT_photon_Det2 + MicT_photon_s_Det2;


    % Select marker data
    MT_marker = MT(pos_marker);
    MT_marker_s = MT_marker*MeasDesc_GlobalResolution; % in s
    channel = bi2de(data_NotOV_bin(:,2:7),'left-msb');
    Channel_marker = channel(pos_marker);



    %fclose(fid);

    fprintf(1,'Ready!  \n\n');
```

```
    fprintf(1,'\nStatistics obtained from the data:\n');
    fprintf(1,'\n%i photons, %i overflows, %i markers.',length(MT_photon), length(data) -
length(index_NotOV), length(MT_marker));
    toc;

    fprintf(1,'\n');
end
```

F.3 MATLAB Script for N&B Analysis on Photon Arrival Time Data from Measurements with Stationary Laser Focus

```
function [NB_eps NB_n] = SegmentwiseNB(valid_MT,binT,I_bg_NB) % BC_Model = -1 for no bleaching
correction


    [Tr_data_NB] = Binning(valid_MT,binT);
    NB_mean = mean(Tr_data_NB(:,2)); NB_var = var(Tr_data_NB(:,2));
    NB_n = ((NB_mean - I_bg_NB)^2)/(NB_var - NB_mean);
    NB_eps = (NB_var - NB_mean)/(NB_mean - I_bg_NB)/binT/1e-6/1000; %kHz


end


function [Tr_data] = Binning(MT,binT)
% Input  - MT = an array of photon arrival time
%        - binT = bin time wanted in us
% Output - Tr_data (first colume = time, second colume = photon counts)

binT = binT*1e-6; % Change unit of bin time to s

% Make the variable Tr_data to keep the intensity-time trace
size_x = ceil(MT(end)/binT);

Tr_data = zeros(size_x, 4);
%Tr_data(:,1)      =      binT*(0:size_x-1);      Tr_data(:,1)      =      Tr_data(:,1)      +
ones(size(Tr_data,1),1).*binT;
Tr_data(:,1) = binT*(1:size_x);

% Calculate number of photons with respect to their bins
% mtbindata = ceil(MT/binT)+1; % Find out at which bin the photons are - Shift the bin by 1
for all to prevent getting bin = 0. shouldn't matter for correlation (and N&B)
% mtidx = find(diff(mtbindata));

mtbindata = ceil(MT/binT); % by using ceil() you will never get bin=0
mtidx = [find(diff(mtbindata)); size_x]; % properly count events for the last bin

Tr_data(mtbindata(mtidx),2) = [mtidx(1); diff(mtidx)];
end
```

F.4 MATLAB Script for Scanning N&B Analysis with Sliding-Window Algorithm

```
% INPUT

cd 'mScarlet in pcDNA-exo'\; % subfolder name
BG = 230; % background (Hz)
Size_box = 1e6; % window size
Size_step = 1e3; % step for shifting the window
size_x = 400; size_y = 400; %number of pixels in each dimension
t_dw = 30e-6; % pixel dwell time (s)

%% READ THE DATA AND INITIALIZATION

fileList = dir('*.tif');
N_Frame = length(fileList);

% Matrix I for intensity
I = zeros(size_x,size_y,N_Frame);
for k = 1:N_Frame
    I1 = imread(fileList(k).name); % Read the images for frame k
    I(:,:,k) = I1;
end

I_1D_rawDat = reshape(I,[],1); % Put photons count into 1-D array.
I_bg = BG*t_dw; % Prepare BG per pixel dweill time

% Number of step to ship in one box
N_shift_1box = Size_box/Size_step;
% sN&B WITH SLIDING BOX CAR

% Set the box
N_box = floor(length(I_1D_rawDat)/Size_box);  I_1D = I_1D_rawDat(1:N_box*Size_box);
if mod(N_box,1) > 0
    fprintf('Select new box size\n');
end

% Slide the box
for j = 1:N_shift_1box

    if j == 1
        I_box = reshape(I_1D,Size_box,[]);
        mean_I_box_1 = mean(I_box,1);
        var_I_box_1 = var(I_box,0,1);
    else
        i1 = j*Size_step; i2 = (j*Size_step) + ((N_box-1)*Size_box) - 1;
        I_box = I_1D(i1:i2);
        I_box = reshape(I_box,Size_box,[]);
        mean_I_box(j-1,:) = mean(I_box,1);
        var_I_box(j-1,:) = var(I_box,0,1);
    end
end

% Put the result together in a 1-D (column) matrix
mean_I_box_1 = mean_I_box_1.'; var_I_box_1 = var_I_box_1.';
mean_I_box = reshape(mean_I_box,[],1); var_I_box = reshape(var_I_box,[],1);
mean_I = [mean_I_box_1;mean_I_box]; var_I = [var_I_box_1;var_I_box];

% N&B formulae
n = ((mean_I-I_bg).^2)./(var_I-mean_I);
eps = (var_I-mean_I)./(mean_I-I_bg)/t_dw/1e3 % kHz
```

```
%% OUTLIER REMOVAL AND AVERAGING

mean_n = mean(n)
n_remOut = rmoutliers(n);
mean_n_rmOut = mean(n_remOut)
SD_n = std(n,0,"all"); SD_n_remOut = std(n_remOut,0,"all");

mean_eps = mean(eps)
eps_remOut = rmoutliers(eps);
mean_eps_remOut = mean(eps_remOut)
SD_eps = std(eps,0,"all"); SD_eps_remOut = std(eps_remOut,0,"all");
```

F.5 MATLAB Script for Automated Segment Selection in Determining Molecular Brightness of Fluorescent Proteins Expressed in the Cytosol of Living Cells

```
function [Rem1] = SelectSegmentFCS(CorrV,FCS_binT)

if FCS_binT == 10
    limT0 = 2; limT1 = 63;
elseif FCS_binT == 5
    limT0 = 4; limT1 = 71;
elseif FCS_binT == 1
    limT0 = 17; limT1 = 116;
else
    error('need to pick new index for FCS segment selection (function: SelectSegmentFCS)');
end


% Calculate mean autocorrelation value between t = 1-20 us
mean_V0 = nanmean(CorrV(1:limT0,:),'all');

% CONDITION
% Calculate mean autocorrelation value after t = 0.01 s
mean_V1 = nanmean(CorrV(limT1:end,:),1);

if sqrt(var(mean_V1)) >= 0.05*mean_V0
    % Remove the curves with correlation values between t = 0.01-1 s more than SD.
    Rem1 = find(mean_V1>=sqrt(var(mean_V1))); %Can change the coefficient, depend on how
strict the critirian should be
else
    Rem1 = -1;
end
end
```

F.6 Python script for cluster removal (for determining the molecular brightness of EVs)

```
import os
import cv2
import numpy as np
from PIL import Image, ImageDraw, ImageFont
from sklearn.cluster import DBSCAN


# Global variables
# ----------------------------------------------------------------
# Threshold value of brightness
threshold = 1.5

# Float value representing the maximum distance of two pixels so that they are still being
seen as close to each other
eps_value = 4

# The number of samples needed close to each other to be considered a cluster
min_samples = 22

# Integer indicating how much around a pixel of a cluster is supposed to be removed.
removalRadius = 4

# Whether to save a reference picture in .png format
saveRefPng = False

# Whether to save a reference picture in black and white in the .tiff format
saveRefTiff = True

# Find clusters in an image and turns them black.
def clustersFindMark(imagePath):
    # Read the image with a 32-bit depth.
    img = cv2.imread(imagePath, flags=(cv2.IMREAD_ANYDEPTH))

    height, width = img.shape[:2]

    # Change from 32-bit to 8-bit for cv2.threshold() function
    img8Bit = img.astype(np.uint8)

    # Load the image again as a .png and convert it to RGB so we can
    # colour it as a reference image later, marking in bright green
    # where we removed a cluster.
    referenceImage = Image.open(imagePath).convert("RGB")
    referenceImage_tiff = np.zeros((height, width), dtype=np.uint8)

    # Threshold the 8bit variant of the image to find pixels of interest
    _, binary = cv2.threshold(img8Bit, threshold, 255, cv2.THRESH_BINARY)

    # Coordinates of pixels that are bright enough to be considered for being part of a
cluster
    brightPixels = np.column_stack(np.where(binary > 0))

    # Identify outlines (contours)
    outlines, _ = cv2.findContours(binary, cv2.RETR_EXTERNAL, cv2.CHAIN_APPROX_SIMPLE)

    numberOfClusters = 0

    # Find and take care of clusters
    if (len(brightPixels) != 0):
```

```
        # Apply DBSCAN to find clusters
        dbscan = DBSCAN(eps=eps_value, min_samples=min_samples)
        dbscan.fit(brightPixels)

        # Amount of clusters in the picture
        numberOfClusters = len(np.unique(dbscan.labels_)) - 1

        # Remove clusters and mark them on the reference picture
        for label in np.unique(dbscan.labels_):
            # Element is noise and will be skipped
            if label == -1:
                continue

            # Get all pixels (in form of their coordinates) that are in a
            # cluster that has to be erased and turn them black for the
            # output image and mark them green for the reference picture.
            clusterMask = dbscan.labels_ == label
            clusters = brightPixels[clusterMask]

            for x, y in clusters:
                # Draw a black circle in the output picture
                # (with radius 'removalRadius') around the
                # current pixel that is part of a cluster.
                # cv2.circle(img, (y, x),  removalRadius, (0, 0, 0), -1)
                #img[y, x] = 0

                # Mark the cluster pixels in the reference pictures, if the option is enabled
                if saveRefPng:
                    referenceImage.putpixel((y, x), (0, 255, 0))
                    ImageDraw.Draw(referenceImage).ellipse([y   -   removalRadius,   x   -
removalRadius,
                                                            y   +   removalRadius,   x   +
removalRadius],
                                                           outline = (0, 0, 255),
                                                           fill = (0, 0, 255),
                                                           width = 1)

                    # Write the number of clusters in the bottom right corner
                    '''ImageDraw.Draw(referenceImage).text((width * 0.94, height * 0.94),
                                                        str(numberOfClusters),
                                                        fill=(255, 255, 0),

font=ImageFont.truetype("calibri.ttf", 12))'''

                if saveRefTiff:
                    # Set only the single coordinate white
                    # referenceImage_tiff[y, x] = 255

                    # Draw the whole erasure circle
                    cv2.circle(referenceImage_tiff,   (y,   x),   removalRadius,   color=255,
thickness = -1)


    # Make a filename for the output image, based on input filename
    currentFolderName = os.path.basename(os.path.dirname(imagePath))
    filename, extension = os.path.splitext(os.path.basename(imagePath))
    outputFilename = f"results/{currentFolderName}/{filename}_clustered{extension}"

    # Save the output image
    cv2.imwrite(outputFilename, img)

    # Saving the references images
    # Save the .png version of the reference image
    if saveRefPng:
        outputFilename = f"results/{currentFolderName}/reference/{filename}_ref.png"
        referenceImage.save(outputFilename)
```

```
    # Save the .tiff version of the reference image
    if saveRefTiff:
        outputFilename = f"results/{currentFolderName}/reference/{filename}_ref.tiff"
        #referenceImage_tiff.save(outputFilename)
        cv2.imwrite(outputFilename, referenceImage_tiff)

# Go through the input folder, lists all .tif / .tiff image files and then processes these
images

def processInputFolder(folderPath):
    # List all files in the folder
    files = os.listdir(folderPath)

    # Filter the folder for .tif / .tiff image files
    imageList = [f for f in files if f.lower().endswith(('.tif', '.tiff'))]

    # Iterate through all the images in the input folder and process them
    for image in imageList:
        imagePath = os.path.join(folderPath, image)
        clustersFindMark(imagePath)


# Current directory of the project
directory = os.path.dirname(__file__)

# Path to the folder containing the input images
inputFolder = os.path.join(directory, "images")

# Path that will contain the output images
resultsFolder = os.path.join(directory, "results")

# Get all the Folders in the inputFolder
subFolders = [f.path for f in os.scandir(inputFolder) if f.is_dir()]

# Create a corresponding folder for each one in the input folder and then process the currently
looked at input subfolder
for subfolder in subFolders:
    subfolderName = os.path.basename(subfolder)
    folderPath = f"{resultsFolder}/{subfolderName}/reference"
    if not os.path.isdir(folderPath):
        os.makedirs(folderPath, mode=0o700, exist_ok=True)

    # Process all images in the current input subfolder
    currentInputFolder = os.path.join(inputFolder, subfolderName)
    processInputFolder(currentInputFolder)
```

F.7 MATLAB Script for Calculating the Objective Function in FIDA to Fit Data from Calibration Measurements of Alexa Fluor 546

```
function objective = Calibration_FIDA(a1_value, B0_value)

N = 5.19;
q_value = 2369; % EPS from FCS - per s
```

```
x =
[7005537;2406073;496598;79226;11059;1350;143;13;4;0;0;0;0;0;0;0;0;0;0;0;0;0;0;0;0;0;0;0;0;0;0;0
;0];

[a2_value, a3_value] = Normalization_B_moments(a1_value, B0_value);
T_value = 30e-6; % bin time - s
lambda = 200; % BG - per s
C = N/((2*a1_value)+(8*a2_value/3)+(4*a3_value));
PCH_Nevents = x./sum(x);
PCH_Nphotons = 0:1:length(PCH_Nevents)-1; PCH_Nphotons = PCH_Nphotons.';

%%PCH_Nevents,

% B0_value = Calculate_B0(a1_value,a2_value,a3_value);
% Convert G(phi) to P(n) - Inverse Fourier transform
N_step_in_Pi = 1000;
phi = 0:pi/N_step_in_Pi:2*pi;
for i = 1:1:length(phi)
    G(i) = Calculate_G(phi(i),q_value,B0_value,T_value,lambda,a1_value,a2_value,a3_value,
C);
end
G1 = G(1:length(phi)-1); G2 = G(2:length(phi)); G_mid = (G1+G2)./2;
phi1 = phi(1:length(phi)-1); phi2 = phi(2:length(phi)); phi_mid = (phi1+phi2)./2;
for n = 1:1:length(PCH_Nphotons)
    e_phi = exp((-complex(0,1)*PCH_Nphotons(n))*phi_mid);
    P_n(n) = real((1/2/pi)*sum(G_mid.*e_phi.*(pi/N_step_in_Pi)));
end

P_n(P_n<0) = 0;
P_n_norm = P_n./sum(P_n); P_n_norm = P_n_norm.';


objective = sum((((P_n_norm(PCH_Nevents>0) -
PCH_Nevents(PCH_Nevents>0))).^2)./PCH_Nevents(PCH_Nevents>0),'all');

end

function [a2_value, a3_value] = Normalization_B_moments(a1_value, B0_value)

syms a2 a3
eqn1 = B0_value*(1.4060*a1_value + 3.3534*a2 + 11.1427*a3) == -1;
eqn2 = (B0_value^2)*(0.2271*a1_value + 0.1905*a2 + 0.0874*a3) == 1;
sol = solve([eqn1,eqn2],[a2,a3]);
a2_value = double(real(sol.a2(1))); a3_value = double(real(sol.a3(1)));

end

function [G] = Calculate_G
(phi_value,q_value,B0_value,T_value,lambda,a1_value,a2_value,a3_value, C)
% calculate f1 and G
f1_in = @(x,phi,q,B0,T,a1,a2,a3) exp((((exp(complex(0,phi)))-1)*q*B0*T*exp(-x)) -
1).*(a1.*x + a2.*x.^2 + a3.*x.^3);
for i = 1:length(C)
    f1(i) = integral(@(x)
f1_in(x,phi_value,q_value,B0_value,T_value,a1_value,a2_value,a3_value), 0, 2);
end
G = exp((((exp(complex(0,phi_value)))-1)*lambda*T_value) + (sum(C.*f1)));
end
```

F.8 MATLAB Script for Calculating the Objective Function in FIDA to Fit Data from Monomeric Reference mScarlet

```
function objective = FIDA_mScarlet(q_value)

a1_value = 6.575;
a2_value = -6.277;
a3_value = 1.004;
B0_value = 1.611;
N = 4.20;
x = 
[2503633;1112863;302596;65887;12361;2229;358;64;7;2;0;0;0;0;0;0;0;0;0;0;0;0;0;0;0;0;0;0;0;0
;0;0;0;0;0;0;0;0;0;0;0;0;0;0;0;0;0;0;0;0;0];

T_value = 30e-6; % s
lambda = 400; % per s
C = N/((2*a1_value)+(8*a2_value/3)+(4*a3_value));
PCH_Nevents = x./sum(x);
PCH_Nphotons = 0:1:length(PCH_Nevents)-1; PCH_Nphotons = PCH_Nphotons.';

%%PCH_Nevents,


% Convert G(phi) to P(n) - Inverse Fourier transform
N_step_in_Pi = 1000;
phi = 0:pi/N_step_in_Pi:2*pi;
for i = 1:1:length(phi)
    G(i) = Calculate_G(phi(i),q_value,B0_value,T_value,lambda,a1_value,a2_value,a3_value, 
C);
end
G1 = G(1:length(phi)-1); G2 = G(2:length(phi)); G_mid = (G1+G2)./2;
phi1 = phi(1:length(phi)-1); phi2 = phi(2:length(phi)); phi_mid = (phi1+phi2)./2;
for n = 1:1:length(PCH_Nphotons)
    e_phi = exp((-complex(0,1)*PCH_Nphotons(n))*phi_mid);
    P_n(n) = real((1/2/pi)*sum(G_mid.*e_phi.*(pi/N_step_in_Pi)));
end

P_n(P_n<0) = 0;
P_n_norm = P_n./sum(P_n); P_n_norm = P_n_norm.';


objective = sum((((P_n_norm(PCH_Nevents>0) - 
PCH_Nevents(PCH_Nevents>0))).^2)./PCH_Nevents(PCH_Nevents>0),'all');

end

function [G] = Calculate_G
(phi_value,q_value,B0_value,T_value,lambda,a1_value,a2_value,a3_value, C)
% calculate f1 and G
f1_in = @(x,phi,q,B0,T,a1,a2,a3) exp((((exp(complex(0,phi)))-1)*q*B0*T*exp(-x)) - 
1).*(a1.*x + a2.*x.^2 + a3.*x.^3);
for i = 1:length(C)
    f1(i) = integral(@(x) 
f1_in(x,phi_value,q_value,B0_value,T_value,a1_value,a2_value,a3_value), 0, 2);
end
G = exp((((exp(complex(0,phi_value)))-1)*lambda*T_value) + (sum(C.*f1)));
end
```

F.8 MATLAB Script for Calculating the Objective Function in FIDA to Fit Data from EVs

```
function objective = FIDA_EV(N1, N2, N3, N4, N5, N6)

a1_value = 9.99;
a2_value = -9.68;
a3_value = 1.59;
B0_value = 1.332;
q_Sc = 2849; % per s
lambda = 400; % per s
N = [N1; N2; N3; N4; N5; N6];
x =
[7862065;5183107;1973155;590076;160162;45190;14200;5451;2407;1226;636;330;208;121;93;42;34;
24;18;13;4;5;4;5;2;1;0;2;2;2;1;0;0;0;1;0;0;1;0;0;0;0;0;0;0;0;0;0;0;0;0;0;0;0;0;0;0;0;0;0;
0;0;0;0;0;0;0;0;0;0;0;0;0;0;0;0;0;0;0;0;0;0;0;0;0;0;0;0;0;0;0;0;0;0;0;0;0;0;0;0;0;0;0;0;
;0;0;0;0;0;0;0;0;0;0;0;0;0;0;0;0;0;0;0;0;0;0;0;0;0;0;0;0;0;0;0;0;0;0;0;0;0;0;0;0;0;0;0;
0;0;0;0;0;0;0;0;0;0;0;0;0;0;0;0;0;0;0;0;0;0;0;0;0;0;0;0;0;0;0;0;0;0;0;0;0;0;0;0;0;0;0;0
;0;0;0];

q_value = [q_Sc*1; q_Sc*20; q_Sc*60; q_Sc*150; q_Sc*300; q_Sc*600];

T_value = 30e-6; % s
C = zeros(length(N),1);
C = N./((2*a1_value)+(8*a2_value/3)+(4*a3_value));
PCH_Nevents = x./sum(x);
PCH_Nphotons = 0:1:length(PCH_Nevents)-1; PCH_Nphotons = PCH_Nphotons.';

%%PCH_Nevents,


% Convert G(phi) to P(n) - Inverse Fourier transform
N_step_in_Pi = 1000;
phi = 0:pi/N_step_in_Pi:2*pi;
for i = 1:1:length(phi)
    G(i) =
Calculate_G_mixed(phi(i),q_value,B0_value,T_value,lambda,a1_value,a2_value,a3_value,C);
end
G1 = G(1:length(phi)-1); G2 = G(2:length(phi)); G_mid = (G1+G2)./2;
phi1 = phi(1:length(phi)-1); phi2 = phi(2:length(phi)); phi_mid = (phi1+phi2)./2;
for n = 1:1:length(PCH_Nphotons)
    e_phi = exp((-complex(0,1)*PCH_Nphotons(n))*phi_mid);
    P_n(n) = real((1/2/pi)*sum(G_mid.*e_phi.*(pi/N_step_in_Pi)));
end

P_n(P_n<0) = 0;
P_n_norm = P_n./sum(P_n); P_n_norm = P_n_norm.';


objective = sum((((P_n_norm(PCH_Nevents>0) -
PCH_Nevents(PCH_Nevents>0))).^2)./PCH_Nevents(PCH_Nevents>0),'all');
objective = objective + sum((((P_n_norm(PCH_Nevents == 0) - PCH_Nevents(PCH_Nevents ==
0))).^2)./1e-7,'all'); % to enable the fitting at 0
end


function [G] = Calculate_G_mixed
(phi_value,q_value,B0_value,T_value,lambda,a1_value,a2_value,a3_value,C)
% calculate f1 and G
f1_in = @(x,phi,q,B0,T,a1,a2,a3) exp((((exp(complex(0,phi)))-1)*q*B0*T*exp(-x)) -
1).*(a1.*x + a2.*x.^2 + a3.*x.^3);
```

```
for i = 1:length(C)
    f1(i) = integral(@(x)
f1_in(x,phi_value,q_value(i),B0_value,T_value,a1_value,a2_value,a3_value), 0, 2);
    Gi(i) = C(i)*f1(i);
end
G = exp((((exp(complex(0,phi_value)))-1)*lambda*T_value) + (sum(Gi)));
end
```

F.9 MATLAB script for correlation calculation using multiple-tau algorithm

```
function[tau,G] = CorrelationCal(data1,data2)

delT = data1(2,1)-data1(1,1); % time resolution = original time bin

% Shorten the longer intensity trace
if length(data1) > length(data2)
   data1(length(data2)+1:end,:) = [];
elseif length(data1) < length(data2)
   data2(length(data1)+1:end,:) = [];
end

p = 16; q = 18;
N_pt = (p/2)*(q+1);  % total no of points in the correlation
t_m = zeros(N_pt,1); G = zeros(N_pt,1);

% Calculate lag time
for m = 1:(p/2)
    t_m(m) = m*delT;
end

for m = ((p/2)+1):((q+1)*(p/2))
    t_m(m) = t_m(m-1) + (delT*(2^floor(2*(m-1-(p/2))/p)));
end

% reconstruction of m_gap
    tidx = 1:N_pt;
    tp = max(0,floor((tidx'-1)/8)-1);
    m_gap(1:p/2) = round((1:p/2)'./pow2(tp(1:p/2)));
    m_gap(p/2+1:N_pt) = 1+round(t_m(p/2+1:N_pt)./pow2(tp(p/2+1:N_pt))/delT);

    % reconstruction of tau
    w = [0, 0.087463, 0.321928, 0.459432, 0.584963, 0.70044, 0.807355, 0.906891];
    w2 = repmat(0:q+3,[p/2, 1]);
    for wi = 1:size(w2,2)
        w2(:,wi) = w2(:,wi) + w';
    end

    w4 = floor(pow2(reshape(w2,[],1)));
    kr = find(diff(w4) == 0);
    w4(kr+1) = [];
    w4(N_pt+1:end) = [];

    tau = w4'*delT;

    F1 = data1(:,2); l1 = length(F1);
    F2 = data2(:,2); l2 = length(F2);
```

```
    for m = 1:p
        g1 = F1(1:l1-m_gap(m));
        g2 = F2(m_gap(m)+1:l2);
        G(m) = sum(g1.*g2)/sum(g1)/sum(g2)*(l1-m_gap(m));
    end

    % CALCULATE CORRELATION VALUES
    for i_g = 2:q


        F1 = sum(...
                reshape(...
                    F1(1:2*floor(length(F1)/2))...
                ,2,[]) ...
            ,1);

        F2 = sum(...
                reshape(...
                    F2(1:2*floor(length(F2)/2))...
                ,2,[])...
            ,1);

        for m = i_g*(p/2)+1:(i_g+1)*p/2
            g1 = F1(1:length(F1)-m_gap(m));
            g2 = F2(m_gap(m)+1:length(F2));
            G(m) = sum(g1.*g2)/sum(g1)/sum(g2)*(length(F1)-m_gap(m));
        end
    end


    % OUTPUT
    G = G - ones(length(G),1);
    tau = tau.';

    if nargin > 2
        Gq = interp1(tau, G, tauA, 'linear');
        tf = find(tauA > tau(N_pt), 1);
        Gq(tf:end) = 0;
        G = Gq;
        tau = tauA;
    end

end
```

F.10 MATLAB script for correlation calculation using time-tag-to-correlation algorithm

```
function[tau,G_Cross,G_Auto1,G_Auto2] =
CorrelationCal_TagTime(MT_photon_Det1,MT_photon_Det2,delT)

p = 16; q = 18;

for m = 1:p
    tau(m) = m*delT;
    [W1,T1] = round_MT(MT_photon_Det1,tau(m));
    [W2,T2] = round_MT(MT_photon_Det2,tau(m));
    meaT_tauUnit = max(max(T1),max(T2)); % M
```

```
    % Cross correlation
    [G1] = CorrCal(W1,T1,W2,T2+1,1,meaT_tauUnit); % Shift the photons from Ch 1
    [G2] = CorrCal(W2,T2,W1,T1+1,1,meaT_tauUnit); % Shift the photons from Ch 2
    G_Cross(m) = (meaT_tauUnit-1)*(G1+G2)/2;

    % Auto correlation
    [G_A1] = CorrCal(W1,T1,W1,T1+1,1,meaT_tauUnit); G_Auto1(m) = (meaT_tauUnit-1)*G_A1; %
Channel 1
    [G_A2] = CorrCal(W2,T2,W2,T2+1,1,meaT_tauUnit); G_Auto2(m) = (meaT_tauUnit-1)*G_A2; %
Channel 2
End
for i_g = 2:q


    for m = i_g*(p/2)+1:(i_g+1)*p/2
        tau(m) = tau(m-1) + (delT*(2^floor(2*(m-1-(p/2))/p)));
        [W1,T1] = round_MT(MT_photon_Det1,tau(m));
        [W2,T2] = round_MT(MT_photon_Det2,tau(m));
        meaT_tauUnit = max(max(T1),max(T2)); % M


        % Cross correlation
        [G1] = CorrCal(W1,T1,W2,T2+1,1,meaT_tauUnit); % Shift the photons from Ch 1
        [G2] = CorrCal(W2,T2,W1,T1+1,1,meaT_tauUnit); % Shift the photons from Ch 2
        G_Cross(m) = (meaT_tauUnit-1)*(G1+G2)/2;

        % Auto correlation
        [G_A1] = CorrCal(W1,T1,W1,T1+1,1,meaT_tauUnit); G_Auto1(m) = (meaT_tauUnit-1)*G_A1;
% Channel 1
        [G_A2] = CorrCal(W2,T2,W2,T2+1,1,meaT_tauUnit); G_Auto2(m) = (meaT_tauUnit-1)*G_A2;
% Channel 2
    end

end

G_Cross = G_Cross-1; G_Cross = G_Cross.';
G_Auto1 = G_Auto1-1; G_Auto1 = G_Auto1.';
G_Auto2 = G_Auto2-1; G_Auto2 = G_Auto2.';
tau = tau.';

end

%% EXTRA FUNCTIONS
function [W,T] = round_MT(MT_photon,binT) % Round MT in binT unit
MT = floor(MT_photon./binT);
[W,T] = groupcounts(MT);
end

function [G] = CorrCal(W1,T1,W2,T2,tau_binUnit,meaT_binUnit) % Round MT in binT unit
% Find the same elements
[comp, Loc2] = ismember(T1,T2);
Loc2(Loc2==0) = [];
N_corr = sum(W1(comp~=0).*W2(Loc2));
N_direct = sum(W1(T1>tau_binUnit));
N_delay = sum(W2(T2<=meaT_binUnit));
G = N_corr/N_direct/N_delay;
end
```

Appendix G

Raw Data Location

All data are stored at the Nienhaus Group, Institute für Angewandte Physik, KIT. Specific datasets can be identified using the main equipment names and/or measurement dates provided in this section.

Data for Chapter 4: General characterization of WNT proteins extracellularly secreted by living cells

Data	Main equipment	Date
Emission spectra of conditioned media	Fluorolog-3	01.03.24, 20.04.24
Qualitative functionality test of mCherry2/mScarlet-WNT	Luciferase reporter assay	01.09.23, 08.09.23
Radius distribution of particles in non-EV, small-EV, and large-EV fractions	Zetasizer (DLS)	-
Relative mCherry2/mScarlet-WNT concentrations in non-EV, small-EV, and large-EV fractions	Fluorolog-3	18.04.23, 04.09.23, 11.09.23, 06.02.24
Comparison of canonical Wnt signaling activities induced by mCherry2-WNT3a in non-EV, small-EV, and large-EV fractions using dual-luciferase reporter assays	Fluorolog-3	20.09.23
	Luciferase reporter assay	23.09.23

Data for Chapter 5: Determination of Wnt protein numbers per particle determined using N&B analysis

Data for determining the maturation efficiencies of mCherry2 and mScarlet expressed in cytosol

Sample	Microscope	Date	Remarks
mCherry2	M2	23–24.07.22, 28–29.07.22	Data measured on 06.07.22 and 14.07.22 were not included in the analysis because they were measured with a different power.
mScarlet	M2	18–19.02.22, 03.04.22	Data measured on 12.02.22 were not included in the analysis because they were measured with a different power.

Data for determining the maturation efficiencies of mCherry2 and mScarlet purified from *E. Coli* using the base-denaturation approach

The data were acquired on 09.09.22 and were stored on the server in the Cary folder.

Data for determining the molecular brightness of non-EV-bound mScarlet-WNT3a/5a/11

Sample type	Microscope	Date	Remark
Molecular brightness of mScarlet-WNT3a/11			
mScarlet-WNT3a	Microtime	14.09.23	-
mScarlet-WNT11	Microtime	14.09.23	-
mScarlet	Microtime	14.09.23	-
Background	Microtime	14.09.23	-
Molecular brightness of mScarlet-WNT5a			
mScarlet-WNT5a	M2	03.05.22	Additional measurement data from earlier days are available, but only the dataset from the final measurement day was used for analysis because by this stage the measurement protocol had been fully optimized, ensuring rigorous control of the measurements.
mScarlet	M2	03.05.22	
Background	M2	03.05.22	

Data for determining the molecular brightness of EVs carrying mScarlet-WNT3a/5a

Only samples that were measured for both molecular brightness and hydrodynamic radius were included in the analysis.

Sample	Microscope	Date	Additional label
Small EVs, mScarlet-WNT3a			
1	Microtime	03.08.23	Sam 1
2	Microtime	03.08.23	Sam 2
3	Microtime	04.08.23	Sam 3
4	Microtime	22.08.23	Sam 4
5	Microtime	22.08.23	Sam 5
6	Microtime	23.09.23	SEC
Small EVs, mScarlet-WNT5a			
1	M2	08.04.22	17_03_22 fresh
2	M2	11.04.22	21_03_22 fresh
3	M2	11.04.22	22_03_22 fresh
4	M2	11.04.22	23_03_22 fresh
Large EVs, mScarlet-WNT3a			
1	Microtime	17.04.23	MV1
2	Microtime	17.04.23	MV2
3	Microtime	18.04.23	MV1
4	Microtime	18.04.23	MV2
Large EVs, mScarlet-WNT5a			
1	M2	03.11.21	Sam A
2	M2	03.11.21	Sam E
3	Microtime	05.05.23	Sam 1
mScarlet			
1	Microtime	03.08.23	mScarlet 1
2	Microtime	03.08.23	mScarlet 2
3	Microtime	04.08.23	-
4	Microtime	13.09.23	-
Background, measured under 0.7 kW cm^{-2} excitation			
1	Microtime	22.08.23	pcDNA 1
2	Microtime	22.08.23	pcDNA 2
3	M2	08.04.22	-
4	Microtime	05.05.23	-
5	Microtime	19.09.23	pcDNA A
6	Microtime	19.09.23	pcDNA B
7	Microtime	20.09.23	-

Sample	Microscope	Date	Additional label
Background, measured under 1.4 kW cm^{-2} excitation			
1	Microtime	03.08.23	pcDNA 1
2	Microtime	03.08.23	pcDNA 2
3	Microtime	04.08.23	-
4	Microtime	13.09.23	-
5	Microtime	06.09.23	pcDNA_1_1
6	Microtime	06.09.23	pcDNA_2_1
7	Microtime	07.09.23	pcDNA 1
8	Microtime	07.09.23	pcDNA 2
9	Microtime	08.09.23	-
10	M2	03.11.21	-

Data for Chapter 6: Hydrodynamic radii of secreted Wnt particles determined using FCS

Data for investigating the flickering of mCherry2 and mScarlet

Sample	Microscope	Date
mCherry2	Microtime	04.07.23, 26.07.23
mScarlet	Microtime	25.01.23

Data for determining the hydrodynamic radii of non-EV-bound mCherry2-WNT3a/5a/11 units determined via translational diffusion

Sample	Microscope	Date
mCherry2		
1	Microtime	04.07.23
2–3	Microtime	26.07.23
mCherry2-WNT3a		
1	Microtime	12.12.23
2	Microtime	11.12.23
3	Microtime	14.12.23
4–5	Microtime	09.08.23
6	Microtime	10.08.23
mCherry2-WNT5a		
1	Microtime	13.07.23
2–3	Microtime	25.07.23

Sample	Microscope	Date
mCherry2-WNT11		
1–2	Microtime	11.12.23
3	Microtime	12.12.23

Data for investigating the rotational Brownian motion of non-EV-bound mCherry2-WNT3a/5a/11 units determined via rotational diffusion

Sample	Microscope	Date	Additional label
Observed rotational diffusion with respect to laser power (Figure 6.4)			
mCherry2-WNT3a	Microtime	18.12.23	-
Autocorrelation functions of non-EV-bound mCherry2-WNT3a/5a/11 (Figure 6.5)			
mCherry2	Microtime	04.12.23	
mCherry2-WNT3a – Sample 1	Microtime	05.12.23	Sam A
mCherry2-WNT3a – Sample 2	Microtime	12.12.23	Sam B
mCherry2-WNT3a – Sample 3	Microtime	14.12.23	Sam C
mCherry2-WNT5a – Sample 1	Microtime	18.12.23	Sam A
mCherry2-WNT5a – Sample 2	Microtime	18.12.23	Sam B
mCherry2-WNT5a – Sample 3	Microtime	18.12.23	Sam C
mCherry2-WNT5a – Sample 3	Microtime	18.12.23	Sam D
mCherry2-WNT11 – Sample 1	Microtime	11.12.23	Sam A
mCherry2-WNT11 – Sample 2	Microtime	11.12.23	Sam B
mCherry2-WNT11 – Sample 3	Microtime	12.12.23	Sam C
mCherry2-WNT11 – Sample 4	Microtime	13.12.23	Sam F

Data for determining the hydrodynamic radii of small and large EVs transporting mScarlet-WNT3a/5a

Only samples that were measured for both molecular brightness and hydrodynamic radius were included in the analysis.

Sample	Microscope	Date	Additional label
Small EVs, mScarlet-WNT3a			
1	Microtime	03.08.23	Sam 1
2	Microtime	03.08.23	Sam 2
3	Microtime	04.08.23	Sam 3
4	Microtime	22.08.23	Sam 4
5	Microtime	22.08.23	Sam 5
6	Microtime	23.09.13	SEC

Sample	Microscope	Date	Additional label
Small EVs, mScarlet-WNT5a			
1	M2	08.04.22	17_03_22 fresh
2	M2	11.04.22	21_03_22 fresh
3	M2	11.04.22	22_03_22 fresh
4	M2	11.04.22	23_03_22 fresh
Large EVs, mScarlet-WNT3a			
1	Microtime	17.04.23	MV1
2	Microtime	17.04.23	MV2
3	Microtime	18.04.23	MV1
4	Microtime	18.04.23	MV2
Large EVs, mScarlet-WNT5a			
1	M2	03.11.21	Sam A
2	M2	03.11.21	Sam E
3	Microtime	05.05.23	Sam 1

Data for Chapter 7: Investigation into co-migrating structures of non-EV-bound Wnt units

Data for investigating the Effect of MβCD on the diffusion coefficients of non-EV-bound mCherry2-WNT3a/5a/11

Sample type	Sample	Microscope	Date
mCherry2-WNT3a	1	Microtime	17.04.24
	2	Microtime	17.04.24
	3	Microtime	18.04.24
mCherry2-WNT5a	1	Microtime	22.04.24
	2	Microtime	22.04.24
	3	Microtime	23.04.24
	4	Microtime	08.05.24
mCherry2	1	Microtime	18.04.24
	2	Microtime	20.04.24
	3	Microtime	23.04.24

Data from dual-color fluorescence cross-correlation spectroscopy measurements on non-EV-bound mCherry2-WNT3a/5a/11 incubated with AB-CoraLite 488

The data were acquired on 29.04.24 using the Microtime setup. The files include an additional label, *50nM*, in their filenames.

Data from dual-color fluorescence cross-correlation spectroscopy measurements on WNT3a proteins co-diffusing with Afamin

The data were acquired on 30.04.24 using the Microtime setup. The files include an additional label, *no FBS*, in their filenames.

Academic Accomplishments

Publications

- Schubert, A, Mongkolsittisilp, A, *et al.* WNT5a export onto extracellular vesicles studied at single-molecule and single-vesicle resolution. *The FEBS Journal* (2025) - *accepted*.

Oral presentations

- Biophysical characterization of extracellular Wnt5a. *SFB1324 Wnt seminar*, Jun 12, 2023. Heidelberg University.
- Quantitative characterization of secreted Wnts. *SFB1324 Wnt seminar*, Mar 7, 2022. Online.
- Analyzing intercellular Wnt trafficking by advanced fluorescence microscopy. *SFB1324 Wnt seminar*, Feb 8, 2021. Online.

Poster presentation

- Schubert, A., Winkler, N., Mongkolsittisilp, A., et al, Extracellular vesicles as carriers of signaling factors in cancer. *Proceedings of the American Association for Cancer Research Annual Meeting 2024*, Apr 5–10, 2024, San Diego, CA. (presented by Schubert, A.)

Supervised theses

- Wittmann, I., Application of fluorescence correlation spectroscopy and number and brightness analysis to characterize secreted WNT3a. Bachelor's Thesis, 2023
- Seiler, A., Anwendung von Fluoreszenz-Fluktuationsspektroskopie an biologischen Proben. Bachelor's Thesis, 2021

Acknowledgements

I would like to acknowledge the following research groups for providing valuable resources and scientific input during the course of this research:

- The Nienhaus group, Institute of Applied Physics, Karlsruhe Institute of Technology
- The Boutros group, Medical Faculty Heidelberg, Heidelberg University
- The Institute of Organic Chemistry, Karlsruhe Institute of Technology
- All collaborators in the SFB1324: Mechanisms and Functions of WNT Signaling

I would also like to express my deepest appreciation to my referees and exam committee members, whose presence and fair evaluation were absolute instrumental in the successful completion of this thesis.

In addition, pursuing a PhD is a mentally challenging journey, and I am deeply grateful to my mentor, Prof. Wolfgang Wernsdorfer, from the Karlsruhe House of Young Scientists (KHYS), for his insightful consultations, which made this journey significantly easier. My sincere thanks also go to the Karlsruhe School of Optics and Photonics (KSOP) for their excellent training programs, which helped me grow into a professional researcher, and to my kind mentor, Dr. Franco Weth, for his unwavering support and guidance through the hardships, leading me to the completion of this thesis.

I am also grateful for my former colleagues who have been especially supportive and kind throughout my academic journey: Dr. Gernot Guigas, Dr. Siqing Dai, Dr. Martin Štefl, and Dr. Manuel Hüpfel.

Furthermore, I would like to thank my friends, who have shared both laughter and frustrations with me along the way: Miyase Tekpınar, Sven Triebskorn, Dr. Hao Jia, Dr. Kathryn Machray, Dr. Terry Weight, Thanyarat Ritdet, and Jakkapong Saksrisuwan. Most importantly, I would not have come this far without the unwavering support of my family – the Mongkolsittisilp and Schecher families, whose support has been my greatest strength.